12-2008

COMPUTIONAL MODELING OF PRECISION MOLDING OF ASPHERIC GLASS OPTICS

Balajee Ananthasayanam
Clemson University, bananth@clemson.edu

COMPUTIONAL MODELING OF PRECISION MOLDING OF ASPHERIC GLASS OPTICS

A Dissertation
Presented to
the Graduate School of
Clemson University

In Partial Fulfillment
of the Requirements for the Degree
Doctor of Philosophy
Mechanical Engineering

---

by
Balajee Ananthasayanam
December 2008

Accepted by:
Dr. Paul F. Joseph, Committee Chair
Dr. Lonny L. Thompson
Dr. Sherrill B. Biggers
Dr. Vincent Y. Blouin
Dr. Mica Grujicic

ABSTRACT

In this dissertation, research in two parallel directions is presented; the first involves the prediction of the final size and shape of a glass lens during a precision glass lens molding process and the second introduces a method to compute and quantify the importance of higher order terms in fracture mechanics for different modes of fracture.

The process of precision lens molding has received attention in recent years due to its potential to mass produce aspherical lenses. Aspherical lenses have significantly better optical properties and conventional lens making techniques are limited to manufacturing of spherical lenses only. The conventional technique involves an iterative procedure of grinding, lapping and polishing to obtain a desired surface profile. However in precision molding, the glass raw material or preform is placed between dies and heated until it becomes soft and molten. Then the dies are pressed against each other to deform the molten glass to take the shape of the dies. After this stage glass is cooled to room temperature by the use of nitrogen gas. Thus, in a single process the lens is made unlike the traditional approach. Although the molding process appears to a better alternative, there are shortcomings that need to be addressed before using the process for mass production. From the point of view of the current study, the shortcomings include both surface profiles and center thickness of the final lens.

In the expensive process of mold preparation, the mold surfaces are first machined to be exact negatives of the required surface profile of the lens. One of the main issues is the deviation of the surface profile of the final molded lens from that of the molds due to the complex, time and temperature dependent stress state experienced by the lens during the approximately 15 minute process of heating, pressing and then cooling. In current practice the deviation of manufactured

lenses is as high as 20 microns, approximately 20 times the allowable deviation according to the optical design specifications. The empirical approach to solving this problem is to compensate the molds by trial and error based on practical experience which is very time-consuming and costly. Usually it takes 3-4 months and a considerable amount of money to compensate the molds to meet current specifications. This has motivated the development of computational solutions to arrive at a compensated mold shape which requires the prediction of the lens deviation within micron level accuracy taking into account process parameters and the complex material behavior of glass.

In this research, ABAQUS, a commercial FEM solver, is used to simulate the process and predict the final size/shape of the lens. The computational study of final size and shape includes a sensitivity analysis of the various material and process parameters. The material parameters include viscoelasticity, structural relaxation and the thermo-rheological behavior of the glass; friction and gap dependent heat transfer at the interface; and the thermo-mechanical properties of the molds. This comprehensive study will not only eliminate some of the parameters which have the least effect on the final size/shape, but also identify the key material properties and substantiate the need to obtain them more accurately through experimentation. At this time it should be mentioned that the material properties of the molding glasses considered are not available.

Friction coefficient at the mold/glass interface is one of the important input parameters in the model. A ring compression test was used in the current research to find the friction coefficient. In this test, a “washer” or a ring shaped specimen is compressed between two flat dies at the molding temperature and the change in internal diameter is correlated to a friction coefficient.

The main strength of this test is the sensitive nature of the inner diameter change during pressing for different friction conditions at the interface. In addition to friction coefficient, approximate viscoelastic material properties and the TRS behavior were also found out using this test from the experimental force and displacement data.

After validating the model to well within one micron, it was determined that the deviation of the lens profile with respect to the molds is primarily caused by structural relaxation of glass, thermal expansion behavior of the molds, friction at the glass/mold interface and time-temperature dependence of the viscoelastic material behavior of glass. Several practical examples/numerical studies that clearly show the cause for the deviation are presented. It is also shown that the deviation in the molded lens is affected by its location with respect to the molds. Finally the process of mold compensation is demonstrated using the computational tool.

In the other parallel direction, a method to determine higher order coefficients in fracture mechanics from the solution of a singular integral equation is presented. The coefficients are defined by

$$\sigma_{rr}(r,0)=\sum_{n=0}^{\infty} k_n (2r)^{n-\frac{1}{2}} + T_n (2r)^n ,$$

which gives the radial stress at a distance, r, in front of the crack tip. In this asymptotic series the stress intensity factor, k_0 is the first coefficient, and the T-stress, T_0 is the second coefficient. For the example of an edge crack in a half space, converged values of the first twelve mode I coefficients (k_n and T_n, n=0,…,5) have been determined, and for an edge crack in a finite width strip, the first six coefficients are presented. Coefficients for an internal crack in a half space are also presented. Results for an edge crack in a finite width strip are used to quantify the size of the

k-dominant zone, the kT-dominant zone and the zones associated with three and four terms, taking into account the entire region around the crack tip. Finally, this method was also applied to fracture problems with Mode-II loading.

DEDICATION

To my parents Mr. Ananthasayanam Srinivasan and Mrs. Leela Mylapore Selvaraj.

ACKNOWLEDGEMENTS

I would like to thank my advisor, Dr. Paul Joseph for his guidance and support.

I would also like to thank Dr. Kathleen Richardson, Dr. Igor Luzinov and Dr. Vincent Blouin, Dr. Laeticia Petit, Dr. Ruslan Burtovy and Scott Gaylord, all from material science and engineering, for working with me closely during the last two years and whose valuable inputs have shaped this research. I would also like to thank Matthew Stairiker and Matthew Tardiff of Edmund Optics for closely working with me and conducting the experiments that I needed for this research.

I would also like to thank my committee members for giving me good suggestions on improving the research as well as the documentation. I have taken courses under almost every professor in my committee and thank them for helping me understand the foundations of solid mechanics and finite element methods.

TABLE OF CONTENTS

Page

Table of Contents (Continued)

Page

Table of Contents (Continued)

Page

Table of Contents (Continued)

Page

LIST OF TABLES

List of Tables (Continued)

LIST OF FIGURES

List of Figures (Continued)

Figure Page

List of Figures (Continued)

Figure Page

List of Figures (Continued)

Figure Page

List of Figures (Continued)

Figure Page

List of Figures (Continued)

Figure Page

List of Figures (Continued)

Figure Page

List of Figures (Continued)

List of Figures (Continued)

Figure Page

CHAPTER ONE

Introduction

In this dissertation, research in two parallel directions is reported; the first involves the prediction of the final size and shape of a glass lens during a precision glass lens molding process and the second introduces a method to compute and quantify the importance of higher order terms in fracture mechanics for different modes of fracture. This latter approach can be used to extend traditional linear elastic fracture mechanics using just the stress intensity factor, which is valid for glass at room temperature, to address fracture due to residual stresses generated in glass during lens molding, that occur at high temperature.

1.1 Introduction

Precision molded glass optics has gained momentum in recent years due to its cost effectiveness for producing aspherical lens profiles [1-6]. Aspherical lens profiles are designed to avoid optical aberration created in conventional spherical lenses. Optical aberration is defined as the inability of all light rays emerging out of a lens to pass through a single point, called the focal point and hence has a tendency to blur the image as shown in Figure 1.1. The surface of a spherical lens conforms to the surface of a sphere whereas an aspherical lens surface does not. An aspherical lens is nothing but a spherical lens whose surface profile is slightly modified to compensate for any optical aberration that would be created in the spherical lens as shown in Figure 1.1. Other advantages of using aspherical elements in optical devices include lens count reduction, easier assemblage and reduced internal reflection [3,4].

The conventional lens manufacturing technique involves an iterative procedure of grinding, lapping and polishing to obtain a desired surface profile [4, 5]. Initially this technique was very costly, but continuous innovations in machining methods and efficient process planning

have reduced cost considerably. However, these innovations are limited to mass production of spherical lenses only. The production of an aspherical lens surface, requires specialized polishing techniques such as Magneto-rheological finishing (MRF) and Precision polishing method [5]. While these techniques are able to produce very high quality lens surfaces, the cost involved in production is very high and the byproducts such as cutting fluids and, lead from certain glass types are dangerous to the environment. More references on these machining methods are given in work of Firestone *et al* [4].

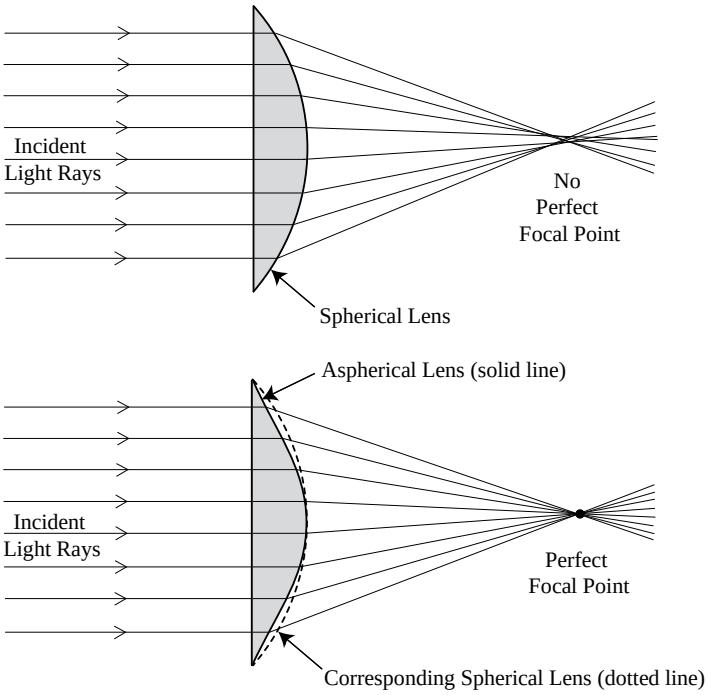

Figure 1.1: Spherical Aberration in a Lens

The precision lens molding process, hence, is a cost effective alternative for mass production of aspherical lenses. An illustration of this process is shown in Figure 1.2. The process begins with a glass preform placed between dies and heated using Infra-red (IR) lamps. The word “preform” is used to address the work piece in precision lens molding terminology because it has already

undergone some machining, grinding and polishing prior to molding. These IR lamps coil around the dies and only the cross-section is shown in the Figure 1.2. Once the glass becomes sufficiently molten, the lower die moves up and presses the lens into the desired shape. Then the entire assembly is cooled by a controlled flow of nitrogen. Thus, the entire shaping is done in one operation which saves machine time and money.

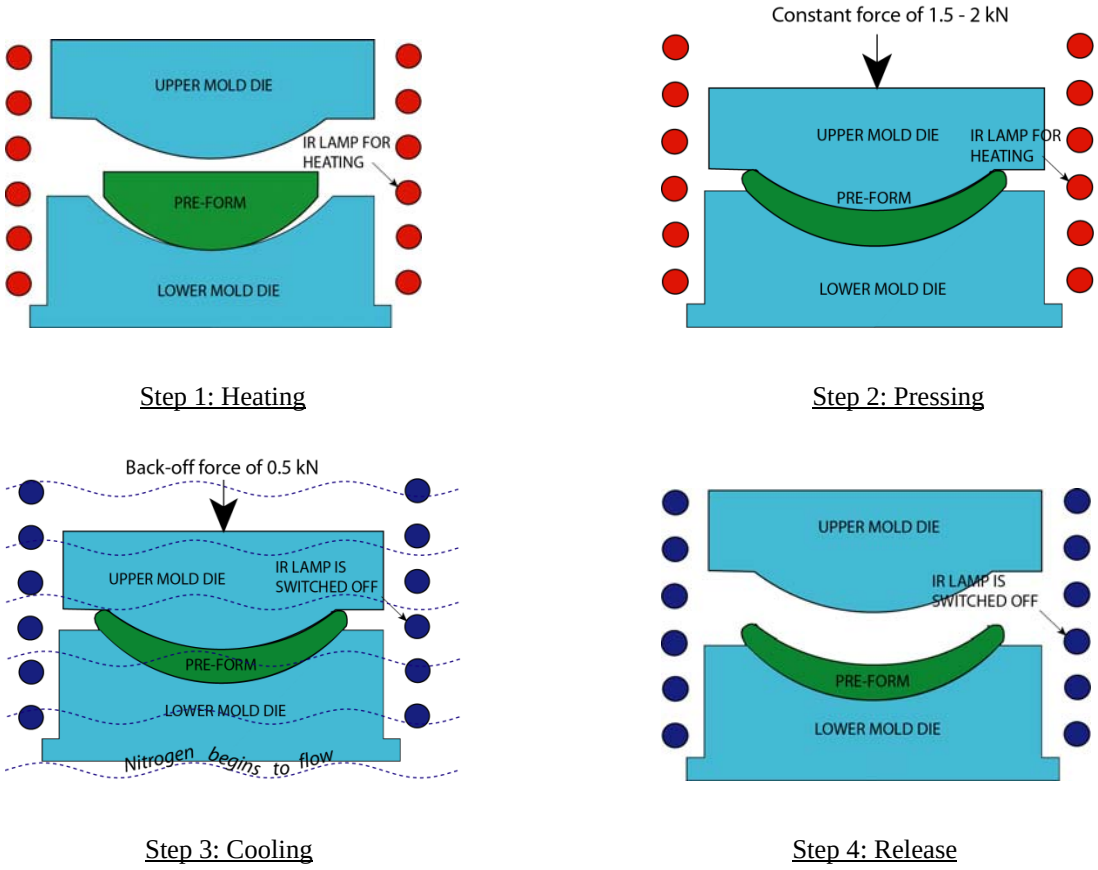

Figure 1.2: Illustration of precision lens molding process.

1.2 Motivation for Current Research

Although the molding technique appears to be a better alternative, there are several shortcomings in the process that need to be overcome before it is used for mass production. From the point of view of the current study, the most important ones are listed below:

(i) Curvature or profile deviation of the lens (see Figure 1.3).

(ii) Birefringence due to residual stresses that are locked in during molding.

(iii) Other issues such as mold life, mold-coating life and adherance of glass material to the mold surface, are mentioned by Jain *et al* [3].

The final geometry (shape and size) of the molded lens is very important in determining its optical properties. For example, if the profile of the lens on either side deviates from the desired profile by a mere 10 microns, aberration is increased greatly. In other words, to control aberration, deviation should be controlled. Typically, the mold surfaces are machined to be exact negatives of the required surface profile of the lens assuming the lens would take the profile of the molds. But in reality, due to the complex mechanical behavior of glass and its strong temperature dependence, the final lens surface at room temperature deviates from the required profile by as much as 20 microns. This is approximately 20 times the allowable deviation according to the optical designers' specifications. Figure 1.3 shows the deviation of a lens profile as a function of radial distance.

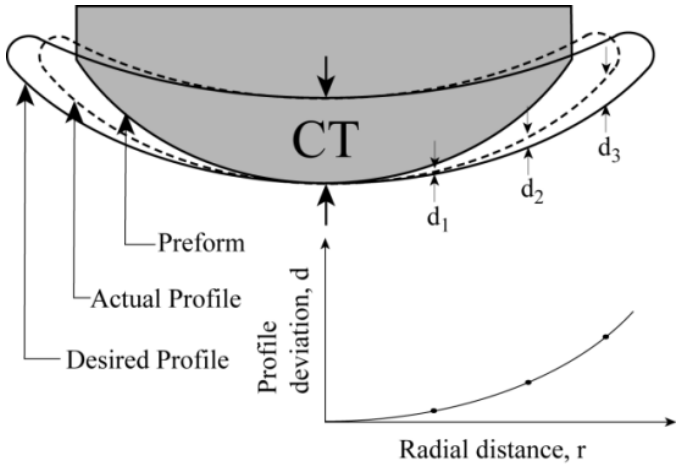

Figure 1.3: The schematic shows the Preform, Center thickness (CT) of the molded lens, desired lens profile and the actual molded lens profile. The maximum allowable profile deviation is in the order of 1 micron.

The current approach to solving this problem is to modify the size and shape of the molds by trial and error, based on practical experience, to compensate for the temperature dependence of the material properties. This is referred to as mold compensation. The main problem is the cost and time required for the mold compensation. The mold compensation is usually done using a separate machine that has a capability to create a surface with a few nanometer surface-finish. Usually, it takes 3-4 months to compensate the molds to meet current product specifications and the cost of re-tooling the mold once is around $4000. This has motivated the development of computational approaches to create a compensated mold shape which requires the prediction of the lens deviation within micron level accuracy taking into account process parameters and the complex material behavior of glass.

An example of mold compensation done at Edmond optics is illustrated in Figure 1.4. In this figure, the solid red line refers to the uncompensated Tungsten-Carbide molds (exact negative of the required lens profile) and the dotted red line refers to the corresponding lens deviation which is approximately 20 microns. In the next iteration, a different mold made of glassy carbon is compensated by the same amount of the lens deviation which is represented by the solid blue line. But the lens still deviates from the zero line by approximately 8 microns in the other direction. This shows that the compensation is highly mold material dependent. In Chapter 6, the exact reason for this kind of behavior, which is the difference in thermal expansion coefficient between the two molds, will be illustrated.

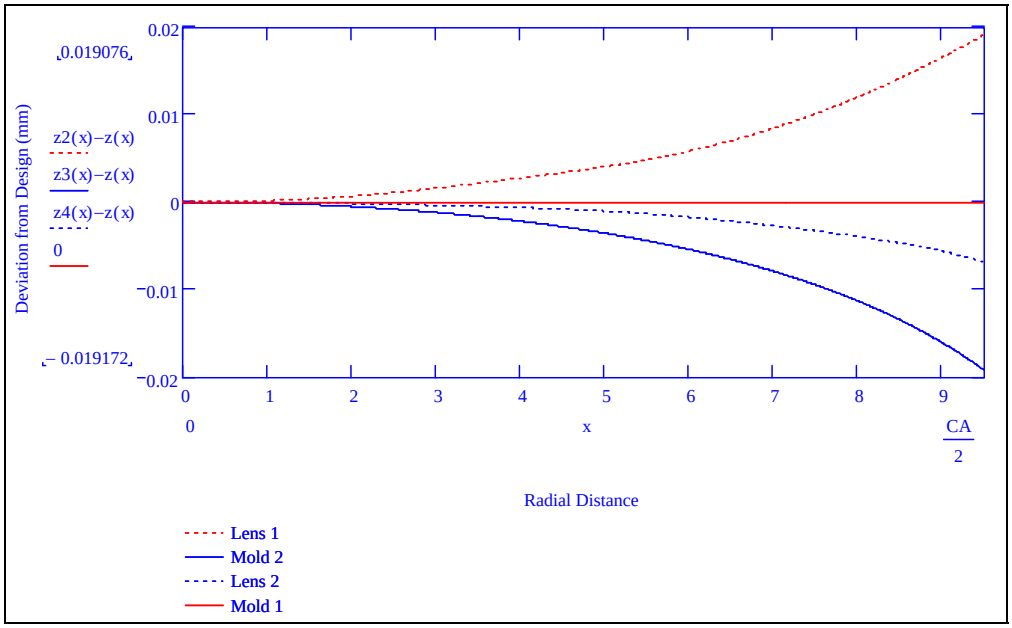

Figure 1.4: Experimental evidence of profile deviation from a lens molding machine. The solid red line corresponds to the uncompensated mold and the dotted red line corresponds to the deviation of the molded lens. In this study a different mold material was used in the second iteration.

1.3 Glass Transition

When subjected to either mechanical or thermal loads, glass behaves in a unique manner in different temperature regions. Unlike metals that have a stable crystalline structure at room temperature, glass is in a non-equilibrium state which is generally referred to as a frozen liquid state or a glassy state [7] as shown in Figure 1.5. Both behave as viscous fluids at high temperature, but take different paths

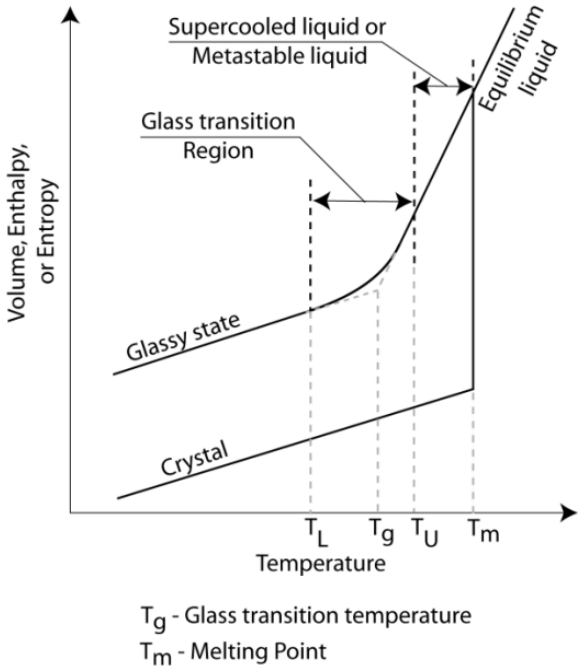

Figure 1.5: Comparison of volume or enthalpy change of glass with that of a metal during heating or cooling.

when cooled below their melting point. Metals exhibit elastic behavior below the melting point while glass exhibits more complex behavior. Glass has three distinct regions namely the liquid region, the transition region, and the glassy region. Under mechanical loading, glass behaves like

i. a viscous fluid in the liquid region,

ii. a viscoelastic fluid in the transition region

iii. an elastic solid in the glassy region.

Under thermal loads, thermal expansion behavior of glass is instantaneous in the liquid and the glassy region while it is time dependent in the transition region. This time-dependent thermal expansion of glass in the transition region referred in the literature as *structural relaxation* phenomenon of glass. Also, specific heat, refractive index, density, viscosity and enthalpy show such type of time-dependence indicating that structural relaxation has an effect on all these properties. The glass transition temperature is approximately the mid-point temperature of the

transition region. This temperature slightly changes during every heating/cooling cycle. If cooled fast, this temperature would be slightly higher than the mid-point temperature while it would be lower if cooled slowly. This behavior of glass is exploited in tempering/annealing of glass to increase the strength (fast cooling) or compliance (slow cooling).

The temperature at which glass is molded is very crucial to the final shape and size of the lens [1]. If glass is molded at temperatures lower than T_g, the material is destroyed as it is too brittle. If on the other hand, glass is heated to a temperature much higher than T_g, then molding becomes easy, but contraction of glass during cooling increases and adverse chemical reactions between glass and mold are more likely to occur, which contribute to mold degradation. Since it is very difficult to control the cooling profile in time and space, and mold degradation is a major obstacle for this technology, it is advantageous to press the lens at temperatures within the glass transition region where glass behaves more as a viscoelastic material, although viscous flow is still the dominant mechanism that allows molding to occur.

1.4 Research Goals

Based on the problems faced by the glass lens molding industry (see Section 1.2) and the complex material behavior of glass in the transition region (see Section 1.3), the goals of this research are summarized as follows:

1. Development of a finite element model of the entire lens molding process that includes heating, pressing and cooling stages in ABAQUS.
2. Implementation of structural relaxation behavior of glass in ABAQUS via user subroutines.
3. Prediction of the final size and shape of the molded glass lens after pressing within micron level accuracy.

4. Investigation of the effect of various material and process parameters on final shape/size prediction.
5. Characterization of friction coefficient at the glass/mold interface under molding conditions.
6. Accurate determination of higher-order terms and their zones of dominance in fracture mechanics for mode I and mode II type of loading using a singular integral equation approach. This research is independent from the lens molding research.

1.5 Past Work in the Literature

A review paper by Brown [8] covers all the research done in developing simulation models for glass pressing operations at high temperature. All the studies make use of the assumption that glass is a Newtonian viscous fluid. Since the current molding process necessitates a lower pressing temperature for better product quality, only the papers where glass is modeled as a viscoelastic material are discussed in this section.

Jain *et al* [9] used stress relaxation data from a cylinder compression test to extract the viscoelastic properties and viscosity data to be used in simulation to predict the stress state at the end of the molding cycle. The other properties such as elastic modulus were measured using a Brillouin light-scattering technique. Their experimental data show that the Young's modulus is fairly constant until the glass transition temperature and then drops drastically. This kind of behavior is also suggested qualitatively in Chapter 5 of Loch *et al* [10]. Finally, a comparison between maximum force measured and that obtained from simulation is made to validate the result. In this paper the molding is done under displacement control and hence the force varies as a function of time. The cooling stage was not modeled in this paper where the complex phenomenon of structural relaxation comes into play. Also, the friction condition at the interface

during the lens molding process and the cylinder compression test is not mentioned in the paper. However in their earlier paper [3], they assumed full sticking. Glass was also assumed to be incompressible.

In a later paper by Jain *et al* [11], the effects of structural relaxation were included in the annealing stage of the lens molding process. However, the temperature dependence of Young's modulus and the compressibility of glass were not included in the simulation. Furthermore, the viscoelastic material was modeled with a single Maxwell element and complete sticking was assumed at the interface of the molds and glass. Their results do not show any influence of cooling rate on the final curve deviation. However, it is a well known fact that stress developed in a glass specimen is strongly cooling-rate dependent and the sandwich seal solution is a good example [12] or any tempering process where the strength of the glass is determined by its cooling rate after it is heated. Hence the displacement field should also be strongly temperature dependent and the reason why their result does show a difference can be attributed to the simplifying assumptions made in their analysis.

S. H. Chang *et al* [13] simulated a glass molding process where glass is modeled as a power-law strain-rate hardening material. A cylindrical compression test was performed on the glass at elevated isothermal temperature and the material constants were evaluated. They also tried to compute the friction at the glass/mold interface from the same experiment. The issue with the model is that the time dependence of the stresses and strains are not included.

J. W. Na *et al* [14] simulated a mold process to predict the birefringence distribution in a molded lens. They used a glass material that is incompressible under volumetric load and linear viscoelastic under shear loads. The effects of structural relaxation were not included in the cooling stage of the process. New preform shapes were used to create a different birefringence patterns which would alter optical properties.

M. Sellier *et al* [15] developed a simplified finite element model of the lens molding process and coupled it with an optimizer to arrive at the compensated mold shape for producing a high-quality lens with a desired surface profile with accuracy of the order of 1μm. This research mainly focused on the optimization part i.e. arriving at the compensated mold shape by minimizing the mismatch between the actual and the desired mold geometry. Some of the advantages of their method are it does not necessitate the parameterization of the mold and the computation of the sensitivities with respect to different material and process parameters. The disadvantage of this method is its small radius of convergence. Although this method was not validated experimentally, theoretically the method converges to a mold shape that minimizes the mismatch or deviation within a micron. Although, the friction model used at the glass/mold interface was not clear, the heat transfer model at the interface between the glass and the mold surfaces was very pertinent to the precision molding process and was adopted in the current research as well; the details are given in the next Chapter.

1.6 Fracture of glass and the possible use of higher order terms

As stated in the Introduction, research in two parallel directions is presented in this dissertation; Chapters 2, 3, 4, 5 and 6 cover research related to the precision lens molding process, and Chapters 7 and 8 introduce a method to compute the higher order terms in fracture mechanics and quantify their importance. As will be shown in Chapter 6, residual stresses are generated in a glass lens during molding and cooling that can easily crack a lens. Furthermore, the maximum tensile stresses can occur at any temperature during cooling; sometimes these peak stresses increase as the lens is cooled and sometimes they decrease. One capability of the current research is to determine material and/or process parameters to avoid such fracture by lowering residual stresses.

In order to predict fracture initiation or fracture patterns in a lens, it is necessary to select a fracture theory. Fracture of glass at room temperature can be predicted using standard linear elastic fracture mechanics (LEFM), which makes use of the stress intensity factor. However, as the temperature increases, LEFM using just the stress intensity factor terms will no longer apply due primarily to non-elastic material behavior in response to high load near the crack tip. For any traditional linear or nonlinear fracture theory to be valid, the asymptotic solution must adequately represent the true stress state far enough away from the crack tip to stay "well outside" of a region too close to the crack tip where the theory is not valid. In Chapters 7 and 8 a method is presented to extend the distance from the crack tip where the asymptotic solution is valid, therefore enabling LEFM to be extended somewhat into the higher temperature range. The use of this method of higher order terms in LEFM for lens molding is left for future work.

1.7 Organization of this Dissertation

In the Chapter 2, the general details of the molding process are introduced, followed by detailed explanations of the aspects that are relevant to the current research. Then, the finite element modeling of the manufacturing process is presented along with the modeling assumptions and thermal and mechanical boundary/initial conditions. Other details such as solver types used, constraints and contact interactions defined, error tolerances set and several other special features of the software used to simulate the real process are described.

In Chapter 3 a typical viscoelastic response of a glass sample (L-BAL35) is given along with the few experiments reported in the literature that are used to characterize this behavior. Then the details of an approximate method used to obtain the viscoelastic material behavior of glass from the ring compression tests are presented. This viscoelastic material characterization was used as a baseline for doing sensitivity analysis in Chapters 5 and 6. All the simulations of

the current research used this material behavior. Finally, the different non-linear curve fitting routines used to characterize the material response are given.

In Chapter 4, the important characteristics of structural relaxation are illustrated and then the different phenomenological models that are widely used to describe this behavior are given. Following this introduction, the implementation and validation of this behavior in the commercial finite element software, ABAQUS, are presented. Finally, experiments used to characterize this behavior along with the input parameters used for this research are given.

In Chapter 5, the friction coefficient at the glass/mold interface, an important parameter in the lens molding simulation is determined using ring compression tests. The details of the experiments and methods to extract the friction coefficient from them are described in detail.

From the work presented in Chapters 2-5, all the necessary input parameters such as initial/boundary conditions, loading, material behavior and interface behavior are known. In Chapter 6 the lens profile deviation from the molds is obtained from the finite element model and compared with the experimental deviation after a convergence study. Once validated, the sensitivity analyses are performed to see the changes in the deviation upon changes in the material and process parameters and the results are presented. Great effort is taken to understand the sources of deviation as well as to identify the important parameters.

In Chapters 7 and 8 research in fracture mechanics is reported. In Chapter 7 a method was given to compute the higher order terms and quantify their zones of dominance for mode I loading. In Chapter 8 the method was extended to compute higher order terms under mode II loadings also and these higher order coefficients were computed for several numerical examples.

Finally, in Chapter 9, the research is summarized, several important conclusions were made based on the experiments and simulations and recommendations for future work are made.

References

1. M. Katsuki, Transferability of glass lens molding, 2nd Intl. Symp. On Adv. Optical Manufacturing Technologies, edited by L. Yang, s. Wen, Y. Chen, E.-B. Kley, Proc. SPIE Int. Soc. Opt. Eng. **6149**(2006), pp. M1-M9.

2. R. O. Maschmeyer, C. A. Andrysick, T. W. Geyer, H. E. Meissner, C. J. Parker, and L. M. Sanford, Precision molded-glass optics, Appl. Opt. **22**(1983), 2410-2412.

3. A. Jain, A. Y. Yi, Numerical Modeling of Viscoelastic Stress Relaxation during Glass Lens Molding Process, J. Am. Ceram. Soc., **88**(2005), pp. 530-535.

4. G. C. Firestone, A. Jain, A.Y. Yi, Precision laboratory apparatus for high temperature compression molding of glass lenses, Rev. Sci. Instrum., **76**(2005),pp. 063101:1-8.

5. A. Y. Yi, A. Jain, Compression Molding of Aspherical Glass Lenses-A combined Experimental and Numerical Analysis, J. Am. Ceram. Soc., **88**(2005), pp. 579-586.

6. A. Jain, G. C. Firestone, A. Y. Yi, Viscosity Measurement by Cylindrical Compression for Numerical Modeling of Precision Lens Molding Process, J. Am. Ceram. Soc., **88**(2005), pp. 2409-2414.

7. S. M. Rekhson, Viscoelasticity of glass, Glass: Science and Technology edited by D. R. uhlmann and N. J. Kreidl , **3** (1986), pp. 1-118.

8. M. Brown, A review of research in numerical simulation for the glass-pressing process, Proc. of the I MECH E Part B J. Eng. Manuf., **221** (2007), Number 9, pp. 1377-1386.

9. A. Jain, A.Y. Yi, Finite element modeling of stress relaxation in glass lens moulding using measured, temperature-dependent elastic modulus and viscosity data of glass, Modelling Simul. Mater. Sci. Eng., **14**(2006),pp. 465-477.

10. H. Loch, D. Krause, Mathematical simulation in glass technology, Springer, 2002.

11. A. Jain, A.Y. Yi, Finite element modeling of structural relaxation during annealing of a precision-molded glass lens, ASME J. Manuf. Sci. Eng., **128**(2006),pp. 683-690.

12. G. W. Scherer, S. M. Rekhson, Viscoelastic-elastic composites: II, General Theory, J. Am. Ceram. Soc., **65**(1982),pp. 399-406.

13. S. H. Chang, Y. M. Lee, T. S. Jung, J. J. Kang, S. K. Hong, G. H. Shin, Y. M. Heo, Simulation of an aspheric glass lens forming behavior in progressive GMP process, NUMIFORM '07, Materials processing and design, 2007, pp. 1055-1060.

14. J.W. Na, S.H. Rhim, S.I. Oh, Prediction of birefringence distribution for optical glass lens, J. Mater. Process. Technol., **187-188**(2006). pp. 407-411.

15. Sellier. M, Breitbach. C, Loch. H, Siedow. N, An iterative algorithm for optimal mould design in high-precision compression molding, *Proceedings of the I MECH E Part B Journal of Engineering Manufacture*, **221**(2007), 25-33(9).

CHAPTER TWO

Details of Molding Process and Modeling Assumptions

2.1 Process Data and Inferred Details from Molding Machine

(a)

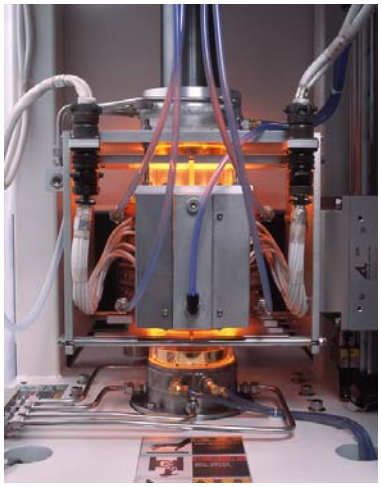

(b) (c)

Figure 2.1: (a) GMP-311VA Toshiba lens molding machine [1] (b) Die assembly with heating coils (c) Mold-Die after the molding process.

The Toshiba lens molding machine (GMP series) as shown in Figure 2.1 was used to mold a test lens made of OHARA L-BAL35 type glass and the process data from the machine is plotted in Figure 2.2. This plot includes temperature, applied force and resulting displacement of the lower mold as a function of time. This process data will be used for the validation study. The entire process takes approximately 23 minutes. The different stages in this precision lens molding process that can be seen in Figure 2.2 are:

(i) Heating (3.5 minutes),

(ii) Soaking (1.8 minutes),

(iii) Isothermal Pressing (2.17 minutes),

(iv) Slow cooling with maintenance force (5.3 minutes), and

(v) Rapid cooling stages (10.3 minutes).

Initial heating is with infra red (IR) lamps that heat the entire molding assembly from 153°C to the molding temperature of 589°C. Once this temperature is reached as indicated on a sensor placed near the molds, then the mold assembly with the preform is maintained at that temperature for 1.8 minutes. This process is called *soaking*. This soaking time is given to the glass prior to pressing because sufficient time is required for the interior of the glass to attain the temperature reading in the sensors, which are located on the outer periphery of the molds. After soaking, the preform was pressed under constant force of 2000N at the molding temperature until a desired displacement is reached. In this machine the force is controlled by a load cell attached to the bottom die. After this primary pressing stage the slow cooling begins to take place in the assembly with IR lamps turned off and cold nitrogen beginning to flow. During this slow cooling stage, a maintenance force of 500N is applied. This is done to prevent any gross shape changes because the glass is still hot and can deform easily. Finally, the lower die moves down reducing the force to zero and creating a small gap. The displacement is fixed at that position for the

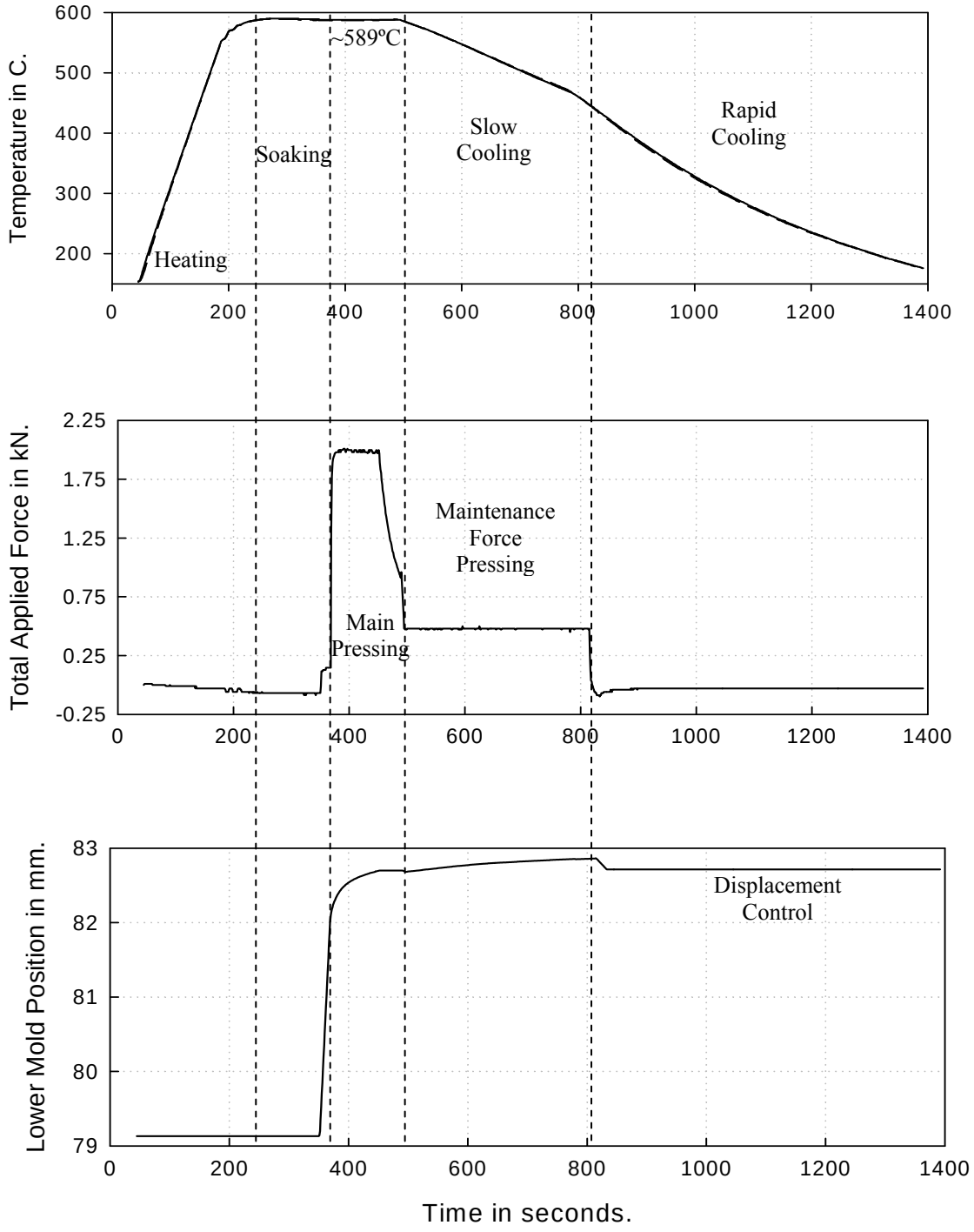

Figure 2.2: Process data from Toshiba lens molding machine, when a lens made of moldable glass material L-BAL35 is pressed at 589°C.

remaining duration of the process. A this time a full flow of nitrogen is triggered which cools the entire assembly in approximately 10 minutes.

Figure 2.3 shows the force and displacement plots during the main pressing, slow cooling and the beginning of the rapid cooling stages in more detail. As seen in this figure, the force quickly ramps up to 2000N and then is maintained for 90 seconds. The main shape change of the preform occurs during this time. The glass preform is pressed to about 0.85mm. Since glass is in the viscoelastic region at this temperature, the corresponding displacement is a function of the glass viscoelastic parameters. Then, the cooling stage begins and the applied force is reduced to 500N. As the glass becomes cooler, it becomes stiffer and hence, the rate of increase of the displacement of the lower mold decreases. The preform is finally pressed by 1.01mm at the end of this stage when the force is removed.

In the next section some of the intricate details that are very important in predicting the lens profile deviation are considered more closely.

2.2 Gap after Pressing

When the force is removed at the end of the slow cooling stage, there is a small gap that is created between the lens and the mold. If the lens lies on the bottom mold, then this gap is created between the top mold and the lens. On the other hand, if it sticks to the top mold, then the gap is created in between the bottom mold and the lens. Both these of scenarios have been observed in practice. In the case that is plotted in Figure 2.2, the lens was actually stuck to the bottom mold. The magnitude of this gap is 0.15mm as shown in Figure 2.3. The amount of this gap is much greater than the elastic recovery of molds and lens combined.

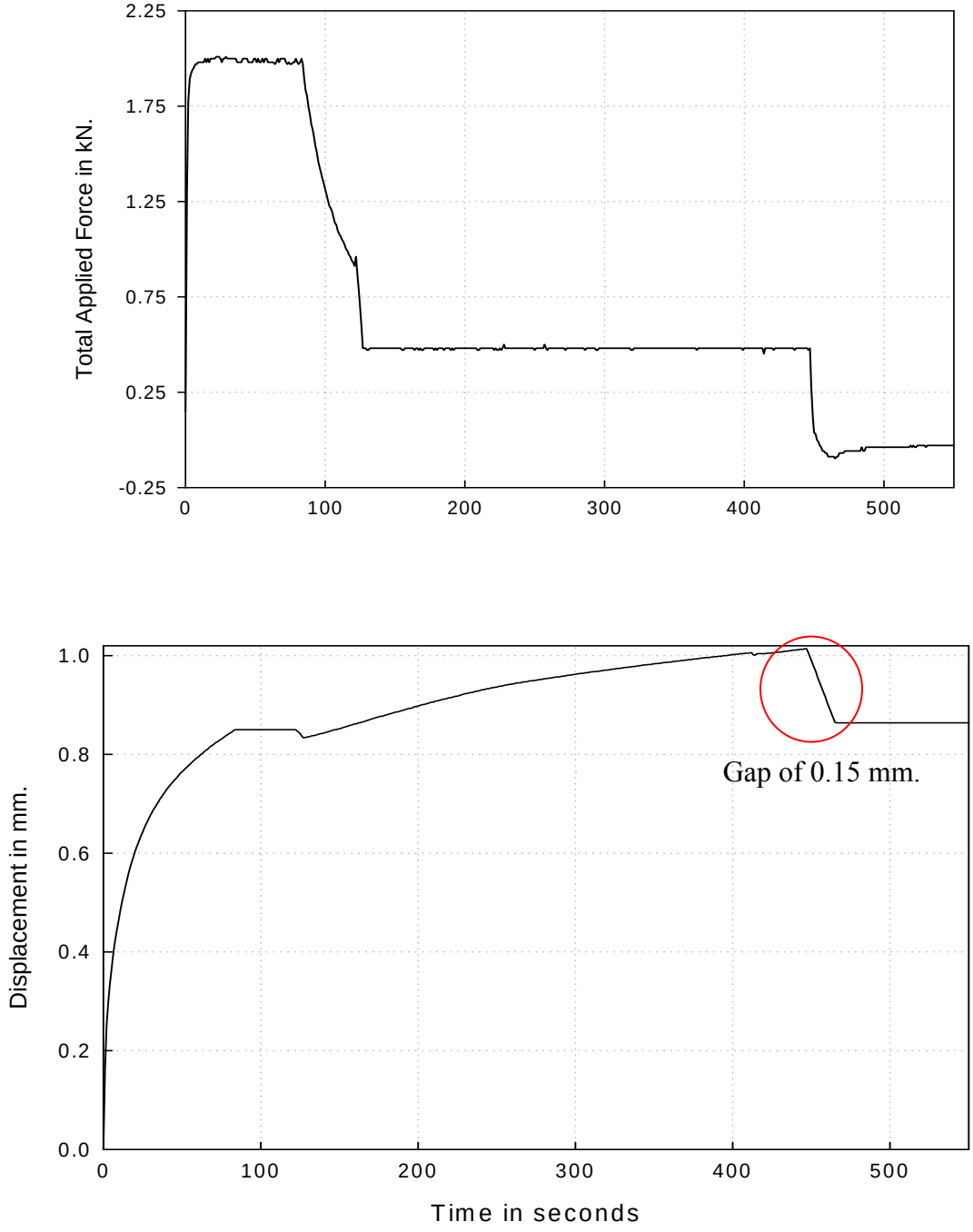

Figure 2.3: Force and displacement plots during the main pressing, slow cooling and beginning of the fast cooling stages of the lens molding process.

A small gap is essential for the proper manufacture of the lens without cracking. If there is no gap then the lens will crack as it is cooled below the glass transition temperature. On the other extreme, if the amount of gap is too large, then the heat transfer between the mold and the lens is reduced greatly and hence the cooling cycle takes longer to complete. The primary mode of heat transfer between the preform and the molds is through contact/gap conductance and then to some extent through radiation. The gap conductance is inversely proportional to the amount of gap. Hence the amount of gap is crucial for the proper manufacture of lenses within a reasonable cycle time.

The knowledge of the position of the lens within the gap is crucial in to predicting the deviation of the molded lens, since the heat transfer is a strong function of the gap and lens position within the gap.. Since the profile deviation is believed to be due to primarily thermal contraction and altering stress state during the cooling process, the position of the gap becomes very important to be able to predict the deviation from simulations. A sensitivity analysis of the profile deviation on the position of gap was done and the results are discussed in Chapter 6.

2.3 Non-uniform Temperature Distribution in Preform during Pressing

Since glass is a poor thermal conductor, the usual soaking time of 2 minutes given to the preform prior to pressing is not be enough to heat the lens to its core. This has been deduced from experience of trying to curve fit the experimental displacement data from the molding machine. Based on a uniform temperature assumption during the pressing stage, the initial part of the displacement curve from the simulations was always overestimated while the final part was always underestimated. This means that the glass preform was initially stiffer when compared to the glass preform towards the end of the pressing cycle. Since glass material behavior is strongly temperature dependent, given that the conductivity of glass is very low and its contact resistance high, a non-uniform temperature distribution was concluded to exist within the preform.

The problem of non-uniform temperature distribution after soaking cannot be avoided in the actual process and thus, heating/soaking stages have to be taken into account in the simulation in order to predict the lens deviation accurately. The soaking time cannot be increased indefinitely to solve this problem, as this would increase the overall cycle time of the molding process, which is considered as one of the main advantage of this process.

2.4 Significance of Mold Coating

In the precision lens molding process, the mold surfaces that come into contact with the glass are usually coated due to the following reasons:

(i) chemically inert mold coatings prevents oxidation and increase the life of the mold,

(ii) coated molds avoid sticking of the freshly molded lens to the mold,

(iii) low friction coating reduces the cycle time thereby reducing the cost of production.

In addition, it also affects the residual stress state and the final size and shape of the lens. Since, that is one of the main goals of this research; a sensitivity analysis was performed to see the effect of changing friction on the final size and shape of the lens and these results are given in Chapter 6.

One other important aspect of the coating is its ability to conduct heat. Since the glass preform is primarily heated/cooled through contact/gap conductance, the conductivity of the coating material becomes significant for the overall success of the process. The contact conductance material behavior used in this analysis is explained in the next section.

2.5 Finite Element Model

The numerical simulation of the lens molding process and the ring compression tests were done using the commercial finite element code ABAQUS. Other software considered included POLYFLOW, ANSYS and MSC-MARC. POLYFLOW was initially used for molding because of its sophisticated adaptive re-meshing capability, but was discarded later due to

limitations with material behavior and cooling. To avoid the problem of the mesh becoming distorted during the pressing stage in ABAQUS, a sufficiently fine mesh was used for glass. Although ABAQUS/Standard solvers do not allow re-meshing, in-built options within ABAQUS include sophisticated material behavior, for example, viscoelasticity and thermo-rheological simplicity (TRS). The details of these behaviors are explained in Chapter 3. The important additional features of structural relaxation and complex thermo-rheological behavior are not available, but can be easily incorporated via user subroutines. User subroutine UEXPAN was used for implementing structural relaxation behavior of glass in ABAQUS and the details are given in Chapter 4.

A *COUPLED-TEMPERATURE DISPLACEMENT type of analysis was used in the simulations because of the two-way coupling that exists between the mechanical and thermal boundary value problems;

(i) the mechanical properties change drastically based on temperature, and

(ii) the heat conduction at the interface was also affected by the changing contact surface.

All the five stages of the actual molding process were included in the simulation as well. An additional step is also defined in the simulation where the lower mold is moved upwards until contact is established between the glass perform and the molds.

2.4.1 Model Geometry

The initial geometry of the model is shown in Figure 2.4. Since the preform and the molds are circular and the loading can be approximated as symmetric around the central axis, only an axi-symmetric model was considered. The glass preform is meshed with 6900 CAX4RT elements, while the upper and lower molds are meshed with 3485 and 2125 CAX4RT elements, respectively.

Two master-slave types of contact interaction pairs were created; one between the bottom surface of the top mold (master) and top surface of the ring (slave) and the other between the top surface of the bottom mold (master) and the bottom surface of the ring (slave). For the tangential behavior at the contact interface, a Coulomb friction model based on penalty formulation was used and for normal behavior, "hard" contact formulation was used. The "hard" contact formulation prevents any penetration of either of the interacting surfaces into the other. Heat transfer across the interface via contact conductance and radiation is also included in the model.

Two coupling constraints are also defined; one between RP_{TOP} (control point) and the top surface of the top mold and the other between RP_{BOT} (control point) and the bottom surface of the bottom mold. However in these constraints only the vertical component of displacement of the slave surfaces were constrained to move along with that of their respective master reference points, while the horizontal components of displacement are allowed to be free. Not only does this represent the actual process more closely, it also eases applying force boundary conditions and extracting displacement response from the results file.

Finally, an axial type of connector element (CONN2D2) is defined between the bottom most point that lies on the axis of the preform and the top most point that lies on the axis of the bottom mold, as shown in Figure 2.4. As explained in Section 2.3, a small gap is created at the end of the slow cooling stage. In the actual process, the freshly molded lens sometimes rests on the bottom mold and sometimes becomes stuck to the top mold. Therefore, depending on process, the connector elements are accordingly defined. Since there is no resistance to the connector spring, a small, finite value of 10 N/m was used for the stiffness of the spring. Initially, instead of the connector spring, a kinematic constraint was used to fix the lens to either of the molds. Since the constraint can be thought of as an infinitely stiff spring, a stress was induced in

both the mold and the lens in the neighborhood of the constrained point and vanishes beyond a certain distance from that point. Since this would alter the stress state in the lens, the kinematic

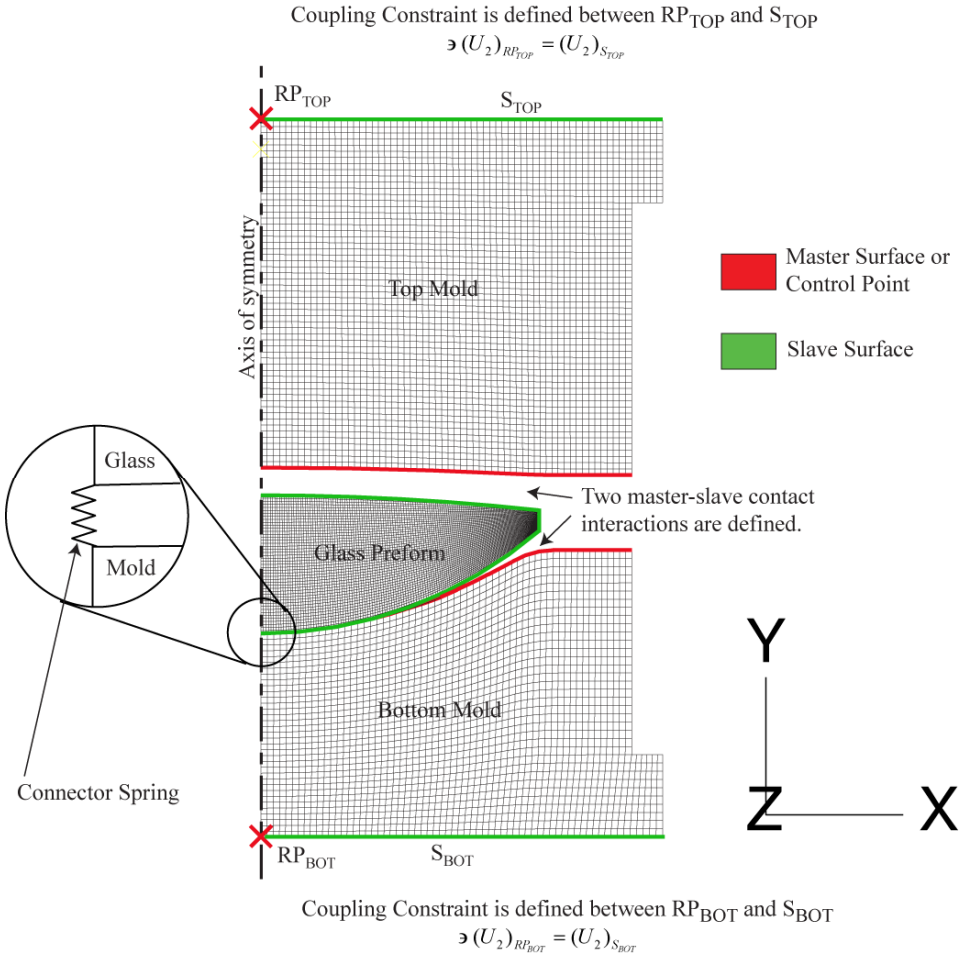

Figure 2.4: Illustration of the Model geometry used in the simulation and all features that valid throughout the simulation.

constraint was replaced by a connector element. It is important to note that the connector spring approach is suitable only when the lens changes shape such that the only contact between the mold and lens is the point at the central axis. If instead the contact is a circle instead of a point, such as for a concave lens surface with a positive deviation like a suction cup, a more involved approach would be necessary.

2.4.2 Material Behavior of Glass and Molds

Table 2.1 summarizes the mechanical and thermal material properties of L-BAL35 molding glass and Tungsten carbide (WC) molds. The specification sheet for L-BAL35 glass is attached in Appendix A.

The elastic properties of glass include Young's modulus that is temperature dependent and Poisson's ratio. It is reported in the literature that the elastic modulus of glass remains fairly constant until just below the glass transition temperature and then decreases drastically and stays constant as temperature increases further [1]. While the room temperature value of the elastic modulus is obtained from the glass specification sheet, the high temperature value given below was chosen because it fits all available experimental data of different molding experiments using L-BAL35.

The specific heat capacity is not only a strong function of temperature, but also changes with the heating/cooling rate, i.e. it exhibits structural relaxation behavior just as the thermal expansion coefficient. In this research the specific heat is defined as a function of temperature that is consistent with the heating and cooling rates for the molding process. If the cooling or heating rates for the process change drastically, then the specific heat must be changed manually. The values reported in the above table were obtained from S.Gaylord [2].

The thermal expansion behavior of glass is more complex than that of the mold; glass is time-dependent and involves more parameters than a simple 'α.' The theory, experiments, the parameters and its implementation in the finite element software that are used in this research are described in Chapter 4.

Property	Glass	Mold
Density, ρ (kg/m^3)	2550	14650
Young's Modulus, E (GPa)	100.8, T $\leq$ 510°C 0.8, T $\geq$ 560°C	570
Poisson's Ratio	0.252	0.22
Specific Heat, c_p (J/kg/K)	1100, T $\leq$ 470°C 1730, T $\geq$ 570°C	314
Thermal Conductivity, κ (W/m/K)	1.126	38
Thermal Expansion Coefficient, α (K^{-1})	*	4.9×10^{-6}
Glass Transition Temperature, T_g (°C)	527	--

Table 2.1: Thermal and mechanical properties of glass and mold. *The thermal expansion behavior of glass is dealt with separately in Chapter 4.

2.4.3 Glass/Mold Interface Behavior

The simulation also accounts for interaction between the glass preform and the mold, both mechanically and thermally. The molds are coated with DLC (Diamond-like-carbon) coating to prevent any chemical reaction between glass and molds and also to ease the release of the lens once molding is over. A master-slave type contact interaction is defined between them with the mold surface being the master surface and the glass surface being the slave surface. These master-slave type contact definitions were used as the glass is much softer than the molds. Care was taken while meshing such that the mold elements are at least 5 times larger than the glass elements. This was done to avoid contact penetration because the master surface can penetrate the slave surface while the slave surface cannot penetrate the master surface. The normal contact behavior was modeled as "hard" contact in ABAQUS while the tangential behavior is modeled using penalty formulation and a Coulomb friction model was used. The experiments and methodology of characterizing the tangential behavior at the interface under molding conditions are described in Chapter 5.

The two surfaces can exchange heat by contact/gap conductance and radiation. The heat transfer between the surfaces, when they are either in contact or separated by a small gap, is defined by

$$q = h_g (T_{slave} - T_{master}) \tag{2.16}$$

where 'q' is the heat flux per unit area in W/m^2, 'h_g' is the contact/gap heat transfer coefficient in W/m^2/K and T_{slave} and T_{master} are the temperatures of the nodes of the contacting slave and master surfaces, respectively. The contact/gap heat transfer coefficient is defined by

$$h_g = \min\left(\frac{\kappa_{air}}{d}, 5000\right) \text{W/m}^2\text{/K}, \tag{2.16}$$

when surfaces are close but not contacting, and h_g = 5000 W/m^2/K, when the surfaces are in contact and it is not pressure dependent. The thermal conductivity of air, κ_{air} is 0.04 W/m/K and 'd' is the gap between the two surfaces as shown in Figure 2.5. The gap-dependent part of the contact conductance model is used from Madhusudana [3], while its maximum value is limited based on Sellier *et al.* [4]. This maximum limit for gap conductance is used to prevent the value from increasing to infinity as the surfaces come very close to each other.

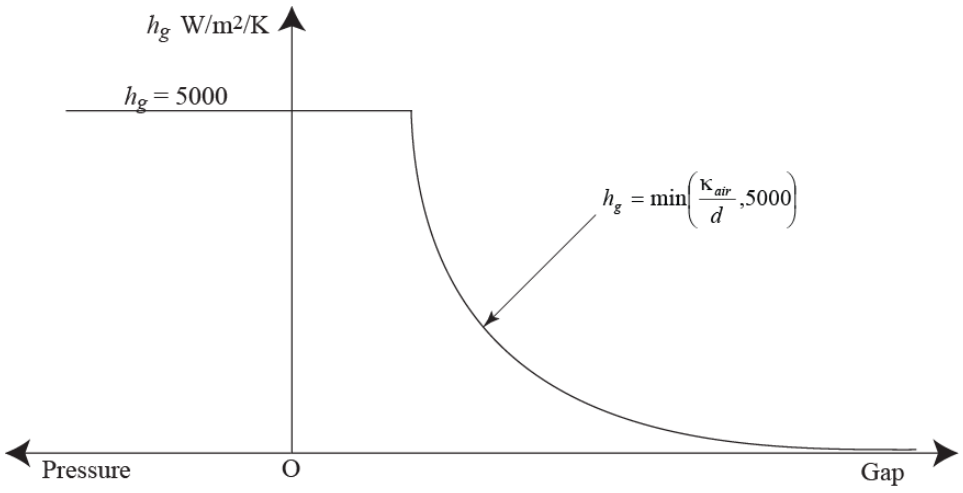

Figure 2.5: Pressure and gap dependent contact conductance model.

Heat transfer at the interface through radiation is given by

$$q = \frac{\sigma}{\left(\frac{1}{\varepsilon_{slave}} + \frac{1}{\varepsilon_{master}} - 1\right)}\left(T_{slave}^4 - T_{master}^4\right) \ \text{W/m}^2 \tag{2.17}$$

where σ is the Stefan-Boltzmann constant (5.67 x 10^{-8}W/m^2/K^4), ε_{slave} = 0.85 is the emissivity of glass surface, and ε_{master} = 0.15 is the emissivity of mold surface.

2.4.4 Mechanical Loading and Boundary Conditions

In the first two stages (heating and soaking), both RP_{TOP} and RP_{BOT} defined in Figure 2.4 are fixed. In the next additional step contact between the molds and glass was established by moving RP_{BOT} by a specified distance, while RP_{TOP} is still fixed at the same position. In fact, RP_{TOP} is fixed at its initial position throughout the analysis. Next a concentrated load of 2000N was applied at RP_{BOT} with amplitude such that it is identical to the force defined in Figure 2.3. In the next stage (slow cooling), the same applied force was reduced to 500N such that it matches the experimental data as before. In the final rapid cooling stage, RP_{BOT} is moved down by a distance of 0.15mm and held there afterwards. In this stage a gap is created between the molds and the glass and heat transfer from glass to molds takes place through contact/gap conductance.

2.4.5 Thermal Boundary Conditions

Temperature boundary conditions on the outer surfaces of the molds were applied as shown in Figure 2.6. A qualitative time history of the temperature shown below in the plot was identical to the sensor temperature reading shown in Figure 2.2. In reality, the temperature is not uniform at all the points on the outer surface of the mold and still this boundary condition is believed to be a good approximation since the molds are made of Tungsten carbide which has a

very high thermal conductivity (See Table 2.1). The heat transfer between the glass and the molds takes place primarily through contact/gap conductance and gap radiation.

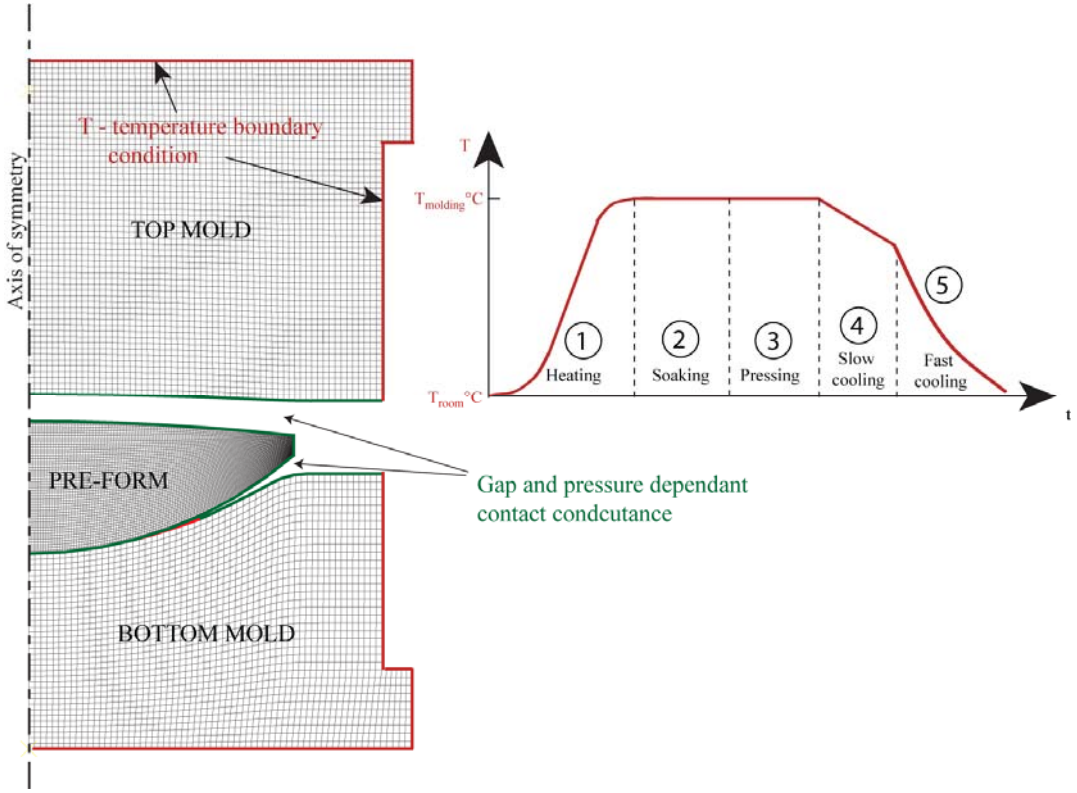

Figure 2.6: Illustration of the thermal boundary conditions applied in the five different stages of the model.

References

1. http://www.toshiba-machine.co.jp/english
2. H. Loch, D. Krause, *Mathematical simulation in glass technology*, Springer, 2002.
3. S. Gaylord, *Thermal and structural properties of moldable glass types*, Master's thesis, Clemson University, December 2008.
4. C.V. Madhusudana (1995), *Thermal contact conductance*, Springer.
5. Sellier. M, Breitbach. C, Loch. H, Siedow. N, An iterative algorithm for optimal mould design in high-precision compression molding, *Proceedings of the I MECH E Part B Journal of Engineering Manufacture*, **221**(2007), 25-33(9).

CHAPTER THREE

Viscoelastic Characterization of Glass

3.1. Viscoelastic Response of Glass in the Transition Region

If a mechanical stress is applied to glass in its transition region, a time–dependent change in dimension or strain occurs. This behavior is called viscoelasticity and a typical linear viscoelastic behavior of glass in its transition region is illustrated in Figure 3.1. A glass sample is subjected to a step load (stress), σ_0, at time $t = t_0$ and maintained a constant until $t = t_1$ when it is removed. The strain response has the three distinct components,

i. instantaneous elastic strain, ε_E,

ii. delayed elastic strain, ε_D, and

iii. viscous flow strain.

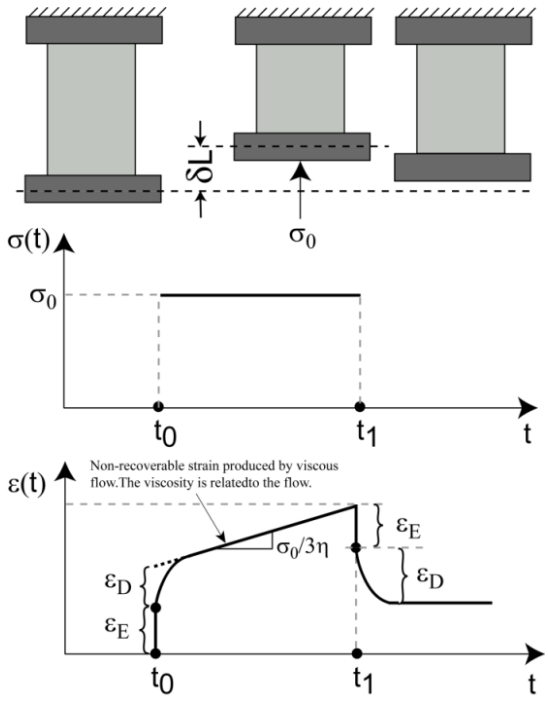

Figure 3.1: Linear visco-elastic behavior of glass in its transition region. After the removal of the load, there is a permanent deformation in glass due to viscous flow.

When the stress is removed, the elastic strains, ε_E and ε_D, are recovered as shown in Figure 3.1 while the viscous strain is permanent. This viscous flow part is the primary driving mechanism for shape change during molding of a glass lens. A Generalized Maxwell's model shown in Figure 3.2 is widely used to fit the linear viscoelastic response of glass. In this model, the springs and dampers are linear. Specifically, for the damper, the stress developed is a linear function of strain rate, i.e.,

$$s_{ij} = 2\eta \frac{d\varepsilon_{ij}}{dt} \tag{3.1}$$

where 'η' is the viscosity of the fluid, s_{ij} is the shear stress and e_{ij} is the shear strain.

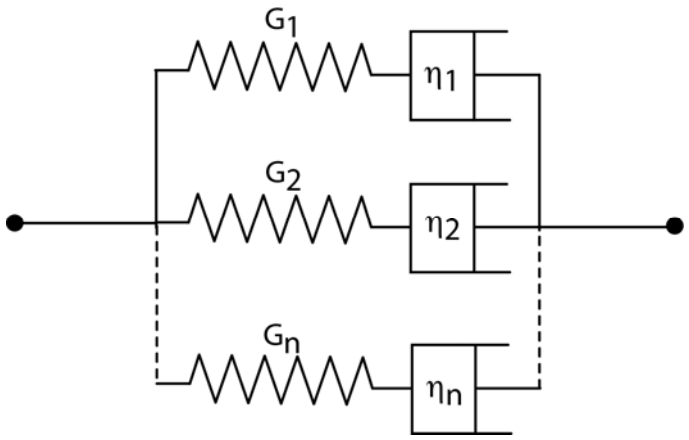

Figure 3.2: Generalized Maxwell's model for linear viscoelastic material behavior of glass.

The constitutive equations of viscoelasticity [1] are given as follows:

$$s_{ij}(t) = \int_0^t G_1(t-t') \frac{\partial e_{ij}(t')}{\partial t'} dt' \tag{3.2}$$

$$\sigma(t) = \int_0^t G_2(t-t') \frac{\partial \varepsilon(t')}{\partial t'} dt' \tag{3.3}$$

where s_{ij} and σ are the deviatoric and dilatational stresses, e_{ij} and ε are corresponding deviatoric and dilatational strains and $G_1(t)$ and $G_2(t)$ are deviatoric and volumetric or dilatational relaxation modulii respectively. The total stress in a viscoelastic element can then be obtained by combining the two parts as given by

$$\sigma_{ij} = s_{ij} + \frac{1}{3}\delta_{ij}\sigma \ . \tag{3.4}$$

The term 'deviatoric' that precedes either the stresses or strains refers to those stresses or strains that cause a change in the shape of a differential viscoelastic element without affecting its volume. On the other hand, the term 'dilatational' refers to change in volume without any change in shape. In glass literature, terms such as hydrostatic and volumetric are also alternatively used for representing dilatational stress and strain, while the term 'shear' is often used to represent deviatoric stresses and strains.

The most widely used time dependent relaxation modulii has the form,

$$G_1(t) = 2G_0 \sum_{i=1}^{n_1} w_i e^{-t/\tau_i} \tag{3.5}$$

$$G_2(t) = 3K_\infty - 3(K_\infty - K_0)\sum_{j=1}^{n_2} v_j e^{-t/\lambda_j} \tag{3.6}$$

where G_0 is the instantaneous elastic shear modulus, K_0 is the instantaneous bulk modulus, K_∞ is the equilibrium bulk modulus, w_i and v_j are weighting factors for deviatoric and volumetric relaxation functions and, τ_i and λ_j are the corresponding relaxation times for the deviatoric and volumetric relaxation functions, respectively. This series of weighted exponential decay terms is called a prony series and the coefficients of the series, including the weights and relaxation times, are called prony coefficients. From (3.6), it is clear that a non-zero equilibrium bulk modulus

prevents any viscous flow or permanent deformation under volumetric loading. Thus, only the deviatoric strains contribute to permanent shape change.

However, other forms have also been used to represent shear viscoelastic behavior of glass. The simplest one being a single term prony series ($n_1 = 1$ in Eq. (5)), while the most complex one being a stretched exponential given by

$$G_1(t) = 2G_0 \exp\left[-\left(\frac{t}{\tau}\right)^b\right]. \tag{3.7}$$

This type of representation for shear relaxation modulii is also called Kohlrausch-William-Watts (KWW) function or simply a b-function. The KWW function was used widely to represent the relaxation modulus before the prony series was introduced, which not only gave more degrees of freedom to fit the experimental data better, but also simplified the mathematical rigor. Duffrene *et al* [2] have illustrated that the KWW function could not completely describe the viscoelastic behavior of glass in the transition region. More references on the inability of the KWW function to represent experimental response of glass are also given in their work. Also most of the Finite Element Solvers, including ABAQUS, POLYFLOW etc. use only a prony series representation to model the viscoelastic behavior.

3.2. Justification for using Linear Viscoelastic Model

Scherer [1] argued that Newtonian-type viscosity behavior of glass is justified as long as the stresses developed in the material do not exceed 100 MPa. His argument is based on work by Li and Uhlmann [3] who applied different constant shear stress to glass samples and measured the strain as a function of time as shown in Figure 3.3. The viscous flow is characterized by a constant slope, i.e., constant strain rate, for each stress that is applied. In Figure 3.4, the equilibrium strain rates are plotted for various constant stresses and a nice linear behavior is

observed until the stress reaches high values. Precisely, a non-linear behavior is seen when the applied stress is in excess of 100 MPa. From a preliminary study of the lens molding process, the maximum stress does not reach beyond 30 MPa during molding and so, the use of a linear viscoelastic model is justified for the current research.

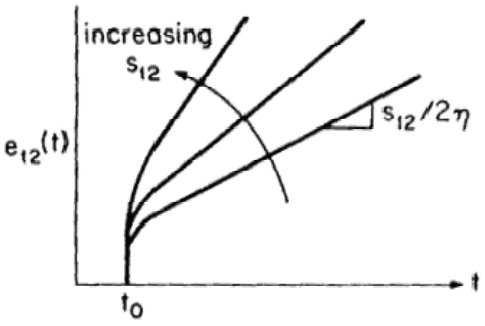

FIGURE 3.1 The shear strain $e_{12}(t)$ caused by a constant shear stress s_{12} asymptotically approaches a constant rate of increase. The viscosity is defined by the slope of the linear portion of the creep curve, $de_{12}/dt = s_{12}/2\eta$. If the slope is proportional to s_{12}, that is, if η is not affected by the stress, then the material is said to exhibit Newtonian viscosity.

Figure 3.3: Creep curve of a glass sample subjected to constant shear stress (Obtained from Scherer 1986 [1])

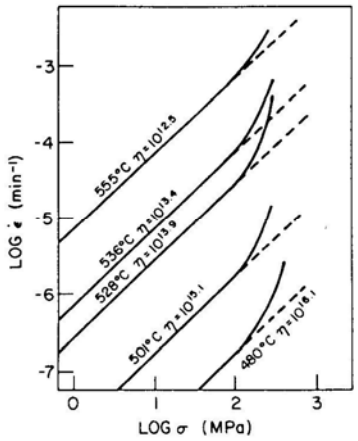

FIGURE 3.2 Data from Li and Uhlmann (1970) show non-Newtonian behavior. At stress levels exceeding 100 MPa the slopes of the curves increase because the viscosity decreases. The indicated viscosities (Pa·s) represent values obtained from tests at low stress levels.

Figure 3.4: Non-Newtonian flow beyond 100 MPa. (Obtained from Scherer 1986 [1])

3.3. Experiments in Literature used for Glass Characterization

All the experiments that are necessary to characterize the elastic (instantaneous) and viscoelastic (time-dependent) properties of glass are explained in this section. This

comprehensive literature study was done to understand the complexities of glass behavior within the transition temperature range. The literature also provides methods to convert the creep and relaxation data into material property coefficients that will be used in the FEM software, ABAQUS. It should be pointed out that from a computational perspective; the degree of sophistication for material behavior characterization is well beyond what is available in the literature or obtainable with our current testing capability. This is a common problem in the computational modeling of realistic material behavior. This is one of the important reasons for the sensitivity analyses presented in Chapters 6. In what follows the experimental approaches are what could ideally be done to obtain the necessary constants for the computational model.

The elastic properties of glass include Young's modulus and Poisson's ratio. From these elastic constants, the shear and bulk moduli are obtained from elasticity equations

$$G_0 = \frac{E_0}{2(1+\nu)} \tag{3.8}$$

$$K_0 = \frac{E_0}{3(1-2\nu)} \ . \tag{3.9}$$

Since glass is viscoelastic at high temperatures, mechanical tests cannot be used to obtain the elastic constants as it can be difficult to distinguish the viscoelastic part from the instantaneous elastic part. Brillouin light scattering technique is generally used for this purpose, where the change in speed of sound travelling through the glass medium is directly related to the Young's modulus [4, 5]. In these tests the Poisson's ratio is assumed to be constant for all temperature. In the literature the Poisson's ratio of most glass is between 0.2 and 0.28 and is reported to be constant at all temperature. Other tests such as Resonant Ultrasound Spectroscopy [6], Ultrasonic echography [7] and Impact analysis can also be used for this purpose. The underlying principle common to all these tests is to pass an elastic wave through the medium (glass) at the desired temperature and relate the measured wave speed to the Young's Modulus.

As there is a fundamental difference in the viscoelastic behavior of glass under pure shear and pure volumetric loading, separate tests are needed under these types of loading to evaluate the corresponding viscoelastic properties. Almost all of the articles [4, 8] related to lens molding simulation obtain their viscoelastic material characterization information from a cylinder compression test. The problems with this test are (i) mixed loading results in stress state will have both shear and hydrostatic components in it and (ii) friction at the glass/die interface should be known apriori.

DeHoff and his co-workers [9, 10] used a beam bending viscometer to obtain the shear viscoelastic behavior assuming the material is elastic compressible, i.e., the time-dependent part of the volumetric stress component is ignored. As shown in Figure 3.5, a beam made out of the glass sample is simply supported at both ends and subjected to a constant mid-point load. The time-dependent, midpoint deflection is measured and the

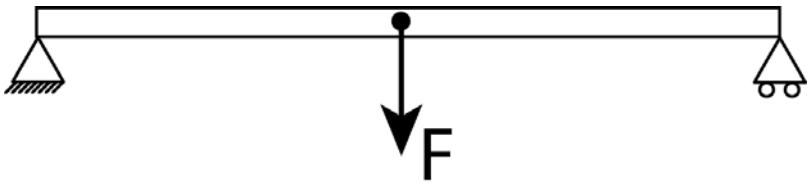

Figure 3.5: Beam-bending viscometer.

viscoelastic properties are extracted. This test was attempted by the glass characterization team in the materials science department based on our suggestion and was not used further due to the following reasons:

- The distinction between the elastic part and the viscoelastic part is not clear and hence a separate test like Brillouin light scattering technique is needed to first characterize the elastic constants.

- The applicable temperature range at which the test can be conducted was limited (around 20°C). The beam is either too stiff or too soft at the temperatures slightly above and below the glass transition temperature.

Duffrene *et al* [5] used a tensile testing machine to stretch a helically coiled spring specimen and a dog-bone specimen, shown in Figure 3.6, to measure the shear and volumetric viscoelastic properties. The instantaneous properties are obtained from a separate experiment such as Brillouin light scattering at different isothermal temperatures. A spring subject to tension is under pure shear and the shear properties were determined first. Then, the uniaxial response of a dog-bone specimen was measured. Although the uniaxial test results in a mixed stress state, with the knowledge of the shear behavior from the previous test, the hydrostatic part in the uniaxial test is extracted indirectly. The theory and mathematical detail in extracting the hydrostatic part from the uniaxial response are explained in a series of papers by Duffrene, Gy and his co-workers [11-13].

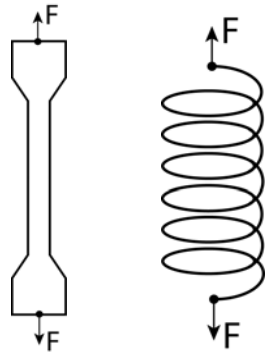

Figure 3.6: Specimen and type of loading used by Duffrene [4] for complete viscoelastic characterization.

3.4. Thermo-rheological behavior of glass (TRS behavior)

The relaxation moduli are strongly temperature dependent. At lower temperatures, the rates of relaxation are very slow, which in the limit can be modeled as elastic behavior, while at higher temperatures they become much faster, which in the limit is pure viscous behavior as shown in Figure 3.7(a). If the relaxation moduli are plotted on a log scale in time for various temperatures as shown in Figure 3.7(b) and all the curves have the same shape, but are only shifted horizontally, then the material is

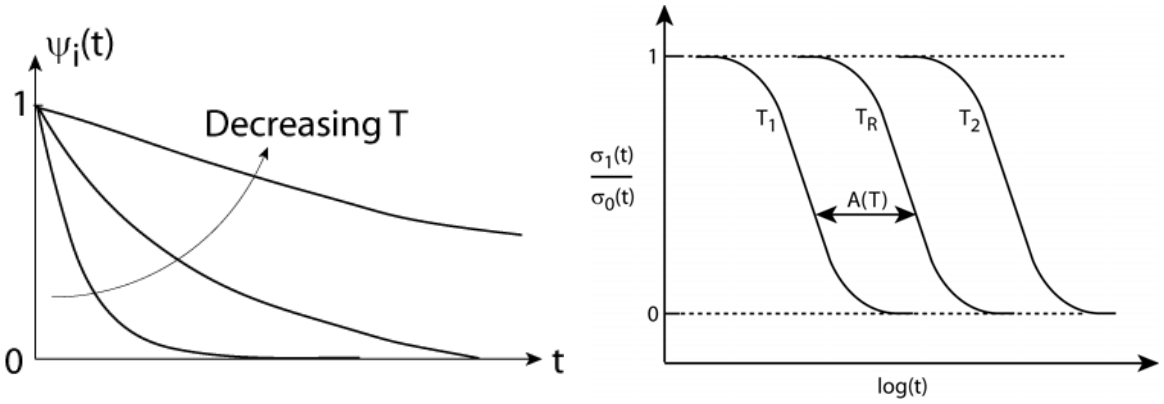

(a) (b)

Figure 3.7: TRS behavior of glass.

said to be thermo-rheologically simple (TRS). If the shift factor is defined as,

$$A(T) = \frac{\tau(T)}{\tau(T_r)} \tag{3.10}$$

then its temperature dependence can be approximated by the WLF (William-Landel-Ferry) equation as

$$\log A(T) = -\frac{C_1(T - T_r)}{C_2 + (T - T_r)} \tag{3.11}$$

where T is the temperature at which the relaxation time is sought, T_R is the reference temperature and C_1 and C_2 are constants of the WLF equation.

The WLF equation that is often used in polymers and glasses to define temperature dependence of the shift factor is only an approximation for the time-temperature dependence as seen in Figure 3.8. The temperature dependence of the shift factor for soda-lime-silica glass that is used in a classical sandwich seal problem [14] is shown below. The WLF fit for the shift factor is only a least square curve-fit and, consequently, does not pass through all the points exactly. Since the vertical scale in this plot is a log scale, a slight difference in the shift factor in this scale is greatly magnified in the linear scale. If the transient stresses that develop during the cooling of a glass sample are very important for a certain application such as the sandwich seal problem, then the WLF equation to represent the time-temperature shift is not good enough. However, if only the final stress state is important, then the WLF equation is good enough. It remains to be seen whether this assumption is good enough for the lens molding simulation and in fact, this temperature dependence of the shift factor would be one of the parameters on which a sensitivity analysis is performed in Chapter 6. If a more accurate representation of the physics is required, either a different equation which fits the data better than WLF equation is required or an interpolation should be used. A user subroutine, UTRS that is available in ABAQUS to implement a more complex dependence of shift factor beyond WLF equation could be used.

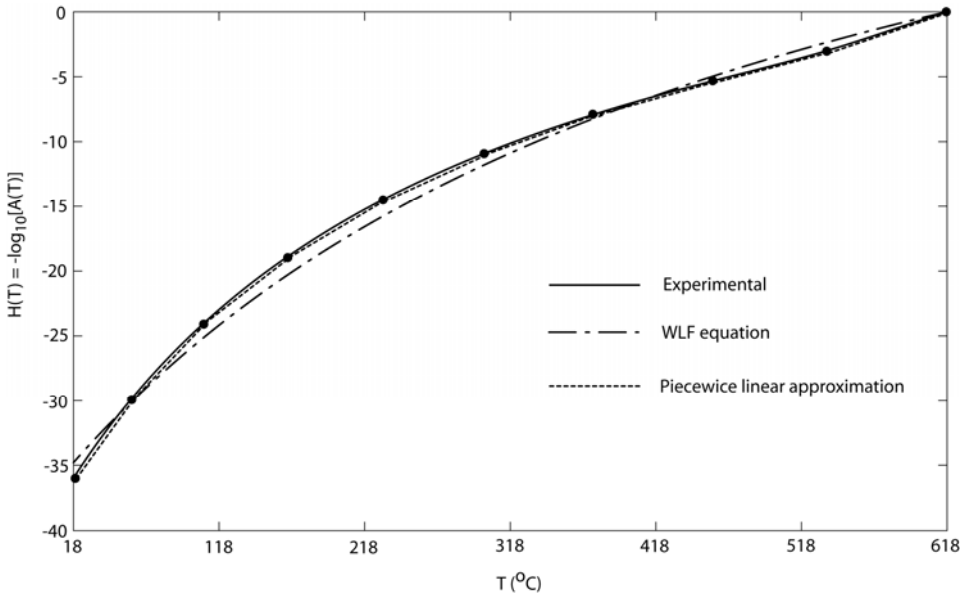

Figure 3.8: Temperature dependence of shift factor, *A(T)*. The data is obtained from a sandwich seal solution that is available in the literature [14].

3.5. Current Viscoelastic Model from Ring Compression Tests

The current viscoelastic model to be used in the simulation of lens molding was obtained from the ring compression test. Initially, the main objective of the ring compression test was to identify the friction coefficient at the glass/die interface based on the work by Male and Depierre [15]. Since the force and displacement data from the lens molding machine are also available as a function of time, a simple viscoelastic material characterization was obtained from this test. In this test, a "washer" shaped specimen is compressed between two flat dies at the molding temperature and the change in internal diameter is correlated to a friction coefficient as shown in Figure 3.9. The strengths of this test are the

i. sensitive nature of the inner diameter change to a slight change in the friction coefficient and
ii. the same lens molding machine could be used to conduct the test.

More details on how to correlate the change in inner diameter to a particular value of friction coefficient will be discussed in detail in Chapter 5. In this chapter, the focus is on extracting the viscoelastic material behavior from the force and displacement data available for the ring compression test.

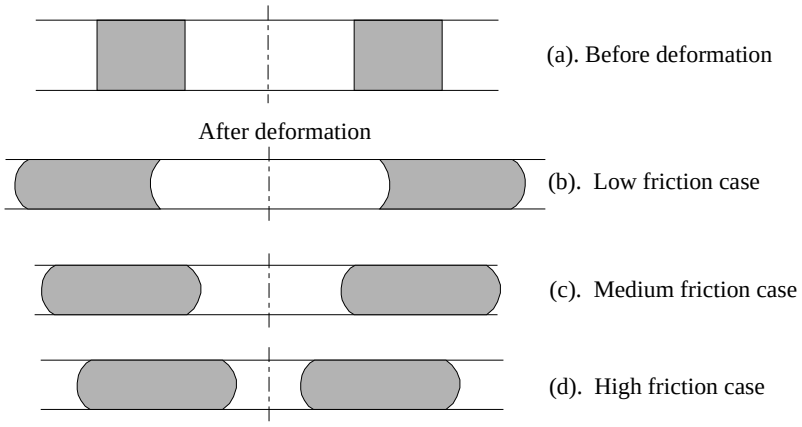

i.

Figure 3.9: Outcome of ring compression tests with different interfacial conditions for the same mold/material pair.

3.5.1. Experiments

The Toshiba lens molding machine (GMP series) was used to conduct the ring compression tests and the details of the processing stages in this machine are explained in Section 1.1. Two rings with dimensions of 19.15mm outer diameter, 9.59 mm inner diameter, and 6.37mm tall were pressed, one at 589°C and the other at 569°C. A temperature of 589°C was chosen as it is the ideal molding temperature for L-BAL35 type glass found from the experience of the lens molder. The other test that was done at 569°C was to extract some information for the TRS behavior. In this research the TRS assumption will be used as there is limited amount of experimental data available.

The pressed rings at 589°C and 569°C are shown in Figure 3.10. It is seen that the ring at 589°C looks larger as it is pressed more than its counterpart. This is because higher temperature reduces the viscosity and therefore the glass ring flows more easily. Also noticed is the fact the inner diameter in both cases has increased, indicating that the friction coefficient is small. In Chapter 5 a friction coefficient of 0.04 based on a Coulomb friction model is determined.

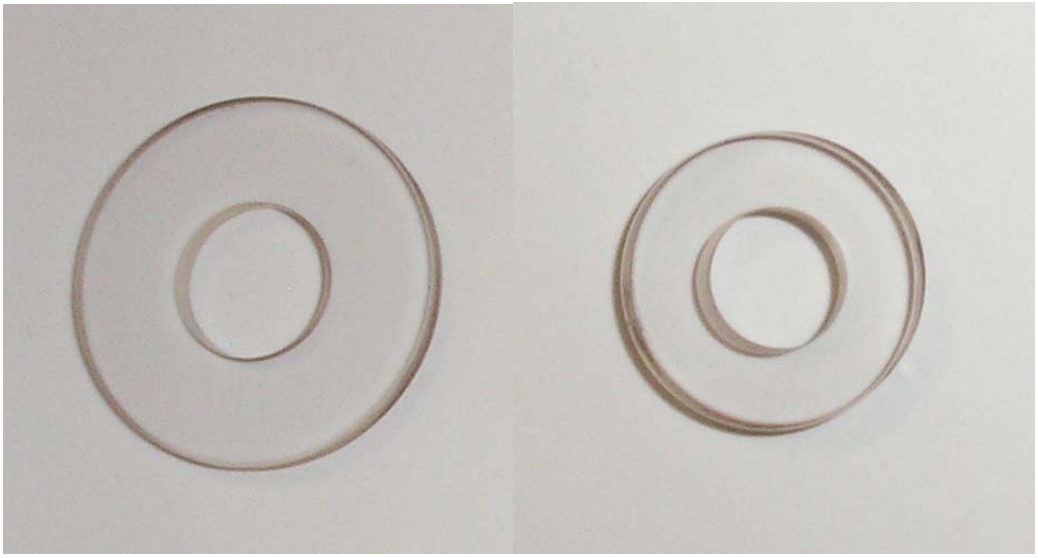

Figure 3.10: The ring that is pressed at 589°C C and 569°C are shown at the left and right respectively.

The temperature of the dies, the value of the controlled force and the corresponding displacements of the dies for tests conducted at 589°C and 569°C are shown in Figures 3.11 and 3.12, respectively. As can be seen in these figures, there are 5 distinct stages namely, heating, soaking, isothermal main pressing, maintenance force pressing with slow cooling and rapid cooling stages. First, the infra red (IR) lamps heats the whole molding assembly from approximately 150°C to the molding temperature in 4 minutes and then it is soaked at that temperature for nearly 9 minutes. This soaking time is given to the glass prior to pressing

because sufficient time is required by glass to attain the temperature reading in the sensors. The usual soaking time for the lens molding process is about 2 minutes. Since the current goal was to characterize the viscoelastic material property at the molding temperature, an unusually long duration of time for soaking was used to make sure uniform temperature is achieved within the glass sample. After soaking, the rings were pressed under constant force of 1500N at the molding temperature until a desired displacement is reached. In this machine the force is controlled by a load cell attached to the bottom die. Then, the slow cooling stage starts as the IR lamps are turned off and cold nitrogen begins to flow. During this slow cooling stage, still a back-off or maintenance force of 500N is applied.

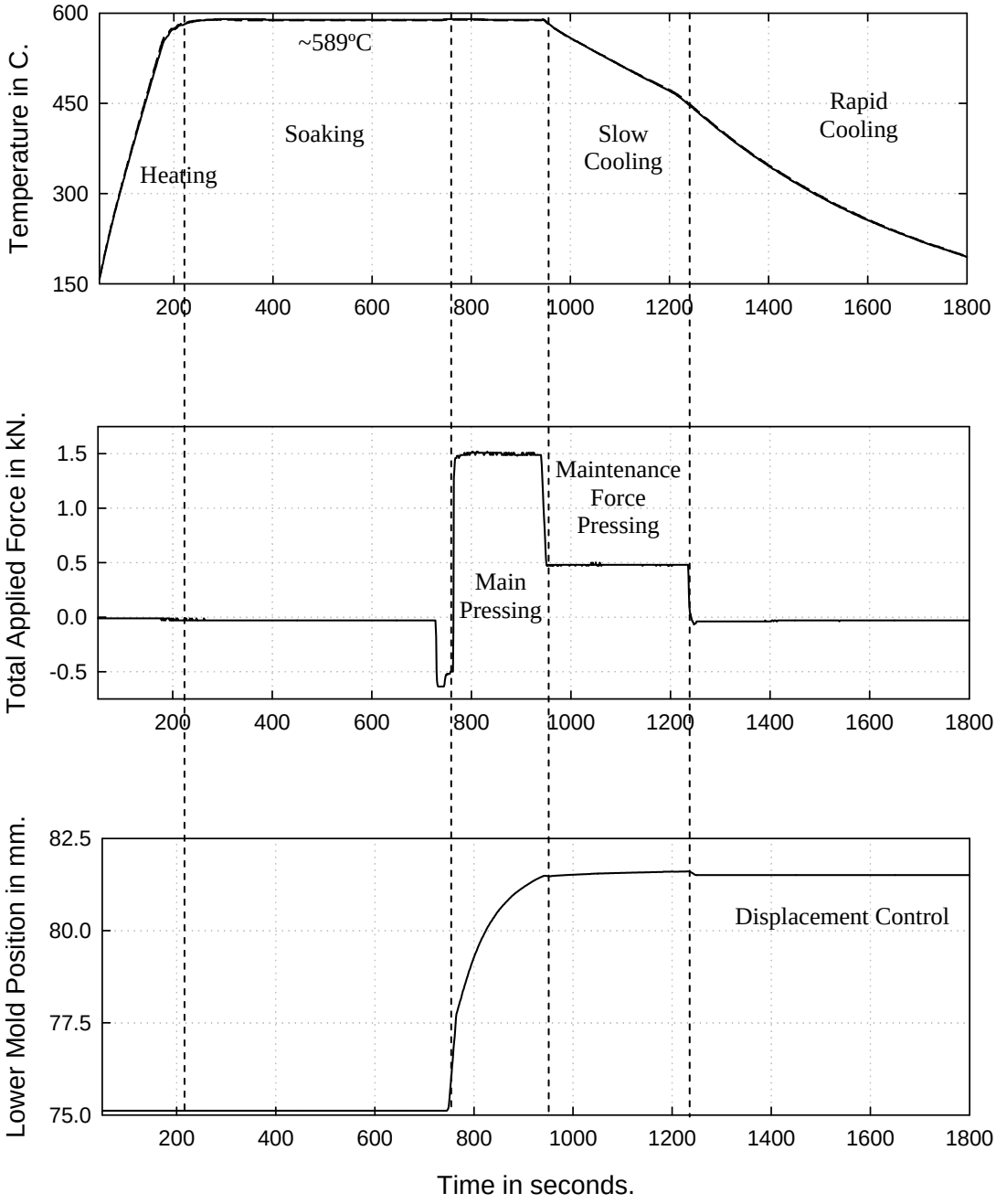

Figure 3.11: Process data from Toshiba lens molding machine, when a ring made of moldable glass material L-BAL35 is pressed at 589°C. The ring dimensions are shown in Figure 3.9. At the beginning of “rapid cooling” stage, force control switches to displacement control. A small gap of 0.15 mm is created. Then, the lower mold is fixed at the current position.

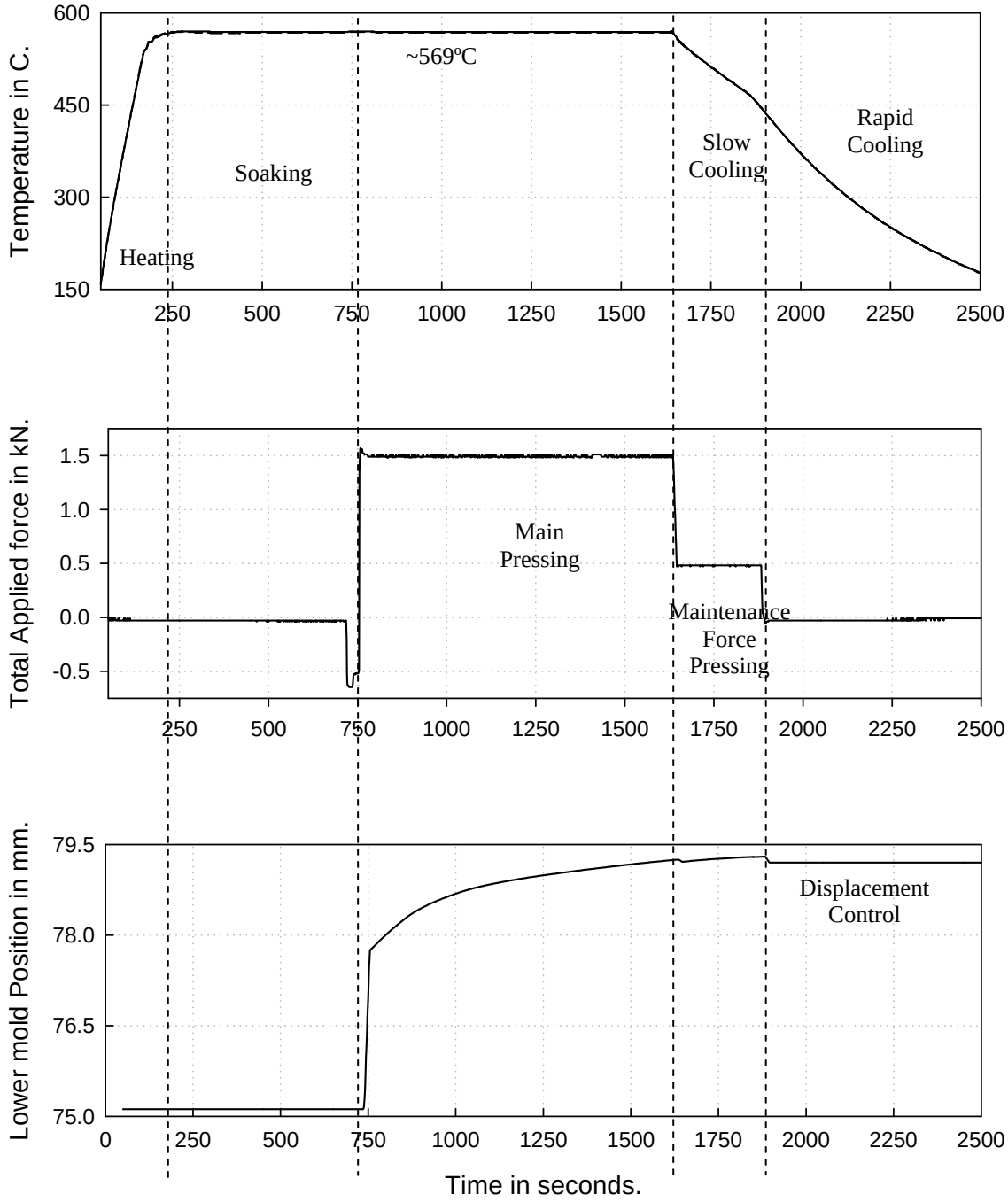

Figure 3.12: Process data from Toshiba lens molding machine, when a ring made of moldable glass material L-BAL35 is pressed at 569°C. The ring dimensions are shown in Figure 3.9. At the beginning of “rapid cooling” stage, force control switches to displacement control. A small gap of 0.15 mm is created. Then, the lower mold is fixed at the current position.

Finally, the lower die moves down reducing the force to zero and creating a small gap (0.15mm) between the glass sample and the upper die. Now, full flow of nitrogen is triggered which cools the entire assembly in approximately10 minutes.

The rest of this chapter will focus on the details of the methodology used to obtain the stress relaxation data and the TRS behavior from these tests.

3.5.2. Method of extraction of Viscoelastic Material Behavior

Ideally an analytical solution could be developed for the ring compression tests and the required viscoelastic material data that best fits the experimental creep data could be determined using a nonlinear curve fitting routine. Unfortunately, barreling of the outer and inner curved surfaces of the ring and frictional contact at the glass/die interface make it too difficult to model it via analytical means. Hence the commercial finite element code ABAQUS was used obtain a numerical solution. A model of the ring compression test was developed in this FEM software with the same mechanical and thermal boundary conditions as the actual test. Also, all the important stages in this process are modeled as different steps in ABAQUS. More details about the model are given in the next subsection. The idea is to give an "initial guess" material behavior for glass which includes instantaneous elastic and time-dependent viscoelastic material behavior. All the other material definitions are given in Chapter 2. The viscoelastic behavior is input in the form of a prony series to the ABAQUS program. The simulation was then run and the displacement response of the bottom mold was compared to the experimental creep response. Depending upon the nature of the response, the weights, the relaxation times and also the number of terms of the prony series are modified and then the analysis is re-run. This process is repeated until the displacement response from the simulation matches the experimental response.

3.5.3. Finite Element Model

The numerical simulation of the ring compression test was done using the commercial finite element code ABAQUS. The initial geometry of the model is shown in Figure 3.13. Since the ring and the molds

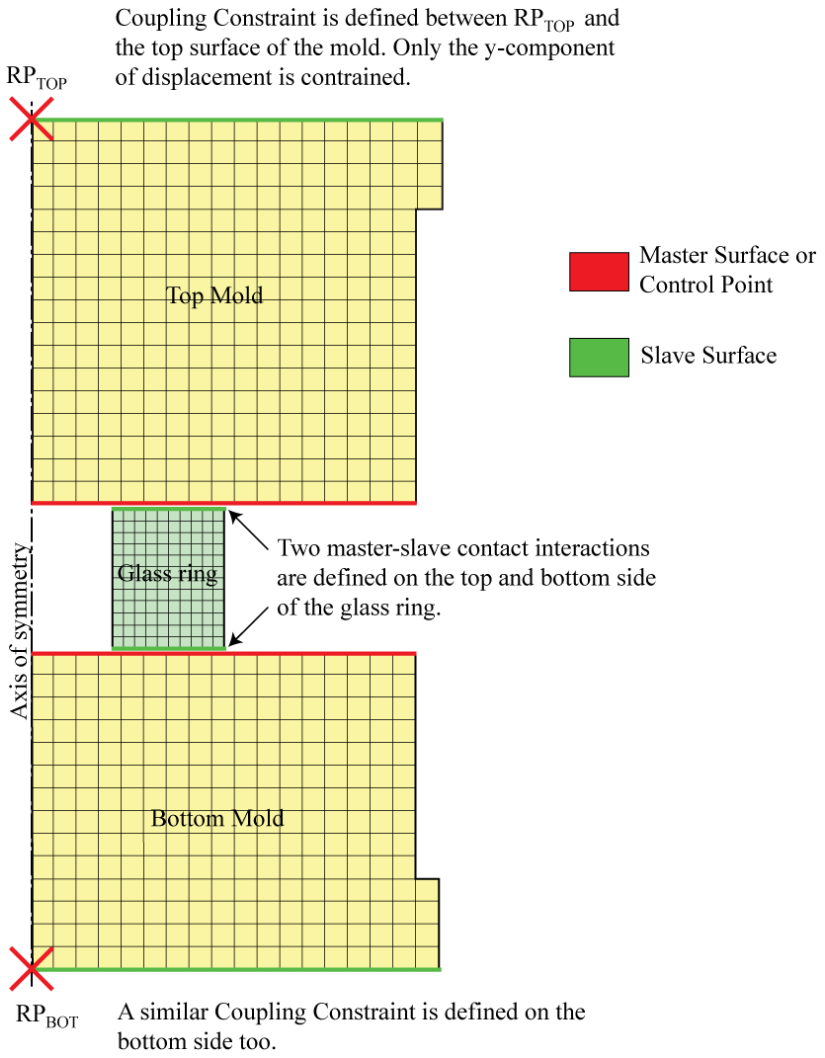

Figure 3.13: Axisymmetric Model used for simulation of the ring compression test.

are circular and the loading can be approximated as symmetric around the central axis; an axi-symmetric model is considered. A *COUPLED-TEMPERATURE DISPLACEMENT type of analysis was used in this simulation as the mechanical properties change drastically with temperature and the heat conduction at the interface is also affected by the changing contact surface. The ring is modeled as a linear viscoelastic material, while both the upper and lower molds are modeled as linear elastic materials. The glass ring is meshed with 3072 CAX4RT elements, while the upper and lower molds are meshed with 1284 and 1107 CAX4RT elements, respectively. Two master-slave type of contact interaction pairs were created; one between top surface of the ring and bottom surface of the top mold and the other between the bottom surface of the ring and top surface of the bottom mold as shown in Figure 3.13 below. A Coulomb friction model based on penalty formulation was used in the simulation with a friction coefficient of 0.04. The normal behavior was modeled as “hard” contact which does not allow any amount of penetration of one surface onto another. The contact conductance behavior is similar to the one used for lens molding and the details of which are already given in Chapter 2. Two coupling constraints are also defined; one between RP_{TOP} and the top surface of the top mold and the other between RP_{BOT} and the bottom surface of the bottom mold as shown in the Figure below. However in these constraints only the vertical components of displacements of the slave surfaces were constrained to move along with that of their respective master reference points while the horizontal components of displacements are allowed to be free. This approach not only represents the actual process more closely, but also eases applying force boundary conditions and extracting displacement response from the results file.

3.5.4. Viscoelastic characterization of L-BAL 35 at 569°C

The data from the ring compression test conducted at 569°C was used to characterize the viscoelastic material behavior of glass. The reason for using the lower temperature data for curve

fitting is the fact that the delayed elastic part or the time-dependent part has a much larger contribution in the overall displacement than the data at higher temperature. The relaxation times will be larger at this temperature and therefore easier to obtain than its counterpart. In fact, this claim is demonstrated in subsection 3.5.7 by using the data at higher temperature to characterize the viscoelastic material behavior.

Using the experimental displacement response at 569°C, the weights, the relaxation times, and the number of terms were varied manually until the response from simulation matched well with the experimental displacement curve. After several iterations, the viscoelastic material properties given in Table 3.1 were arrived at, that produced a displacement response as shown in Figure 3.14. A 4 term prony series was used for the shear relaxation function, while just one term was used for the hydrostatic relaxation function. The weight for the hydrostatic relaxation function is related to the ratio of the equilibrium and the instantaneous bulk modulus as shown in Table 3.1.

Shear Relaxation Function, $\psi_1(t)$		Hydrostatic Relaxation Function, $\psi_2(t)$		TRS behavior	
w_i	τ_i (s)	$\nu_i = 1 - \frac{K_\infty}{K_0}$	λ_i (s)	T_R (°C)	569
0.5794458	4.75	0.85	10	C_1	12.41
0.3624554	6				
0.03	11			C_2	129
0.028	930				

Table 3.1: Viscoelastic characterization of L-BAL35 glass at 569°C including WLF parameters for time-temperature dependence.

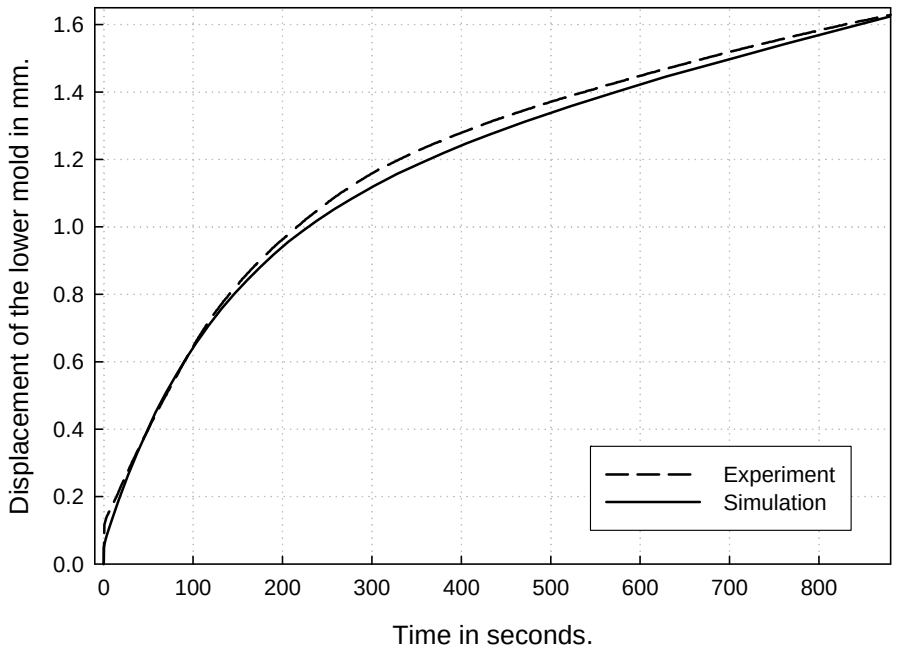

Figure 3.14: Comparison of experimental and simulated response of the displacement of the lower mold when the ring was pressed at 569°C. The simulation was based on input material properties given in Table 3.1.

3.5.5. Viscoelastic characterization of L-BAL 35 at 589°C

Using the viscoelastic material parameters at 569°C and assuming TRS behavior, a shift factor, A(T) of 46.3 was found out to best fit the experimental data of the displacement of the lower mold when the ring was pressed at 589°C as shown in Figure 3.15. Although the initial part of the simulated response is more compliant than the experimental response, towards the end of the pressing cycle, the current viscoelastic model does perform well.

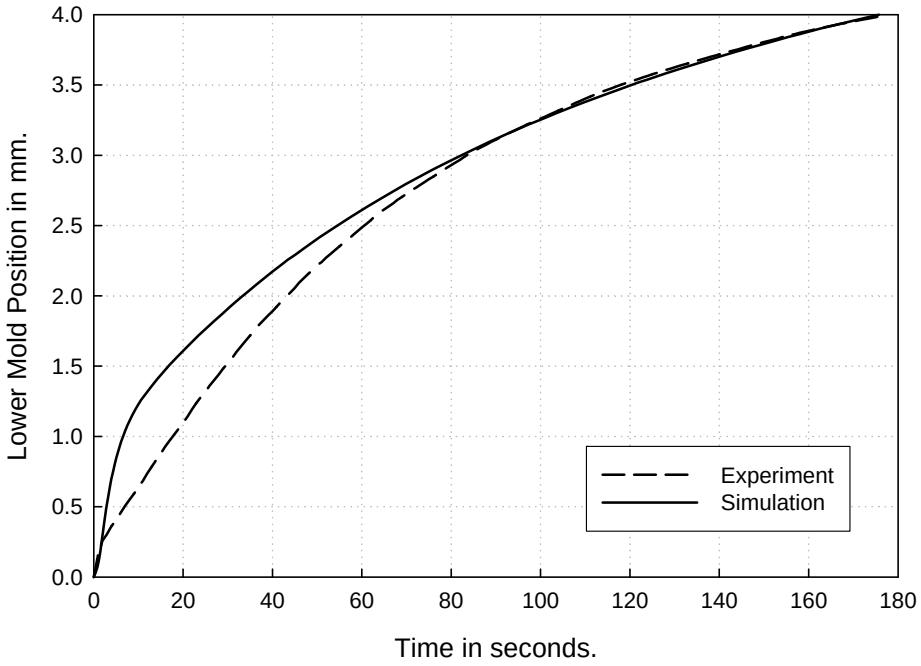

Figure 3.15: Comparison of experimental and simulated response of the displacement of the lower mold when the ring was pressed at 589°C. The simulation was based on input material properties given in Table 3.1.

In order to obtain the TRS behavior completely, at least three data points are required on the shift factor A(T) vs. temperature curve to fit a WLF equation given in Eq. (3.11). Since only two points are available, one for each temperature, the third point was obtained from information on T_L, the lowest temperature of the glass transition region. Below this temperature the glass structure becomes frozen and the glass behaves as purely elastic. For L-BAL35 glass, T_L is 440°C which was obtained from thermal expansion and specific heat experiments. Since the same mechanism give rise to time-dependence in specific heat and thermal expansion, the same value of T_L was assumed to apply to viscoelastic behavior as well. When the denominator of Eq. (3.11) becomes zero, then the material becomes

purely elastic. Using this condition and T_R = 569°C, a value of 129°C was assigned to C_2. Now the value of C1 was found based on the two points obtained from the two experiments conducted at two different temperatures and it is given in Table 3.1.

3.5.6. Other possibilities

In the preceding sections it is argued that characterizing the viscoelastic material behavior at the lower temperature was more beneficial as the relaxation times are larger, which makes their determination easier. To prove that the claim made earlier was correct, the experimental data at 589°C is fit first. Application of this fit to the ring experiment conducted at 569°C will reveal the better approach.

Shear Relaxation Function, $\psi_1(t)$		Hydrostatic Relaxation Function, $\psi_2(t)$	
w_i	τ_i (s)	$v_i = 1 - \frac{K_\infty}{K_0}$	λ_i (s)
0.34	0.1	0.85	0.15
0.43	0.62		
0.23	1.7		

Table 3.2: Viscoelastic characterization of glass at 589°C.

The same procedure detailed in Section 3.5.2 was used to arrive at a reasonable viscoelastic characterization, that when used in the ABAQUS simulation, produced a response that matched the data well. The viscoelastic parameters that produced such a response are given in Table 3.2 and the corresponding response is shown in Figure 3.16(a). The simulated response follows the experimental trend very well.

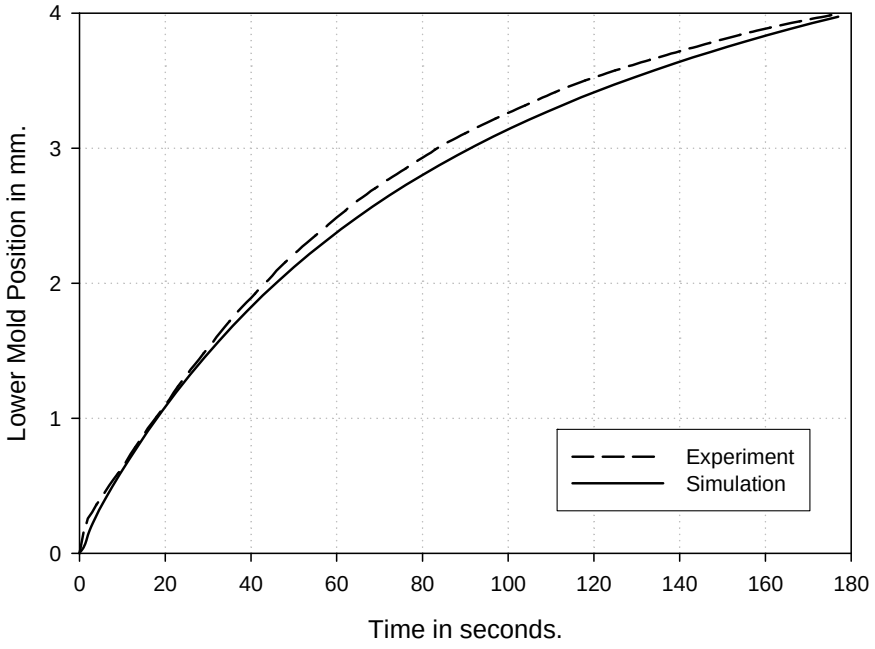

(a) Comparison of experimental and simulated response at 589°C.

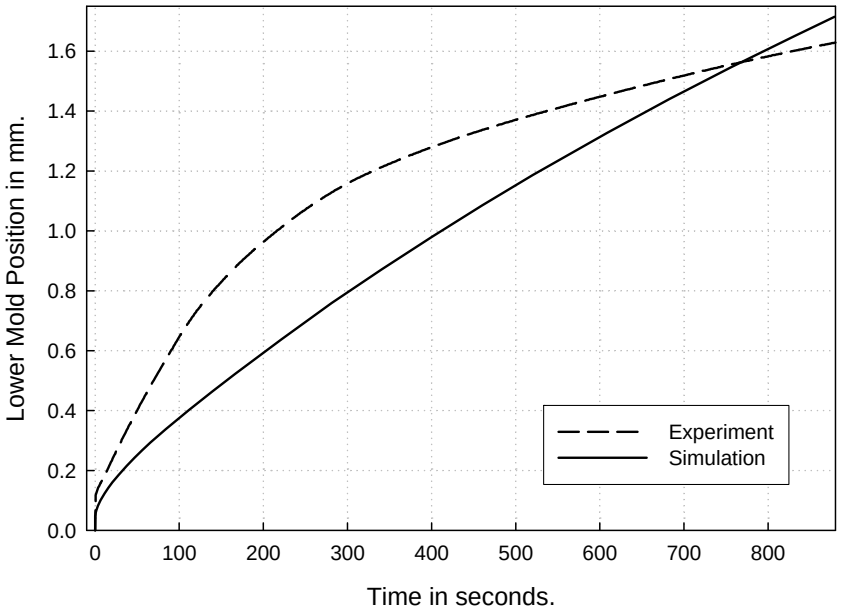

(b) Comparison of experimental and simulated response at 569°C.

Figure 3.16: Viscoelastic characterization was done using the experimental data at 589°C and that relaxation function was shifted to T = 589°C assuming TRS behavior.

Now if the relaxation function just obtained was shifted horizontally to the left so that it corresponds to T = 569°C under the TRS assumption, and when it was used to simulate the ring compression test at 569°C, the corresponding response it produced is shown in Figure 3.16(b). Observing that Figure 3.16b is not as good a fit as that of Figure 3.15, shows that using the current approach, it is easier to use the lower temperature data for the master curve. Therefore, the viscoelastic material properties given in Table 3.1 will be used for the remainder of the simulations.

3.5.7. Sensitivity of Viscosity of Glass on the Displacement Data

The shear relaxation function, $G_1(t)$ is related to the equilibrium viscosity, η, of the glass as

$$\tau_{avg} = \sum_{i=1}^{n} w_i \tau_i = \frac{\eta}{G_0} \tag{3.12}$$

where 'τ_{avg}' is the weighted average of the relaxation times. Based on the viscoelastic material parameters given in Table 3.1and the elastic properties given in Table 2.1 of Chapter 2, the viscosities of L-BAL35 at 589°C and 569°C were calculated to be $10^{8.7}$ Pa.s and $10^{10.4}$ Pa.s, respectively. In this research the viscosities were not known ahead of time and hence they are calculated as an output from the viscoelastic characterization using Eq. (3.12). However, the viscosity of L-BAL35 glass as a function of temperature was available at a later point in time and is shown in Figure 3.17. From the softening point the viscosity curve for L-BAL35 was determined as indicated in Figure 3.17. The softening point of glass is defined as the temperature at which the viscosity equals $10^{7.6}$ Poise. From this figure, the experimental viscosity at the molding temperature of 589°C is approximately $10^{7.75}$ Pa.s which is lower than the viscosity computed from the ring compression tests.

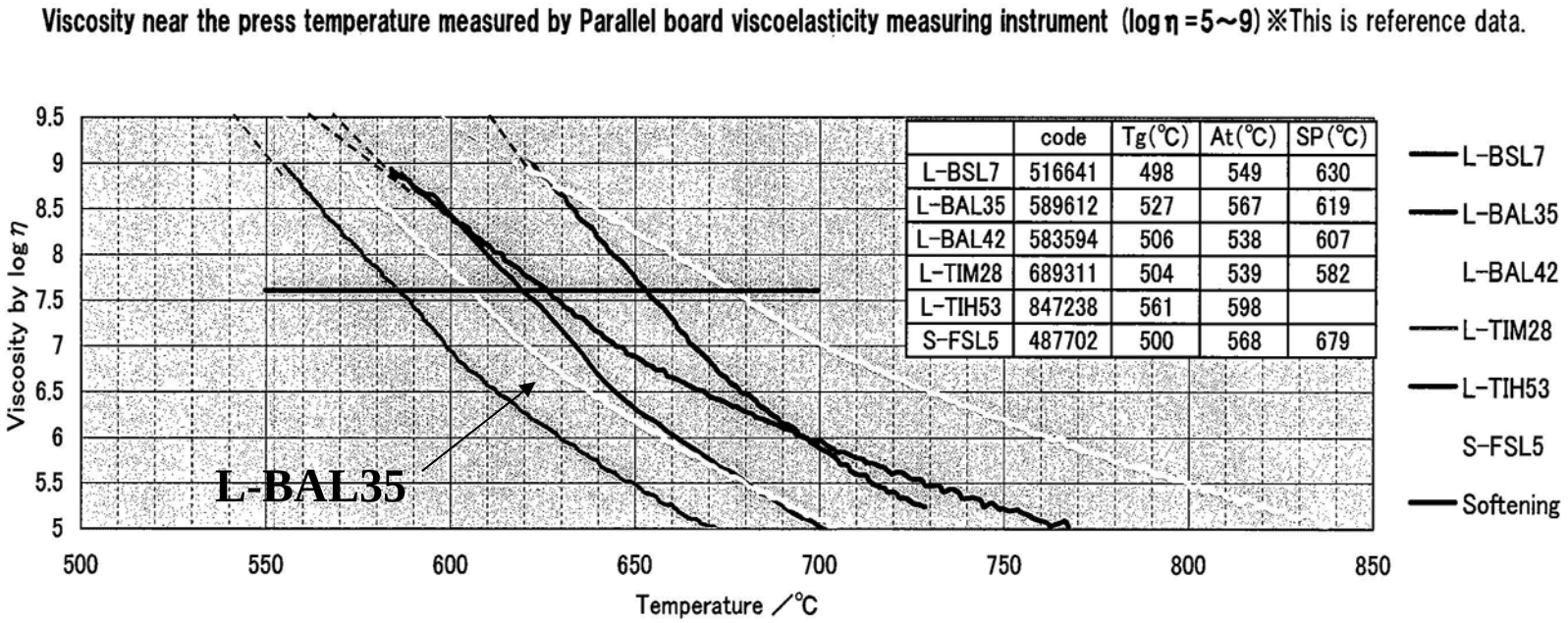

Figure 3.17: Viscosity – Temperature curve of L-BAL35 molding glass near the pressing [16]

3.6. Conclusions

In this chapter a typical linear viscoelastic response of glass in the transition region was illustrated, with all the necessary details, and its constitutive equations were given. The relevant experiments that are reported in the literature to have been used to characterize this behavior were then reviewed. Different specimen shapes have been used in the literature, from simple cylinders to complex ones such as glass helical springs. All the advantages and disadvantages of each experiment were discussed.

In the current research, a ring compression test was used to characterize the friction behavior at the glass/mold interface and to obtain the viscoelastic material behavior of glass at the molding temperature. Then the methodologies to extract the parameters associated with these behaviors were outlined. For this purpose, a finite element model of the ring compression test was created. The viscoelastic material parameters were varied in the ABAQUS simulation manually until the experimental response matched the simulated one. After several iterations the viscoelastic material properties given in Table 3.1 were determined. This material definition led to a displacement response that was close to the experimental one at 569°C. The qualities of the input parameters were then checked by using it to simulate the ring compression test at 589°C. Thus, this viscoelastic material behavior that is reported in Table 3.1 will be used in all the future sensitivity analysis studies, the results of which are reported in Chapters 6 and 7.

References

1. G. Scherer (1986), *Relaxation in glass and composites*, John Wiley and Sons.
2. L. Duffrene, R. Gy, H. Burlet, and R. Piques, Viscoelastic behavior of a soda-lime-silica glass: inadequacy of the KWW function, Journal of non-crystalline solids, 2**15**(1997), pp. 208-217.

3. J. H. Li and D. R. Uhlmann, The flow of glass at high stress levels : I. Non-Newtonian behavior of homogeneous 0.08 Rb_2O·0.92 SiO_2 glasses, *Journal of Non-Crystalline Solids,* **3**(1970), 127 – 147.

4. A. Jain, A.Y. Yi, Finite element modeling of stress relaxation in glass lens moulding using measured, temperature-dependent elastic modulus and viscosity data of glass, Modelling Simul. Mater. Sci. Eng., **14**(2006),pp. 465-477.

5. L. Duffrene, R. Gy, H. Burlet, and R. Piques, Multiaxial linear viscoelastic behavior of a soda-lime-silica glass based on a generalized Maxwell model, J. Rheology,**41**(1997), pp. 1021-1038.

6. http://www.ms.ornl.gov/htmlhome/uc_mechanical.shtml

7. Y. Gueguen, J-C. Sangleboeuf, V. Keryvin, T. Rouxel, E. A. King, E. Robin, G. Delaizir, B. Bureau, X-H. Zhang and P. Lucas, Sub-Tg viscoelastic behavior of chalcogenide glasses, anomalous viscous flow and stress relaxation, J. Cer. Soc. Jpn, **116**(2008), pp. 890-895.

8. S. H. Chang, Y. M. Lee, T. S. Jung, J. J. Kang, S. K. Hong, G. H. Shin, Y. M. Heo, Simulation of an aspheric glass lens forming behavior in progressive GMP process, NUMIFORM '07, Materials processing and design: Modeling, simulation and applications, edited by J. M. A. Cesar de Sa and A. D. Santos, 2007, pp. 1055-1060.

9. P. H. DeHoff, K. J. Anusavice, Creep functions of dental ceramics measured in a beam-bending viscometer, Dental Materials, **20**(2004), pp. 297-304.

10. P.H. DeHoff, K. J. Anusavice, Shear stress relaxation of dental ceramics determined from creep behavior, Dental Materials, **20**(2004), pp. 717-725.

11. R. Gy, On the equilibrium isothermal compressibility of soda-lime-silica glass, Journal of non-crystalline solids, **128**(1991), pp. 101-108.

12. R. Gy, L. Duffrene, M. Labrot, New insights into the viscoelasticity of glass, Journal of non-crystalline solids, **175**(1994), pp. 103-117.

13. L. Duffrene, R. Gy, Viscoelastic constants of a soda-lime-silica glass, Journal of non-crystalline solids, **211**(1997), pp. 30-38.

14. G. W. Scherer, S. M. Rekhson, Viscoelastic-elastic composites: II, General Theory, J. Am. Ceram. Soc., **65**(1982),pp. 399-406.

15. A.T. Male and V. Depierre, The validity of mathematical solutions for determining friction from the ring compression test, ASME J. Lubr. Technol., **92**(1970), pp. 389-397.

16. Viscosity data of Ohara's L-BAL35 molding glass.

CHAPTER FOUR

Structural Relaxation and its Implementation

4.1. Structural Relaxation – An Introduction

When glass is subjected to a sudden change in temperature within its transition region, a time dependent change in its volume occurs as shown in Figure 4.1. This behavior is referred to as structural relaxation. Specific heat, refractive index, density, viscosity and enthalpy also show such type of time-dependence indicating that structural relaxation has an effect on all these properties. For a formal understanding of the phenomena of structural relaxation, please refer to G. Scherer [1]. In this section the characteristics of structural relaxation that are relevant to the lens molding process are given. The response in Figure 4.1 clearly shows that there is an instantaneous change in the property and a time dependent change in the property, which is analogous to stress relaxation.

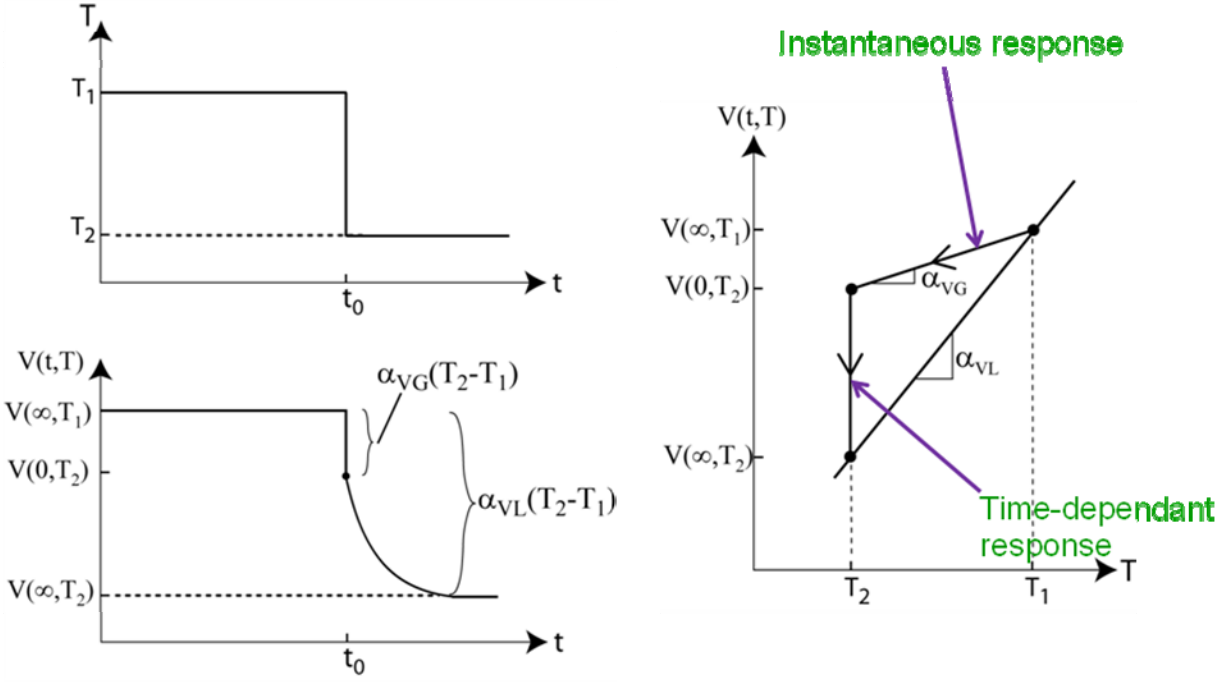

Figure 4.1: Effect of structural relaxation on volume of the glass specimen subjected to a sudden temperature change.

In Figure 4.1, the liquid and glassy thermal expansion coefficients, denoted by α_{VL} and α_{VG} respectively, are constants for a particular glass type. While the instantaneous change in the property occurs along the glass slope in the Volume-Temperature plot, the time-dependent change in the property occurs in the vertical direction towards the equilibrium liquid line as shown in V-T curve. Recall from the section on Glass Transition in Chapter 1 that when a glass sample is continuously cooled, the path of the volume-temperature curve consists approximately of two straight lines; the slope of the straight line in the higher temperature range is the equilibrium liquid slope denoted by α_l and the slope of the straight line in lower temperature range is the glassy slope α_g.

An important property of the structural relaxation of glass is its nonlinear behavior with respect to a finite temperature jump, ΔT. When two similar glass samples that were equilibrated at two different temperatures T_1 and T_3 are suddenly placed in an environment that is at temperature T_2, then the corresponding volume change is shown in Figure 4.2 below. The figure shows that for a positive temperature jump ($+\Delta T = T_2 - T_3$), the relaxation process takes longer to attain equilibrium, than for a negative temperature jump ($-\Delta T = T_1 - T_2$). Hence heating and cooling are not the same with respect to structural relaxation which makes it nonlinear.

The structural relaxation process is strongly dependent on the cooling rate. Next, consider a more realistic case of a glass sample continuously cooled at a constant rate, q. As evident in Figure 4.3 (a), the more quickly the glass sample is cooled, the sooner it would depart from the equilibrium liquid line. The glass sample that is cooled at the slowest rate, q_1 will depart from the equilibrium line very late during the cooling process and will have the maximum volume shrinkage. When the glass sample is cooled very slowly, there is enough time for the molecules to come to an equilibrium configuration or a compact arrangement resulting in maximum

shrinkage. Since T_g is defined approximately at the midpoint of the transition region, T_g is high for a glass sample that is cooled quickly and vice versa.

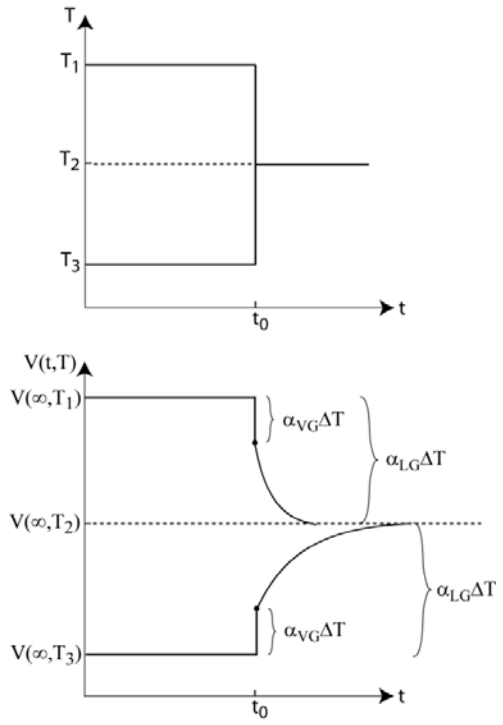

Figure 4.2: Nonlinear behavior with respect to a temperature jump, ΔT.

Another important quantity in the structural relaxation process is the concept of fictive temperature. Ficitve temperautre, T_f, is defined as the quantity that quantifies the amount of structural relaxation that has occurred in a glass sample. When the temperature is high, then the structural relaxation process is almost instantaneous which is characterized by fictive temperautre being equal to the actual temperature of the sample as shown in Figure 4.3(b). As the glass is cooled further, the energy available for molecular re-arrangements decreases and hence the relaxation process becomes more sluggish. At this stage the fictive temperature departs from the actual temperature. The actual temperature reduces at a constat rate while the fictive temperature reduces more slowly. Finally, when the energy available becomes very low, the structure does

not relax. Then the glass structure is frozen although it has not reached the equilibrium configuration. At this stage, the fictive temperature stops reducing and becomes a constant. The value at which the fictive temperautre reaches a constant value is the *true* glass transition temperature, T_g. In the next section, several models of structural relaxation that lead to the final

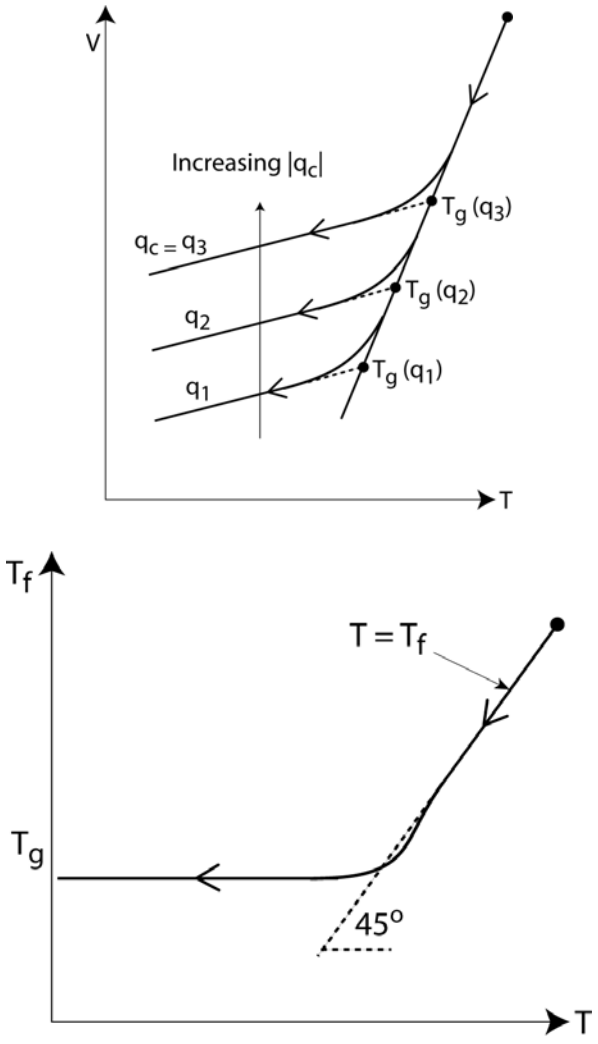

Figure 4.3: Evolution of property for a continuously cooled glass sample. Figure 4.3 (a) illustrates the dependance of cooling rate on T_g and Figure 4.3 (b) illustrates the variation of fictive temperature, Tf as a function of temperature as the sample is continuously cooled.

satisfactory model of structural relaxation are summarized. In all these models, differential equations were developed to determine the fictive temperature when a glass sample is subjected to thermal loading. Once the fictive temperature is known, any property that obeys structural relaxation can be determined.

4.2. Different Models of Structural Relaxation

The first model of structural relaxation behavior of glass was proposed by A. Q. Tool in 1946 [2]. In his model the rate of change of fictive temperature is proportional to its deviation from the actual temperature. Tool's equation is

$$\frac{dT_f}{dt} = \frac{T - T_f}{\tau_p} \tag{4.1}$$

where T is the actual temperature of glass, T_f is the fictive temperature and τ_p is the structural relaxation time. Tool was the first to propose the term fictive temperature and the term 'fictive' is used because it is not a physical quantity, but purely a mathematical quantity that quantifies the state of the altering structure. Initially, Tool made the relaxation time only a function of actual temperature,

$$\tau_p = \tau_0 \exp[-AT] \tag{4.2}$$

where τ_0 and A are constants and then made structural relaxation time not only dependent upon temperature, but also on the changing structure and developed the following equation

$$\tau_p = \tau_0 \exp[-A_1 T - A_2 T_f] \,, \tag{4.3}$$

which makes Tool's equation *nonlinear*. There is no theoretical justification for this equation and with this assumption (4.2), he was able to describe some of the experimental data, but not all of it.

Narayanaswamy [3] removed the nonlinearity in the equations by using the concept of reduced time similar to one used to account for the temperature dependence of viscoelastic behavior. He also transformed the Tool's differential equation into an integral equation,

$$T_f(t) = T(t) - \int_0^t M\left(\xi(t) - \xi(t')\right)\frac{dT_f(t')}{dt'}dt' \tag{4.4}$$

where

$$M(\xi) = \exp\left[-\left(\frac{\xi}{\tau}\right)^b\right], \tag{4.5}$$

a stretched exponential also called Kohlrausch shape function and the reduced time is defined by

$$\xi(t) = \int_0^t \exp\left[\frac{H}{T_R} - \frac{xH}{T(t')} - \frac{(1-x)H}{T_f(t')}\right]dt' \tag{4.6}$$

where '*H*' is the activation energy constant, '*x*' is the nonlinearity parameter, T_R is the reference temperature at which the structural relaxation function, $M(\xi)$ is defined and '*b*' is the Kohlrausch shape factor. The important contributions of Narayanaswamy are

i. Removing the nonlinearity in Tool's equation
ii. Replacing the relaxation mechanism that was based on a single relaxation time with a stretched exponential which takes the "memory" effect into account.

His model was able to describe all the experimental data, although solving the equations was very tedious.

Later, Moynihan [4] combined equations (4.5) and (4.6) to obtain

$$\frac{dT_f}{dt} = -\frac{d\xi}{dt}\int_0^t \frac{dM(\xi - \xi')}{d\xi}dT(\xi') \tag{4.7}$$

and replaced the stretched exponential with a prony series of the form,

$$M(\xi) = \sum_{i=1}^{n} g_i \exp\left(-\frac{\xi}{\tau_i}\right) \quad \text{э} \quad \sum_{i=1}^{n} g_i = 1. \tag{4.8}$$

This modification made the solution of differential equations much simpler. Instead of solving a single nonlinear differential equation as in Narayanaswamy's model, now it is enough to solve 'n'

linear differential equations, where 'n' is the number of terms used in the prony series to define the structural relaxation mechanism. Each linear equation defined below

$$\frac{dT_{fi}}{dt} = -\frac{T_{fi} - T}{\tau_i}\frac{d\xi}{dt}, \quad i = 1, 2, ..., n \tag{4.9}$$

is similar to Tool's equation. In (4.9), T_{fi} are called partial fictive temperatures and the total fictive temperature, T_f is obtained using

$$T_f = \sum_{i=1}^{n} g_i T_{fi} \, . \tag{4.10}$$

Equation (4.6) and equations (4.8-4.10) which describe the experimental data very well and it is often referred to as TNM-model of structural relaxation. It should be remembered that this model is a phenomenological one and there is no physics-based justification to these equations. Table 4.1compares the evolution of the models with respect to its mathematical simplicity, ability to capture the physics and the type of relaxation functions used for modeling structural relaxation of glass.

	Tool (1946)	Narayanaswamy (1971)	Moynihan (1975)
Relaxation function used	$\exp\left[-\frac{t}{\tau}\right]$	$\exp\left[-\left(\frac{t}{\tau_i}\right)^b\right]$	$\sum_{i=1}^{n_1} w_i \exp\left[-\frac{t}{\tau_i}\right]$
Memory effect or ability to capture physics	NO	YES	YES
Mathematical simplicity	YES	NO	YES

Table 4.1: Comparison of the different structural relaxation models with respect to its ability to capture the physics, mathematical simplicity and the type of relaxation functions used.

Markovsky *et al* [5] gave a semi-implicit finite difference scheme to solve the Tool's equation given in equation (4.9) and they claim that this method is more efficient and stable for

calculating the fictive temperature than the integral form given in equation (4.4). Using equation (4.6) in equation (4.9), we get the differential form the Tool's equation

$$\frac{dT_{fi}}{dt} = \frac{T - T_{fi}}{\tau_i} \exp\left[\frac{H}{T_R} - \frac{xH}{T(t')} - \frac{(1-x)H}{T_f(t')} \right]. \tag{4.11}$$

with initial conditions $T_f(0) = T_0$ and $T_{fi}(0) = T_0$, when cooling from an initial temperature that is much higher than T_g was considered. However, if heating was considered, say from room temperature, the initial conditions $T_f(0) = T_g$ and $T_{fi}(0) = T_g$ were used. Using backward-Euler method or the implicit method, equation (4.11) can be discretized to obtain

$$\frac{T_{fi}(N) - T_{fi}(N-1)}{dt} = \frac{T(N) - T_{fi}(N)}{\tau_i} \exp\left[\frac{H}{T_R} - \frac{xH}{T(N)} - \frac{(1-x)H}{T_f(N-1)} \right]. \tag{4.12}$$

From equation (4.12), $T_{fi}(N)$ could be obtained easily. Equation (4.12) is not a fully implicit discretization because the fictive temperature in the last term of the exponent is evaluated at t_{N-1} and not at t_N. This makes the solution of the differential equation easier to obtain and without loss of accuracy. They also prove that this method is unconditionally stable for any time step, *dt*, smaller or larger than any of the relaxation times.

4.3. Implementation of Structural Relaxation Behavior in ABAQUS

Structural relaxation behavior of glass can be implemented in ABAQUS by adding time-dependence to the thermal expansion coefficient. This is analogous to adding time-dependence or viscoelastic behavior to a linear elastic material. The volume change of a glass sample when it is cooled continuously at a constant rate is shown in Figure 4.4. The slope of this V-T curve, also called the thermal expansion coefficient of glass, is plotted below in Figure 4.4. While the liquid and glassy thermal expansion coefficients are constants for a particular glass

type, the transition of α from liquid to solid during cooling is not constant and is strongly dependent on the cooling rate and the four structural relaxation parameters, H, x, β, and τ_0. When glass is in liquid state, the volumetric thermal strain is defined as

$$d\varepsilon_V(t) = \alpha_{VL} dT \tag{4.13}$$

and when it is in the solid, frozen or glassy state, the strain is defined as

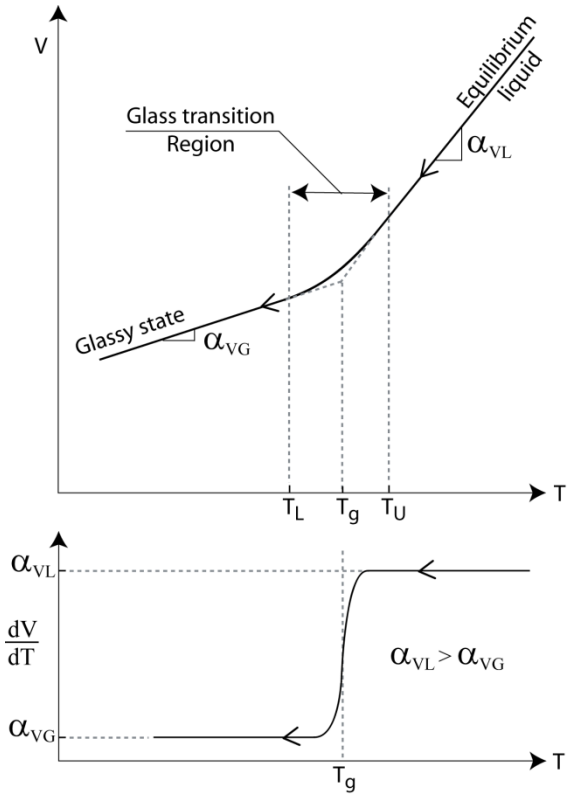

Figure 4.4: Typical Volume-Temperature curve of glass for a certain constant cooling rate is shown on top. The thermal expansion coefficient which is the derivative of the volume with respect to temperature is shown on the bottom.

$$d\varepsilon_V(t) = \alpha_{VG} dT \,. \tag{4.14}$$

However, when the glass is in the transition region between the solid and the liquid regions, the strain is not only dependent upon the temperature, but also on the fictive temperature as defined below:

$$d\varepsilon_V(t) = \alpha_{VG}dT + (\alpha_{VL} - \alpha_{VG})dT_f . \quad (4.15)$$

In ABAQUS, the structural relaxation behavior is implemented using the subroutine UEXPAN. The user subroutine was written in Intel Visual Fortran version 9.1 which is the only version that is compatible

with ABAQUS 6.7. This subroutine must be called at the beginning of every time increment and the new value is assigned to it according to the input parameters and the structural relaxation model. Several solution dependent state variables (SDVs) were used to save the partial and total fictive temperatures since those values from the previous time step are needed for the current time step (see equation (4.12)).

First the number of solution dependent state variables (SDVs) was defined in the input file using the *DEPVAR keyword which represents the partial and total fictive temperatures. Then initial values of these SDVs were input using the *INITIAL SOLUTION keyword. If only cooling was modeled, then SDVs were initialized to be equal to the initial temperature and if heating and cooling were both modeled as in the current case, then the SDVs were initialized to be equal to the glass transition temperature. Then the *EXPANSION keyword was used with the USER option to override the standard feature and invoke the subroutine. Since glass is isotropic, only one thermal expansion coefficient needs to be defined. In the subroutine, all the material parameters that govern the structural relaxation behavior were defined first. Then Markovsky *et al* semi-implicit scheme [5] was used to numerically solve Tool's equation for total fictive temperature and compute the new thermal expansion values for the next time increment using equation (4.15) during the thermal cycle. The new value of the thermal expansion coefficient was used in the calculation. Since the previous values of the fictive temperatures are needed in the calculations (See equation (4.12)), the newly computed fictive temperatures were stored in the SDVs deleting the old ones.

4.4. Validation of the Subroutine using Sandwich Seal Solution

The user-subroutine written to implement structural relaxation was tested with a sandwich seal solution available in the literature [6]. In this paper an aluminum layer was sandwiched between two glass layers as shown in Figure 4.5 and heated to 618^{o}C. Then the glass was allowed to stabilize, i.e. given time for the structural relaxation process to equilibrate. Finally, the sandwich seal is cooled continuously at a constant rate of 3^{o}C/min until room temperature is reached. The stress developed in the glass layer during this continuous cooling is plotted as a function of temperature in Figure 4.6. Although aluminum is elastic, the stress is continuously varying with time because glass behavior is time-dependent. The experimental data and corresponding numerical solution of Scherer *et al* [6] are compared with the solution obtained from ABAQUS in Figure 4.7. In the ABAQUS model a prony series was used instead of the b-function representation used in the paper. The other approximation in the ABAQUS model was to come up with a separate shear and volumetric property by curve fitting the uniaxial material behavior used by Scherer *et al*[6]. The slight difference in the plots is attributed to these reasons.

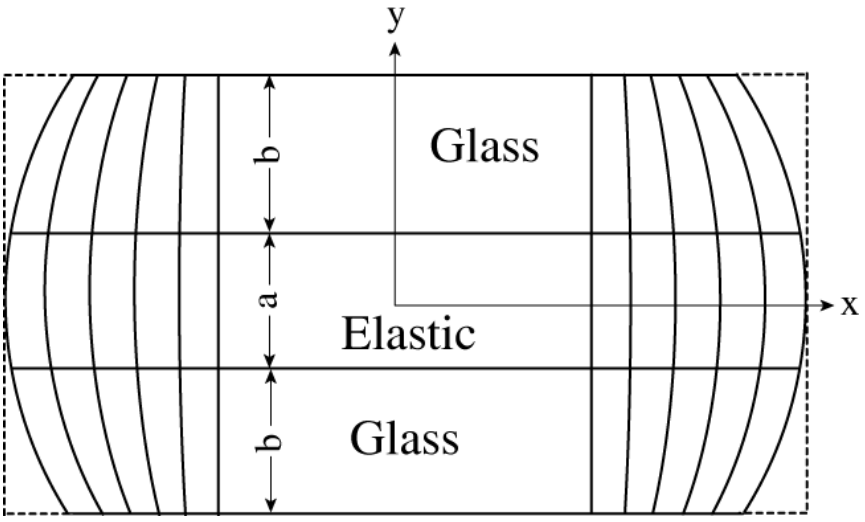

Figure 4.5: Schematic of a sandwich seal

An important point from this validation study was the realization that the TRS assumption using the WLF equation was not adequate for this analysis. Although the WLF-fit looked good as shown in Figure 3.8, the stress state predicted by the model did not correlate with the data of Scherer *et al* [6]. Once the WLF equation was replaced with a piecewise linear interpolation using the UTRS subroutine, the prediction of stress state improved and is the result shown in Figure 4.6. Thus TRS behavior does qualify as one of the parameters for which a sensitivity analysis should be done. This also requires that creep or relaxation experiments be done over a wide range of temperatures.

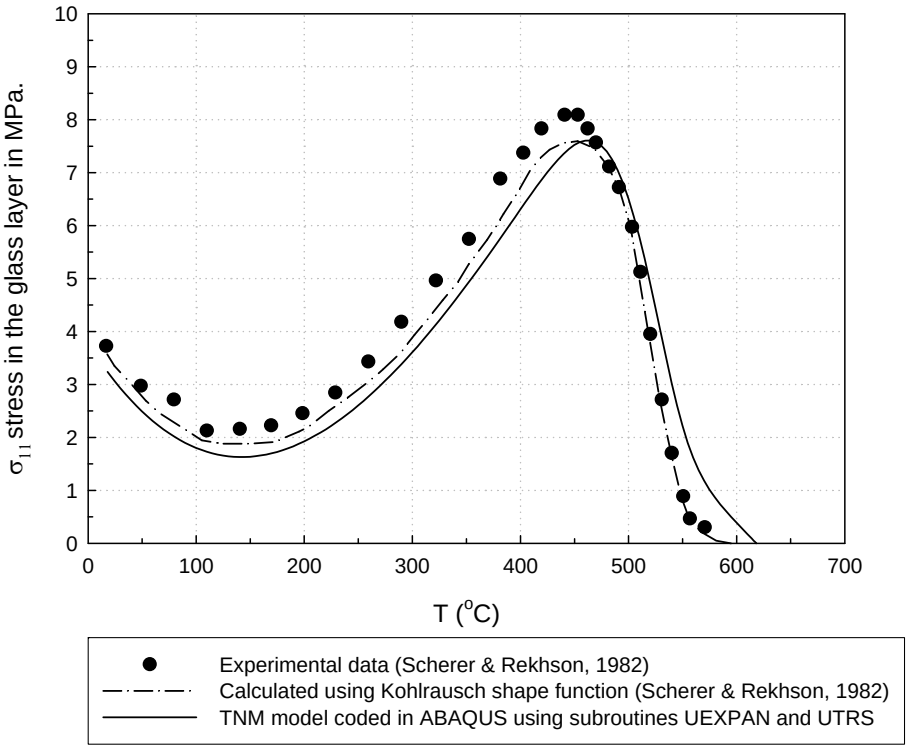

Figure 4.6: Stress in the glass layer developed in a glass-alumina-glass sandwich seal when the stabilized composite was cooled at a constant rate of 3°C/min from 618°C to room temperature.

4.5. Experiments

The input parameters required for modeling structural relaxation behavior in the finite element code were obtained from experiments conducted on a Thermo-Mechanical Analyzer (TMA) and Differential Scanning Calorimetry (DSC). The TMA was used to obtain the liquid and solid thermal expansion coefficients of L-BAL35 glass and DSC measurements of specific heat of glass were used to obtain the rate dependent structural relaxation behavior. More details on the experimental techniques, their drawbacks and methods of extraction of parameters are discussed in the master's thesis of S. Gaylord [7]. Only the basic working principle of these experiments and some assumptions that are relevant to the modeling part are discussed below.

To obtain the thermal expansion coefficients using TMA, rectangular glass rods of dimensions 4x4x15mm were heated from a specified temperature much below the T_g at a constant rate of 2K/min and their change of lengths were measured using an LVDT sensor. The thermal expansion coefficients were obtained by differentiating the change in length with respect to the change in temperature and then dividing it by its initial height. The thermal expansion coefficient below the T_g is a weak linear function of temperature and then increases significantly in the transition region before settling down to a constant value corresponding to the liquid thermal expansion coefficient. The main problem with this technique is the small force of approximately 0.05N the sensor applies on the glass sample to measure the length change is high enough to crush the sample at high temperature.

Therefore DSC measurements, which do not have this problem at high temperature, were used to obtain the structural relaxation parameters for the model. Specific heat of glass is one of the quantities that exhibits structural relaxation behavior. Using DSC the specific heat of glass can be measured very accurately. Hence this technique was employed to obtain the parameters that govern the relaxation kinetic of glass. It has been argued in the study of S.

Gaylord [7] that the relaxation kinetics of volume expansion is practically indistinguishable from that of the specific heat or viscosity and more references that used this assumption are also cited. A glass sample that is equilibrated at a temperature much lower than T_g is heated at two different heating rates of 4K/min and 8K/min and the specific heat is measured as a function of temperature. Then, the TNM-model parameters ($\Delta H/R$, β, x, τ_0) are adjusted until the simulation result matches with the experimental output at both heating rates. The nonlinear curve fitting routine, '*nlintool*' in MATLAB was used for this purpose.

4.6. Input Parameters for the Model

The TNM-model parameters based on DSC measurements have to be converted to a form that is acceptable by the finite element code. The TNM-model parameters of structural relaxation based on differential scanning calorimetry (DSC) are

$$\left(\frac{\Delta H}{R}, x, \beta, \tau_0\right). \tag{4.12}$$

However, the finite element code requires structural relaxation parameters defined at a reference temperature T_R given below:

$$\left(\frac{\Delta H}{R}, x, \beta, \tau_R\right) \tag{4.13}$$

This set of parameters for describing the structural relaxation phenomenon was adopted from the sandwich seal solution given by Scherer and Rekhson [6]. The structural relaxation time at any temperature based on the TNM-model is defined by

$$\tau(T) = \tau_0 \exp\left[\frac{\Delta H}{R}\left(\frac{x}{T} + \frac{1-x}{T_f}\right)\right]. \tag{4.14}$$

In order to convert DSC structural relaxation parameters to a form that is suitable for the finite element code, set an arbitrary temperature as T_R that is 50°C to 100°C higher than the glass transition temperature, T_g. Since the structural relaxation process is faster at higher temperature, the difference between the actual and the fictive temperature will be negligible and we can write

$$\tau_R = \tau(T_R) = \tau_0 \exp\left[\frac{\Delta H}{R}\left(\frac{1}{T_R}\right)\right]. \tag{4.15}$$

Now that the stretched exponential function that describes the structural relaxation phenomenon at the reference temperature is known, a *nonlinear* curve fitting routine in MATLAB ('nlintool') was used to convert it into a prony series defined below:

$$\exp\left[-\left(\frac{t}{\tau_R}\right)^{\beta}\right] = \sum_{i=1}^{n} v_i \exp\left(-\frac{t}{\tau_{Ri}}\right), \qquad \text{э} \sum_{i=1}^{n} v_i = 1. \tag{4.16}$$

Specifically, a 6 term prony series was used to approximate the stretched exponential relaxation function. The structural relaxation parameters along with the liquid and solid thermal expansion coefficients used in this research are tabulated in Table 4.2.

Solid coefficient of thermal expansion, α_g (K^{-1})	OHARA specification sheet	8.1×10^{-6}	
	Material's team estimation*	$(8.2 \pm 0.1) \times 10^{-6}$	
Liquid coefficient of thermal expansion, α_l (K^{-1})		$(70 \pm 0.1) \times 10^{-6}$	
Activation Energy constant, $\frac{\Delta H}{R}$ K		90,608 ± 4531	
Nonlinearity parameter, x		0.745 ± 0.04	
Relaxation function			
Kohlrausch stretched exponential		Prony series(T_R = 589°C)	
β	τ_0	w_i	τ_i
0.802 ± 0.04	$(2.44 \pm 0.13) \times 10^{-47}$	0.003004346609272	0.000165648223973
		0.011767474355289	0.001616362404278
		0.041060645287153	0.008650020133289
		0.143150900641670	0.034211773715847
		0.440142323112237	0.100029032082410
		0.360874309994379	0.198400444406796

Table 4.2: Input material parameters for TNM-model of structural relaxation of LBAL-35 glass. *Unless otherwise stated, all the values in this table are obtained from the material characterization team [2].

References

1. G. Scherer (1986), *Relaxation in glass and composites*, John Wiley and Sons.
2. A. Q. Tool, Relation between inelastic deformability and thermal expansion of glass in its annealing range, J. Am. Ceram. Soc., **29**(1946), pp. 240-253.
3. O. S. Narayanaswamy, A model of structural relaxation in glass, , J. Am. Ceram. Soc., **54**(1971), pp. 491-498.
4. C. T. Moynihan, A. J. Easteal, M. A. Debolt, J. Tucker, Dependance of the fictive temperature of glass on cooling rate, , J. Am. Ceram. Soc., **59**(1975),pp. 12-16.
5. A. Markovsky, T. F. Soules, V. Chen, M. R. Vukcevich, Mathematical and computational aspects of a general viscoelastic theory, Journal of rheology, **31**(1987), pp. 785-813.

6. G. W. Scherer, S. M. Rekhson, Viscoelastic-elastic composites: II, General Theory, J. Am. Ceram. Soc., **65**(1982),pp. 399-406.

7. S. Gaylord, *Thermal and structural properties of moldable glass types*, MS thesis, Clemson University, August 2008.

CHAPTER FIVE

Interface Friction and the Ring Compression Test

5.1. Importance of friction in precision molding processes

Friction behavior at the mold/work piece interface is an important factor in precision molding processes due to the following reasons:

a) Final size/shape and residual stress state of the molded component are affected.

b) Deformation loads or pressing force is increased. This indirectly leads to energy wastage and increased cycle time that can be directly related to increased production costs.

c) Wear is increased on the mold surface coating which decreases its life

d) Surface quality of the lens is affected as the mold wears [1-3].

The current research is focused mainly on the computational determination of the effects of variations in material and interface properties, as well as the process parameters associated with the final size and shape of the molded component. All the articles related to glass pressing assume either complete sticking of the glass to the molds once the surfaces come into contact [4-6] or an assumed friction coefficient between them[7], including frictionless interface [8]; the reason being lack of available data in the literature. Since friction behavior at the glass/mold interface is an input for the computational model, the goal of this study is to characterize friction behavior accurately between glass and die within the molding temperature range and to see if there is any temperature dependence or dependence of the material properties of glass.

5.2. Literature Review of Friction Measuring Techniques

Several techniques to measure friction under different circumstances are presented in the literature. For example, the embedded pin technique can be used for measuring friction in cold rolling processes, while the draw bead test, open-die backward extrusion test, pull-out test and

twist compression test can be used to evaluate lubricants and measure friction in metal forming processes [9]. More references on other friction measuring tests are given in the work of Schey [10]. Of all the methods, the ring compression test is widely used to measure friction in bulk metal forming applications and has been referred to as the "unoffical standard test" by Robinson *et al* [3].

In the ring compression test a ring or washer shaped specimen is pressed between flat dies and the change in internal diameter is related to the interfacial friction behavior [1]. Male and Depierre [1] used this test to quantify the friction behavior at the die/work piece interface and evaluate the effect of lubrication in bulk metal forming applications. The schematic of different outcomes caused by different interface conditions are shown in Figure 5.1. If the friction at the interface is low or close to zero, all material flow is directed radially outward. As a result, both the internal and the external diameter increase. For the opposite case of high friction, the inner diameter decreases while the outer diameter increases. If the friction is somewhere in between these two extremes the inner diameter may increase or decrease depending primarily on the level of friction. The key feature of this experiment is the sensitive nature of the inner diameter to the level of friction. The outer diameter, which always increases, is not very sensitive to the level of friction.

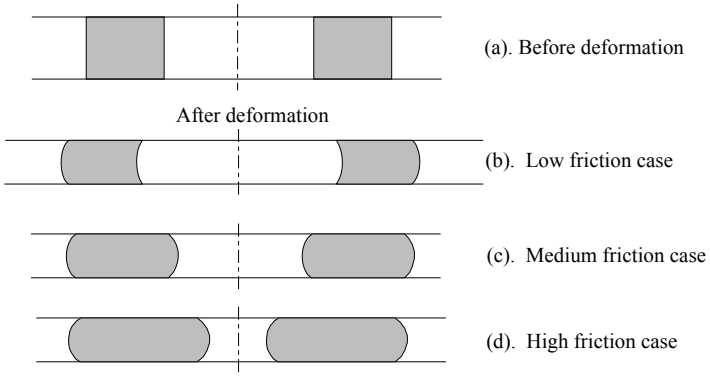

Figure 5.1: Outcome of ring compression tests with different interfacial conditions for the same mold/material pair.

Due to the sensitive nature of the change in inner diameter during pressing, the ring compression test was used in the current research to characterize the friction behavior at the glass/mold interface. In addition, this test is advantageous due to the following reasons:

a) This test closely resembles the actual molding process and hence the results of this experiment are considered more reliable when used in the lens molding simulations.

b) The molding machine used for lenses can be used to conduct the friction tests.

5.3. Friction Model at the Glass/Mold Interface

In this section the friction models suitable for pressing processes are reviewed and the appropriate model for the ring compression test for glass is selected. The most commonly used friction model is the Coulomb model defined by

$$\begin{aligned} \tau &< \mu\sigma \text{, for sticking} \\ \tau &= \mu\sigma \text{, for slipping} \end{aligned} \tag{1}$$

where 'τ' is the interface shear stress, 'μ' is the Coulomb's sliding friction coefficient, and 'σ' is the interface normal pressure. This coefficient 'μ' can depend on surface roughness, normal contact pressure, relative sliding velocity, temperatures of the contacting surfaces etc. If, for example, the sliding velocity varies over a large range, then the friction coefficient can be defined to be a function of the sliding velocity, $\dot{g}_T$ as

$$\mu(\dot{g}_T) = \mu_D + (\mu_S - \mu_D)\exp\left(-c\left\|\dot{g}_T\right\|\right) \tag{2}$$

where 'μ_S' is the static friction coefficient, 'μ_D' is the dynamic friction coefficient and 'c' is an additional parameter which controls the speed of transition from static to the dynamic coefficient [11]. In the context of bulk forming and more specifically, precision glass molding under force control, the sliding velocity does not vary much and hence a constant value of sliding friction

coefficient was be used in this research. On the contact surface the transition boundary from stick to slip is not known apriori and is an unknown, which makes the problem nonlinear. Current FEM solvers such as ABAQUS [12] can handle this type of nonlinearity and this solver is used in this study.

In metal forming operations, where the normal stress is typically very high, the above Coulomb model would predict very high shear stresses without slip. Since in practice there is relative sliding between the work piece and the mold surface, an upper limit for shear stress that is independent of the normal stress is suggested in the literature [11]. Mathematically, this revised Coulomb law can be expressed as:

$$\tau < \frac{m\sigma_Y}{\sqrt{3}}, \text{ for sticking} \qquad (3)$$
$$\tau = \frac{m\sigma_Y}{\sqrt{3}}, \text{ for slipping}$$

where m is the interface friction factor and σ_Y is the yield strength of the work piece. Defining

$$\tau_{\max} = \min\left(\mu\sigma, \frac{m\sigma_Y}{\sqrt{3}}\right) \qquad (4)$$

equations (2) and (3) can be combined as follows:

$$\tau < \tau_{\max}, \text{ for sticking} \qquad (5)$$
$$\tau = \tau_{\max}, \text{ for slipping.}$$

This law, which is similar to as elastic-perfectly plastic plasticity behavior, is shown in Figure 5.2.

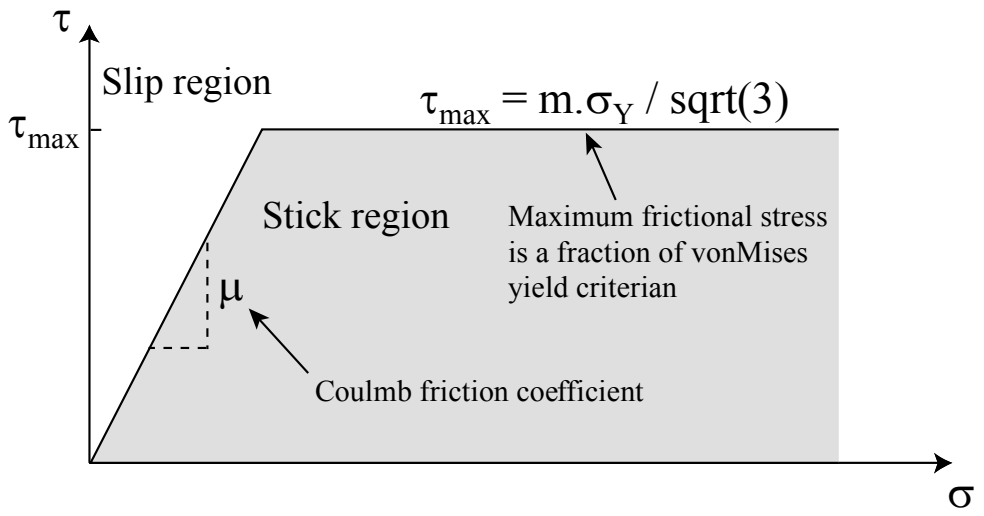

Figure 5.2: A friction model that incorporates the Coulomb model and with a maximum value of the shear stress.

Another approximation often justified in the literature is to omit the Coulomb part of the friction model in Figure 5.2, which replaces the condition of Equation (4) with simply

$$\tau_{\max} = \frac{m\sigma_Y}{\sqrt{3}} \quad . \tag{6}$$

This approximation makes the experimental characterization simpler and thus, is widely used. For metals where the σ_y is the yield stress, the interface friction factor ranges from *0* to *1*. A value of $m = 0$ allows slipping without resistance at the interface while $m = 1$ does not allow slipping at all. In the latter case, when the maximum shear stress is reached, the material in the interior starts flowing while no slipping occurs at the interface. In the next paragraph friction models appropriate for glass in the transition temperature range are considered.

Glass at room temperature is essentially a solid and therefore, the standard Coulomb model of friction given by Equation (2) is the most appropriate. Glass at high temperature behaves like a viscous fluid, and therefore a no-slip boundary condition is generally used [13,14], where the friction model depends on the relationship between shear stress and the flow field.

However, there is one study of glass at high temperature by Falipou *et al*. [15], where a Coulomb model was used to represent friction when glass is viscous. They were able to match experimental results with an analytical solution based on this assumption. In their study a molten hot glass cylinder was drawn through a funnel and the kinetic energy lost during the process was measured. The loss in kinetic energy was attributed to the dissipated strain energy and frictional dissipation with the walls. Knowing the viscosity of the glass, the friction coefficient could be easily evaluated, but the accuracy of this method greatly depends on the characterization of the material behavior of the glass, which is a disadvantage when glass is visco-elastic due to the lack of availability of stress relaxation parameters. Since a Coulomb model was successfully used in the solid state and sometimes even in the liquid state, it is logical to use the same model in the transition range also. The next important question is whether to use an upper limit or not, similar to the one used for metal forming (Figure 5.2). Since the molding process takes place under force control and glass flows easily at the molding temperature when compared to crystalline solids, the shear stresses developed at the glass/mold interface are not high. Therefore an upper limit was not considered in the current study.

5.4. Friction Calibration Curves (FCC)

Male and Depierre [1] gave a set of curves called the universal friction calibration curves to quantify the continuous change in inner diameter during pressing to a particular friction coefficient. Curves are drawn for a series of friction coefficients, using simplified analytical solutions of the ring compression test. Experimental data points are plotted on these friction calibration curves and the theoretical curve that corresponds to the best fit is concluded to be the friction coefficient of that interface. Male and Depierre [1] made the following simplifying assumptions to obtain their analytical solution:

1. The die is rigid.
2. There is no barreling on either of the curved surfaces.
3. The shear stress distribution from the inner to the outer diameter is the same on all horizontal planes of the ring including the top and bottom surface of the ring.
4. The material is incompressible, and
5. There is no strain hardening of the material.

Male and Depierre [1] used a standard specimen shape with outer diameter, inner diameter and height in the ratios of 6 to 3 to 2, believing that their analysis and assumptions were well suited to this geometry. They also assumed a maximum friction stress model as described in Equations (5) and (6) to obtain these friction calibration curves.

Sofuoglu *et al* [2] realized the potential of this test to accurately characterize friction behavior for a variety of applications because of the sensitive nature of the internal diameter to respond to different friction conditions. The only drawback of the work of Male and Depierre [1] was the simplifying assumptions they made to generate the friction calibration curves. So Sofuoglu *et al* [2] used finite element method to generate the friction calibration curves and relaxed all the simplifying assumptions Male and Depierre made. Besides improving the accuracy of the calibration curves, they also showed that these curves are dependent on material properties. They pressed black and white plasticine which has different material properties under the same friction conditions and showed that the friction curves change drastically.

The friction calibration curves in the current study, for both metals to compare with [1] and for glass for the study of lens molding in Chapter 6, were generated using a finite element solution without making any of the above listed assumptions. These FEM results will be presented in Section 5.7.

5.5. Experiments

The Toshiba lens molding machine (GMP series) was used to conduct the ring compression tests. Several rings were made of molding glass material L-BAL35 with dimensions of 19.15mm outer diameter, 9.59 mm inner diameter, and 6.37mm tall such that the standard ring ratio OD:ID:H = 6:3:2 was maintained. Since a finite element solution is sought to generate the friction calibration curves in the current research, a ring of any dimension could have been used. Several rings were pressed at 589°C and 569°C to several different Center Thickness (CT) values using identical molding conditions as used in the glass lens molding operation. In the ring compression test the CT was equal to the thickness of the ring itself as flat molds were being used. A temperature of 589°C was chosen as it is the ideal molding temperature for L-BAL35 type glass and a friction coefficient at this temperature is desired, while the other temperature was chosen to see the dependence of friction coefficient on temperature. Examples of two pressed rings, one at 589°C and the other at 569°C are shown in Figure 5.3. The molds were coated with DLC (Diamond-like-carbon) coating to prevent any chemical reaction between glass and molds during the molding stage and also to ease the release of lens once molding is over.

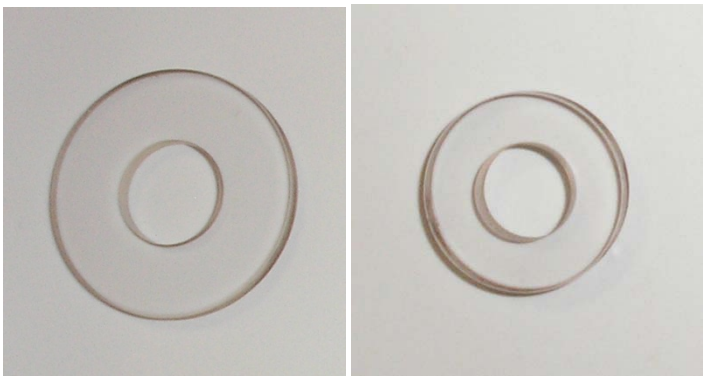

Figure 5.3. The rings that were pressed to a maximum CT at 589°C C and 569°C are shown at the left and right respectively.

The *evolution* of the inner diameter as the ring is being pressed under force control is very crucial to linking it to a particular friction coefficient. In most metal forming operations, the ring is accessible at all times during the pressing operation as the entire test is conducted at room temperature. Therefore, one specimen can be used to generate the entire experimental curve. However, in the case of glass, the ring is accessible only after the molding process is complete i.e., after the ring has been released and cooled to room temperature. Therefore, for each data point of CT, a new ring had to be pressed and the data from each of these experiments were combined to generate the evolution of the inner diameter. Care was taken such that *no* processing parameters were changed except CT, when generating the evolution of the inner diameter experimental data.

5.6. Finite Element Model

The numerical simulation of the ring compression test was done using the commercial finite element code ABAQUS. A "*COUPLED-TEMPERATURE DISPLACEMENT" type of analysis was used in this simulation as the mechanical properties change drastically with temperature and the heat conduction at the interface is also affected by the changing contact surface. All the pressing and cooling stages were modeled.

5.6.1 Model Geometry

The initial geometry of the model is shown in Figure 5.4. Since the ring and the molds are circular and the loading can be approximated as symmetric around the central axis, an axi-symmetric model is used. The ring is modeled as a linear viscoelastic material, while both the upper and lower molds are modeled as linear elastic materials. The glass ring is meshed with 3072 CAX4RT elements, while the upper and lower molds are meshed with 1284 and 1107 CAX4RT elements, respectively. Two master-slave type of contact interaction pairs were created; one between the top surface of the ring and bottom surface of the top mold and the other between

the bottom surface of the ring and top surface of the bottom mold as shown in Figure 5.4. A Coulomb friction model based on penalty formulation was used in the simulation. The normal behavior was modeled as "hard" contact which does not allow penetration of one surface onto another. The contact conductance behavior is similar to the one used for lens molding presented in Chapter 2. Two coupling constraints are also defined; one between RP_{TOP} and the top surface of the top mold and the other between RP_{BOT} and the bottom surface of the bottom mold as shown in the Figure 5.4. However in these constraints only the vertical components of displacements of the slave surfaces were constrained to move along with that of their respective master reference points while the horizontal components of displacements are allowed to remain free. This represents the actual process and simplifies applying force boundary conditions and extracting displacement response from the results file.

5.6.2 Material Behavior of Glass and Molds

The L-BAL glass ring was modeled as a linear viscoelastic material and the viscoelastic material property definitions are given in Table 3.1 of Chapter 3. The molds are modeled as linear elastic materials. The elastic and thermal properties of both the molds and the glass are given in Table 2.1 of Chapter 2. The details of the structural relaxation mechanism in the model are explained in Chapter 4 while the structural relaxation parameters used in the simulation are given in Table 4.2.

5.6.3 Interface Behavior

The simulation also accounts for interaction between the glass preform and the mold, both mechanically and thermally. A master-slave type contact interaction is defined between them with the mold surface as the master surface and glass surface being the slave surface. This master-slave type contact definition was used as the glass is much softer than the molds. Also

care was taken while meshing such that the mold elements are at least 5 times larger than the glass elements. This was done to avoid contact penetration because the master surface can penetrate the slave surface while the slave surface cannot penetrate the master surface. The normal contact behavior was modeled as "hard" contact in ABAQUS while the tangential behavior is modeled using a penalty formulation with a Coulomb friction model.

The thermal behavior of the interface is given in Section 2.4.3 of Chapter 2.

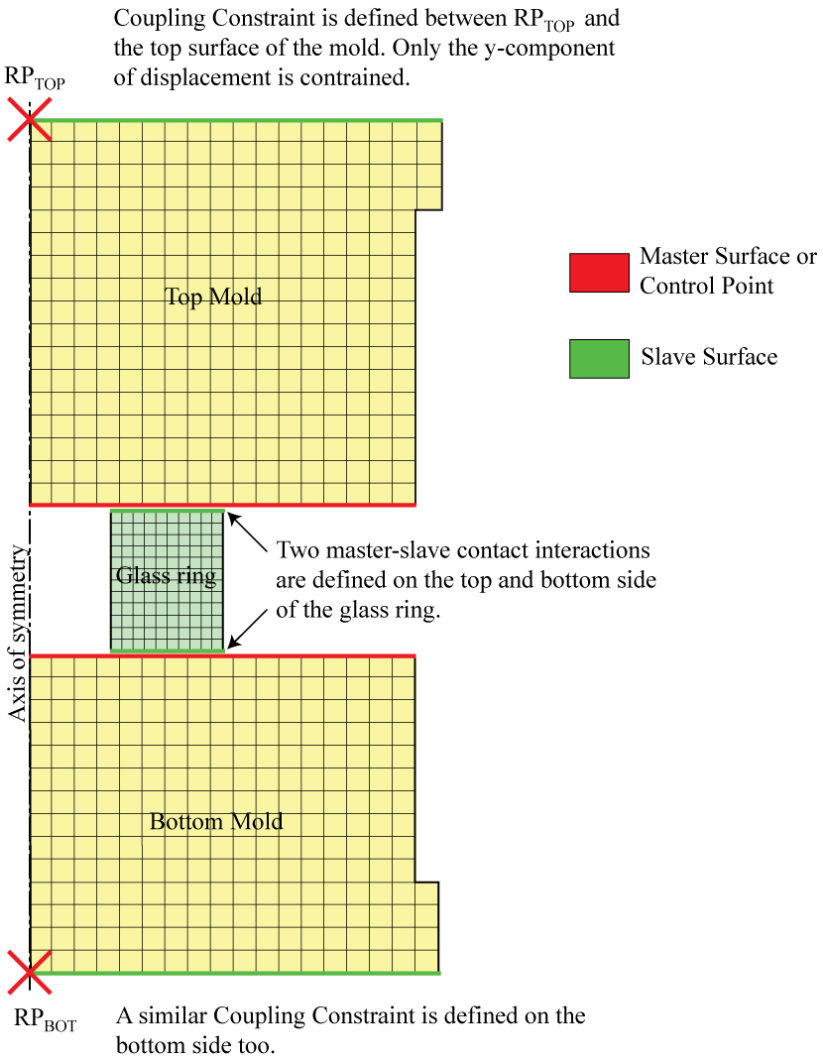

Figure 5.4: Axisymmetric Model used for simulation of the ring compression test.

5.7. Results and Discussion

5.7.1. Friction Calibration Curves for Metal forming using Finite Element Solution

The friction calibration curves in the current research were generated using a finite element solution after all the assumptions made by Male and Depierre were relaxed. This study on metal forming which is unrelated to the glass/mold interface friction is done to point out that some of the anomalies of this test arise only due to the simplified analytical solution and to substantiate the strength of the test if a more accurate solution(finite element solution) is available. For example, the barreling and shear stress variation along the vertical axis previously neglected by Male and Depierre can be included in FE simulations very easily. In Figure 5.5 below, the experimental data [4] for various metals and interface conditions were calibrated with curves obtained using finite element solutions. The friction-factor model described by Eq. (5) was used to model the ring-die interface. Since ABAQUS requires a Coulomb friction coefficient, a very high value was input such that it does not have any effect on the results. From the results it is clear that the best fit friction factors are different from those of Male and Depierre [1]. For brass with either one of the lubricants, their friction factors were slightly lower than the finite element solutions. For mild steel with smooth dies, their friction factor is slightly higher than the FEM solution. For mild steel with rough dies, the finite element solution suggests a friction factor of 0.63 while their solution suggests a value between 1.14 and 1.4. This latter case is evidence that the barreling and shear stress distribution assumptions made in the original model start to have an effect on the accuracy of the curves as the shear stresses increase. The results in Figure 5.5 show that for low levels of friction, the FEM solutions and simplified analytical solutions are very close.

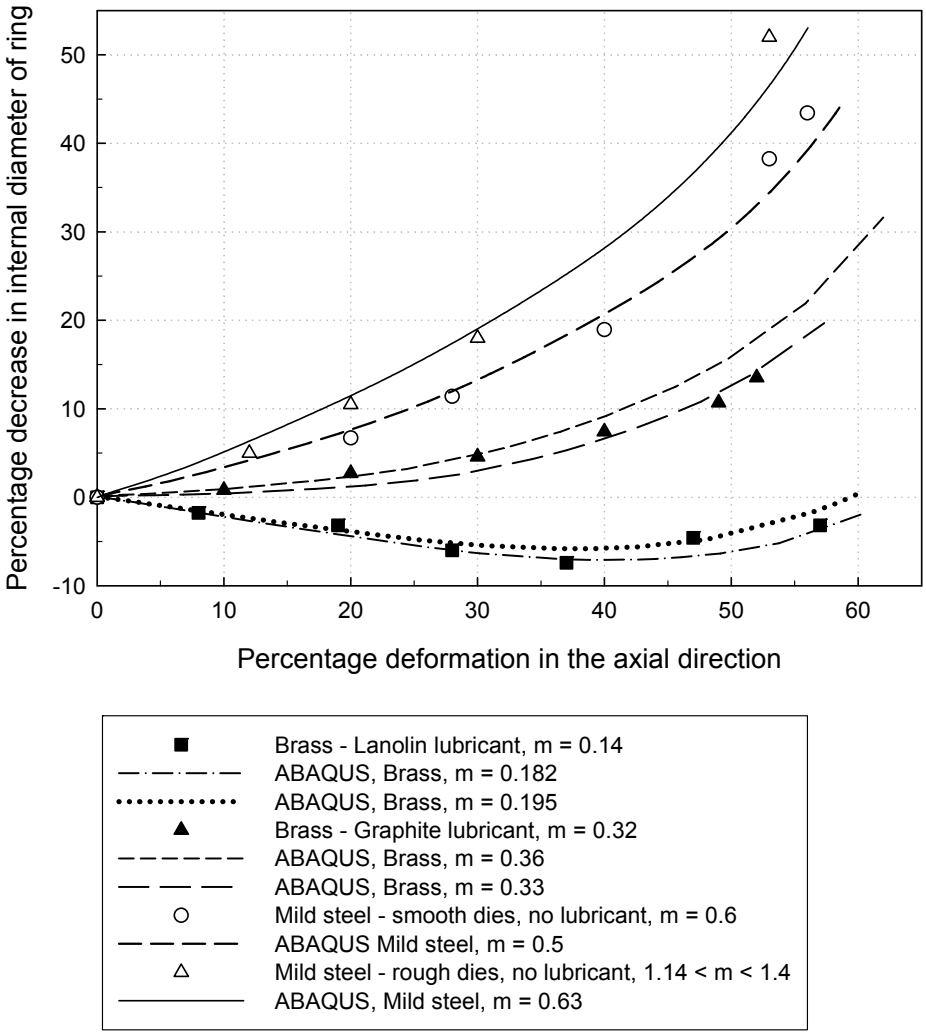

Figure 5.5: Comparison of experimental data from Male and Depierre [1] with FEM solutions instead of their simplified analytical solutions. The values of *m* that accompany the experimental results of Male and Depierre [1] are their predictions.

5.7.2.Friction Calibration Curves at the Glass/Mold Interface for molding process

The friction calibration curves were generated from the finite element solutions of the ring compression tests as shown in Figure 5.6, while the deformed configuration of the ring during the pressing stage is shown in Figure 5.7. The experimental data points are also shown in Figure 5.6 and from the plot, it is concluded that the friction coefficient between the L-BAL preform and the

DLC coated mold is approximately 0.04. The squares and the circles are experimental data points when sufficient time was given to the glass ring to reach a more uniform temperature distribution. It should be mentioned that some of the rings corresponding to the squares were not exactly circular, but more elliptical and those data points were ignored.

Next, a sensitivity analysis was performed to study the dependence of the temperature and thermal shrinkage on the curves. The temperature at which a ring was pressed was lowered and then the ring was pressed. It should be noted that the viscoelastic material properties would change drastically when the temperature is lowered by 20°C. Still, no deviation of the friction curve was observed. Hence the outcome of the ring compression test can be concluded to be independent of temperature with respect to viscoelastic material parameters. However, if the friction condition at the interface is affected by the temperature, then the outcome of the test would be different. Next, the effect of thermal shrinkage on the curves was studied. Since the rings are accessible only after the entire process is over, when conducting the experiments, several rings were pressed to different heights and the data was combined to generate the inner diameter evolution curve. Since the ring shrinks due to structural relaxation, the effect of this shrinkage was studied and shown by circles in Figure 5.8. Again the shrinkage effects are very small compared the gross changes in the inner diameter. Hence, it is concluded that the cooling need not be modeled in the simulation when generating the calibration curves.

Finally, the material property dependence of the friction calibration curves was studied. Male and Depierre[1] argued that their friction calibration curves were universal for any material and hence called their curves “universal friction calibration curves.”However, Sofuoglu *et al* [2] showed, for plasticine, that the curves do change a lot for different material behavior. In this current study two different stress relaxation functions were used and corresponding calibration curves were

generated for three cases as shown in Figure 5.9. From the plots, it is clear that there is some dependence of material property on the curves, but it is well within the range of experimental uncertainty and hence it is concluded that the material property does not affect the curves substantially.

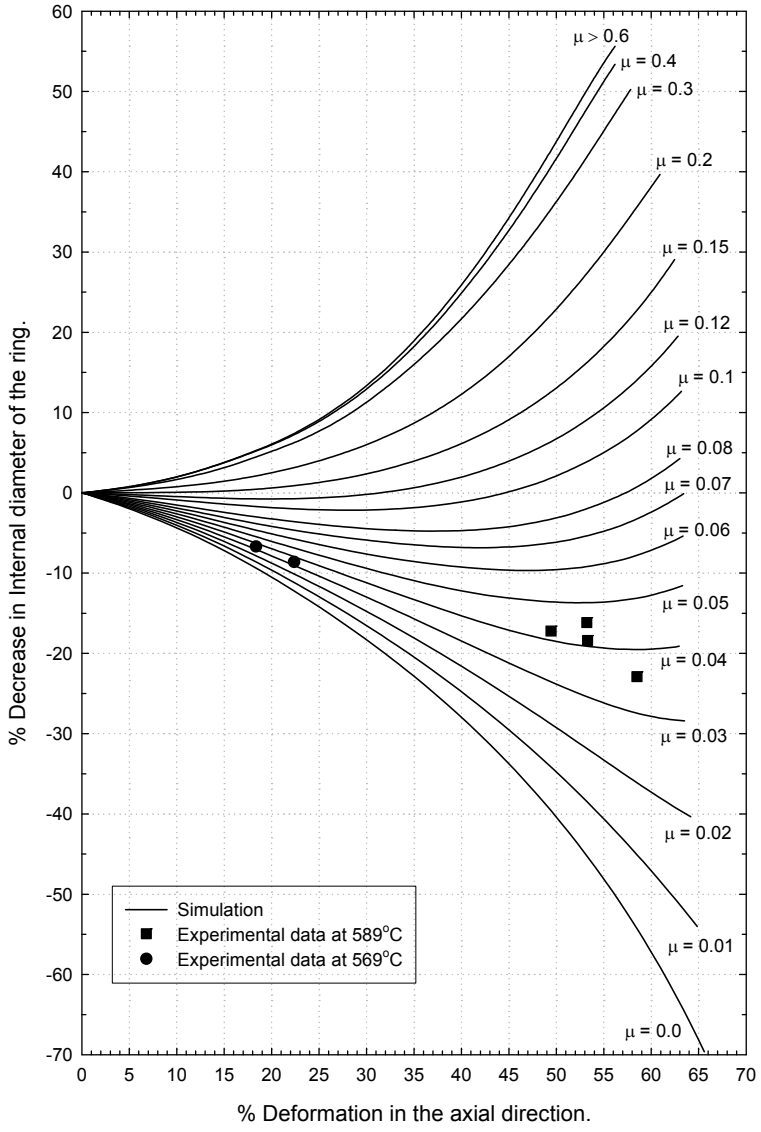

Figure 5.6: Friction calibration curves for glass in its transition range. When generating the experimental data points, a soaking time of 600 seconds was used to ensure a uniform temperature distribution in the rings before pressing began.

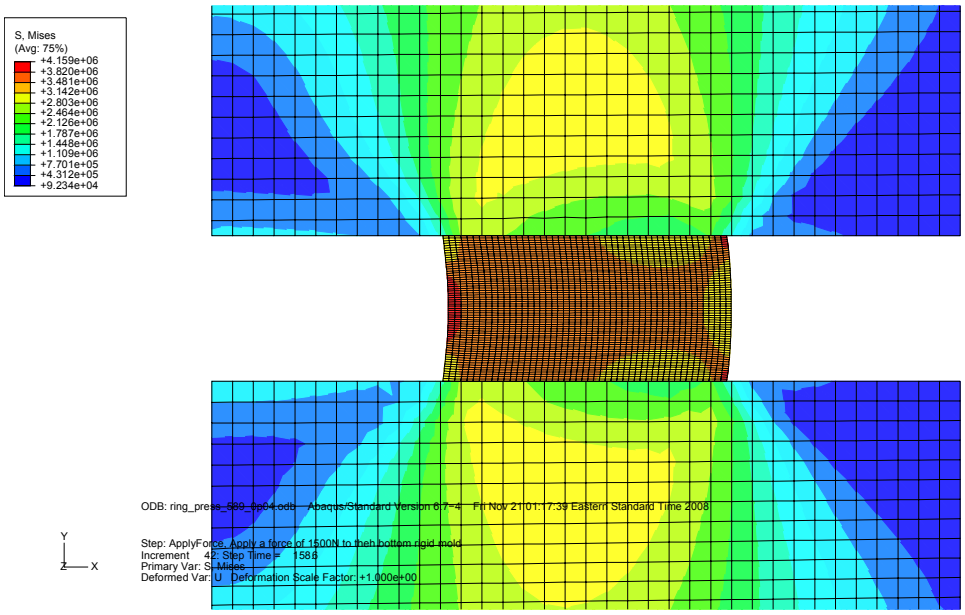

Figure 5.7: Deformed configuration of the ring pressed between flat molds at 589^{o}C.

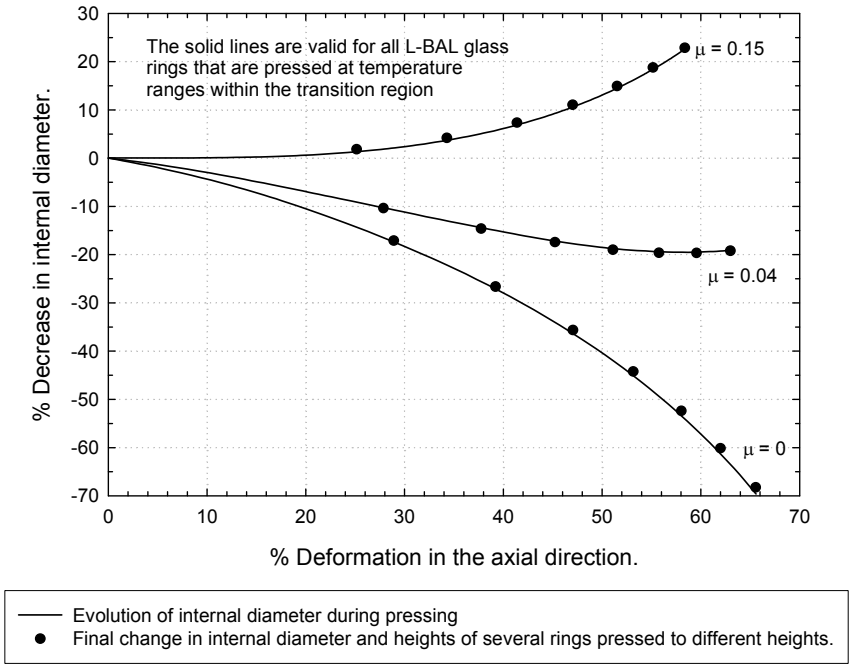

Figure 5.8: Study of sensitivity of Friction calibration curves upon temperature and thermal shrinkage.

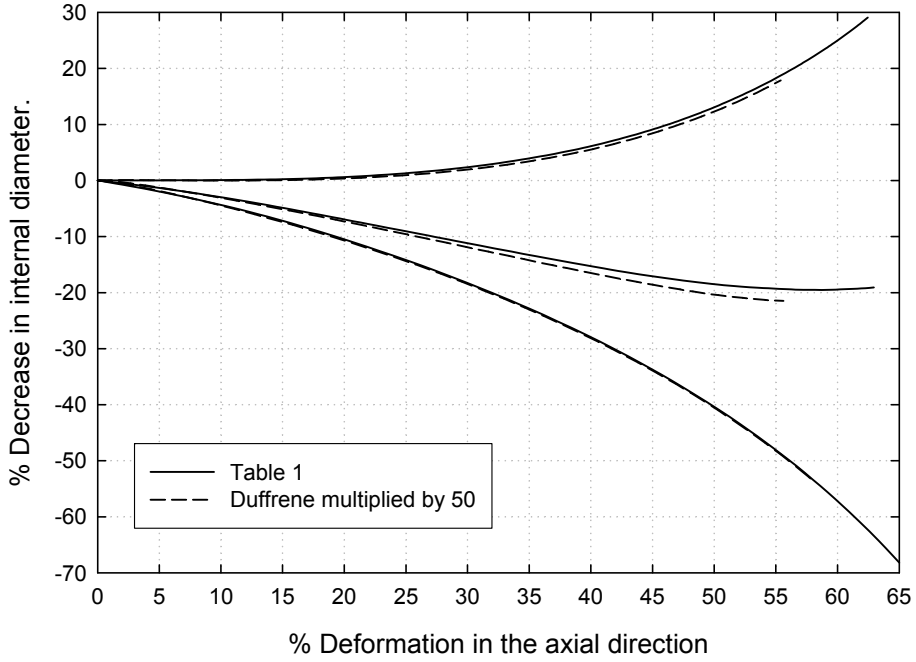

(a) Friction calibration curves for different stress relaxation functions.

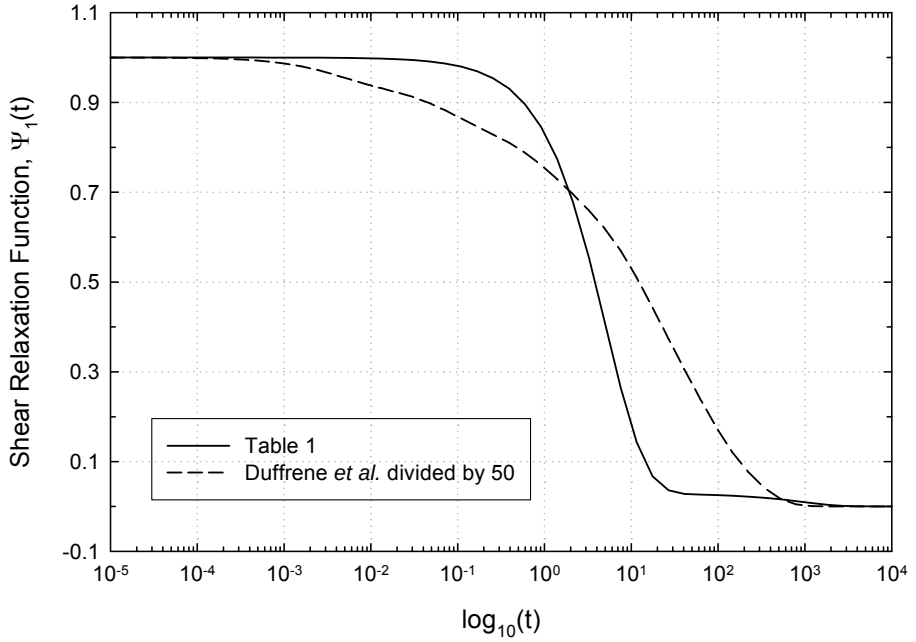

(b) Shear stress relaxation functions used to generate the curves in (a).

Figure 5.9: Study of sensitivity of Friction calibration curves upon stress relaxation function.

References

1. A.T. Male and V. Depierre, The validity of mathematical solutions for determining friction from the ring compression test, ASME J. Lubr. Technol., **92**(1970), pp. 389-397.

2. H. Sofuoglu, H. Gedikli, J. Rasty, Determination of friction coefficient by employing the ring compression test, ASME J. Eng. Mater. Technol., **123**(2001), pp. 338-348.

3. T. Robinson, H. Ou, C.G. Armstrong, Study on ring compression test using physical modeling and FE simulation, J. Mater. Process. Technol., **153/154** (2004), pp. 54-59.

4. A. Jain, A.Y. Yi, Finite element modeling of structural relaxation during annealing of a precision-molded glass lens, J. manuf. sci. eng., **128** (2006), pp. 683-690.

5. A. Jain, A.Y. Yi, Numerical modeling of viscoelastic stress relaxation during glass lens forming process, J. Am. Ceram. Soc., **88** (2005), pp. 530-535.

6. A.Y. Yi, A. Jain, Compression molding of aspherical glass lenses – A combined experimental and numerical analysis, J. Am. Ceram. Soc., **88** (2005), pp. 579-586.

7. A. Jain, G.C. Firestone, A.Y. Yi, Viscosity measurement by cylindrical compression for numerical modeling of precision lens molding process, J. Am. Ceram. Soc.,**88** (2005), pp. 2409-2414.

8. Sellier. M, Breitbach. C, Loch. H, Siedow. N, An iterative algorithm for optimal mould design in high-precision compression molding, *Proceedings of the I MECH E Part B Journal of Engineering Manufacture*, **221**(2007), 25-33(9).

9. F. Wang, J. G. Lenard, An experimental study of interfacial friction-hot ring compression, J. Eng. Mat. Technol, **114**(1992), pp. 13-18.

10. J. A. Schey, Tribology in Metal working: Friction, lubrication and wear, ASM, 1983.

11. P. Wriggers, Computational contact mechanics, Springer-Verlag, Berlin, Heidelberg (2006).

12. ABAQUS Version 6.7 User Documentation, Dassault systems Inc. (2007).

13. S. W. Rienstra and T. D. Chandra, Analytical approximations to the viscous glass-flow problem in the mould-plunger pressing process, including an investigation of boundary conditions, J. Eng. Math., **39**(2001), pp. 241-259.

14. Polyflow version 3.11, User Documentation, ANSYS Inc. 2007, Lebanon, NH.

15. M. Falipou, F. Sicloroff and C. Donnet, New method for measuring the friction between hot viscous glass and metals, Glass Sci. Technol. 72 (1999), pp. 59-66.

CHAPTER SIX

Sensitivity Analysis of Material Properties and Process Parameters on Profile Deviation

In this Chapter, after presenting a validation study, sensitivity analysis is reported regarding the effects of various process parameters and material properties on the final size and shape, i.e., profile deviation, of a molded lens. The profile deviation, or simply deviation, is illustrated in Figure 1-3. Unless noted otherwise, the deviation in this Chapter is defined as the difference between the final lens shape at room temperature and that of the mold, i.e., the "desired profile" in Figure 1-3 is the mold shape. This investigation does not take into account, for example, the effect of a stress state that could lead to lens failure. So, for example, while this sensitivity analysis might show that final size and shape are the same for two cases, one case could actually crack the lens while the other could result in an acceptable lens. One final point is that all results obtained are for a material defined by the input parameters obtained by experimental data and from the literature. While this glass is intended to be LBAL-35, if one or more of the material characterizations of the various input parameters are not accurate, then it is possible to generate results that do not agree with the actual molding of this glass type. In this regard, stress relaxation and gap conductance are of the most concern.

As will be shown, deviation is due to a combination of thermal expansion, stress relaxation and residual stresses. An investigation of the effects of thermal expansion is straightforward, while the influences of stress relaxation and residual stresses are not so easy to isolate given the thermo-mechanical coupling in the problem. Changes in all the important process and material parameters have been considered. As a review of these quantities, the process and the modeling details are given in Chapter 2, while additional details of the viscoelastic properties, structural

relaxation properties and interface friction properties are given in Chapters 3, 4 and 5 respectively.

6.1 Validation and Convergence of Model with Experiment

A validation geometry and process parameters were selected by Matt Stairiker and Matt Tardiff of Edmund Optics using L-BAL35. The process parameters are defined in Figure 2.1. This set of process parameters will be the baseline for the sensitivity analysis throughout this Chapter. The preform shape and final lens shape as predicted by simulation are presented in Figure 6.1. This bi-convex lens will be referred to as the "validation case."

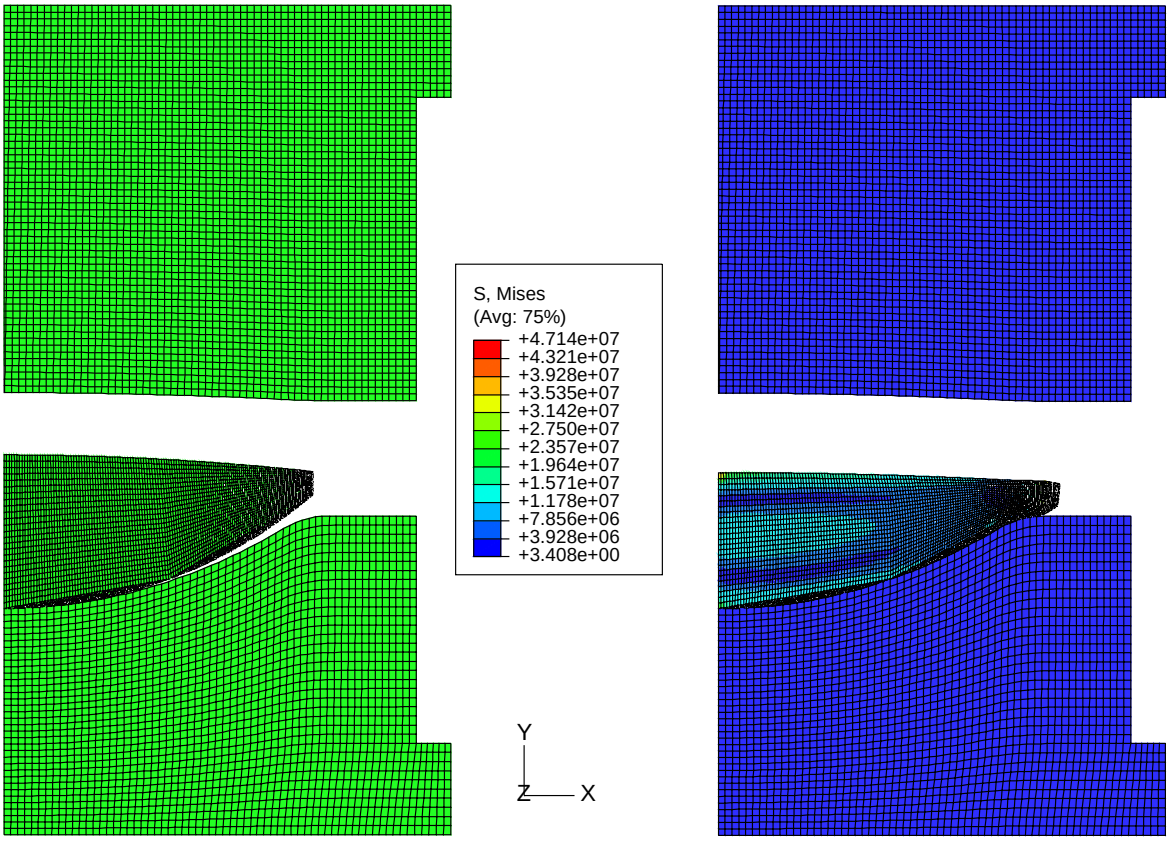

Figure 6.1: Initial and deformed configurations for the validation case.

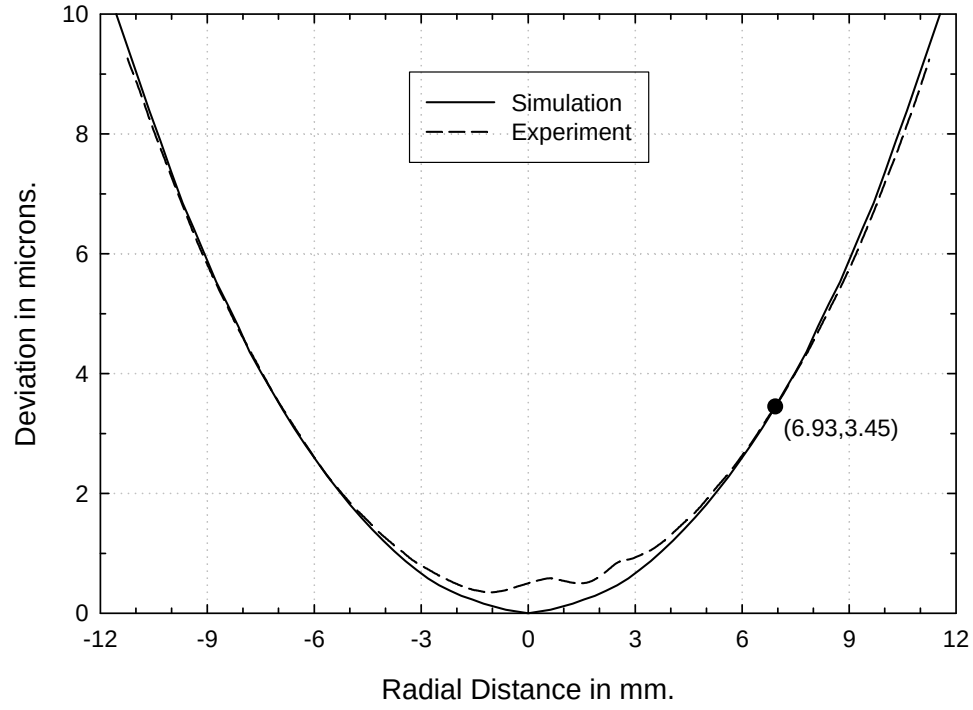

(a)

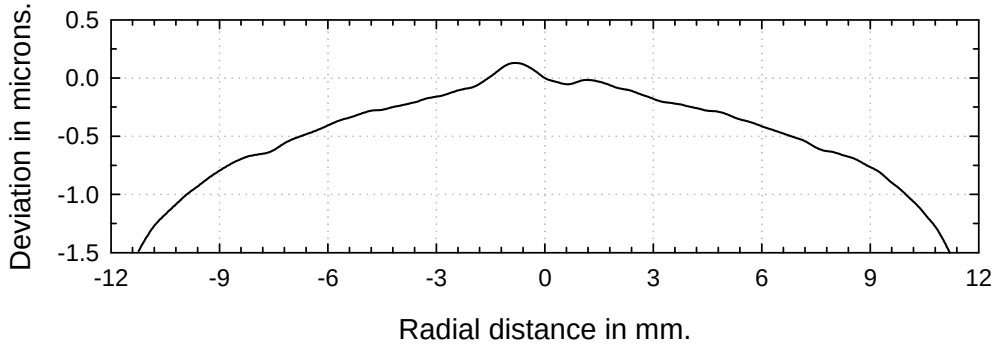

(b)

Figure 6.2: (a) Comparison of experimental and simulation deviation. Since the origin in the experimental data is poorly defined, the point shown is where the data is matched. (b) Experimental mold deviation measured with respect to aspherical surface defined by Z(Y) defined in Eq (1). The values of parameters that define Z(Y) are given below in Table 1. Since the mold deviates from the formula by as much as 1.5 microns and the asymmetry near the origin, the shifting of the origin in (a) is justified.

In Figure 6.2a the deviations from the simulation and from measurements at Edmund Optics are presented. Due to the difficulty of defining the actual zero point in the measured lens, the curves are matched at an arbitrarily selected point, which as shown in the figure, is taken to be 6.93 mm to the right of center. In order to explain the unusual profile near the center of the measured lens, in Figure 6.2b experimental data for the deviation between the measured mold shape and the mathematically defined mold shape,

$$Z(Y) = \frac{CY^2}{1+\sqrt{1-(1+k)C^2Y^2}} + EY^4 + FY^6 + GY^8 + HY^{10} \tag{6.1}$$

is presented. Taken together, these figures show that the primary source of the error between the simulation, which assumes a mold profile given by the above mathematical definition, and the data in Figure 6.2a is due to the discrepancy in Figure 6.2b. A perfectly ground mold would have a deviation of zero in Figure 6.2b. The constants in Equation 6.1 are presented in Table 6.1.

C = 1/R	0.045140613
k	-2.271309
E	1.954456e-5
F	-1.756349e-8
G	2.597437e-11
H	-2.414065e-14

Table 6.1: Aspherical surface parameters.

To show that the model has converged and produced a mesh independent solution, in Figure 6.3 three solutions using different meshes are presented. In addition to increasing the mesh from 4544 to 6959 elements for the preform in the very fine mesh, the strain-error tolerance has also been reduced from 0.005 to 0.001. Strain-error tolerance or CETOL parameter as defined in ABAQUS is nothing but the maximum difference between two consecutive creep strain

increments. It controls the accuracy of the integration scheme. The run time on a DELL dual quad core 64-bit processor with 16 GB of memory is 45 minutes for the fine mesh and 70 minutes for the very fine mesh. In subsequent studies the fine mesh will be used.

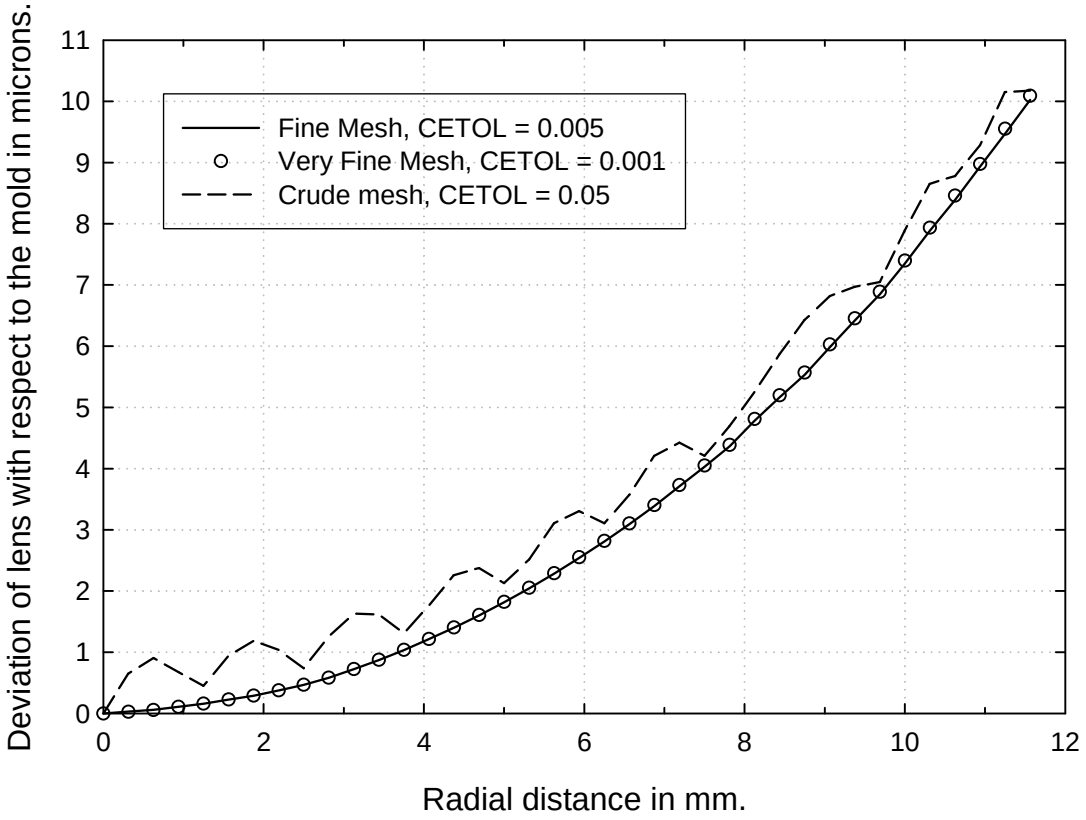

Figure 6.3: A convergence study was performed to study the variations in the final deviation based on three different meshes and three different strain-error tolerances CETOL. The maximum error between the fine and very fine meshes is less than 0.05 microns.

6.2 The effect of thermal expansion and mold deformation

Thermal expansion of the glass is the primary reason for deviation in the lens molding process. This is the reason why the deviation, as defined by the difference between final lens shape and the mold, will usually be positive on the convex side of a lens, i.e., a sphere of glass when cooled will have a smaller radius and glass typically has a higher average CTE than the mold material. As

discussed in Chapter 4, in this study thermal expansion is addressed using the structural relaxation model of Tool, Narayanaswamy and Moynihan [1]. The four parameters that define the structural relaxation model presented in Section 4.6 of Chapter 4 will now be used in a sensitivity analysis. Specifically these are the activation energy constant $\frac{\Delta H}{R}$, nonlinearity parameter *x*, time constant parameter τ_0, and the Kohlrausch shape function β. Sensitivity analyses for these parameters are presented in Figures 6.4, 6.5, 6.6 and 6.7, respectively. The deviation due to the effect of structural relaxation, which is temperature history dependent thermal expansion, is most easily understood by considering the lower part of each of these figures, where the instantaneous thermal expansion coefficient is presented as a function of temperature for a uniformly cooled volume of glass. Given that volume change is proportional to the integral of thermal expansion with respect to temperature, the effect of the change in sensitivity parameter values is clearly illustrated in these lower figures since the more area under the curve, the more volume change due to thermal expansion. It is understood that within the computational model, each material point experiences a different temperature as a function of time and therefore has a different cooling rate.

This set of four figures shows the importance of the activation energy parameter, $\frac{\Delta H}{R}$ in Figure 6.4 and the time constant parameter, β in Figure 6.6 in compensating a lens. Glasses with different values of these parameters must be compensated differently. Clearly from a computational point of view, it is essential to have the structural relaxation parameters well defined.

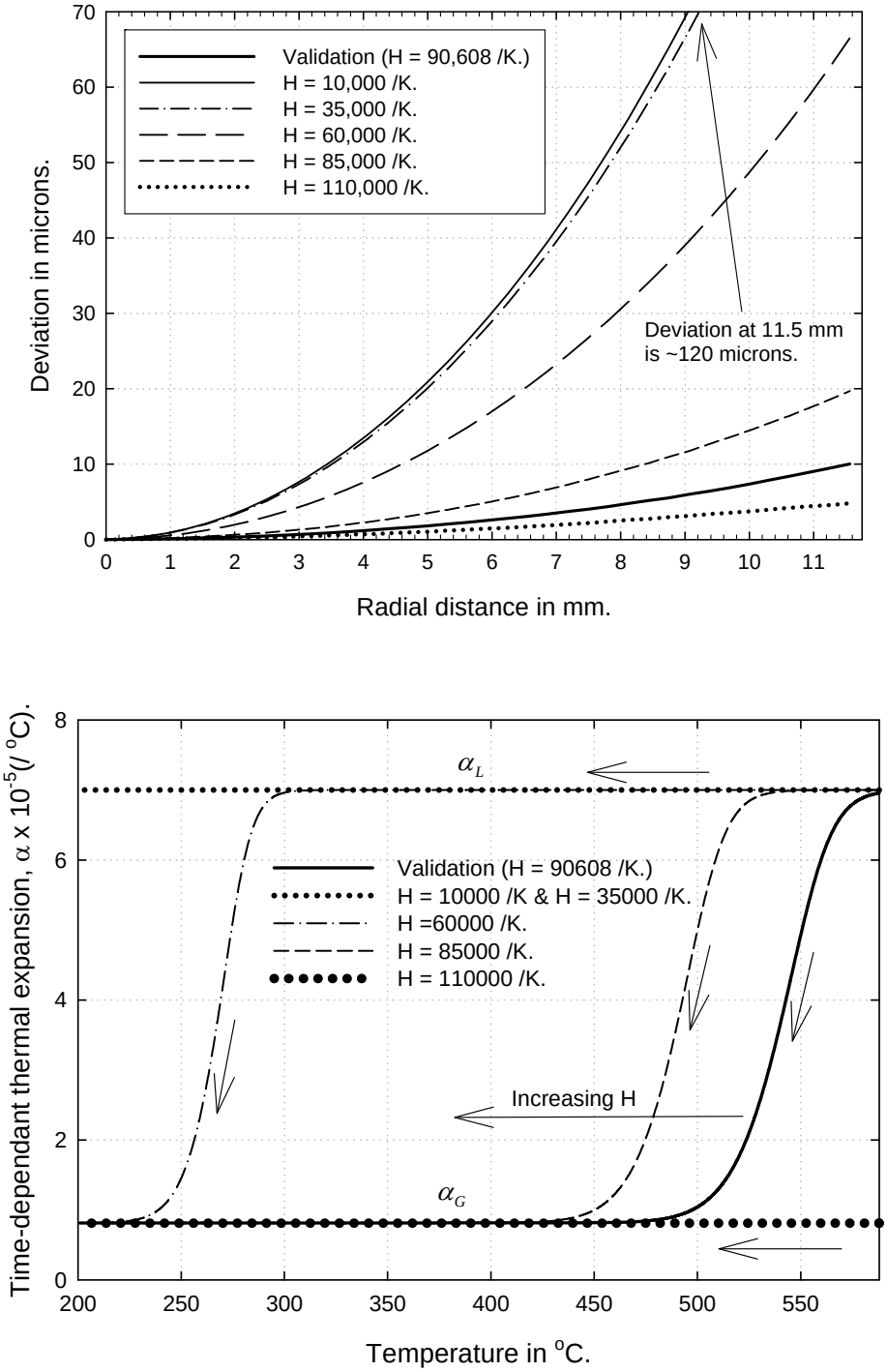

Figure 6.4: Sensitivity of the activation energy constant on deviation is shown in the top figure. In the lower one, the change in thermal expansion coefficient due to structural relaxation phenomena during cooling at an average cooling rate of approximately 25°C/min is shown for various activation energy constants. The arrows in the lower figure indicate the cooling direction.

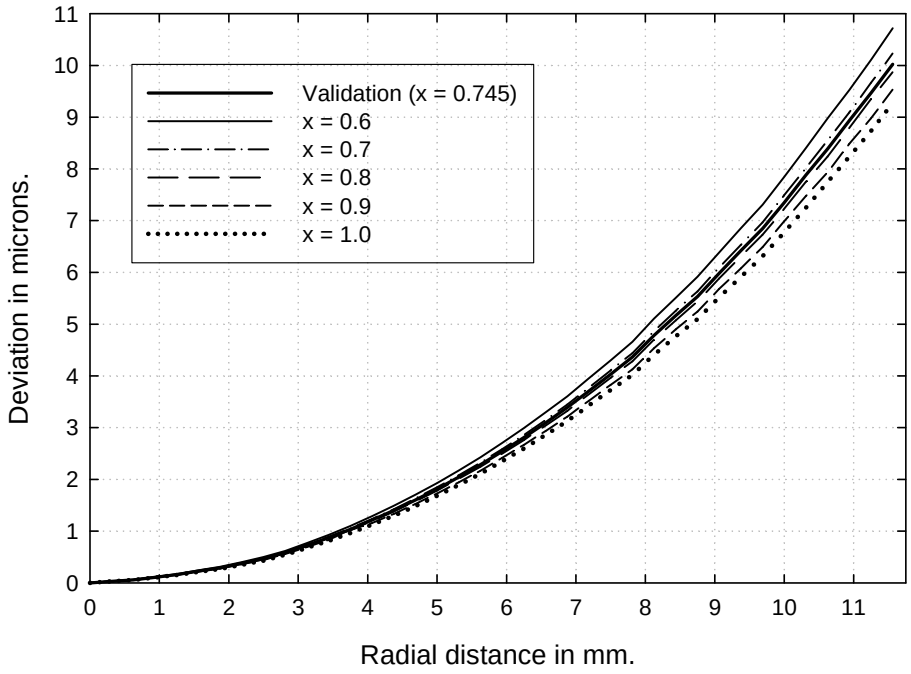

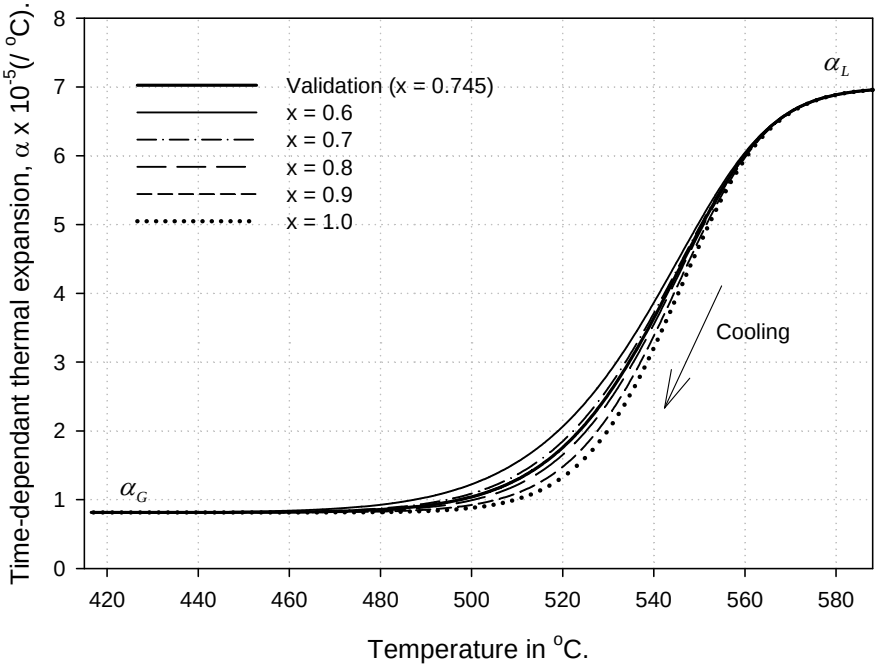

Figure 6.5: Sensitivity of the nonlinearity parameter, *x*, on deviation is shown in the top figure. In the lower one, the change in thermal expansion coefficient due to structural relaxation phenomena during cooling at an average cooling rate of approximately 25°C/min is shown for various nonlinearity parameters.

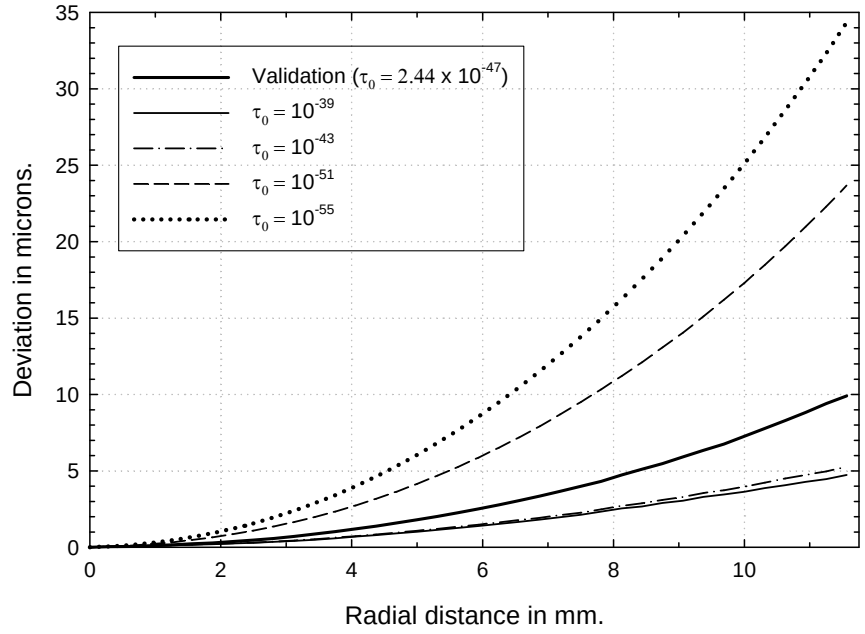

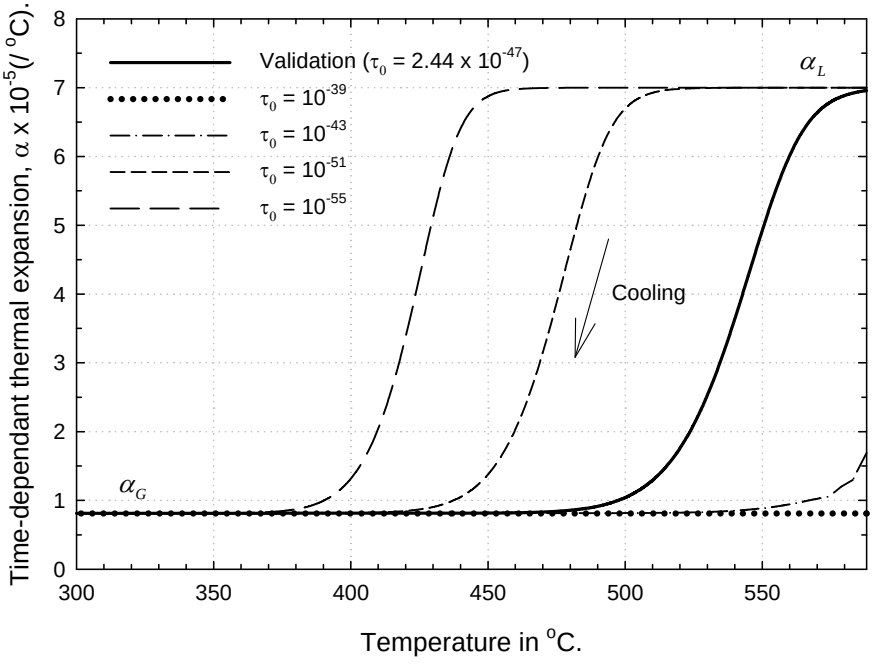

Figure 6.6: Sensitivity of the time constant, τ_0, on deviation is shown in the top figure. In the lower one, the change in thermal expansion coefficient due to structural relaxation phenomena during cooling at an average cooling rate of approximately 25°C/min is shown for various time constants.

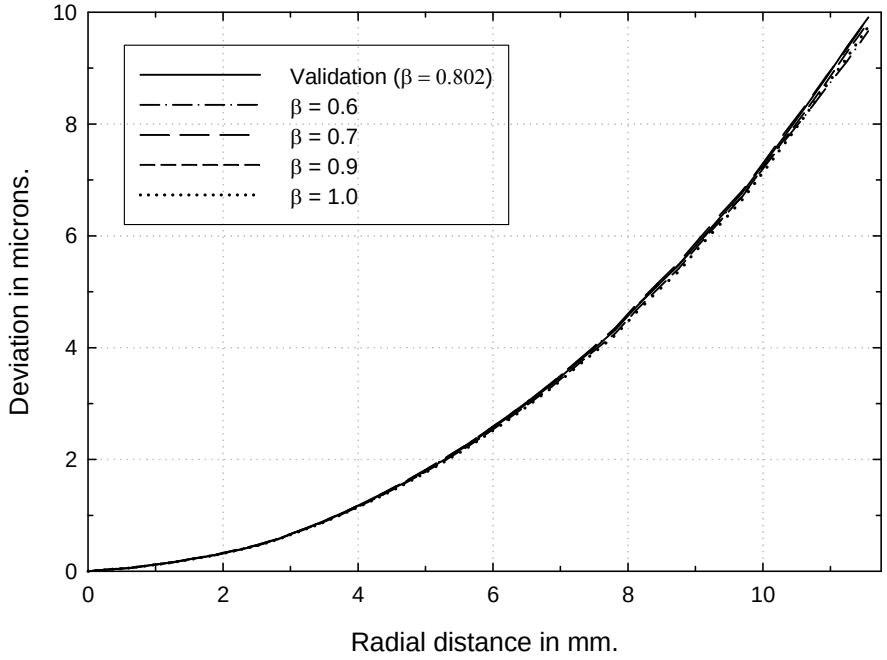

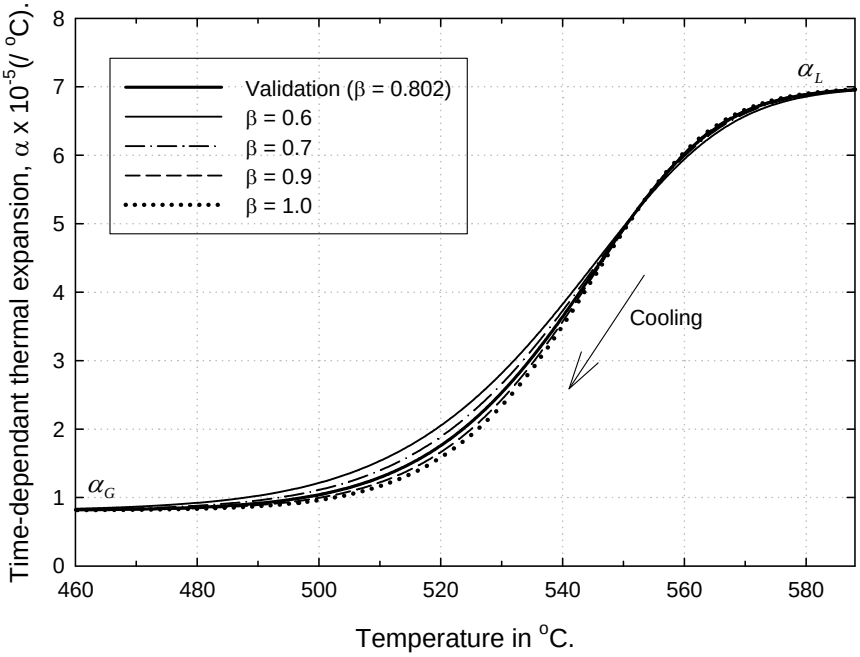

Figure 6.7: Sensitivity of the Kohlrausch factor, β, on deviation is shown in the top figure. In the lower one, the change in thermal expansion coefficient due to structural relaxation phenomena during cooling at an average cooling rate of approximately 25°C/min is shown for various Kohlrausch factors.

The thermal expansion coefficient of the mold, which is modeled as an elastic material and hence does not display structural relaxation, is also an important parameter. In Figure 6.8 the effect of thermal expansion coefficient clearly shows a significant effect on deviation. In fact, if the thermal expansion of the mold is large enough, the deviation will be negative.

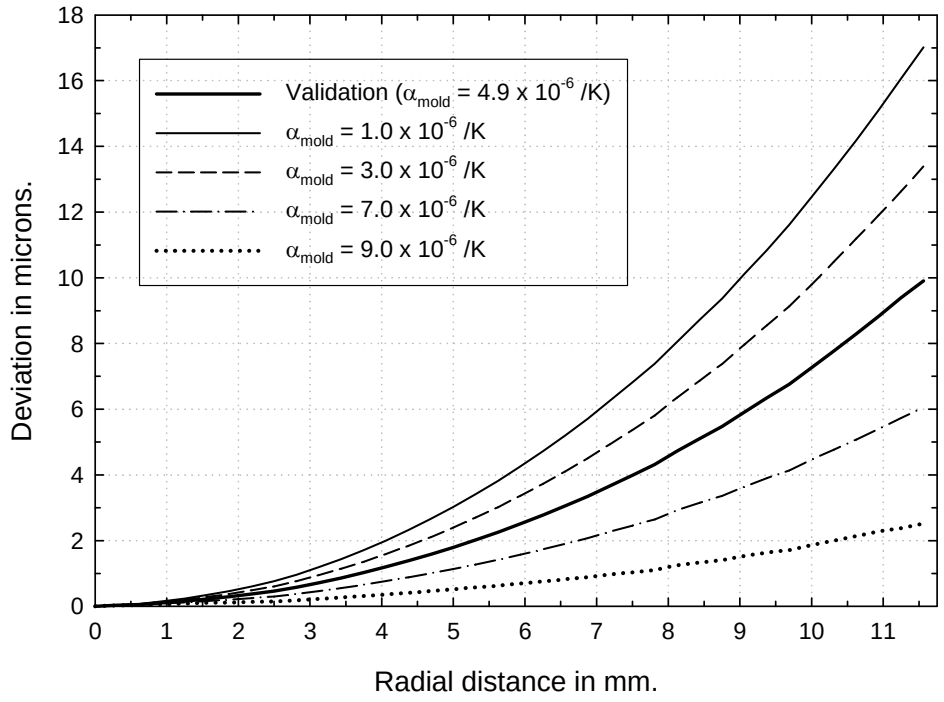

Figure 6.8: Sensitivity of the thermal expansion coefficient of the mold on the lens deviation.

The mold shape during molding can also change due to deformation. Therefore, related to the results of Figure 6.8 are those of Figure 6.9 where the effect of elastic modulus of the mold is presented. Clearly as the mold becomes less stiff, the deviation for this lens geometry is shown to decrease. The validation case with E = 570 GPa is extremely close to the limiting case of rigid molds. Therefore, these results can be used to determine if deformation of the mold can be neglected in a simulation by assuming the molds to be rigid.

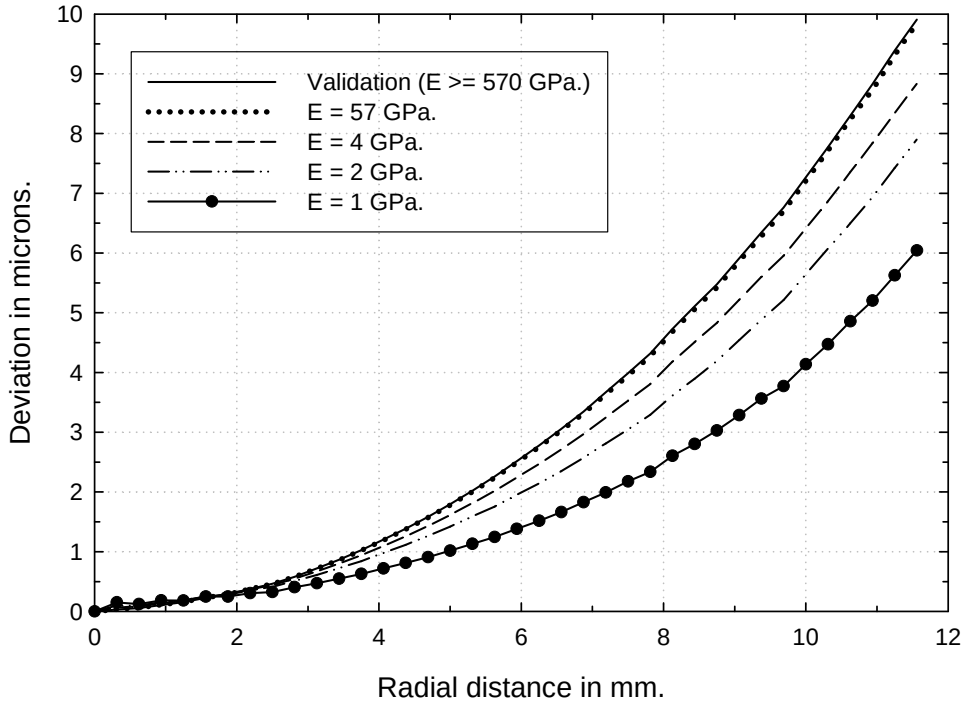

Figure 6.9: Sensitivity of the elastic modulus of the mold on the lens deviation.

Before studying residual stresses and stress relaxation, a simple calculation is made in which the effects of thermal expansion are considered independent of mechanical loading. Consider a glass sphere with radius equal to that of the convex side of the validation geometry that is at the molding temperature. If this glass cools to room temperature *uniformly*, what constant (average) thermal expansion coefficient is necessary to create a 10 micron deviation? A simple calculation gives a coefficient of thermal expansion approximately ten times smaller than the range shown in Figure 6.4b. This means that without the thermal and mechanical constraints of the mold, the deviation would be approximately ten times larger. There are two reasons why the actual deviation is much less. The first is non-uniform cooling which gives the effect shown in Figure 4.3.For example, if the bottom of the lens cools slower than the top, then the bottom will

experience more volume decrease which kinematically reduces the deviation. The second reason is stress relaxation, which will act to reduce deviation by allowing the glass to take the shape of the mold. In the next section the effects of stress relaxation and residual stresses are investigated.

6.3 The effect of residual stresses and stress relaxation

The final deviation is a combination of thermal expansion due to temperature change, stress relaxation while the glass is still visco-elastic and residual stresses which can cause shape change when the lens is released at the end of the maintenance force as shown in Figures 2.1 and 2.2. The difficult contribution to predict is from stress relaxation and residual stresses since there are two significant sources of stress; mechanical stresses due to pressing and thermal stresses due to non-uniform temperature distribution and history. Since the stress state due to both sources depends heavily on lens geometry, a second lens shape is introduced as presented in Figure 6.10. This “steep meniscus” shape is believed to be more difficult to compensate than the validation geometry.

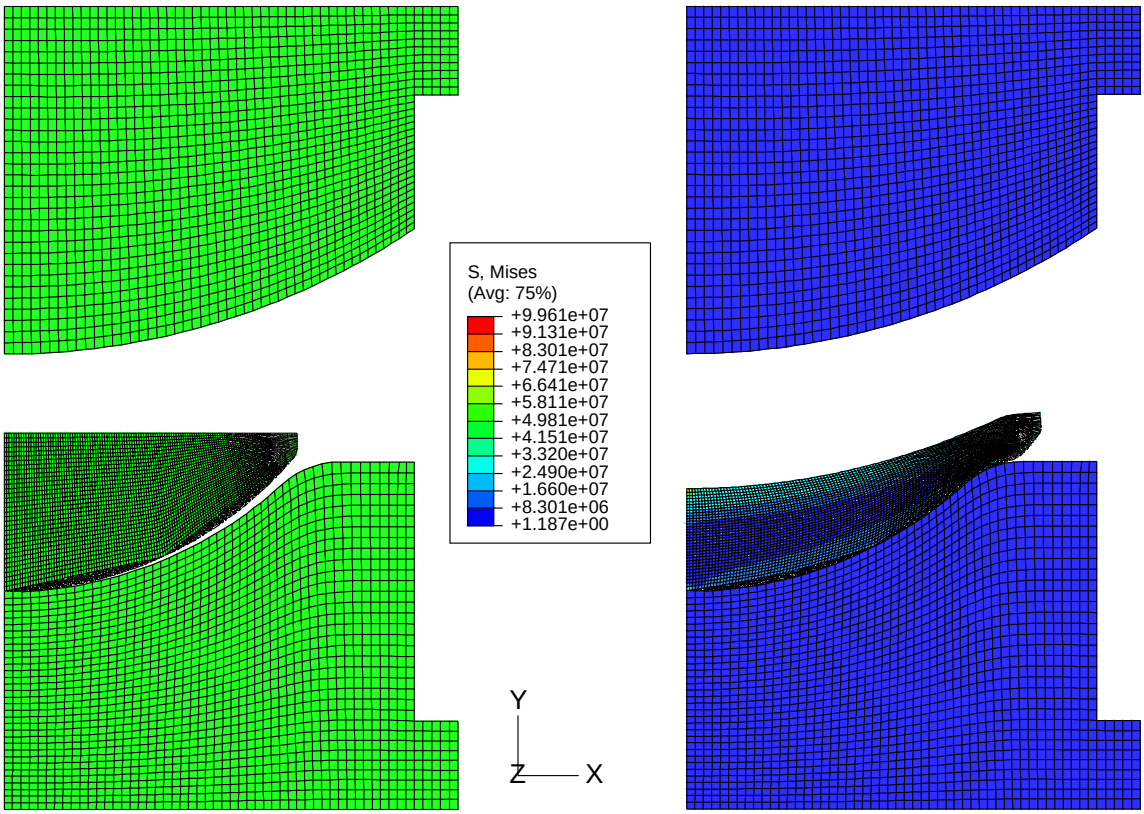

Figure 6.10: Initial and deformed configurations for the steep meniscus lens molding process. In Figure 6.11 the deviation between the steep meniscus and the validation geometry are compared. The smaller radius of curvature produces a larger deviation as expected, since a flat surface will have almost no deviation.

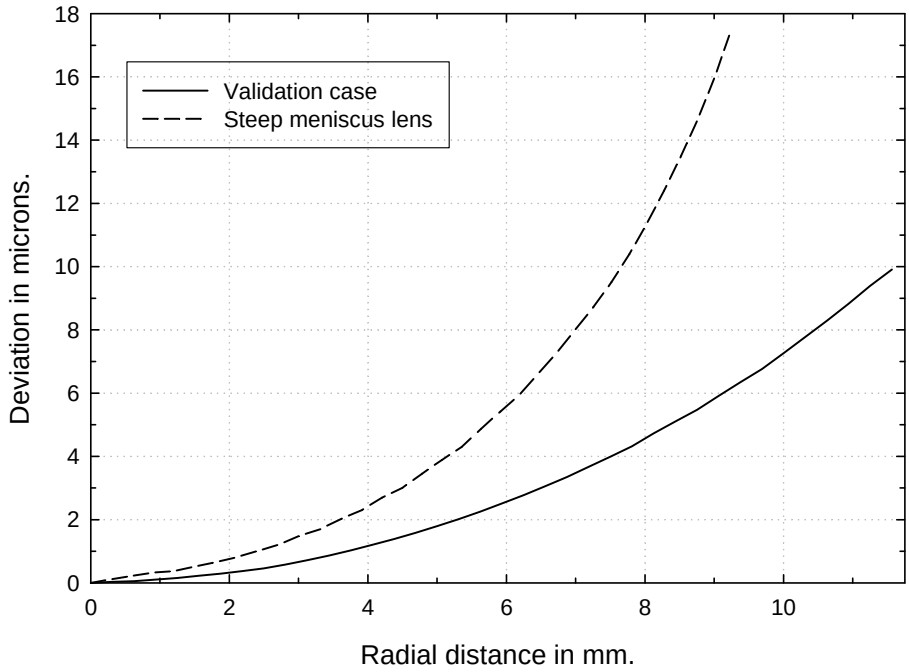

Figure 6.11: Sensitivity of preform and mold shapes on deviation.

The reason for the choice of the steep meniscus lens for the study of residual stresses is shown in Figure 6.12, where the stress state at the indicated section and time is plotted for both the validation and steep meniscus lenses. The validation case has a nearly symmetric stress distribution much like tempered glass, which, after release, would have little effect on deviation. The steep meniscus case, however, has a near linear stress distribution, which can be thought of as compressive force plus bending moment, which would tend to change shape, especially if the lens were designed to be thinner. After release the stress distribution shown in Figure 6.12b keeps this near linear profile, but *increases* in magnitude, a stress state that develops in time and remains in the lens at room temperature. This increase in the σ_{11} stress shows that the molds apply a stress distribution to the lens that opposes an increase in deviation, and when removed, the lens experiences a positive deviation. It makes sense that the molds oppose the thermal effect of wanting to create a positive deviation, but there is an unknown effect of the residual stresses

generated during pressing. The challenge is to determine the relative contributions of thermal expansion, stress relaxation and residual stress to the deviation, which is clearly a function of the lens shape.

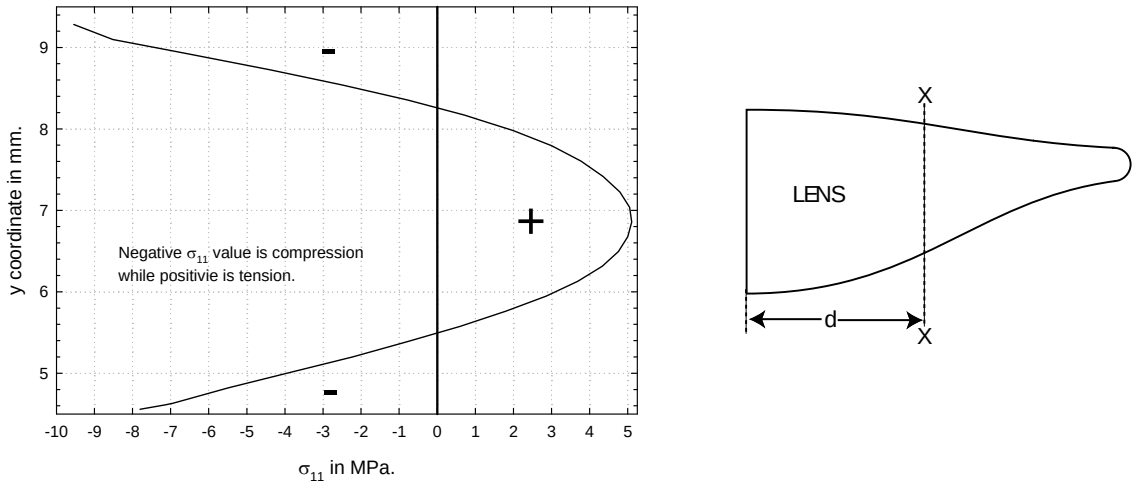

(a) Stress state of the validation geometry

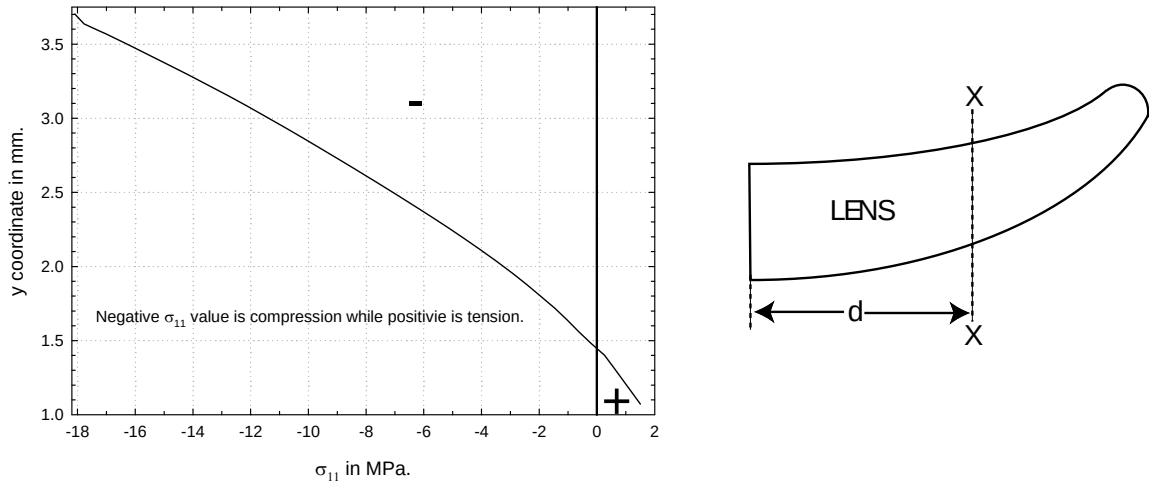

(b) Stress state of the steep meniscus lens geometry.

Figure 6.12: Stress state (σ_{11}) at the end of the slow cooling phase, just before the gap is created, at a vertical section that is approximately d = 5mm from the axis of symmetry for both geometries.

In order to isolate the effect of stresses generated during molding from those of thermal effects, a numerical experiment is performed in which all thermal expansion is "turned off" in the computational model for both the molds and the glass. Therefore, the only factors causing deviation are mechanical. As shown in Figure 6.9, the effect of mold deformation for the current case of E = 570 GPa compared to the rigid result is negligible. Therefore, this numerical experiment isolates the effect of stresses generated in the glass due to pressing and friction. The deviations for the two lens shapes are presented in Figure 6.13, which shows clearly that the steep meniscus has a non-negligible but small positive deviation, while the validation case is very near zero.

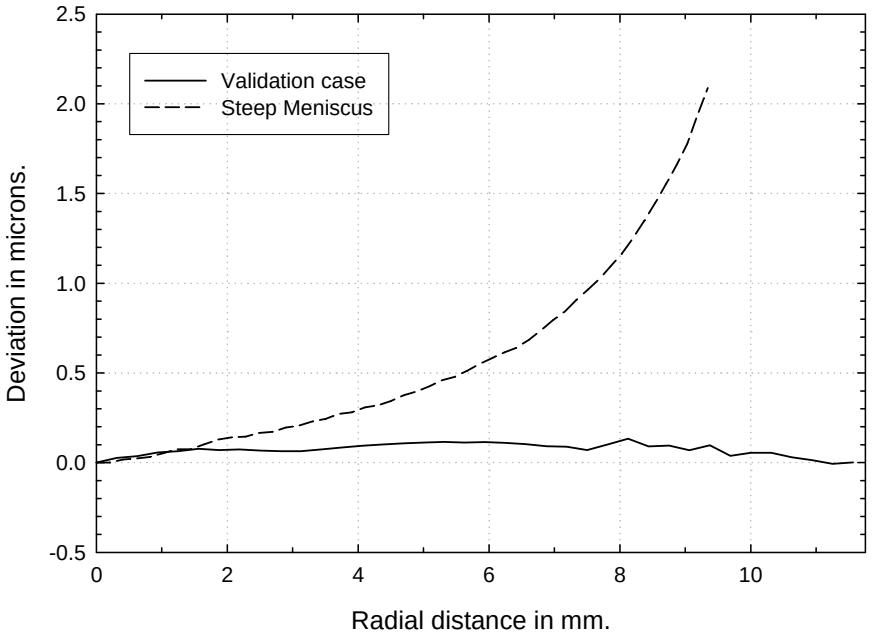

Figure 6.13: Sensitivity of the preform and mold shapes on deviation when the coefficient of thermal expansion is artificially set to zero. This analysis was done to study the sensitivity of deviation on residual stresses alone. This deviation arises when the gap was created and stays constant until the end of the molding process.

As shown in Figure 6.14, by neglecting all thermal expansion effects, the residual stress distribution is changed significantly for the validation case from what was presented in Figure

6.12. In this case the stress distribution for Figure 6.14a does not change significantly in time and therefore, there is no deviation once the lens is released from the mold. For the steep meniscus case, there is an increase is the σ_{11} stress level as the lens is released, so a small positive deviation results. Therefore, it appears that the residual stress state developed during pressing of the steep meniscus lens wants to *increase* deviation, which is the same tendency as thermal expansion.

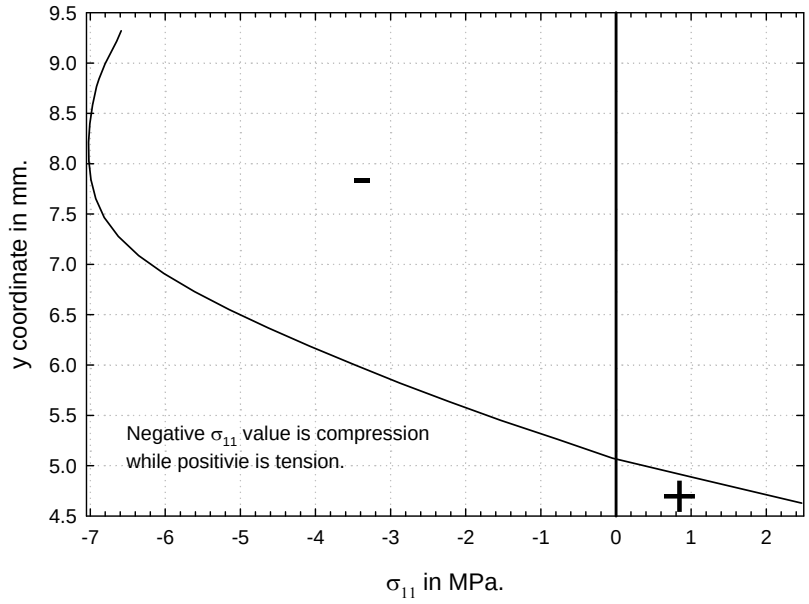

(a) Stress state of the validation geometry

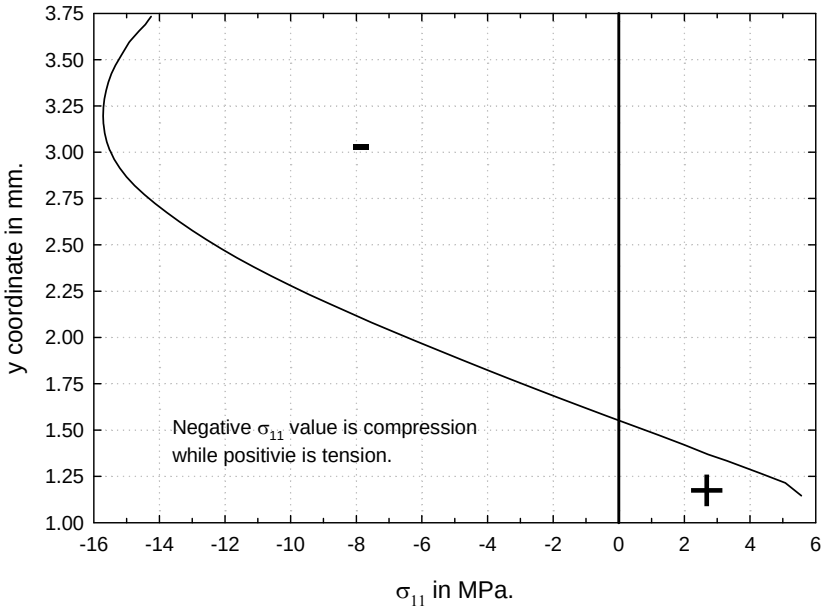

(b) Stress state of the steep meniscus lens geometry.

Figure 6.14: Stress state (σ_{11}) at the end of the slow cooling phase at a vertical section that is approximately 5mm from the axis of symmetry for both geometries when α = 0.0 /K.

In the discussion accompanying Figures 6.11-14, the moment of release of the lens from the molds is very important in understanding how deviation is created. Therefore, the focus now is on the creation of the gap, when the maintenance force is removed. Following Figure 2.1 and 2.2, during this 19 second period when this 0.15 mm gap is created by lowering the bottom mold at constant speed, the deviation of the lens shape from the mold shape is allowed to start. The possibility of a relatively rapid shape change is controlled by the residual stresses generated during pressing, the TRS behavior of the material which defines the relaxation time for these stresses, and the temperature at which the gap is created. In Figure 6.15, the deviation curves of Figure 6.11 are repeated, also including the deviation just after the gap is created. This intermediate deviation is defined with respect to the mold shape at the current temperature, not at room temperature. Therefore, the dashed line in Figure 6.15 represents the "jump" in deviation as the lens quickly changes shape as the constraint of the mold is removed. While this result doesn't separate thermal from residual stress effects, it does show that most of the difference between the two lens types occurs before the gap is created. Furthermore, in the special case of Figure 6.13 where no thermal expansion is allowed, almost all of the deviation occurred during the 19 second interval when the gap was formed.

In the next series of results some possible effects of this gap are investigated. Specifically these include the effects of: friction to change mechanical loading, pressing force and molding temperature to change mechanical loading, TRS behavior to study the effect of relaxation time and the time (temperature) at which the gap is created.

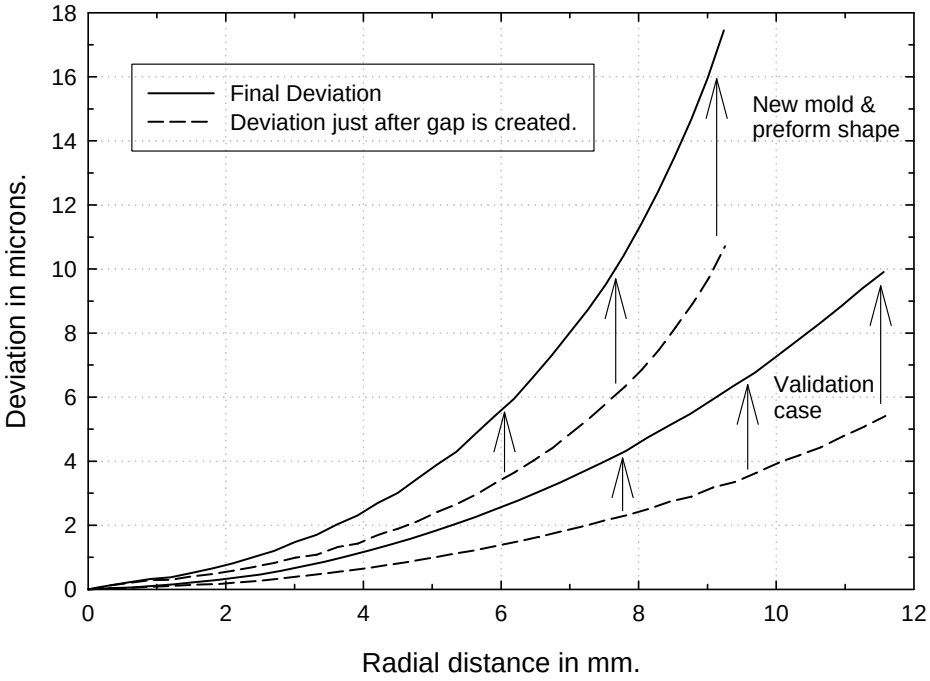

Figure 6.15: Same as Figure 6.11, except that the deviation immediately after the gap is created is also shown.

The shear stresses applied to the surface of the lens during the pressing phase are a function of both friction and the shape of the perform/mold combination. Given that our lens geometries are fixed in this study, this effect can be artificially created by using different friction scenarios. Furthermore, one way to determine the effect of residual stresses on deviation is through numerical experiments involving friction, since by changing the coefficient of friction, the residual stress state is changed. In Figure 6.17 three different friction coefficients are used for the validation geometry. The case of a coefficient of friction of "1" does have a significant effect. In Figure 6.18 two additional cases are used which have high friction on one side of the lens, and no friction on the other side. The deviation difference between these two cases is significantly different. The conclusion from these two friction figures is that there can easily be cases,

including perform shape, mold shape and friction behavior, that have a non-negligible, 1-2 micron deviation due to residual stress.

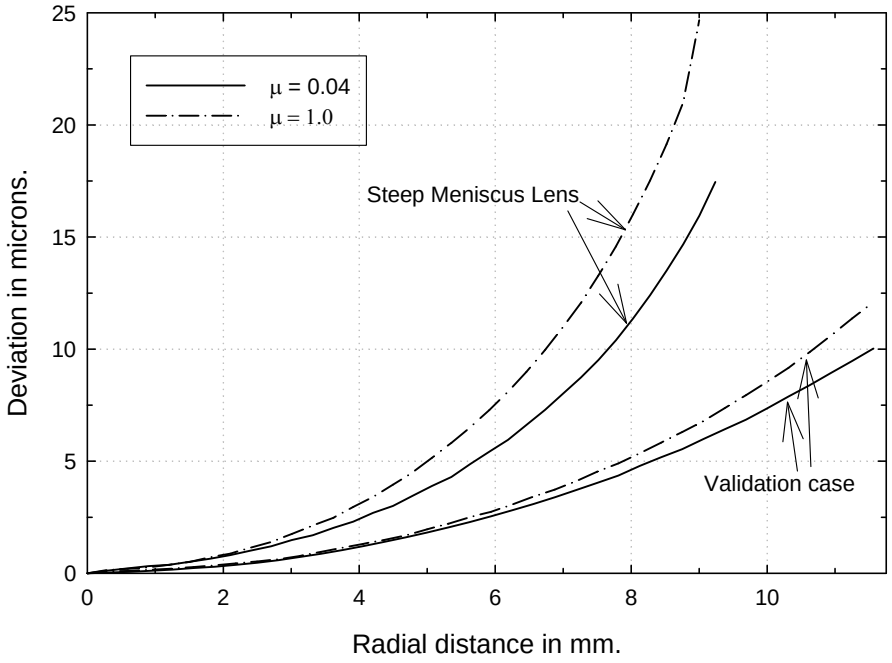

Figure 6.16: Sensitivity of coefficient of friction at the glass/mold interface on final deviation.

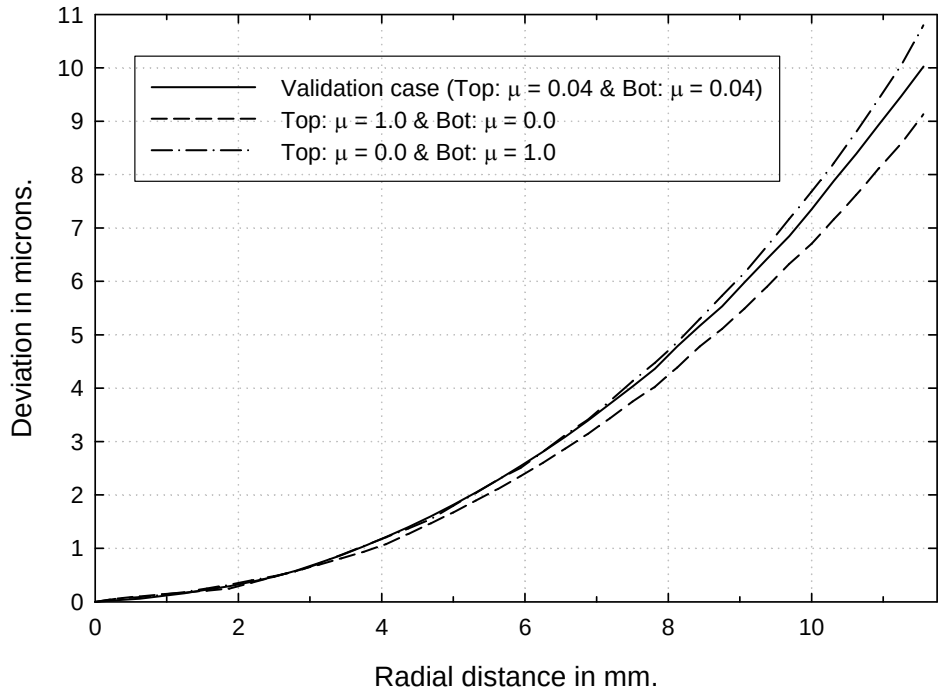

Figure 6.17: Sensitivity of different friction coefficients on the top and bottom surfaces for the validation case.

The molding force and molding temperature will now be varied to see how stress state affects deviation. In this case the pressing time must also be adjusted to achieve the same center thickness, which requires a reliable characterization of stress relaxation and the associated TRS behavior. In Figure 6.18 for several scenarios of force and time, very little differences in deviation occur. The lower part of the figure shows the detail of how center thickness is achieved through control of the lower mold position.

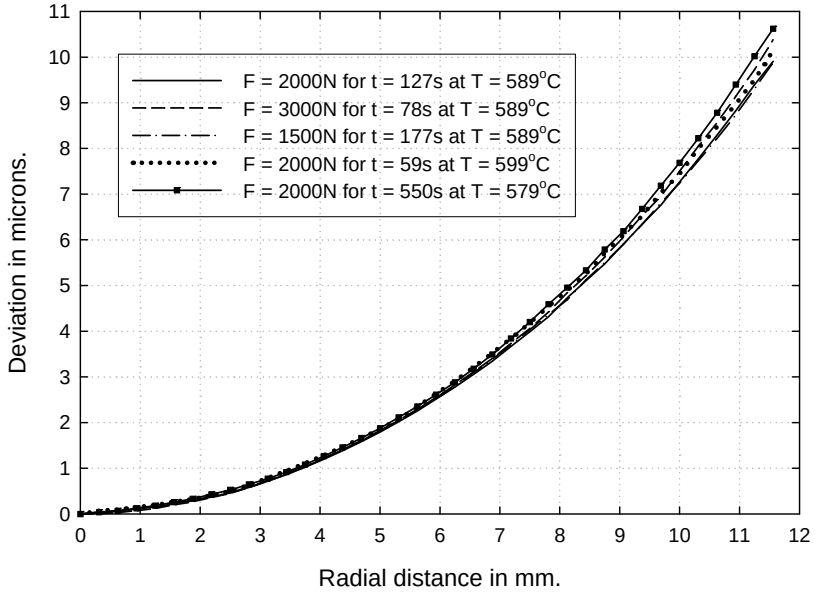

(a) Sensitivity analysis on Molding force and Molding temperature.

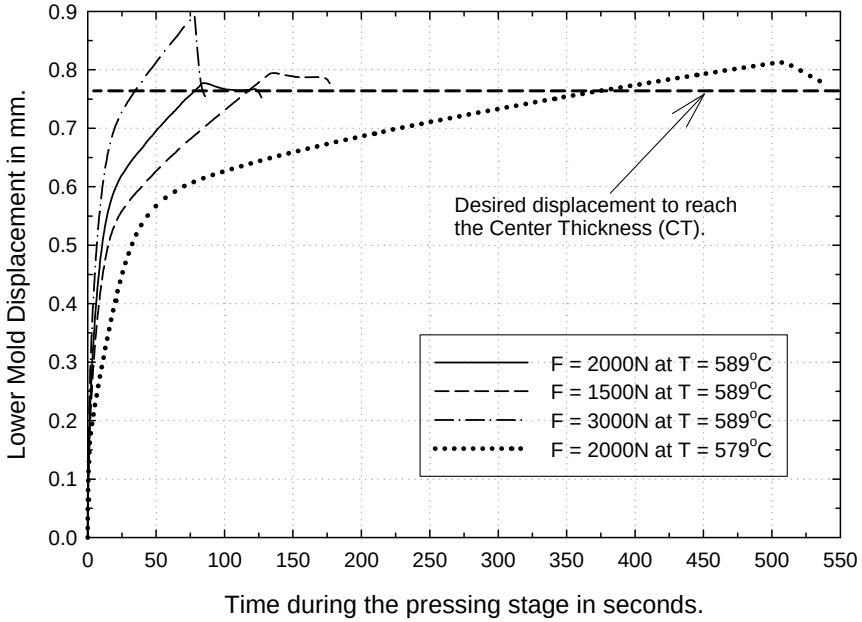

(b) Corresponding displacement of the lower mold as a function of time.

Figure 6.18: Sensitivity analysis of the different process parameters during the pressing stage on deviation. The same Center Thickness (CT) was achieved in all the different cases.

In Figures 6.16 and 6.17 friction was used to modify the stress state in the lens. The stress state can also be modified by changing the TRS behavior, as this affects the way the stresses relax and therefore changes the stress state at the time the gap is created. In Figures 6.19 and 6.20 two different TRS studies have been conducted for both lens types. In Figure 6.19 (b), all the three TRS different behaviors pass through a common point at 589˚C, whereas in Figure 6.20 (b) all the three different cases behave the same way in the temperature range 569˚C – 589˚C. By comparing the two Figures, it is seen that deviation is sensitive to the TRS behavior at temperatures near the molding temperature (569˚C – 589˚C). In Figure 6.19, as seen by the values of deviation in Table 6.2, all the differences in deviation occur when the gap is created, not during subsequent cooling at lower temperature. Referring to Figure 6.19, it is seen that if relaxation times increase at a slower rate (doted curve), viscosity of glass also increases at a slower rate and hence the material flows easily. Since the material is able to flow, it can better accommodate the change in shape driven by cooling, thereby decreasing the deviation. Conversely, if relaxation times increase at a faster rate (dashed curve) the deviation increases since viscosity increases at higher temperature, which reduces the time for the glass to adjust.

TRS Behavior (T_R = 588^{o}C, C_2 = 149^{o}C)	Increase in deviation from when gap is created to the end of the process (μm)	
	Validation case	Steep Meniscus Lens
C_1 = 6	6.545	4.62
C_1 = 12.4085	6.61	4.49
C_1 = 25	6.48	4.33

Table 6.2: Comparison of increase in deviation from the time when the gap is created until the end of the process for various TRS behaviors.

Referring to Figure 6.20, the three different TRS behaviors differ only below 569˚C and very little change in deviations occurs. This implies that the TRS behavior at temperatures near the molding temperature is very crucial to predicting the deviation accurately.

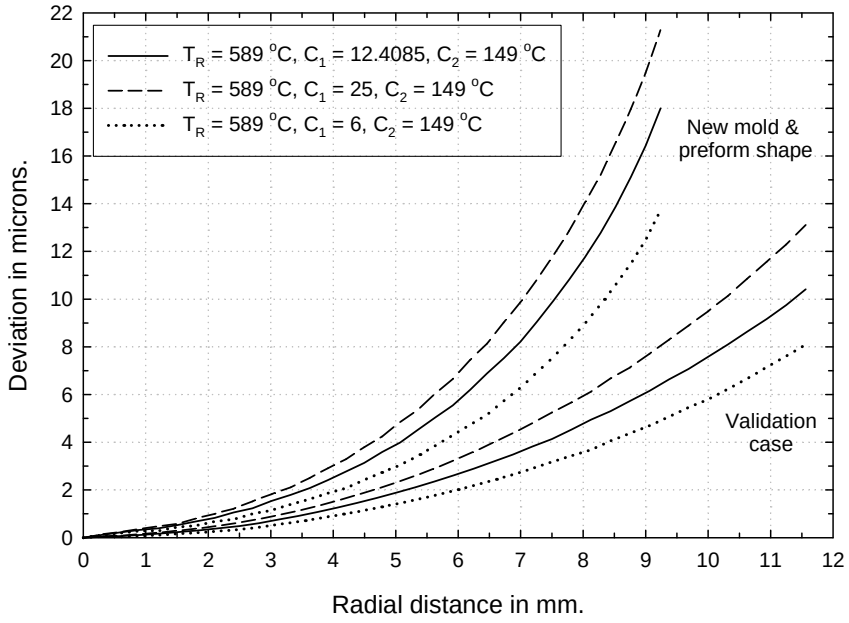

(a)

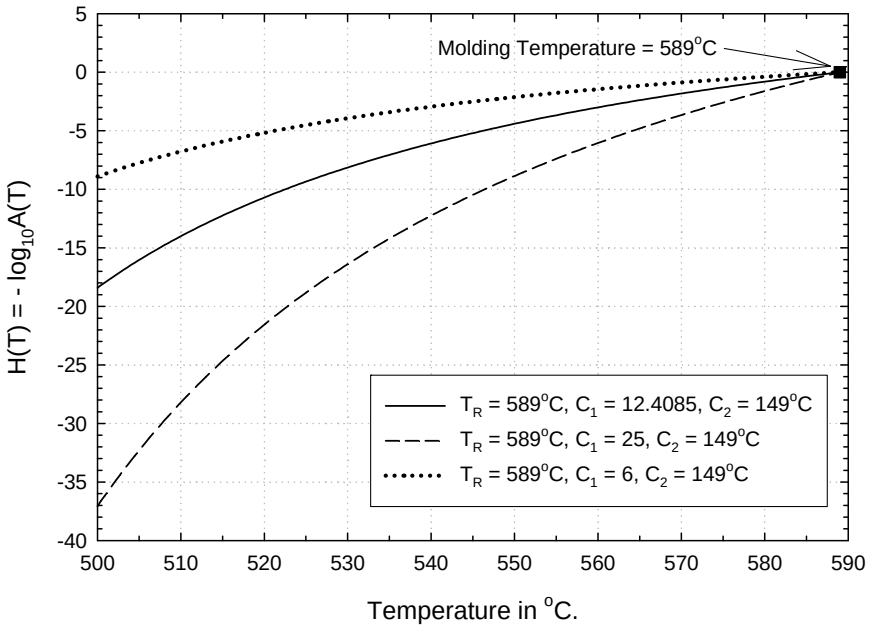

(b)

Figure 6.19: (a) Sensitivity of TRS behavior on deviation. (b) Illustration of different temperature dependence of shift factor A(T) while maintaining T_L = 440°C.

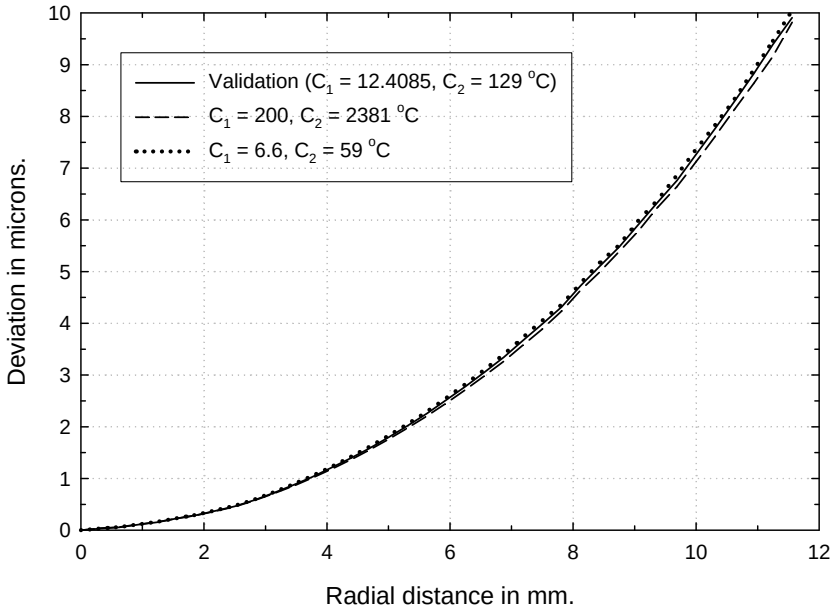

(a)

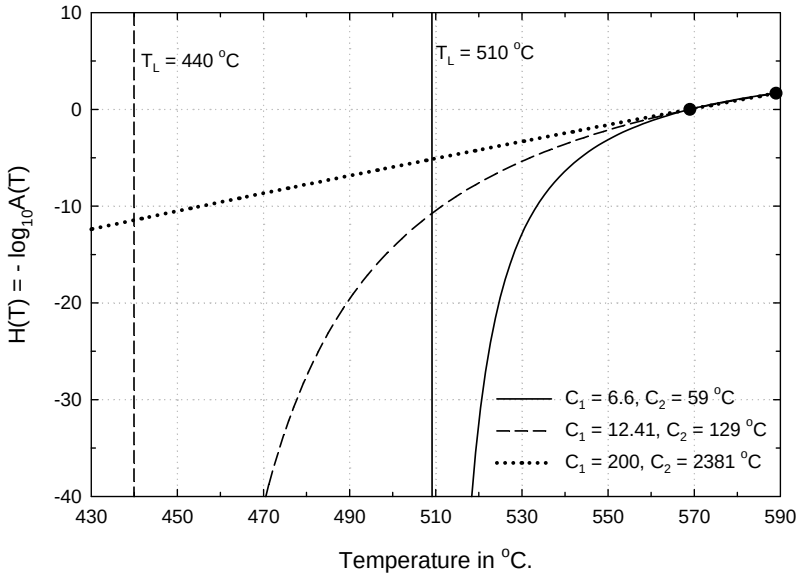

(b)

Figure 6.20: (a) Sensitivity of TRS behavior on deviation where T_R = 569°C. (b) Illustration of different TRS behavior while making sure that the shift factor curve A(T) passes through the two points indicated.

One final set of results to study the effect of residual stresses on deviation was carried out by changing the temperature at which the gap appears while maintaining the cooling rate. As shown in Figure 6.21 the deviations are found to be sensitive to the temperature at which the gap is created, although this effect is small for realistic times at which the gap appears.

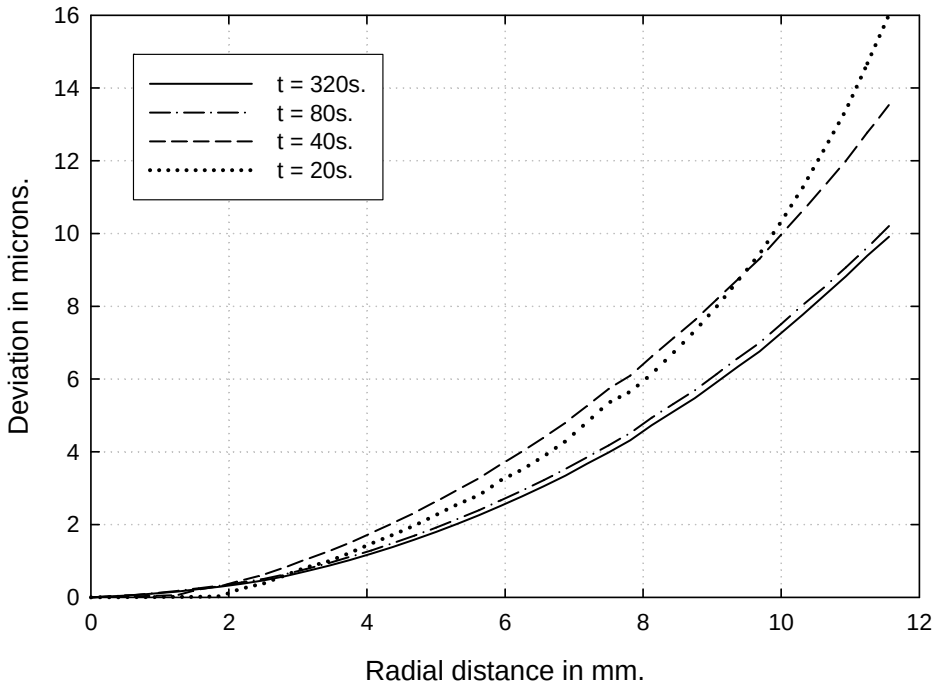

Figure 6.21: Comparison of final deviation for various durations of the slow cooling stage (with a maintenance force of 500N.) of the precision molding process. The case 't = 320s' corresponds to the validation case. The cooling rate in all these simulations was kept constant at 25.875°C/min. Therefore, for the case 't = 320s,' the gap would be created when the temperature at the end of the slow cooling stage is around 450K, whereas for the case 't = 20s,' the gap would be created at 579K.

6.4 Thermal properties and cooling rates

Given that structural relaxation behavior of the glass (Figures 6.4 and 6.6) and the thermal expansion behavior of the mold (Figure 6.8) are perhaps the most important parameters that affect sensitivity for final size and shape, it is important to consider other thermal properties. In Figures 6.22 a sensitivity analysis of deviation to the thermal conductivities of both glass and molds is illustrated. When the thermal conductivity of glass is made unusually high (equal to that of the mold in this case), then there is a small thermal gradient across the thickness of the lens. In other words, the lens is said to undergo uniform cooling everywhere. Hence the lens shrinks as a whole without any resistance from thermal stresses which increases the deviation as shown in Figure 6.22a. If the thermal conductivity of the molds is decreased such that it is close to the thermal conductivity of glass, then the molds also cool slowly. Hence there are no thermal gradients in the lens and it shrinks more uniformly without resistance form thermal stresses giving rise to more deviation.

One of the difficulties in the model is the establishment of temperature boundary condition. In Figure 6.23, the sensitivity of cooling rates during the rapid cooling stage on deviation is studied. For extreme variations in the cooling rates from 7.6°C/min to 262°C/min, the change in deviation is only 2 microns. Hence we can conclude that within practical range of cooling rates, the deviation does not change appreciably.

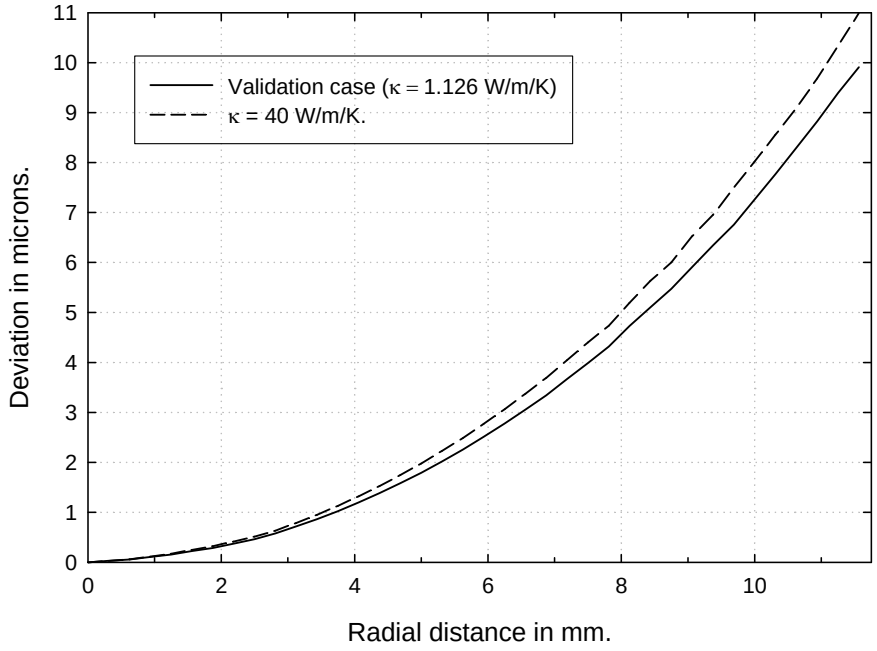

(a) Sensitivity of thermal conductivity of glass on deviation.

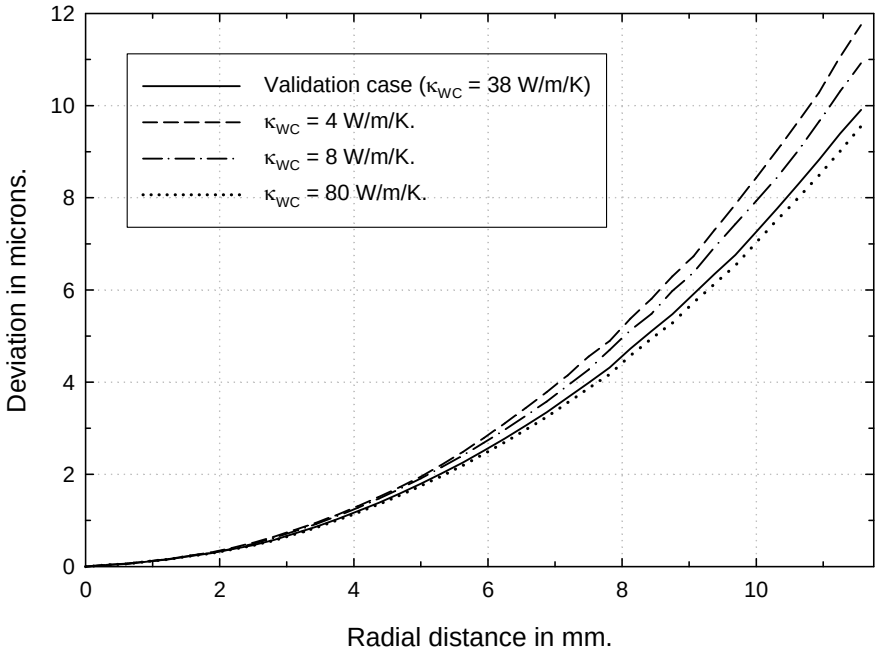

(b) Sensitivity of thermal conductivity of the mold on deviation.

Figure 6.22: Sensitivity of thermal conductivity of mold and glass on deviation

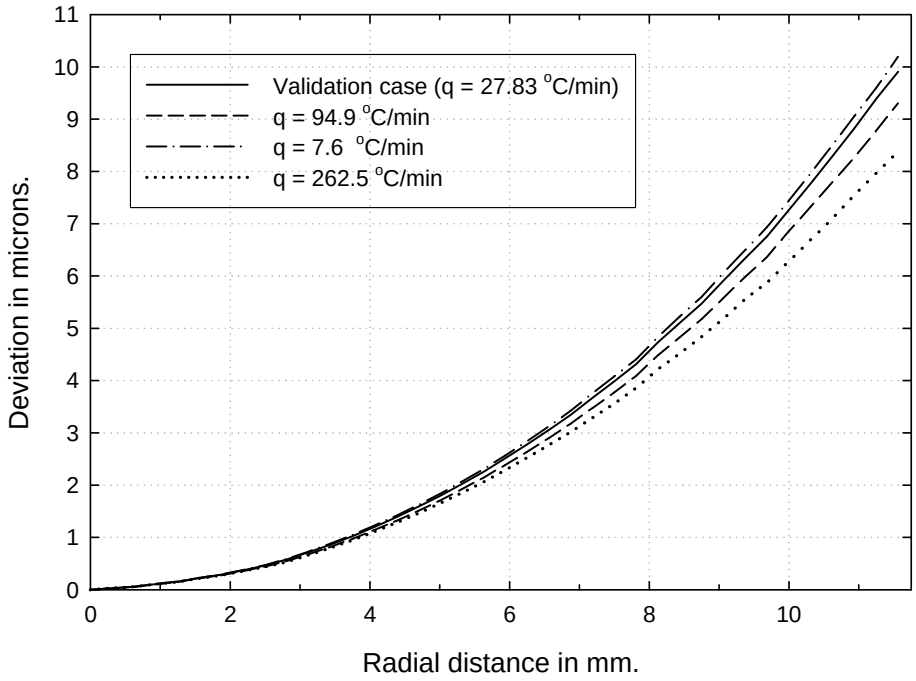

Figure 6.23: Sensitivity of various cooling rates during the rapid cooling stage (after the gap is created) on the final deviation.

One last parameter to consider that has an effect on the temperature distribution in the lens, and therefore, through structural relaxation, on the final size and shape of the lens is the contact conductance (see Figure 2.3 and Section 2.4.3). By changing the parameters in the gap conductance model it was determined that very little differences in the deviation occur. A good way to study the importance of gap conductance, which can also be an issue in lens molding, is to change the location of the lens with respect to the upper and lower molds once the gap is created. In Figure 6.24 the deviation is plotted for both lens types when the lens "sticks" to the upper mold instead of the baseline case considered previously when the lens rested on the lower mold. The non-negligible difference between these two cases shows the importance of the gap conductance, and of knowing the location of the lens when the initial release from one of the molds occurs.

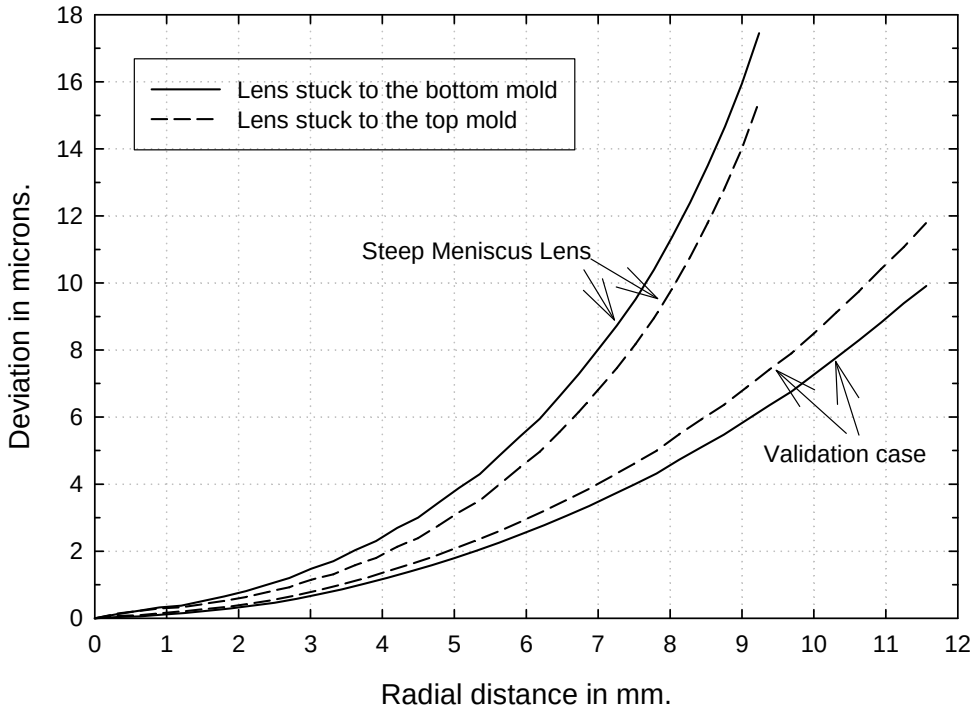

Figure 6.24: Change in deviation observed depending on whether the lens sticks to the top mold or lies on the bottom mold for the two different geometries considered.

The final set of results in this Chapter addresses the matter of compensation. Here the sensitivity parameter is a very slight change in the mold profile. A simple procedure for compensation is adopted in which the target shape of the lens is assumed to be the mold shape. In this case a naïve first guess of the mold shape is the desired target shape. Then in the first iteration the mold is changed by the deviation, assuming the deviation of the new mold will be identical to that of the previous mold. Our results for deviation shape presented in Figure 6.25, where deviation is now defined as the difference between the lens shape and the desired shape show that this is basically true, as the “after compensation” result is near zero. These results show that if the lens rests in the same place for both the first guess and the first

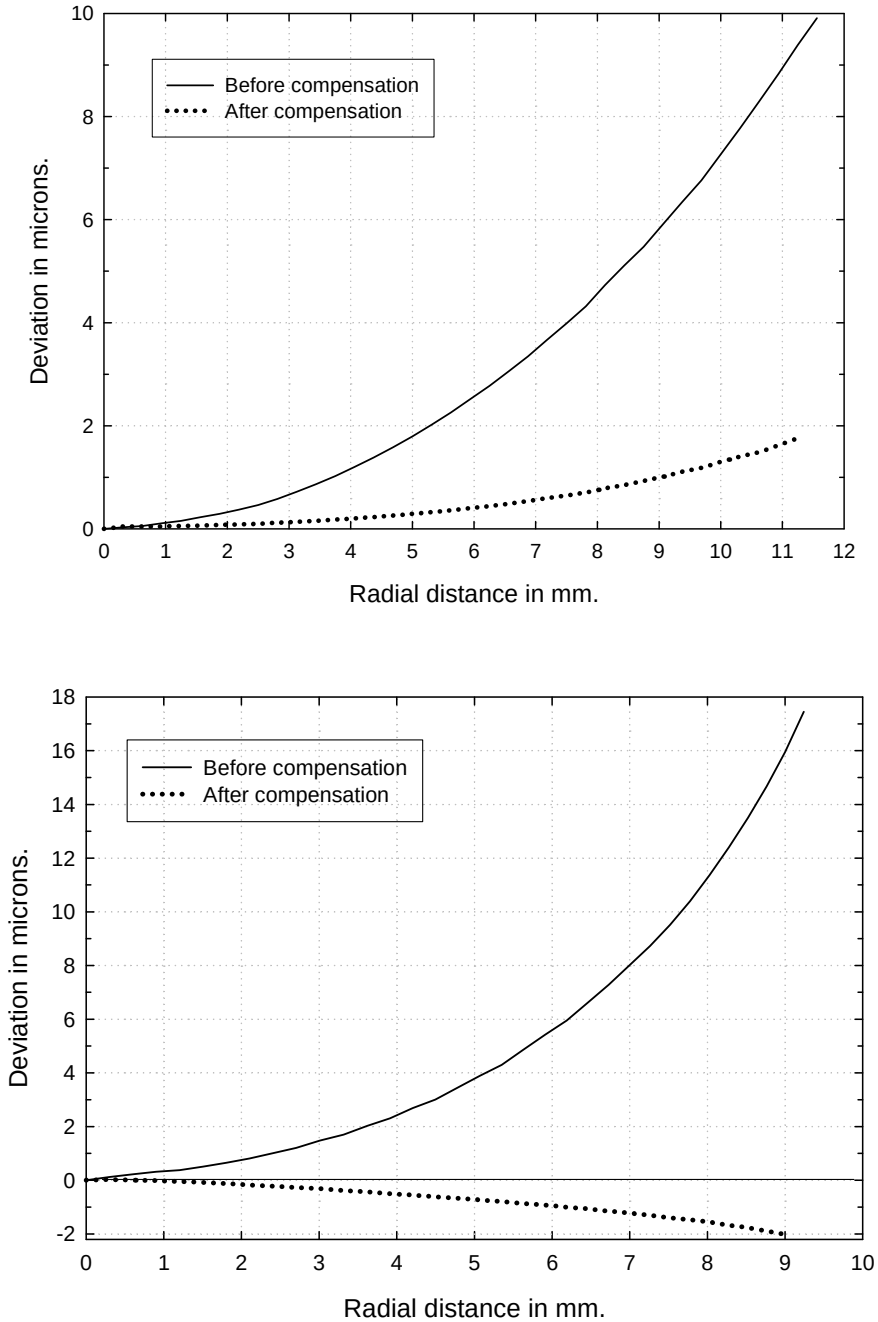

Figure 6.25: Demonstration of mold compensation for a bi-convex and steep meniscus lens geometry. The lens lies on the bottom mold surface before compensation and sticks to the top mold surface after compensation.

iteration, the deviation is not predicted to be sensitive to a slight change in mold shape. In order to have a non-zero deviation after the first iteration, the lens is now considered to stick to the upper mold after compensation. In this case, as expected from Figure 6.24, the results of 6.25 show the need for a second iteration.

References

1. G. Scherer (1986), *Relaxation in glass and composites*, John Wiley and Sons.

CHAPTER 7

Determination of Mode-I higher order coefficients and zones of dominance in fracture mechanics

7.1. Introduction

A method to determine higher order coefficients from the solution of a singular integral equation is presented. The coefficients are defined by $\sigma_{rr}(r,0) = \sum_{n=0}^{\infty} k_n (2r)^{n-\frac{1}{2}} + T_n (2r)^n$, which gives the radial stress at a distance, r, in front of the crack tip. In this asymptotic series the stress intensity factor, k_0 is the first coefficient, and the T-stress, T_0 is the second coefficient. For the example of an edge crack in a half space, converged values of the first twelve mode I coefficients (k_n and T_n, n=0,…,5) have been determined, and for an edge crack in a finite width strip, the first six coefficients are presented. Coefficients for an internal crack in a half space are also presented. Results for an edge crack in a finite width strip are used to quantify the size of the k-dominant zone, the kT-dominant zone and the zones associated with three and four terms, taking into account the entire region around the crack tip.

Williams [1] was the first to express stresses and strains near the tip of a crack in terms of an asymptotic series for small distances from the crack tip. Using the polar coordinate system in Figure 7.1a, the asymptotic form of the stresses and displacements for the symmetric, mode I case of loading can be expressed as

$$\sigma_{ij}(r,\theta) = \sum_{n=0}^{\infty} k_n^I (2r)^{n-\frac{1}{2}} f_{ij}^{Ik}(n,\theta) + \sum_{n=0}^{\infty} T_n^I (2r)^n f_{ij}^{In}(n,\theta), \quad (1)$$

$$2\mu u_i(r,\theta) = \sum_{n=0}^{\infty} k_n^I (2r)^{n+\frac{1}{2}} g_i^{In}(n,\theta) + \sum_{n=0}^{\infty} T_n^I (2r)^{n+1} g_i^{In}(n,\theta), \; i = r,\theta\,, \quad (2)$$

where the angular functions for both modes I and II are presented in Appendix B. Within the main body of the paper the superscript "I" will be omitted since only mode I is considered in this study, i.e., $k_n = k_n^I$ and $T_n = T_n^I$. These coefficients are referred to as the stress intensity factor coefficients and T-stress coefficients, respectively.

The application of linear elastic fracture mechanics (LEFM) involves two length scales, one physical and the other mathematical. In terms of a radius of a circle centered at the crack tip, the physical length

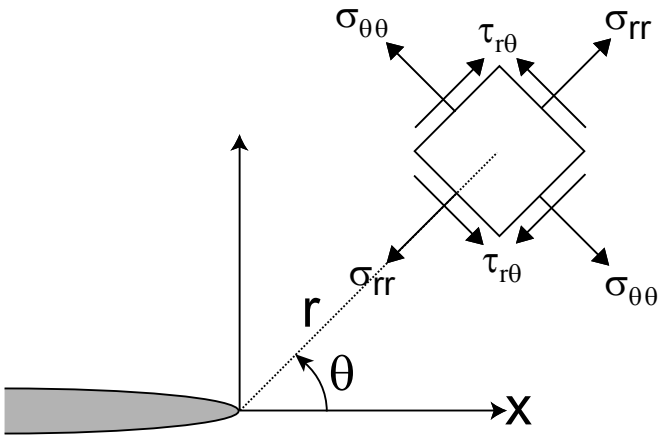

Figure 7.1a.

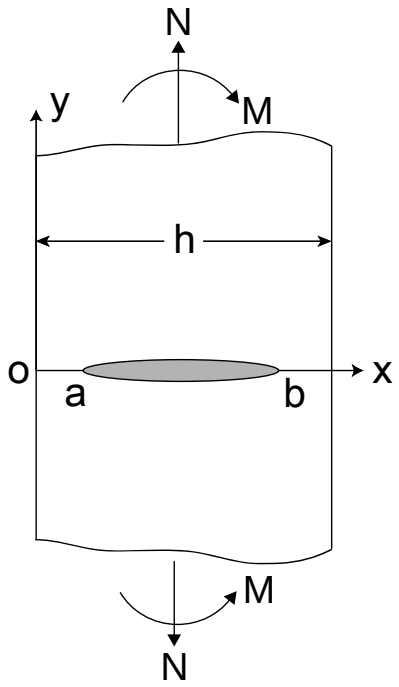

Figure 7.1b.

Figure 7.1: Problem geometry for the region around the crack tip (Figure 7.1a) and for a crack in an infinite strip (Figure 7.1b).

scale (r_p) defines the zone in which all phenomena not accounted for by LEFM occur, while the mathematical length scale (r_m) defines the zone in which the truncation of the infinite series, (1) and (2), to one term is adequate. By a Saint Venant's type of argument, one requires,

approximately, $r_m \approx 3r_p$ for some acceptable level of error that is used to define r_m (see Hutchinson [2]). The focus of the current study is the effect of the higher order terms on the mathematical length scale.

Perhaps the most important work with higher order terms has been with the elastic T-stress, which corresponds to T_0 in (1-2). Larsson and Carlsson [3] were the first to demonstrate the importance of this quantity in fracture. They showed that the T-stress has an affect on the plastic zone size and shape, which led these authors to conclude that the T-stress might play a role in characterizing the necessary conditions for fracture in the presence of significant yielding. The work of Levers and Randon [4] provides further evidence of the importance of the T-stress as a secondary fracture parameter, which can be used to explain differences in the fracture behavior of two specimens that are subjected to the same applied stress intensity level. This behavior has been verified in an elastic-plastic analysis by Betegon and Hancock [5], who showed that a negative T-stress tends to lower stresses near a crack tip, which makes the material appear tougher at the same applied J-level than if a positive T-stress exists. This later study follows the important study of Li and Wang [6] who revealed a case in nonlinear fracture where a two-parameter criterion is important; see also the study by Chao and Zhu [7] and references. Loghin and Joseph [8,9] have also shown that in the mixed mode nonlinear crack problem, a double root does not always occur in the leading HRR term, giving an increased importance to the higher order terms.

Because of studies such as [3-5] several authors have given results for the elastic T-stress. Most of this work is based on the finite element method [10,11]. Excellent reviews of the development of finite element formulations dedicated to a direct determination of stress intensity factors and T-stress coefficients are given by Karihaloo and Xiao [12] and Song [13].

Other approaches used to obtain the T-stress include Seed and Nowell [14] who used a singular integral equation approach for an inclined edge crack in a half space, Olsen [15] who used the boundary element method and Fett [16] who used the boundary collocation method.

From the point of view of the current study, coefficients of terms of higher order than the T-stress term are of interest. For this case Fett [16], Karihaloo and Xiao [12,17], Xiao, et al. [18] and Song [13] have provided the key methods and solutions. In particular Karihaloo and Xiao [12] have used a special element (hybrid crack element) that allows for a direct calculation of the coefficients of higher order coefficients and Song [13], who has extended the scaled boundary finite-element method to determine directly higher order coefficients.

In the current study, which is based on Capitaneanu [19], the method of singular integral equations is used to determine coefficients in the series given by (1). The method differs from that of Seed and Nowell [14] in the numerical approach which we believe is a more convenient and more accurate one for determining higher order coefficients ($n > 0$). Using these higher order coefficients, full-field solutions for stress are compared with the asymptotic stress fields to quantify zones of dominance for up to four terms for the cases of tension and bending in an edge cracked strip.

7.2. Formulation

The symmetric case of mode I is presented in the formulation. Based on the numerical solution of a singular integral equation, the mode I coefficients, $k_n = k_n^I$ and $T_n = T_n^I$ in the series (1) and (2), are determined for both an internal and an edge crack.

7.2.1. The singular integral equation.

Consider a planer crack along the $y = 0$ line that extends from $x = a$ to $x = b$ (Figure 7.1b). For the mode I mixed boundary conditions,

$$V(x) = u_y(x,0^+) - u_y(x,0^-) = 0, \quad 0 < x < a, \ b < x \tag{3}$$

$$\sigma_{yy}(x,0) = -p(x), \quad a < x < b \tag{4}$$

the resulting singular integral equation of the first kind can be represented by

$$\int_a^b \frac{\phi(t)}{t-x}\,dt + \int_a^b \phi(t)\,K(x,t)\,dt = -\pi\frac{1+\kappa}{2\mu}p(x), \quad a < x < b\,, \tag{5}$$

where $\phi(t)$ is the derivitive of the crack opening displacement (COD) defined by

$$\phi(t) = \frac{d}{dt}\left[u_y(t,0^+) - u_y(t,0^-)\right] = \frac{dV}{dt} \quad , \tag{6}$$

and K(x,t) is a Fredholm kernel associated with the geometry of the particular crack problem under investigation. This equation can be solved for the unknown, $\phi(t)$ by using numerical methods. Once this function is determined, all of the field quantities can be determined in terms of integrals of ϕ. For example, the expression for the stress parallel to the line of the crack along y = 0 is given by

$$\frac{\pi(1+\kappa)}{2\mu}\sigma_{xx}(x,0) = \int_a^b \frac{\phi(t)}{t-x}\,dt + \int_a^b \phi(t)\,L(x,t)\,dt\,, \tag{7}$$

and the displacement component in the direction parallel to the crack is of the form,

$$\frac{\pi(1+\kappa)}{2}u_x(x,0) = -\frac{1-\kappa}{4}\int_a^b \frac{V(t)}{t-x}\,dt + \int_a^b V(t)\,M(x,t)\,dt\,, \tag{8}$$

where V(t) is the crack opening displacement defined by (6). Once again, the kernels L(x,t) and M(x,t) are associated with a particular problem (see Results Section for examples).

7.2.2. The internal crack.

For the case of an internal crack contained in a single material, the integral equation can be written in normalized form as

$$\int_{-1}^{+1}\frac{f(q)}{\sqrt{1-q^2}(q-s)}dq+\frac{b-a}{2}\int_{-1}^{+1}\frac{f(q)}{\sqrt{1-q^2}}K(x,t)\,dq=-\pi\frac{p(s)}{\sigma_0}\quad,\quad -1\le s\le 1\,,\qquad(9)$$

where

$$t=\frac{b-a}{2}q+\frac{b+a}{2},\quad x=\frac{b-a}{2}s+\frac{b+a}{2},\quad \phi(t)=\frac{f(q)}{\sqrt{1-q^2}}\frac{(1+\kappa)\sigma_0}{2\mu}\quad .\qquad(10)$$

A numerical solution is sought in the approximate form

$$f(q)=\sum_{m=1}^{N}c_m T_m^{Ch}(q)\,,\qquad(11)$$

where the T_m^{Ch} are Chebychev polynomials of the first kind. Due to the orthogonality of these polynomials, by starting the sum at m = 1, the function f(q) satisfies the condition

$$\int_a^b\phi(t)dt=0\quad .\qquad(12)$$

Following Kaya and Erdogan [20] and Erdogan and Joseph [21] for the details of the numerical procedure, once f(q) is determined, the crack opening displacement is given by

$$V(s)=-\frac{b-a}{2}\frac{(1+\kappa)\sigma_0}{2\mu}\sum_{m=1}^{N}\frac{c_m}{m}\sqrt{1-s^2}\,U_{m-1}(s)\,,\quad -1<s<1\,,\qquad(13)$$

where the $U_{m-1}(s)$ are Chebychev polynomials of the second kind.

At the crack tip at x = b, the expression (2) is used to obtain the asymptotic expression for the crack opening displacement as

$$V(r)=-u_\theta(r,+\pi)+u_\theta(r,-\pi)=\frac{1+\kappa}{2\mu}\sum_{n=0}^{\infty}(-1)^n\frac{k_n}{2n+1}(2r)^{n+\frac{1}{2}}\quad ,\qquad(14)$$

which in terms of (1 - s), can be expressed as

$$V(s)=-u_\theta(r,+\pi)+u_\theta(r,-\pi)=\frac{1+\kappa}{2\mu}\sum_{n=0}^{\infty}(-1)^n\frac{k_n(b-a)^{n+\frac{1}{2}}}{2n+1}(1-s)^{n+\frac{1}{2}}\quad .\qquad(15)$$

The next step is to expand V(s) from (13) about s = 1, which requires the expresion,

$$\frac{1}{m}\sqrt{1-s^2}\,U_{m-1}(s)=\frac{1}{m}\sin\left[m\left(\cos^{-1}s\right)\right]=\sqrt{2(1-s)}\sum_{n=0}^{\infty}d_n^m(1-s)^n\,, \tag{16}$$

where the d_n^m are

$$d_0^m=1,\; d_n^m=\frac{d_{n-1}^m}{n(2n+1)}\left[\left(\frac{2n-1}{2}\right)^2-m^2\right]. \tag{17}$$

Given (16), the two expressions for the crack opening displacement from (13) and (15) can be matched term by term to give the approximation for the coefficients at the right crack tip (x = b),

$$\frac{k_n(b)(b-a)^n}{\sigma_0\sqrt{\frac{b-a}{2}}}=(-1)^{n+1}(2n+1)\sum_{m=1}^{N}c_m d_n^m\,,\; n=0,1,2,...,N. \tag{18}$$

The n = 0 term gives the stress intensity factor, while the n > 0 terms correspond to the higher order k_n coefficients. The coefficients for the left crack tip (x = a) are determined in a similar manner as

$$\frac{k_n(a)(b-a)^n}{\sigma_0\sqrt{\frac{b-a}{2}}}=(-1)^{n+1}(2n+1)\sum_{m=1}^{N}(-1)^{m+1}c_m d_n^m\,,\; n=0,1,2,...,N. \tag{19}$$

The T-stress coefficients, T_n in equations (1) and (2), can be determined by $\sigma_{xx}(x,0) = \sigma_{\pi\pi}(r,\pi)$ using (B.15). For the right crack tip, and for small values of (1 - s), the two integrals of (7) are treated separately. The singular integral can be expressed as

$$\frac{1}{\sigma_0}\frac{2\mu}{1+\kappa}\frac{1}{\pi}\int_a^b\frac{\phi(t)}{t-x}\,dt=\frac{1}{\pi}\int_{-1}^{1}\frac{\sum_{m=1}^{N}c_m T_m^{Ch}(q)}{(q-s)\sqrt{1-q^2}}\,dq$$

$$=\sum_{m=1}^{N}c_m U_{m-1}(s)=\sum_{n=0}^{N}\sum_{m=1}^{N}c_m m e_n^m(1-s)^n\,, \tag{20}$$

where the e_n^m are

$$e_0^m = 1,\ e_n^m = \frac{n^2 - m^2}{n(2n+1)} e_{n-1}^m. \tag{21}$$

The Fredholm integral expanded about s = 1 (x = b) is given by

$$\frac{1}{\sigma_0}\frac{2\mu}{1+\kappa}\frac{1}{\pi}\int_a^b \phi(t)L(x,t)\,dt = \sum_{n=0}^{M} h_n^b (1-s)^n + O(1-s)^{M+1}, \tag{22}$$

where the h_n^b are constants determined by integration of known functions and M is any desired integer less than or equal to N. Comparing the sum of the two expressions (20) and (22) with (B.15) gives for the right crack tip,

$$\frac{T_n (b-a)^n}{\sigma_0} = (-1)^n \left\{ \sum_{m=1}^{N} c_m m e_n^m + h_n^b \right\},\ n = 0,1,2,...,M. \tag{23}$$

The analogous result for the left crack tip at x = a, is given by

$$\frac{T_n (b-a)^n}{\sigma_0} = (-1)^n \left\{ \sum_{m=1}^{N} (-1)^{m+1} c_m m e_n^m + h_n^a \right\},\ n = 0,1,2,...,M, \tag{24}$$

where h_n^a are constants similar to h_n^b in (22) for an expansion about s = -1, i.e., $h_n^a (1+s)^n$. An alternative approach for the evaluation of the T_n coefficients, that avoids the analytical evaluation of the singular integral in (20), matches the difference in normal stresses along the upper surface of the crack. This approach will be presented in the next section for the case of an edge crack.

7.2.3. The edge crack.

Referring to Figure 7.1b, an edge crack of length b is assumed to exist from x = 0 to x = b. In this case, the normalized singular integral equation can be expressed as,

$$\int_{-1}^{+1} \frac{f(q)}{\sqrt{1-q}(q-s)}\,dq + \frac{b}{2}\int_{-1}^{+1} \frac{f(q)}{\sqrt{1-q}} K(x,t)\,dq = -\pi \frac{p(s)}{\sigma_0} \quad ,\quad -1 \le s \le 1, \tag{25}$$

where

$$t = \frac{b}{2}q + \frac{b}{2}, \quad x = \frac{b}{2}s + \frac{b}{2}, \quad \phi(t) = \frac{f(q)}{\sqrt{1-q}} \frac{(1+\kappa)\sigma_0}{2\mu} \quad . \tag{26}$$

The form of the function f(q) is approximated as the $(N-1)^{th}$ order polynomial,

$$f(q) = \sum_{m=0}^{N-1} c_m P_m^{(\alpha,\beta)}(q) \, , \tag{27}$$

where the $P_m^{(\alpha,\beta)}(q)$ are Jacobi polynomials associated with the weight function, $w(q) = (1-q)^{\alpha}(1+q)^{\beta}$, which for an edge crack requires α = -1/2 and β = 0. The derivative of the crack opening displacement can therefore be expressed as

$$\frac{2}{b}\frac{2\mu}{(1+\kappa)\sigma_0}\frac{dV(s)}{ds} = \frac{f(s)}{\sqrt{1-s}} = \frac{1}{\sqrt{1-s}} \sum_{m=0}^{N-1} c_m P_m^{\left(-\frac{1}{2},0\right)}(s), \quad -1 < s < 1 \, , \tag{28}$$

which has an associated displacement given by

$$\frac{2}{b}\frac{2\mu}{(1+\kappa)\sigma_0} V(s) = -\sqrt{1-s}\left[2c_0 + (1+s)\sum_{m=1}^{N-1} \frac{c_m}{2m} P_{m-1}^{\left(\frac{1}{2},1\right)}(s) \right], \quad -1 < s < 1 \quad . \tag{29}$$

In order to obtain the k_n coefficients, the displacement derivative from (28) will be matched with the series expression from Appendix C. Starting with (B.18) and using (26), the displacement can be written as

$$V(s) = -u_\theta(r,+\pi) + u_\theta(r,-\pi) = \frac{1+\kappa}{2\mu} \sum_{n=0}^{\infty} (-1)^n \frac{k_n b^{n+\frac{1}{2}}}{2n+1} (1-s)^{n+\frac{1}{2}} \, , \tag{30}$$

which has the derivative

$$\frac{2}{b}\frac{2\mu}{(1+\kappa)}\frac{dV(s)}{ds} = \frac{1}{\sqrt{1-s}} \sum_{n=0}^{\infty} (-1)^{n+1} k_n b^{n-\frac{1}{2}} (1-s)^n . \tag{31}$$

Taking into account an N-1[th] order Taylor series of f(s) expanded about s = 1, the derivative of the crack opening displacement from (28) can be expressed as

$$\frac{2}{b}\frac{2\mu}{(1+\kappa)\sigma_0}\frac{dV(s)}{ds}=\frac{1}{\sqrt{1-s}}\sum_{n=0}^{N-1}\frac{(-1)^n}{n!}\left.\frac{d^n f}{ds^n}\right|_{s=1}(1-s)^n \quad -1<s<1. \tag{32}$$

Comparing (31) and (32) gives the following result,

$$\frac{k_n b^n}{\sigma_0\sqrt{b}}=-\frac{1}{n!}\left.\frac{d^n f}{ds^n}\right|_{s=1}=-\frac{1}{n!}f^n(1). \tag{33}$$

The n[th] derivative of f(s) from (27) at s = 1 can be obtained for $\alpha>-1$, $\beta>-1$, $\alpha\neq 0,1,2,...$, as

$$f^n(1)=n!\sum_{m=n}^{N-1}c_m d_n^m, \tag{34}$$

where the d_n^m can be expressed in terms of binomial coefficients (see pages 10 and 775 of Abramowitz and Stegun [22]) as

$$d_n^m=\frac{1}{2^n}\sum_{j=0}^{n}\binom{m+\alpha}{m-j}\binom{m+\beta}{j}\binom{m-j}{n-j}. \tag{35}$$

For α = -1/2 and β = 0, this reduces to

$$d_0^m=\binom{m-1/2}{m}=\frac{1\times 3\times 5\times\cdots\times(2m-1)}{2\times 4\times 6\times\cdots\times(2m)},$$

$$d_n^m=\frac{(2m+2n-1)(m-n+1)}{2n(2n-1)}d_{n-1}^m \quad . \tag{36}$$

Convergence of (33) using (34) becomes more difficult as n increases due to the behavior of the coefficients from (36), especially for crack problems that require large values of N. In this case due to the m^2 multiplier in the recurrance relationship of (36), very accurate values of c_m are required for large m. An alternative to (34) is a backward finite difference evaluation of the n[th]

derivative of f(s) at s = 1, which takes advantage of the expression (27) to evaluate the function at any desired point. Another approach is to replace (27) with

$$f(q) = \sum_{m=0}^{N-1} \bar{c}_m (1-q)^m \ , \tag{37}$$

for which

$$\frac{k_n b^n}{\sigma_0 \sqrt{b}} = (-1)^{n+1} \bar{c}_n \ . \tag{38}$$

These approaches will be discussed further in the results section.

The T-stress coefficients, T_n in equations (1) and (2), can be determined by $\sigma_{xx}(x,0) = \sigma_{rr}(r,\pi)$ as seen by (B.15). For small values of (1 - s), the two integrals of (7) are treated separately. The singular integral can be expressed as:

$$\frac{1}{\sigma_0}\frac{2\mu}{1+\kappa}\frac{1}{\pi}\int_0^b \frac{\phi(t)}{t-x}\,dt = \frac{1}{\pi}\int_{-1}^{1} \frac{\sum_{m=0}^{N-1} c_m P_m^{(-\frac{1}{2},0)}(q)}{(q-s)\sqrt{1-q}}\,dq = \sum_{m=0}^{N-1} c_m \sum_{n=0}^{\infty} e_n^m (1-s)^n \ , \ |s| \le 1 , \tag{39}$$

where, from Tricomi [23], the e_n^m can be expressed in terms of gamma and factorial functions as

$$e_n^m = \frac{(-1)^m}{\pi 2^{n+\frac{1}{2}}} \frac{(m+n)!\,\Gamma\left(-m+n+\frac{1}{2}\right)}{n!\,\Gamma\left(n+\frac{3}{2}\right)} \ . \tag{40}$$

The Fredholm integral of (7) is given by

$$\frac{1}{\sigma_0}\frac{2\mu}{1+\kappa}\frac{1}{\pi}\int_0^b \phi(t) L(x,t)\,dt = \sum_{n=0}^{M} h_n (1-s)^n + O(1-s)^{M+1} \ , \tag{41}$$

where the h_n are constants determined by integration of known functions. Comparing the sum of the two expressions (39) and (41) with equation (1) for $\sigma_{rr}(r,\pi)$ gives,

$$\frac{T_n b^n}{\sigma_0} = (-1)^n \left\{ \sum_{m=0}^{N-1} c_m e_n^m + h_n \right\}, \; n = 0,1,2,...,M. \tag{42}$$

An alternative approach that avoids the analytical evaluation of the singular integral in (39) is to match the difference in the normal stresses along the line of the crack. From (5) and (7) the difference in these normal stresses can be expressed as

$$\sigma_{yy} - \sigma_{xx} = \frac{2\mu}{\pi(1+\kappa)} \int_0^b \phi(t)\left[K(x,t) - L(x,t)\right]dt = \sigma_0 \sum_{n=0}^{M} h_n^* (1-s)^n + O(1-s)^{M+1}, \tag{43}$$

where the integral is expanded about s = 1 (x = b) and the h_n^* are constants determined by integration of known functions. The comparable expression in terms of the T_n constants is obtained from (B.10) and (B.11) or from (B.15) along with the boundary condition that $\sigma_{yy} = 0$ on the upper crack face. Given (26), this relationship can be expressed as

$$\sigma_{yy} - \sigma_{xx} = \sum_{n=0}^{\infty} (-1)^{n+1} T_n (2r)^n = \sum_{n=0}^{\infty} (-1)^{n+1} T_n b^n (1-s)^n. \tag{44}$$

Matching coefficients of (43) and (44) gives the result

$$\frac{T_n b^n}{\sigma_0} = (-1)^{n+1} h_n^*, \; n = 0,1,2,...,M \quad , \tag{45}$$

which is an alternative to (42).

7.3. Results

Referring to Figure 7.1b for geometry, examples are considered for the symmetric (mode I) problems of an edge crack (a = 0) and an internal crack (0 < a < b) in a half space and for an edge crack in an infinite strip.

7.3.1. Edge crack in a half space.

For the case of a crack in a half space, as given by the small b/h limit of the problem geometry in Figure 7.1b, the kernels K(x,t), L(x,t) and M(x,t) of (5,7,8) are

$$K(x,t)=\left[-\frac{1}{t+x}+\frac{6x}{(t+x)^2}-\frac{4x^2}{(t+x)^3}\right], \tag{46}$$

$$L(x,t)=\left[-\frac{1}{t+x}-\frac{2x}{(t+x)^2}+\frac{4x^2}{(t+x)^3}\right]. \tag{47}$$

$$M(x,t)=\left[\frac{1}{4}\frac{1-\kappa}{t+x}-\frac{1}{2}\frac{x(\kappa-1)}{(t+x)^2}-\frac{2x^2}{(t+x)^3}\right]. \tag{48}$$

Values of k_n and T_n for an edge crack in a half space subjected to uniform tension, σ_0, are presented in Table 7.1 for the methods disscussed previously. An important finding for the current approach is that the k_n coefficients become increasingly difficult to determine as n increases, which is expected based on (27) and (33). This difficulty is quantified by noting that in order to obtain two significant digits for k_5, it was necessary to obtain twelve digits of accuracy in the stress intensity factor, k_0! This required values of N as large as 300. It is important to emphasize that very accurate solutions for k_0 and T_0 are obtained for much smaller values of N, for example, normalized values of these quantities for N = 8 are 1.121517 and -0.525976, respectively. All the significant figures are presented in Table 7.1 to emphasize that convergence becomes more difficult for higher order coefficients, but also to demonstrate

n	$\frac{k_n^I b^n}{\sigma_0 \sqrt{b}}$				$\frac{T_n^I b^n}{\sigma_0}$	
	Using the closed form solution from (33-36)	Using numerical differentiation of data from (27)	Using power series (37-38) with end points not included	Using power series (37-38) with end points included	Using (39-42)	Using (43-45)
0	1.121522255230	1.12152225523	1.121522256	1.121522255	-0.52596760110	-0.525967601099
1	0.2417745989	0.241774599	0.24177460	0.2417746	-0.19249148	-0.1924914897
2	0.02799	0.0279898	0.0279898	0.0279898	0.0536	0.0535774111
3	?	-0.019298	-0.019298	-0.019298	?	-0.010859509
4		0.00748	0.00748	0.0075		0.89023553E-03
5		-0.0024	-0.0024	-0.002		0.60563208E-03
6		?	?	?		-0.47728107E-03
10						-0.15471344E-04

Table 7.1: Asymptotic coefficients defined by Equations (1) and (2) for an edge crack in a half space.

the accuracy of the numerical approach. Following Kaya and Erdogan [20] the normalized stress intensity factor as presented by Koiter [24] has been evaluated to thirteen significant figures as 1.121522255231, which shows that the current numerical solution provides a stress intensity factor that is correct to twelve digits.

The results for the T stress coefficients in the fifth and sixth columns of Table 7.1 were obtained from the normal stress components. The x-component of the displacement of the crack surfaces in (8) along with (B.16) gave identical results as those presented in the fifth column of Table 7.1. What was not expected was the ease with which the T_n coefficients could be obtained using the method given by Equations (43-45), which easily provided upwards of thirty coefficients. The closed form approches for both k_n in the first column of Table 7.1 and T_n in the fifth column lead to numerical error more quickly than the more numerically obtained results. A convergence study comparing the approaches for the determination of k_2 and T_2 is presented in Table 7.2.

N	$k_2 b^2/(\sigma_0\sqrt{b})$			$T_2 b^2/(\sigma_0)$	
	From (33-36)	$O(h^6)$ Numerical differentiation	Power series (37-38), endpoints not included	From (39-42)	From (43-45)
10	0.0311062	0.031104977	0.038082462	0.040545	0.05357817283
30	0.0279259	0.027765697	0.027973921	0.054450	0.05357741160
60	0.0279903	0.027990507	0.027988724	0.053565	0.05357741101
90	0.0279909	0.027989754	0.027989636	0.053532	0.05357741109
120	0.0279902	0.027989964	0.027988228	0.053554	0.05357741109
180	0.0279896	0.027989828	0.027989900	0.053587	0.05357741109
210	0.0279894	0.027989831	0.027989812		0.05357741109
240		0.027989830	0.027989796		0.05357741109
270		0.027989830	0.027989839		0.05357741109
300		0.027989830	0.027989826		0.05357741109

Table 7.2: Convergence study of asymptotic coefficients for n = 2 from Table 7.1.

These results show the difficulty with the closed form expressions, (33-36) and (39-42) for n = 2 when a large value of N is used. There is no such difficulty for this example for n = 0 or n = 1.

In order to show how the series (30) represents the crack opening displacement, the results in Figure 7.2 include the numerically determined crack opening displacement from (29) along with one, two- and three-term representations from (30). In normalized form, taking into account the first three asymptotic k_n-terms and the relationship between x and s provided by (26), (30) becomes

$$\frac{2\mu}{1+\kappa}\frac{V(x)}{\sigma_0}\frac{1}{\sqrt{2b(b-x)}} = \frac{k_0}{\sigma_0\sqrt{b}} - \frac{1}{3}\frac{k_1 b}{\sigma_0\sqrt{b}}\frac{2(b-x)}{b} + \frac{1}{5}\frac{k_2 b^2}{\sigma_0\sqrt{b}}\left[\frac{2(b-x)}{b}\right]^2 + \cdots \quad (49)$$

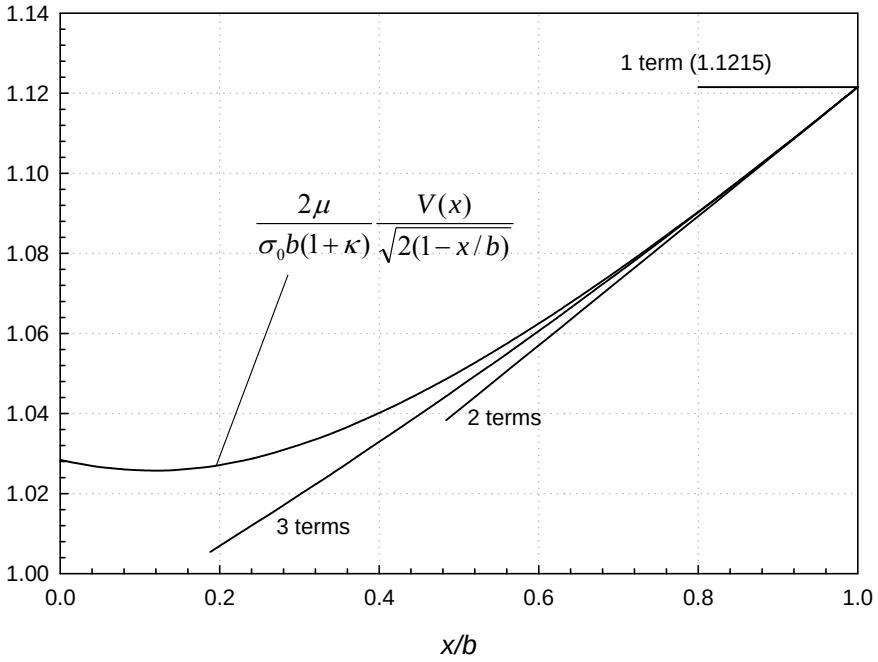

Figure 7.2: Comparison of asymptotic expressions of the crack opening displacement (49) with the full-field solution for an edge crack in a half-space. The k_n coefficients of the asymptotic expansions are listed in Table 7.1.

The companion results in Figure 7.3 are for the stress parallel to the crack determined from (7) using (20) and (22). The asymptotic form is given by (B.15), which in normalized form for the first three T-terms is

$$\frac{\sigma_x(x,0)}{\sigma_0} = \frac{T_0}{\sigma_0} - \frac{T_1 b}{\sigma_0}\frac{2(b-x)}{b} + \frac{T_2 b^2}{\sigma_0}\left[\frac{2(b-x)}{b}\right]^2 + \cdots . \tag{50}$$

These results give an indication of the region over which an asymptotic expression can be used to approximate the full field in the limit as the crack tip is approached. For example, from Equation (50) the following shows how the single term representation for the σ_x stress on the crack surface, i.e., $\sigma_x(x,0) = T_0$, improves as T_1/T_0 decreases:

$$\frac{\sigma_x(x,0)}{T_0} = 1 - \frac{T_1}{T_0} 2(b-x) + \frac{T_2}{T_0}\left[2(b-x)\right]^2 + \cdots . \tag{51}$$

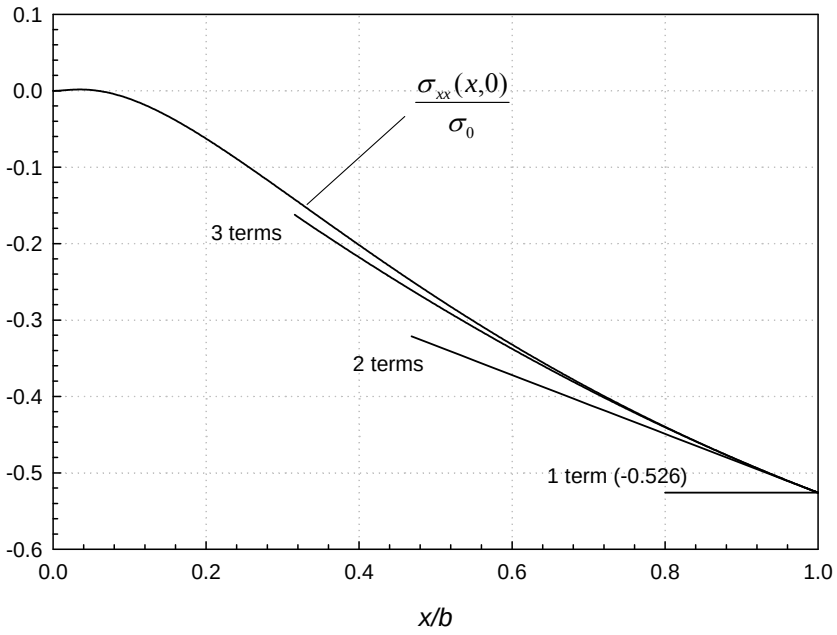

Figure 7.3: Comparison of asymptotic expressions of the stress parallel to the crack flanks (50) with the full-field solution for an edge crack in a half-space. The T_n coefficients of the asymptotic expansions are listed in Table 7.1.

Similarly, in the limit as the crack tip is approached, the size of the two-term asymptotic zone for this case increases as T_2/T_1 becomes smaller, which is demonstrated by rearrangement of (50) to give:

$$-\frac{\sigma_x(x,0) - T_0}{T_1 2(b-x)} = 1 - \frac{T_2}{T_1}\left[2(b-x)\right] + \cdots . \tag{52}$$

A difficulty to be investigated later is that the practical application of these asymptotic solutions does not involve this limit, but rather applies "near" the crack tip. In this case the higher order terms, which can be discarded in the above limit, become involved.

7.3.2. Internal crack in a half space.

For the case of an internal crack there is an additional length parameter, as both the length and location of the crack must be specified. In this study the nondimensional parameter a/(b-a) is used to define the crack geometry. The asymptotic coefficients at both crack tips for a range of this value are presented in Table 7.3 for uniform tension.

$\frac{a}{b-a}$	n	$\frac{k_n(a)(b-a)^n}{\sigma_0\sqrt{\frac{b-a}{2}}}$	$\frac{k_n(b)(b-a)^n}{\sigma_0\sqrt{\frac{b-a}{2}}}$	$\frac{T_n(a)(b-a)^n}{\sigma_0}$	$\frac{T_n(b)(b-a)^n}{\sigma_0}$
0	0		1.5861		-0.5260
	1		0.3419		-0.1925
	2		0.03958		0.0536
0.001	0	6.4879	1.3811	-82.666	-0.7310
0.01	0	2.8820	1.3009	-11.9911	-0.8135
	1	-3.6145	0.5678	-78.5983	-0.01498
	2	-1593.2	-0.09116	5433.4	-0.03451
0.1	0	1.4637	1.1626	-2.2989	-0.9516
	1	1.4495	0.68295	-2.2078	0.04827
	2	-5.4113	-0.1530	5.3678	-0.04847
1.0	0	1.0345	1.0246	-1.0525	-1.0124
	1	0.7928	0.7563	-0.03140	0.01109
	2	-0.15525	-0.1627	-0.005743	-0.003148
$\rightarrow \infty$	0	1	1	-1	-1
	1	3/4	3/4	0	0
	2	-5/32	-5/32	0	0

Table 7.3: Asymptotic coefficients for an internal crack in a half space.

It is observed that as the crack tip approaches the free surface, the higher order coefficients for both the k and the T series increase in magnitude. For example, for a/(b – a) = 0.01 and n=2, the normalized values at the left crack tip at x = a are $k_2 = -1593$ and $T_2 = 5433$. The result of this is a diminishing zone of convergence for the asymptotic series at the left crack tip, which results in a smaller zone where the stress intensity factor is dominant. The important point is that the values of the coefficients in Table 7.3 quantify this loss of dominance, which leads to a breakdown in the application of linear elastic fracture mechanics. A graphical representation of this behavior for

the crack opening displacement is presented in Figure 7.4. The steep slope at the left crack tip in Figure 7.4 (top) for decreasing a/(b - a) illustrates this breakdown. This point is further reinforced in Figure 7.4 (bottom) by the small zone within which the asymptotic expressions match the numerical curve. In Figure 7.5 the normal stress parallel to the crack flanks is presented which shows the same difficulties

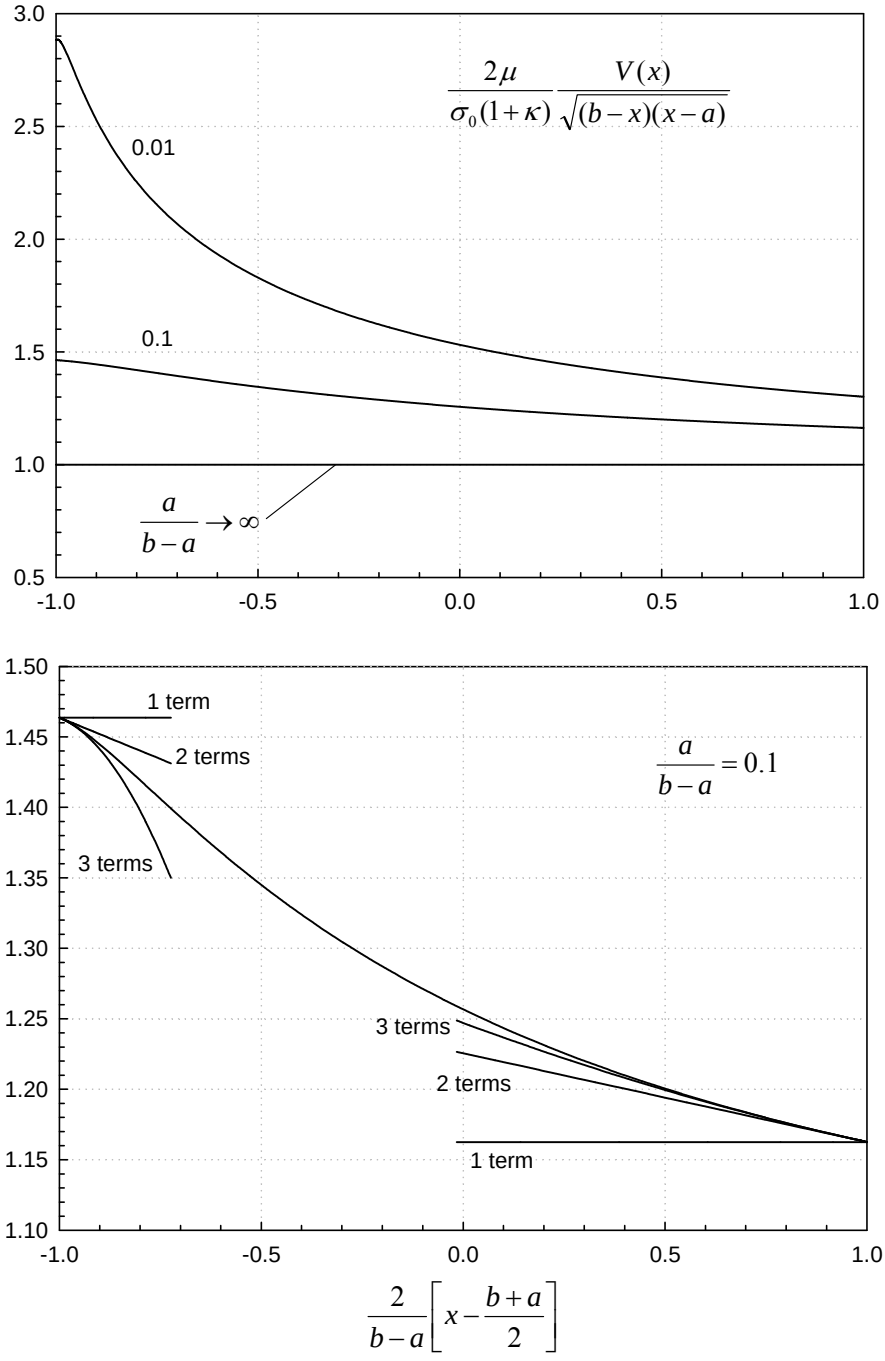

Figure 7.4: Normalized crack opening displacement for an internal crack in a half space subjected to uniform tension at infinity. In the lower figure a comparison of asymptotic expressions (53a) with the full field solution at both crack tips for *a/(b-a) = 0.1* is presented. The k_n coefficients of the asymptotic expansions are listed in Table 7.3.

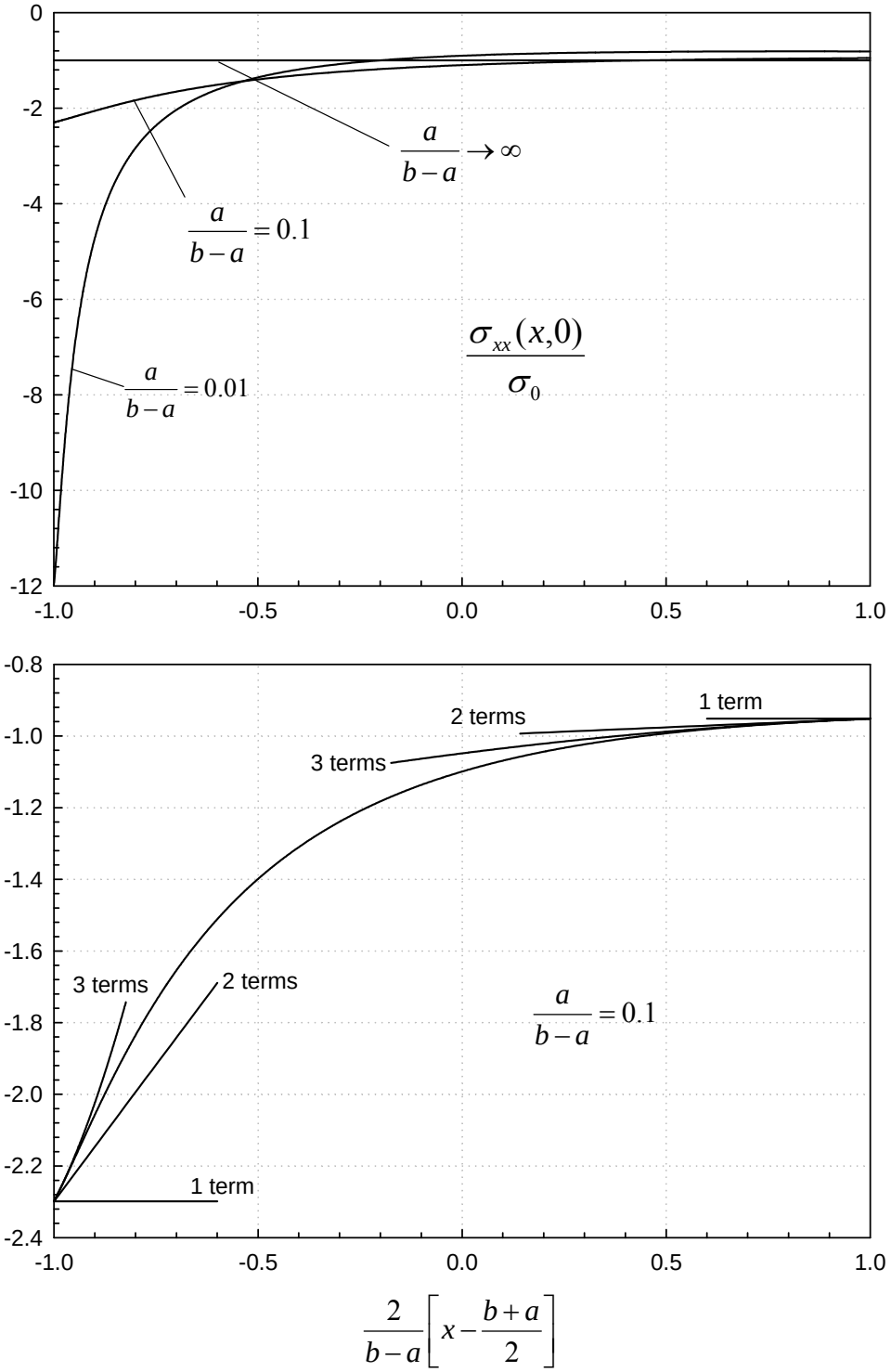

Figure 7.5: Same as Figure 7.4 for the T-stress using (53b).

indicated by Figure 7.4. The asymptotic expressions at the right crack tip (x = b) again represent the solution better than the expressions at the left crack tip (x = a). The expressions for the crack tips at a (s = -1) and b (s = 1) are respectively,

$$\frac{2\mu}{\sigma_0(1+\kappa)}\frac{V(x)}{\sqrt{(b-x)(x-a)}} = k_0 + \left(\frac{-k_1}{3}+\frac{k_0}{4}\right)(1\pm s)+\left(\frac{k_2}{5}-\frac{k_1}{12}+\frac{3k_0}{32}\right)(1\pm s)^2+\cdots .$$

$$\frac{\sigma_x(x,0)}{\sigma_0} = \frac{T_0}{\sigma_0} - \frac{T_1(b-a)}{\sigma_0}(1\pm s)+\frac{T_2(b-a)^2}{\sigma_0}(1\pm s)^2+\cdots . \qquad (53a,b)$$

7.3.3. Edge crack in a finite width strip.

For the case of a crack in an infinite strip (Figure 7.1b), the kernels K(x,t) and L(x,t) are presented in Appendix C. For this crack problem Sham [11] has presented stress intensity factors and the T-stress for both tension and bending and Karihaloo and Xiao [17] have reported the first five coefficients in bending. Both studies are based on the finite element method. The data in Table 7.4 provides a comparison of selected results from these authors with those of the current approach. In the current study the strip is infinite in the vertical direction (Figure 7.1b), while in the other studies the values correspond to cases where the height is large, but finite. Based on the studies by Civelek and Erdogan [25] and Isida [26], who quantify the effect of height on stress intensity factors, the three methods should agree to the number of digits presented for the stress intensity factor. It is noted that great care has been taken in the current study to provide exact values of all the coefficients for the number of significant figures presented. Accuracy and the ability to do deep cracks are the strengths of the proposed method. Given this, all three sets of results agree to reasonable accuracy. In addition to tension and bending, in this study as in the study by Cordes and Joseph [27], the crack surface loading is given by

$$\sigma_{yy}(x,0)/\sigma_m = (1-2x/h)^m,\ m = 0,1,2,3. \qquad (54)$$

The stress used for normalization is identical to that given in equations (10) and (26) except that σ_m replaces σ_0. Furthermore, the loadings per unit thickness in Figure 7.1b for tension and bending are respectively given by

$$\sigma_0 = N/h, \quad \sigma_1 = 6M/h^2. \tag{55}$$

Coefficients	$b/h = 0.2$			$b/h = 0.6$		
	Current method	Ref. [17]	Ref.[11]	Current method	Ref. [17]	Ref. [11]
$k_0/(\sigma_0\sqrt{b})$	1.0553	1.0548	1.0534	1.9140	1.9115	1.9110
T_0/σ_0	-0.2382	-0.2389	-0.24072	0.8339	0.8330	0.82751
$k_1 b/(\sigma_0\sqrt{b})$	-0.1112	-0.1094	-	-2.9719	-2.9636	-
$T_1 b/\sigma_0$	0.01899	0.01807	-	1.1199	1.1191	-
$k_2 b^2/(\sigma_0\sqrt{b})$	-0.05056	-0.05041	-	0.9887	0.9874	-

Table 7.4: Comparison of the first five asymptotic coefficients for the case of an edge crack in a strip subjected to pure bending (see B.3) for conversion of coefficients).

The results for the first six coefficients are presented in Tables 7.5, 7.6, 7.7 and 7.8, respectively for tension, bending, quadratic and cubic loadings [19]. While the difficulty with convergence increases with crack depth, all the digits presented in these tables are believed to be correct. Superposition of loadings represented by values in these tables leads to stress and displacement field solutions near a crack tip under rather general loading conditions that are valid well beyond the k-dominant zone. Once again the T_n coefficients for $n > 1$ can easily be obtained for large n using (45), for example, for tensile loading and b/h = 0.8, $b^{30}T_{30}/\sigma_0 = 1168.06$ is obtained for N = 14 and higher. It is noted that for the prediction of k_n, $N > n$ is required, whereas there is no such constraint for the T_n coefficients.

b/h	$\frac{k_0^I}{\sigma_0\sqrt{b}}$	$\frac{T_0^I}{\sigma_0}$	$\frac{k_1^I b}{\sigma_0\sqrt{b}}$	$\frac{T_1^I b}{\sigma_0}$	$\frac{k_2^I b^2}{\sigma_0\sqrt{b}}$	$\frac{T_2^I b^2}{\sigma_0}$
0.0	1.1215	-0.5260	0.2418	-0.1925	0.02799	0.05358
0.1	1.1892	-0.5502	0.2460	-0.19865	0.02762	0.05687
0.2	1.3673	-0.5890	0.21695	-0.1994	0.02018	0.06456
0.3	1.6599	-0.6103	0.08426	-0.1754	-0.00717	0.07754
0.4	2.1114	-0.57825	-0.2873	-0.09055	-0.09324	0.11284
0.5	2.8246	-0.4217	-1.2293	0.1617	0.3742	0.25254
0.6	4.0331	0.03814	-3.6968	0.9509	-1.3954	0.89892
0.7	6.3549	1.3614	-11.1150	3.8845	-5.9297	4.5399
0.8	11.9553	6.0073	-41.20845	19.3849	-35.824	35.8374
0.9	34.6311	35.7416	-297.651	213.71	-565.27	850.24
0.95	99.111	166.27	-1875.8	1971.7	-7429	16267

Table 7.5: Asymptotic coefficients for an edge crack in a strip for uniform tension.

b/h	$\frac{k_0^I}{\sigma_1\sqrt{b}}$	$\frac{T_0^I}{\sigma_1}$	$\frac{k_1^I b}{\sigma_1\sqrt{b}}$	$\frac{T_1^I b}{\sigma_1}$	$\frac{k_2^I b^2}{\sigma_1\sqrt{b}}$	$\frac{T_2^I b^2}{\sigma_1}$
0.0	1.1215	-0.5260	0.2418	-0.1925	0.02799	0.05358
0.1	1.0472	-0.3779	0.07967	-0.089525	-0.00834	0.05594
0.2	1.0553	-0.2382	-0.1112	0.01899	-0.05056	0.06149
0.3	1.1241	-0.07917	-0.3773	0.14665	-0.1070	0.06994
0.4	1.2606	0.1208	-0.7909	0.3138	-0.20045	0.09220
0.5	1.4972	0.3975	-1.51245	0.5772	0.4048	0.17588
0.6	1.9140	0.8339	-2.9719	1.1199	-0.9887	0.52900
0.7	2.7252	1.67525	-6.6091	2.6732	-3.1930	2.3040
0.8	4.6764	3.92685	-19.3927	9.5642	-15.931	15.7808
0.9	12.4615	15.8050	-116.042	84.495	-215.67	324.54
0.95	34.299	63.197	-674.06	713.06	-2644	5792

Table 7.6: Asymptotic coefficients for an edge crack in a strip for bending.

b/h	$\frac{k_0^I}{\sigma_2\sqrt{b}}$	$\frac{T_0^I}{\sigma_2}$	$\frac{k_1^I b}{\sigma_2\sqrt{b}}$	$\frac{T_1^I b}{\sigma_2}$	$\frac{k_2^I b^2}{\sigma_2\sqrt{b}}$	$\frac{T_2^I b^2}{\sigma_2}$
0.0	1.1215	-0.5260	0.2418	-0.1925	0.02799	0.05358
0.1	0.9268	-0.2428	-0.04008	-0.02112	-0.01973	0.04498
0.2	0.8362	-0.03797	-0.2539	0.07443	-0.02331	0.01856
0.3	0.82015	0.1116	-0.4320	0.10396	0.01158	-0.02634
0.4	0.8822	0.2187	-0.6204	0.08060	0.06914	-0.08153
0.5	1.05146	0.3056	-0.9299	0.04403	0.09723	-0.11262
0.6	1.4036	0.4321	-1.6817	0.1283	-0.1001	0.03128
0.7	2.1432	0.7888	-4.0254	0.8943	-1.4777	1.2235
0.8	3.99085	2.2079	-13.88915	5.8774	-11.3925	11.8185
0.9	11.5432	11.9773	-99.2168	70.673	-188.12	284.13
0.95	33.037	55.435	-625.2	656.90	-2476	5424

Table 7.7: Asymptotic coefficients for an edge crack in a strip for quadratic loading.

b/h	$\frac{k_0^I}{\sigma_3\sqrt{b}}$	$\frac{T_0^I}{\sigma_3}$	$\frac{k_1^I b}{\sigma_3\sqrt{b}}$	$\frac{T_1^I b}{\sigma_3}$	$\frac{k_2^I b^2}{\sigma_3\sqrt{b}}$	$\frac{T_2^I b^2}{\sigma_3}$
0.0	1.1215	-0.5260	0.2418	-0.1925	0.02799	0.05358
0.1	0.8245	-0.1374	-0.1246	0.01863	-0.01623	0.02999
0.2	0.6794	0.07350	-0.3018	0.06356	0.02463	-0.01621
0.3	0.6358	0.1711	-0.38125	0.02184	0.08851	-0.04962
0.4	0.6788	0.2088	-0.4647	-0.02464	0.1052	-0.02742
0.5	0.8143	0.2491	-0.7068	0.02751	-0.02393	0.11355
0.6	1.07904	0.3842	-1.4243	0.3549	-0.5089	0.5266
0.7	1.5909	0.8039	-3.5377	1.4537	-2.1272	1.9104
0.8	2.7870	2.15025	-11.2764	5.9463	-10.2073	10.3468
0.9	7.4743	9.3734	-69.4838	51.337	-130.37	195.30
0.95	20.580	37.880	-404.4	428.48	-1587	3474

Table 7.8: Asymptotic coefficients for an edge crack in a strip for cubic loading.

In all loading cases the T-stress is negative for short cracks and positive for long cracks. Betegon and Hancock [5] demonstrated the importance of the sign of the T-stress by showing how the stress field very close to the crack tip is sensitive to negative T-stress when material yielding is taken into account. The k_1 coefficient has the opposite trend as the T-stress, being positive for small cracks and becoming negative for large cracks. The second T coefficient has a similar trend as the T-stress except for the case of cubic loading. The results of these sign changes of coefficients can be visualized by plotting the normal stresses ahead of the crack tip. In

Figures 7.6-7.8, for uniform tension and b/h = 0.1, 0.3 and 0.8, respectively, both σ_x and σ_y are compared to the asymptotic expressions using the coefficients from Table 7.5. In order to avoid infinite values of this stress, the stress is multiplied by the square root of r in such a way that the value of this quantity at the crack tip location is the stress intensity factor. The resulting expressions from (B.10) and (B.11) are

$$\sqrt{2r}\sigma_{xx}(x,0) = k_0 + T_0\sqrt{2r} + k_1(2r) + \dots , \tag{56a}$$

$$\sqrt{2r}\sigma_{yy}(x,0) = k_0 + k_1(2r) + \dots , \tag{56b}$$

where r = x – b. In the case of σ_x, both the k and T coefficients are required in the expansion. The insert in Figure 7.6a shows clearly how the higher the order of the expansion, the better the agreement with the full-field solution in the limit as r approaches zero. As long as r is "small enough," the asymptotic solutions improve as the order of the expansion increases. However, from a practical point of view, it is possible that the behavior of the solutions beyond such values of r is important. For example, in Figures 7.6a and 7.7a, note how the 2-term expressions follow the full-field curves so well, beyond the expected range of applicability. In these cases the T-stress is negative. However, in Figure 7.8a, which is for a deep crack, this 2-term expansion becomes very poor when the T-stress is positive since k_1 is negative and large in magnitude. This would indicate that the kT-dominant zone becomes much smaller, and that at least three terms are required to have a reasonable approximation of the stress for deep cracks. This issue of an expansion "getting lucky" will be duscussed further within the context of additional results. The effect of the sign

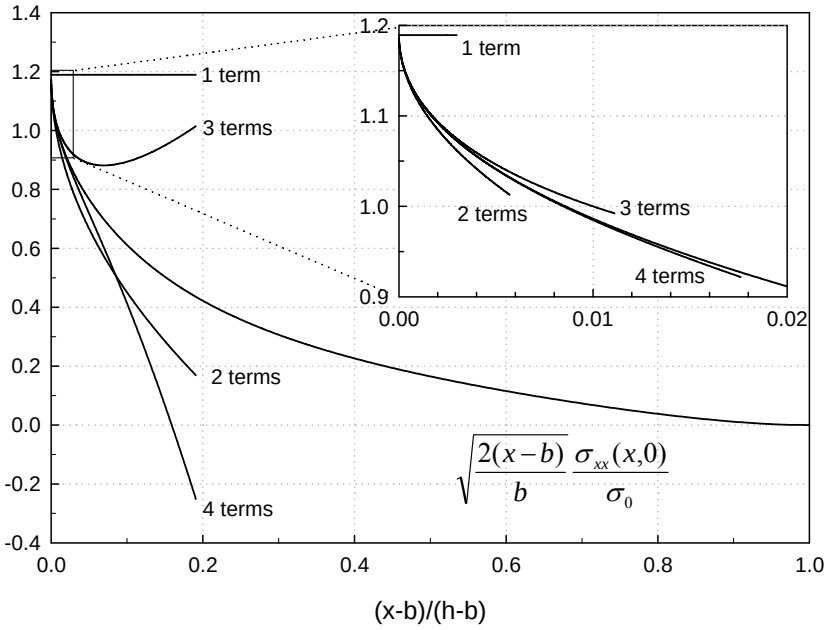

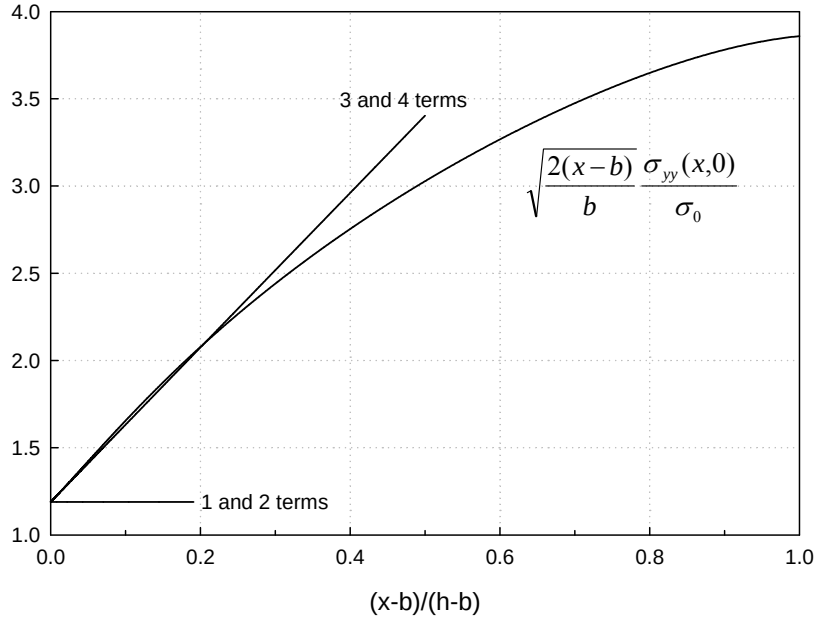

Figure 7.6: Comparisons are made between the full-field solution and the asymptotic solutions (56) for an edge crack with a crack depth *b/h = 0.1*, when subjected to uniform tension. The upper figure is for σ_x and the lower for σ_y. The coefficients are listed in Table 7.5.

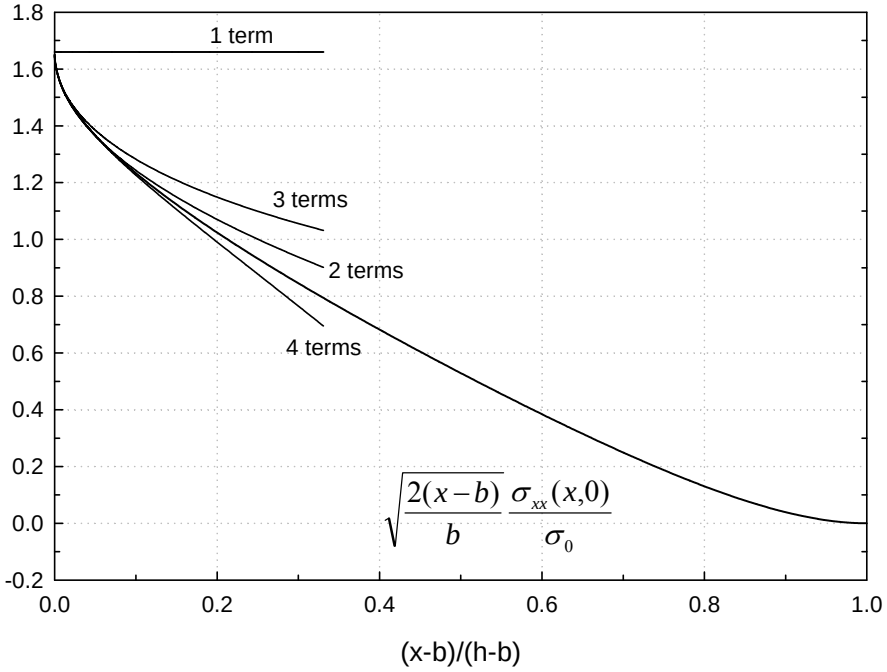

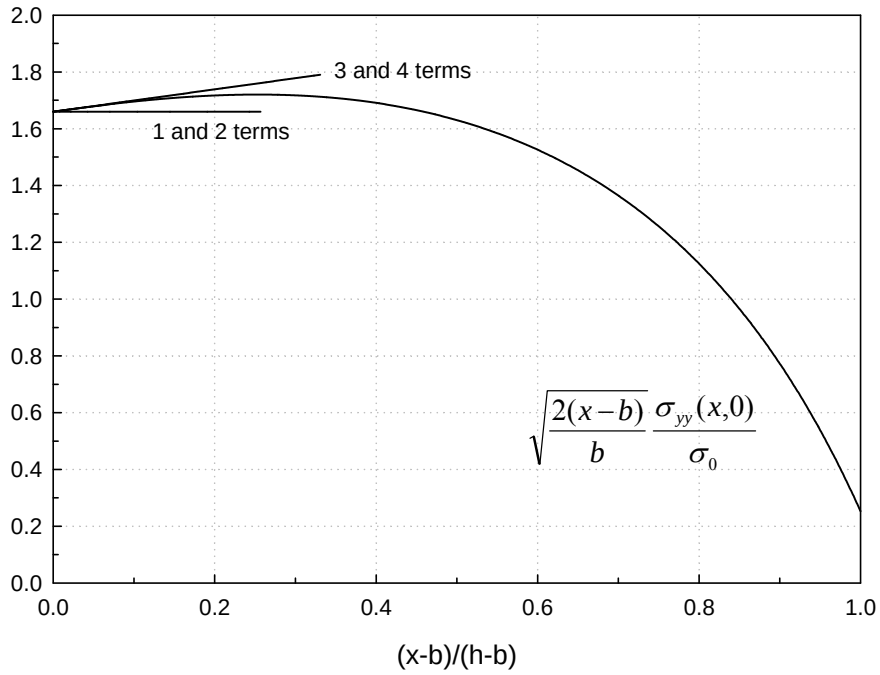

Figure 7.7: Same as Figure 7.6 for *b/h = 0.3*.

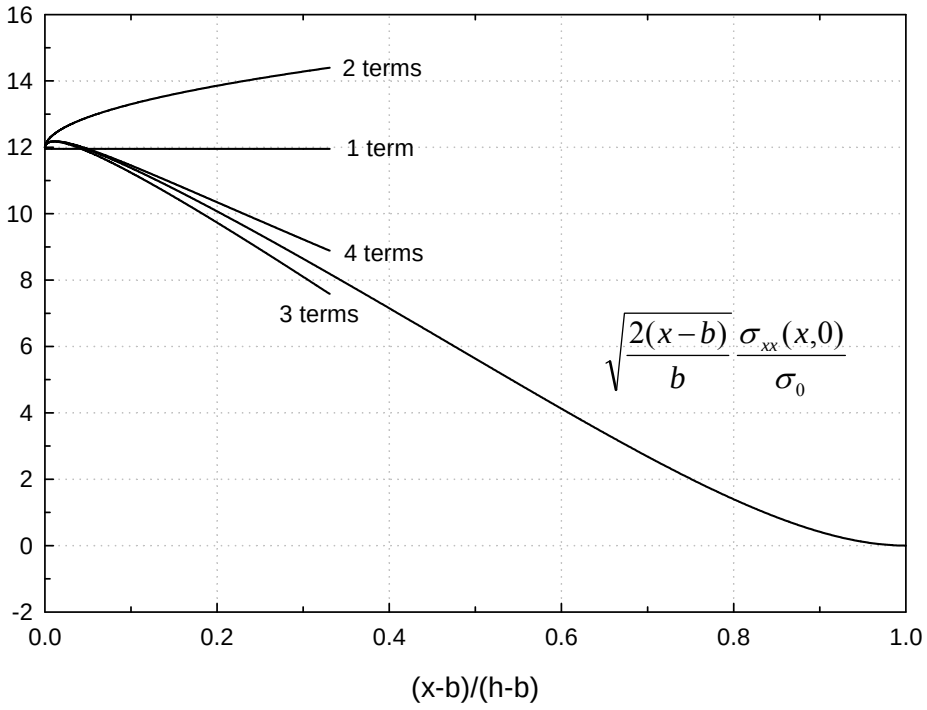

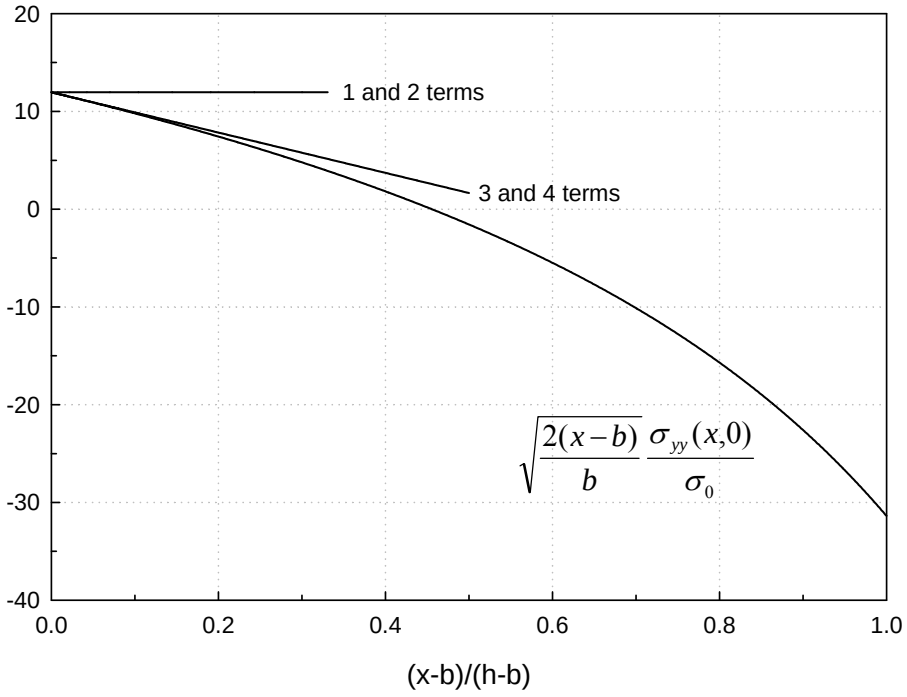

Figure 7.8: Same as Figure 7.6 for *b/h = 0.8*.

change in k_1 can be observed in Figures 7.6b, 7.7b and 7.8b, since from (56b) σ_y along the y = 0 line does not include the T_n coefficients.

In order to see how the asymptotic approximations vary in the angular coordinate, θ, in Figures 7.9a-c and 7.10a-c the equivalent stress,

$$\sigma_e = \frac{1}{\sqrt{2}}\left[(\sigma_{rr}-\sigma_{\theta\theta})^2+(\sigma_{rr}-\sigma_{zz})^2+(\sigma_{\theta\theta}-\sigma_{zz})^2+6(\tau_{r\theta}^2+\tau_{rz}^2+\tau_{\theta z}^2)\right]^{1/2}, \qquad (57)$$

is compared to asymptotic expressions for one, two, three and four terms. The loading used for these figures is uniform tension. Assumming conditions of plane strain, where in terms of the Poisson's ratio, ν,

$$\sigma_{zz} = \nu(\sigma_{rr}+\sigma_{\theta\theta}), \qquad (58)$$

the first three terms of the expansion of the equivalent stress are given by

$$\sigma_e(r,\theta) = \frac{k_0^I}{4\sqrt{r}}\sqrt{4(1-2\nu)^2(1+\cos\theta)+6\sin^2\theta}+\frac{T_0^I}{4}\frac{3\cos\frac{5\theta}{2}+\cos\frac{\theta}{2}(1-16\nu+16\nu^2)}{\sqrt{2(1-2\nu)^2(1+\cos\theta)+3\sin^2\theta}}$$

$$+\left\{\frac{T_0^I T_0^I}{4k_0^I}\frac{8(1-\nu+\nu^2)}{\sqrt{4(1-2\nu)^2(1+\cos\theta)+6\sin^2\theta}}-\frac{T_0^I T_0^I}{4k_0^I}\frac{\left(3\cos\frac{5\theta}{2}+\cos\frac{\theta}{2}(1-16\nu+16\nu^2)\right)^2}{\left(4(1-2\nu)^2(1+\cos\theta)+6\sin^2\theta\right)^{3/2}}\right.$$

$$\left.+\frac{k_1^I}{4}\frac{(1+\cos\theta)(5-32\nu+32\nu^2)+3+3\cos(3\theta)}{\sqrt{4(1-2\nu)^2(1+\cos\theta)+6\sin^2\theta}}\right\}\sqrt{r}+O(r). \qquad (59)$$

Three values of the Poisson's ratio are used in each of Figures 7.9 and 7.10, which correspond to cases a, b and c. These values are respectively, ν = 0.0, 0.3 and 0.5. The plane stress result for

the equivalent stress corresponds to $\nu = 0$. In Figures 7.9a-c the crack depth is b/h = 0.1 and the stress is evaluated at r/b = 0.3, where r and b are defined in Figure 7.1. Figures 7.9a-c show how in general the comparison improves as more terms are taken, although this is not necessarily true for all values of theta at such a large value of r/b. It is also important to realize that the asymptotic solutions can be good for some values of theta and very poor for others. In Figures 7.10a-c, a very deep crack is considered using the parameters, b/h = 0.8 and r/b = 0.06. In this case it can be observed how the third term is important at even a relatively small value of r/b. A few general observations can be made based on an examination of (59) for the important case of ductile metals with $\nu = 0.3$ using constants from Tables 7.5 and 7.6. The k-dominant zone is larger for plane stress than for plane strain for all crack depths. This is concluded by considering the ratio of the second term of (59) to the first. Also, for deep cracks, which corresponds to b/h larger than about 0.5, the kt-dominant zone is larger for plane strain ($\nu = 0.3$) than for plane stress. This is determined based on a ratio of the third term of (59) to the sum of the first two terms. Relative to the contribution of the leading term, a positive T-stress will increase the effective stress in front of the crack tip at $\theta = 0$, while in the region of maximum effective stress, which occurs at $\theta = \arccos\left((1-2\nu)^2/3\right)$, a positive T-stress will decrease the effective stress. A negative T-stress has the opposite trend. Following the study by Betegon and Hancock [5], a negative T-stress tends to promote crack tip plasticity which makes the material appear to have a higher fracture toughness. Similarly, in the study by Larsson and Carlsson [3], a negative T-stress has a larger plastic zone indicating a more effective redistribution of stress.

Before considering zones of dominance, one final result is presented in Figure 7.11 that takes advantage of the full-field capability for the determination of stress. In this figure, the stress $\sigma_{yy}(0, y)$ is plotted for y > 0 at the free surface of a half space with an edge crack. The result is

interesting since the maximum compressive stress occurs very near a half crack length away from the crack. This result could be used to estimate an unknown depth of an edge crack that has been located on a surface.

The remaining results quantify the error between the full-field stresses and the asymptotic expressions all around the crack tip. As stated in the Introduction, this is the focus of this study and the reason why the higher order coefficients are of interest. The error measure introduced by Lee and Rosakis [28] is used as follows,

$$e_A = 100\sqrt{\frac{\left(\sigma_{rr}^{FF} - \sigma_{rr}^{A}\right)^2 + \left(\sigma_{\theta\theta}^{FF} - \sigma_{\theta\theta}^{A}\right)^2 + 2\left(\tau_{r\theta}^{FF} - \tau_{r\theta}^{A}\right)^2}{\left(\sigma_{rr}^{FF}\right)^2 + \left(\sigma_{\theta\theta}^{FF}\right)^2 + 2\left(\tau_{r\theta}^{FF}\right)^2}}, A = 1,2,3,4, \qquad (60)$$

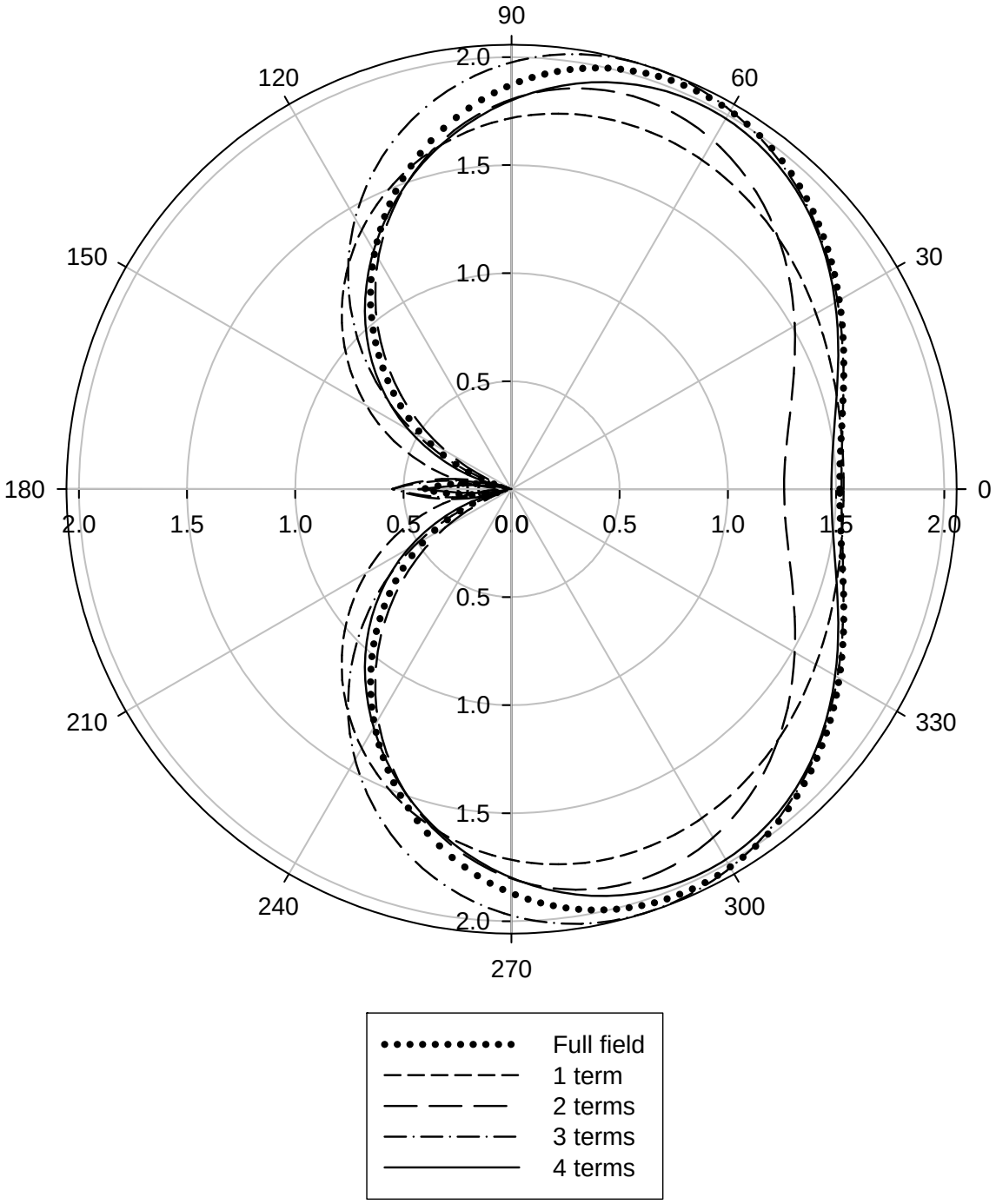

Figure 7.9a: The asymptotic expressions (59) of the normalized equivalent stress, σ_e/σ_0, are compared with the full-field solution all around the crack tip for an edge crack in a strip with a crack depth of *b/h = 0.1* at *r/b = 0.3* for $\nu = 0$. The asymptotic coefficients are listed in Table 7.5.

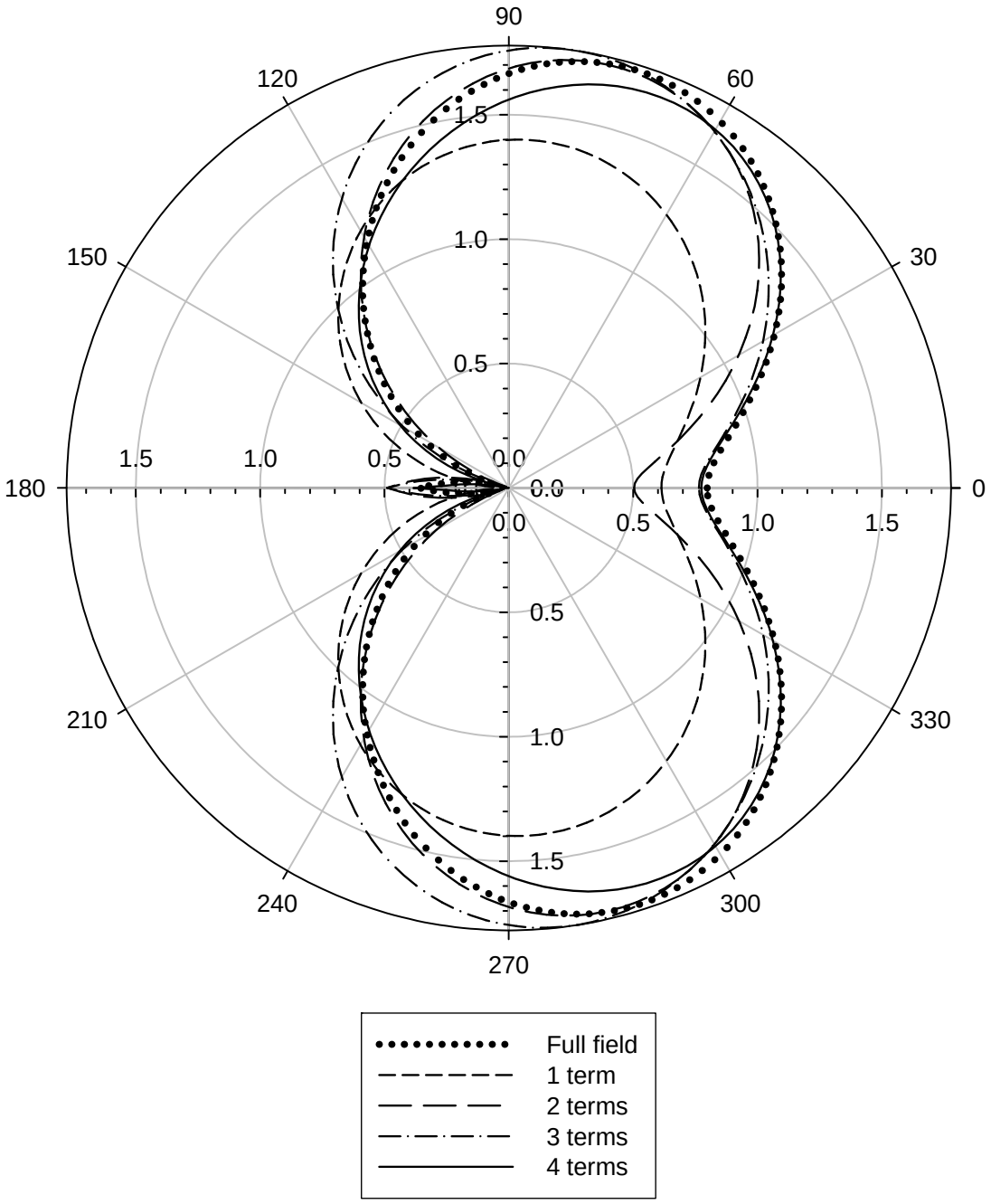

Figure 7.9b: Same as Figure 7.9a for $\nu = 0.3$.

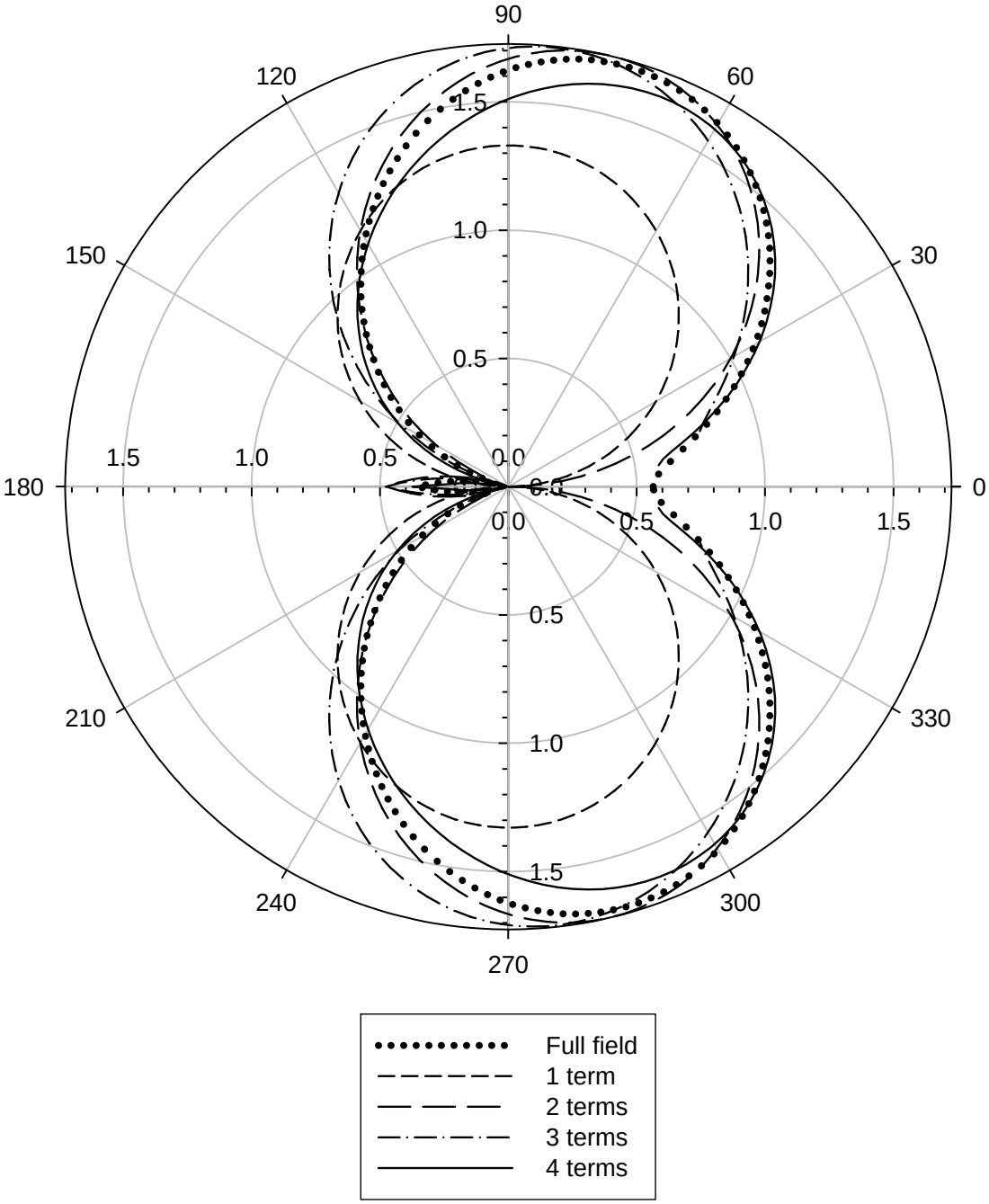

Figure 7.9c: Same as Figure 7.9a for $\nu = 0.5$.

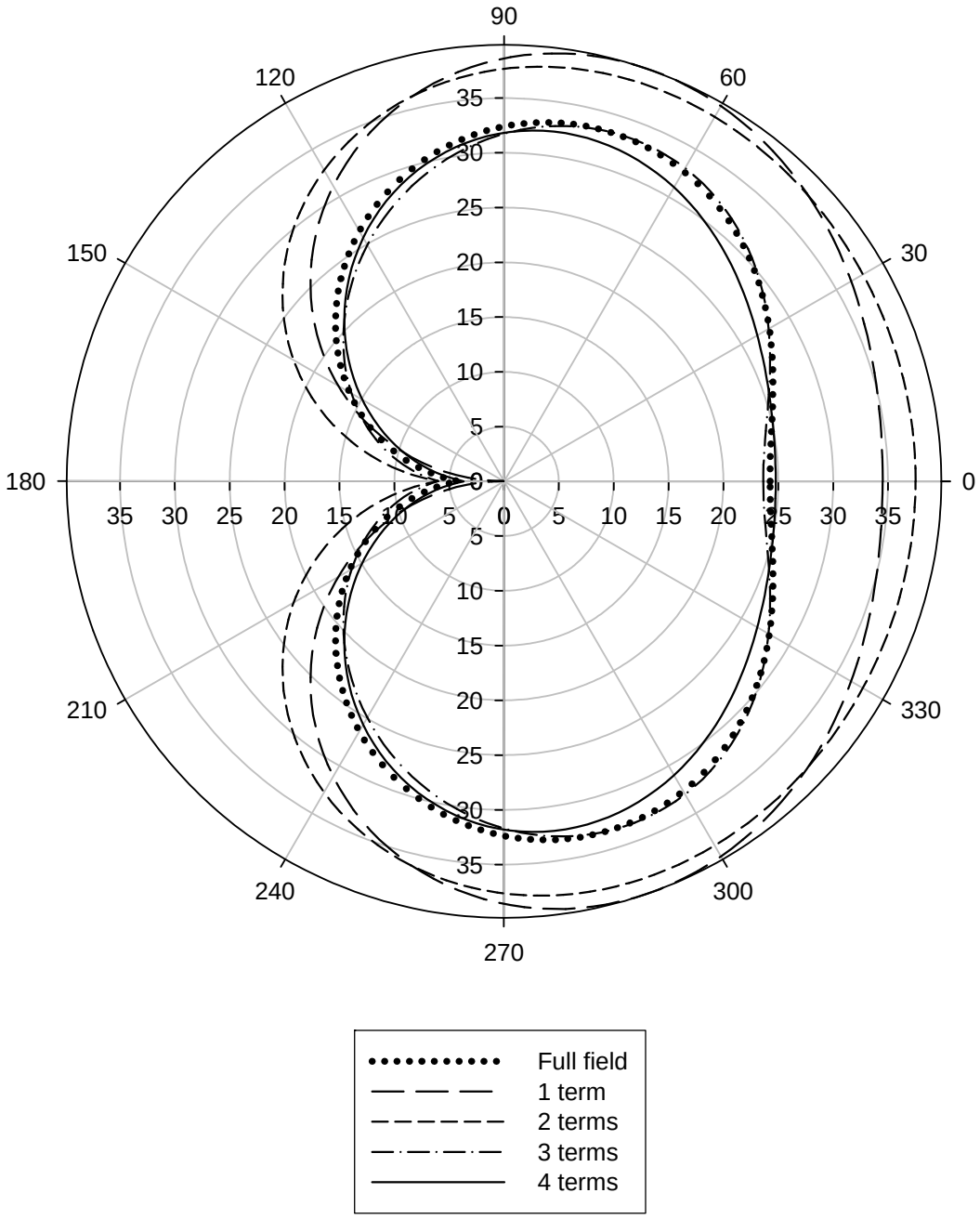

Figure 7.10a: The asymptotic expressions (59) of the normalized equivalent stress, σ_e/σ_0, are compared with the full-field solution all around the crack tip for an edge crack in a strip with a crack depth of *b/h = 0.8* at *r/b = 0.06* for $\nu = 0$. The asymptotic coefficients are listed in Table 7.5.

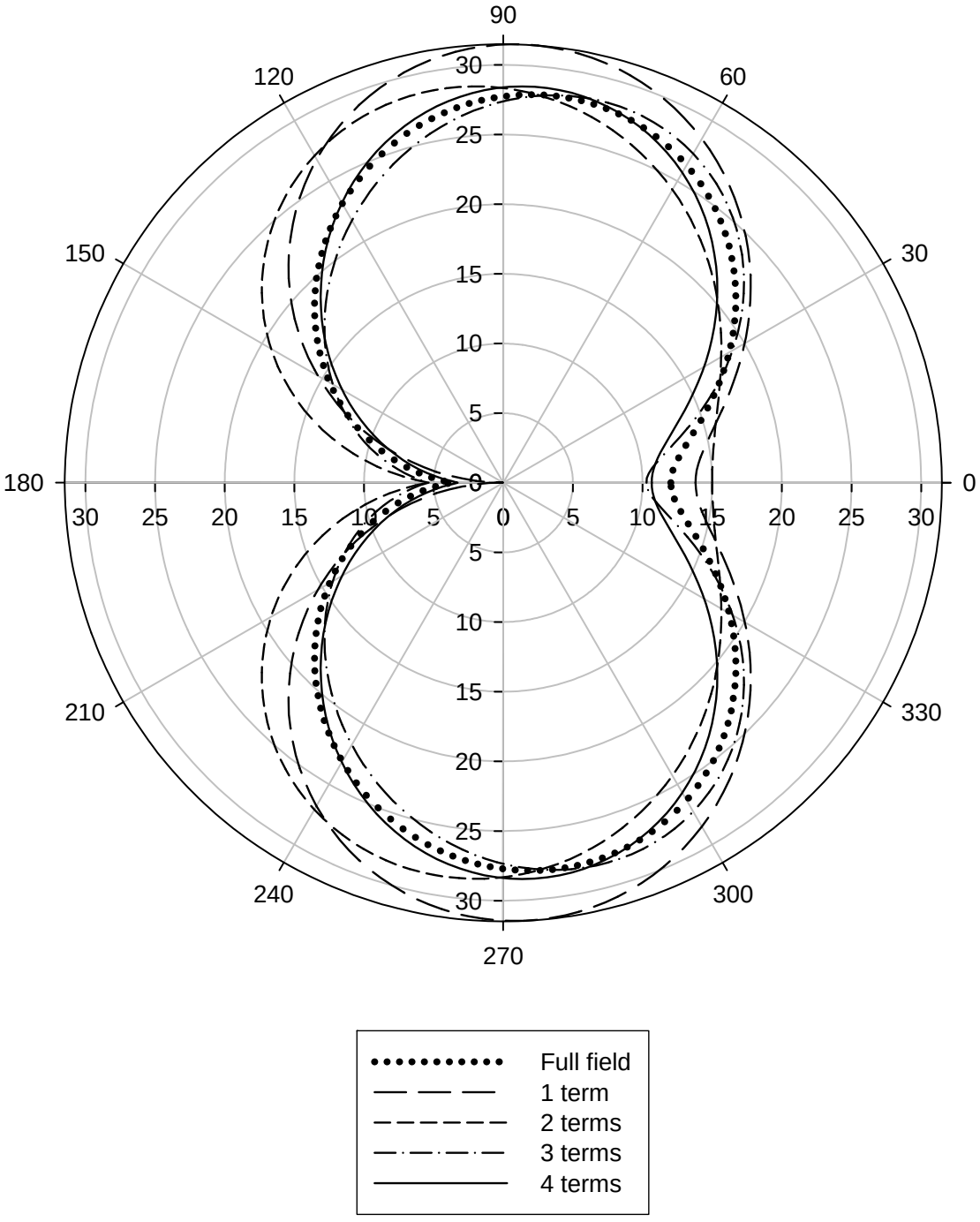

Figure 7.10b: Same as Figure 7.10a for $\nu = 0.3$.

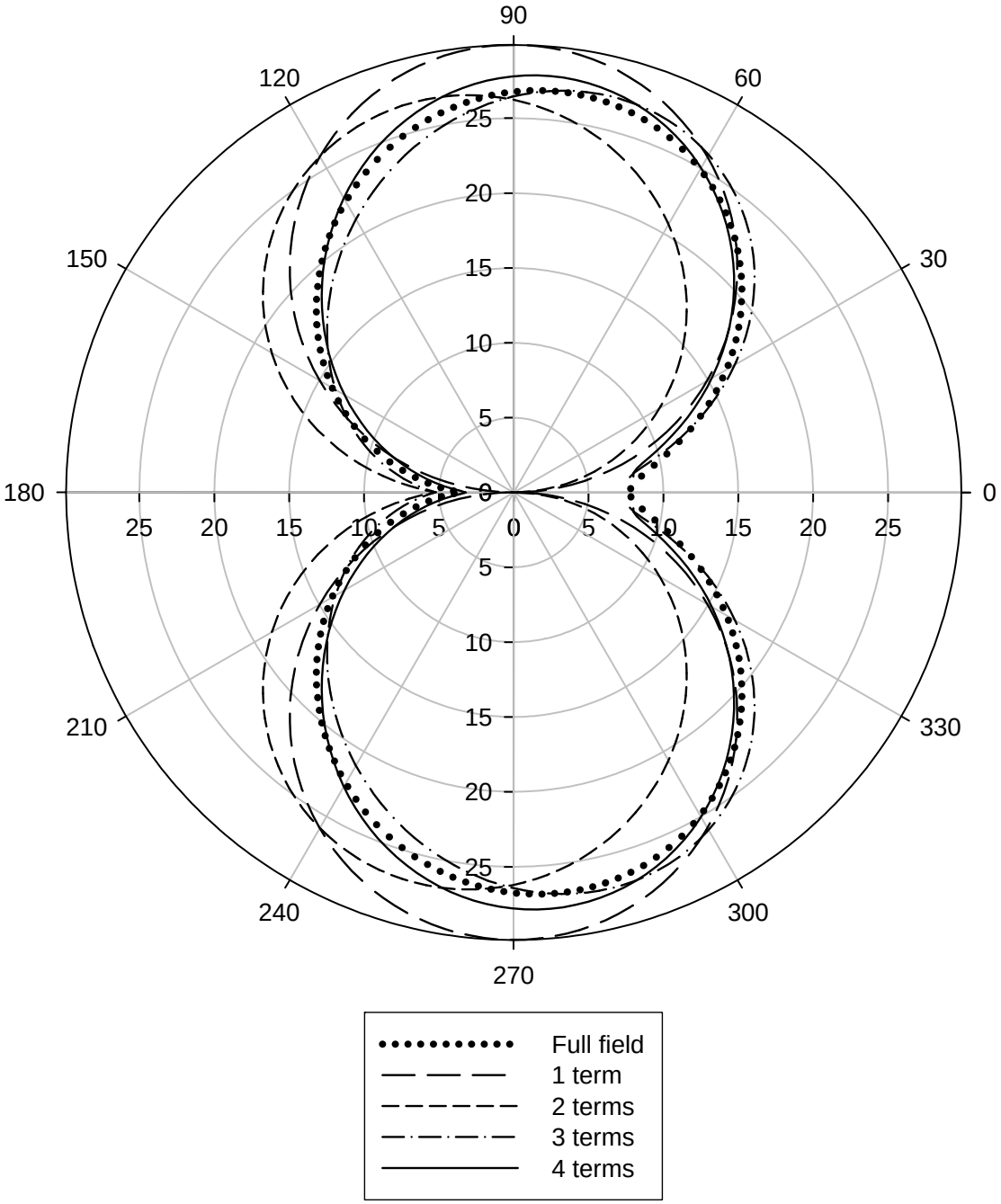

Figure 7.10c: Same as Figure 7.10a for ν = 0.5.

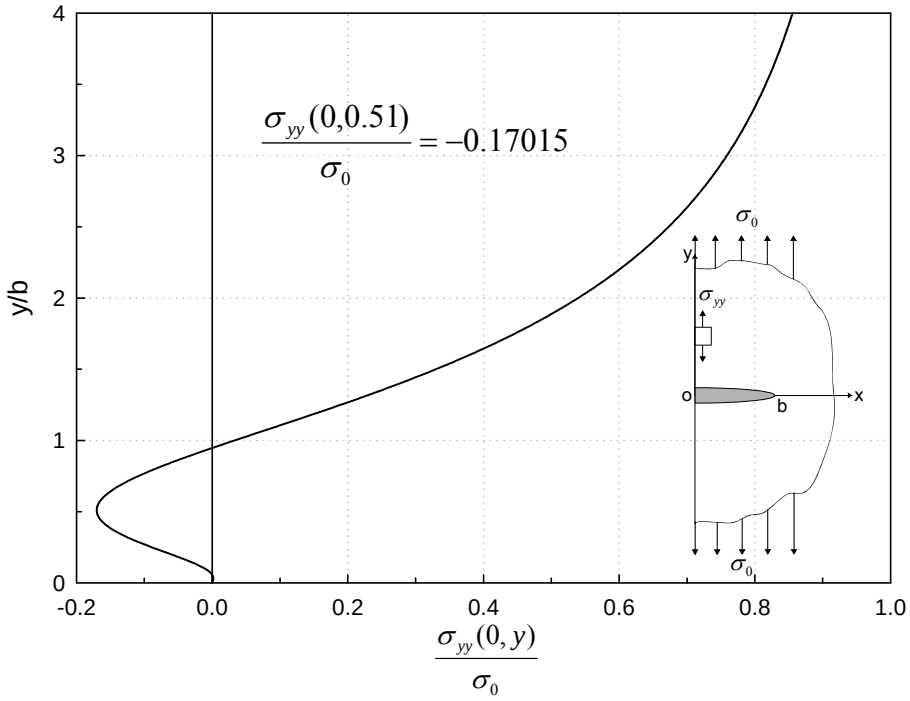

Figure 7.11: The normal stress in the y-direction at the free surface of a half-space with an edge crack subjected to uniform tension.

where the superscript "A" corresponds to asymptotic solutions using 1, 2, 3 and 4 terms and "FF" corresponds to full-field. In Figure 7.12 an error value of 10% is selected for the uniform tension case of an edge crack with b/h = 0.1. This result clearly shows how the match between the full-field expressions and the asymptotic expressions improve as more terms are taken. Furthermore, this plot is representative of a typical result using (60). The multiplicative factor of 2 associated with the shear stress in (60) helps to make this region more circular. Before providing results for other crack geometries, consider the use of (60) when the full-field solution is not available.

In Figure 7.12b the results of Figure 7.12a are approximated by replacing the full-field solution with a six-term asymptotic solution. The six-term solution was obtained by substituting

the Table 7.5 coefficients into (1). Comparison of the zone of dominance results in Figures 7.12a and 7.12b *quantifies the effect* of this approximation for 1, 2, 3 and 4 term asymptotic solutions for a fixed percent error of 10% and b/h = 0.1. Clearly as the percent error decreases and/or the number of asymptotic terms decreases, the comparisons must improve. For example, the single term solutions are nearly identical. However, for such a large error measure as 10%, which is practical from an engineering point of view, caution should be applied when using the results in Tables 7.2, 7.5-7.8 without having access to the true full-field solution.

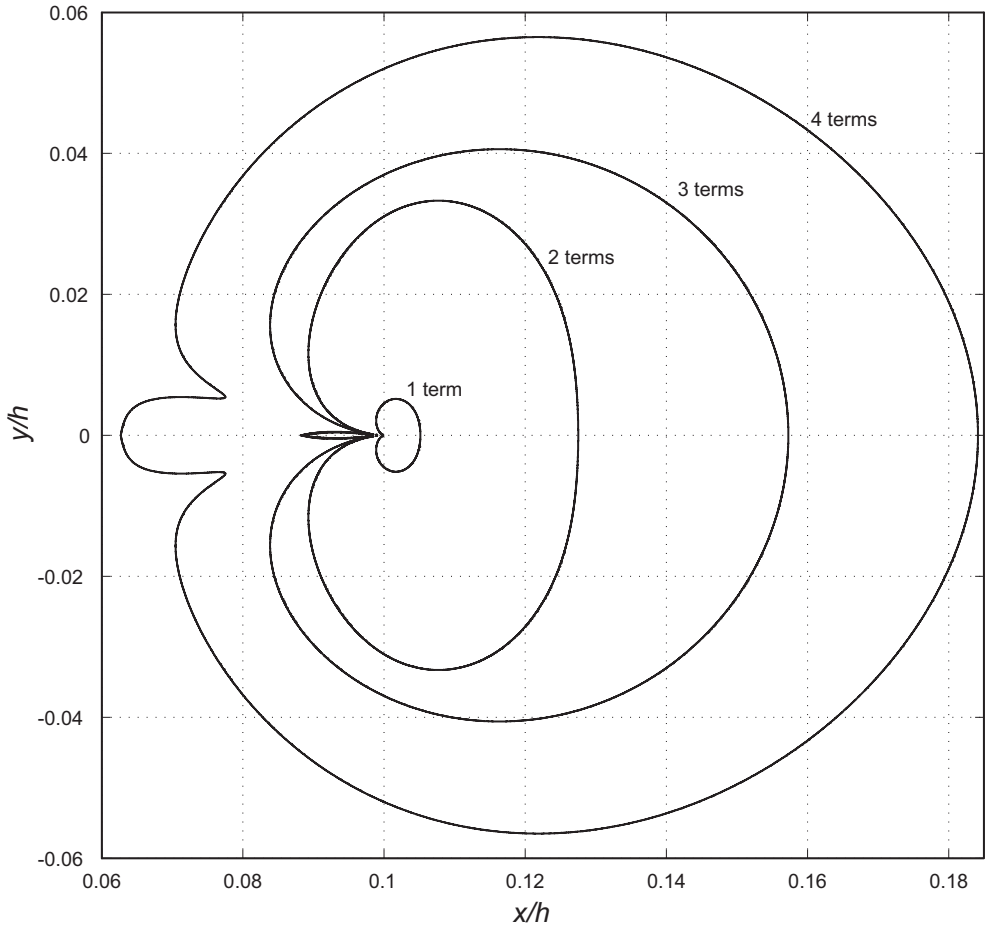

Figure 7.12a: Region of dominance as quantified by the error measure (60) equal to 10% for an edge crack in a strip with normalized depth, *b/h = 0.1*.

The remaining zone of dominance results in this study are obtained using the full-field solution in (60). In Figure 7.13, which is identical to Figure 7.12 except that b/h = 0.3, an anomally occurs for the 2-term expression. In this case the 2-term solution "gets lucky" using a 10% error criterion. A 5% error measure is used for this same geometry in Figure 7.14 which presents more realistic fields, even though a two term expansion appears to be better than three terms. This can be understood by referring back to Figure 7.7, which shows that if the error tolarance is large enough, indeed two terms can be better than three. The asymptotic solutions are valid in the limit as r approaches zero. If a large value of r is used or if a large error difference is used, then more terms is not necessarily better

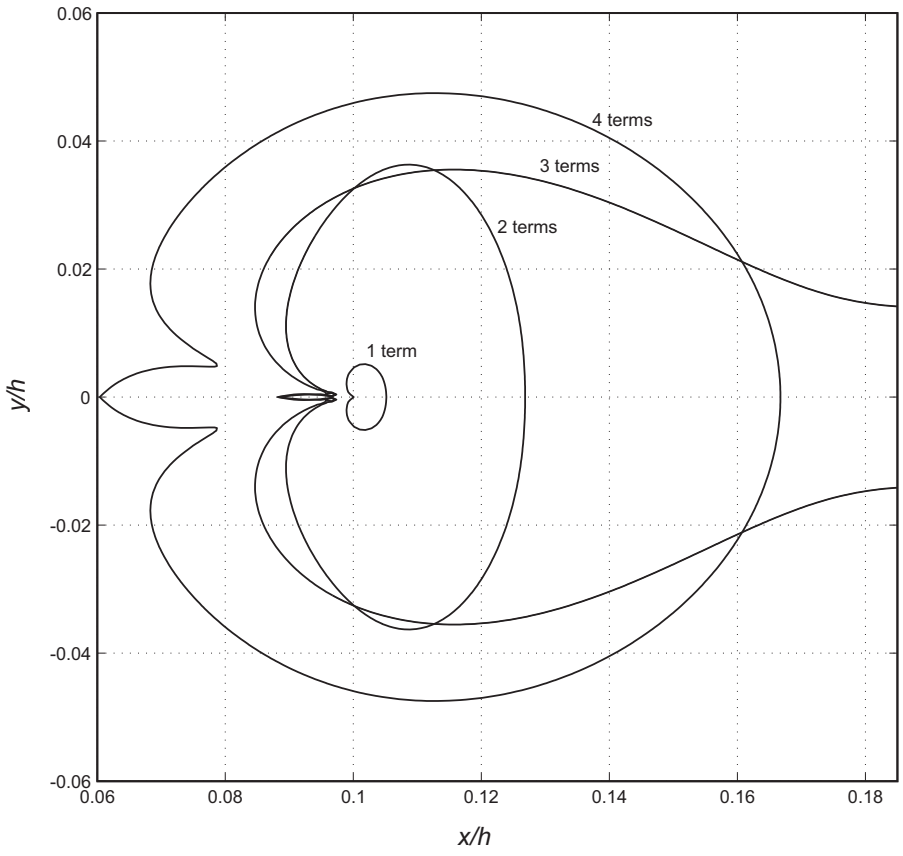

Figure 7.12b: Same as Figure 7.12a except that a six term approximation is used instead of the full-field numerical solution.

than less. The last figure of this type is presented in Figure 7.15 for b/h = 0.6 with a 10% error. For this crack depth, the T-stress from Table 7.5 is close to zero, indicating why one and two terms are nearly identical.

As can be observed from Figures 7.12-7.15, the domain of constant error is roughly circular with the center of the circle shifted to the right of the crack tip. In Figures 7.16-7.19 the size of these domains is quantified by the values at $\theta = 0$ and 90 degrees. In Figure 7.16, for edge crack depths ranging from b/h = 0.0 to 0.9, these results are presented for uniform tension using an error measure of 10%, while in Figure 7.17 the error is reduced to 1%. In Figures 7.18 and 7.19, the case of bending is presented using once again, error values of 10% and 1%, respectively. In all these plots there appears to be three distinct regions corresponding to shallow cracks, intermediate depth cracks and deep cracks. For shallow cracks the behavior is simple and more terms is better. For deep cracks the third term becomes important and the fourth term is not so important for these error values. For intermediate depth cracks the results are confusing due to the unexpected behavior of the two-term solutions which appear to be better than the three- and four-term solutions. The important point is that this is true for all theta, as shown, for example, in Figures 7.13 and 7.14.

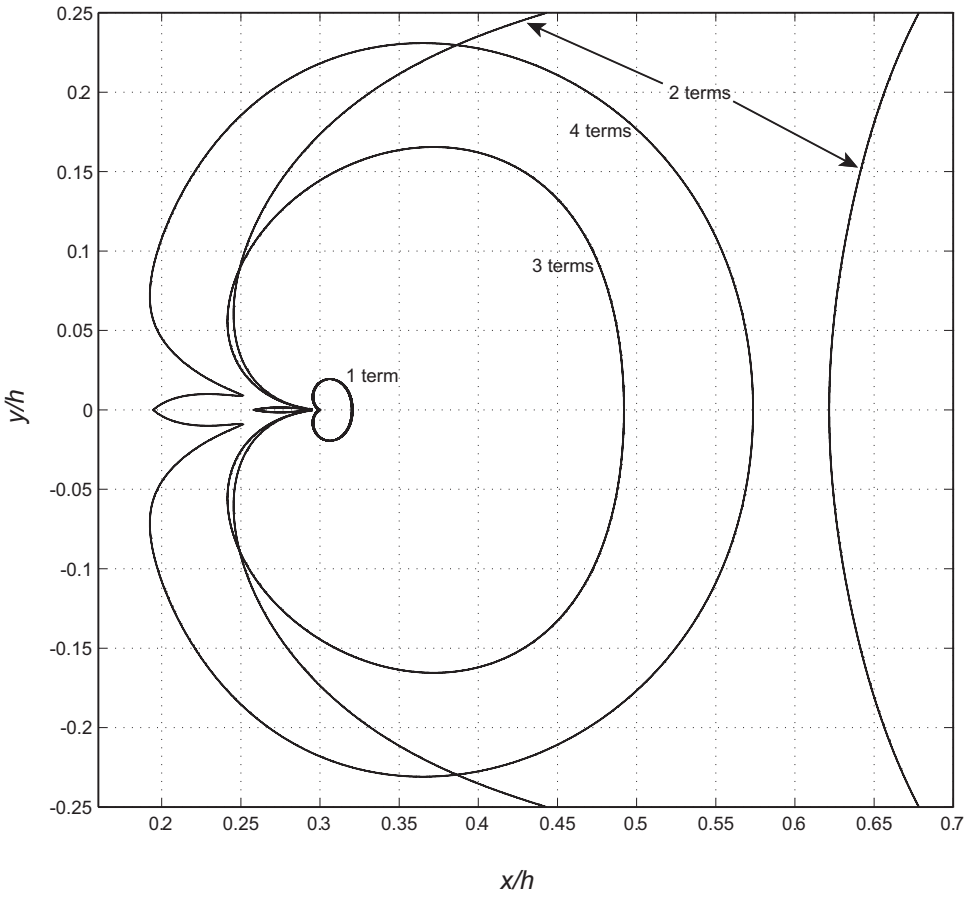

Figure 7.13: Region of dominance as quantified by the error measure (60) equal to 10% for an edge crack in a strip with normalized depth, *b/h = 0.3*.

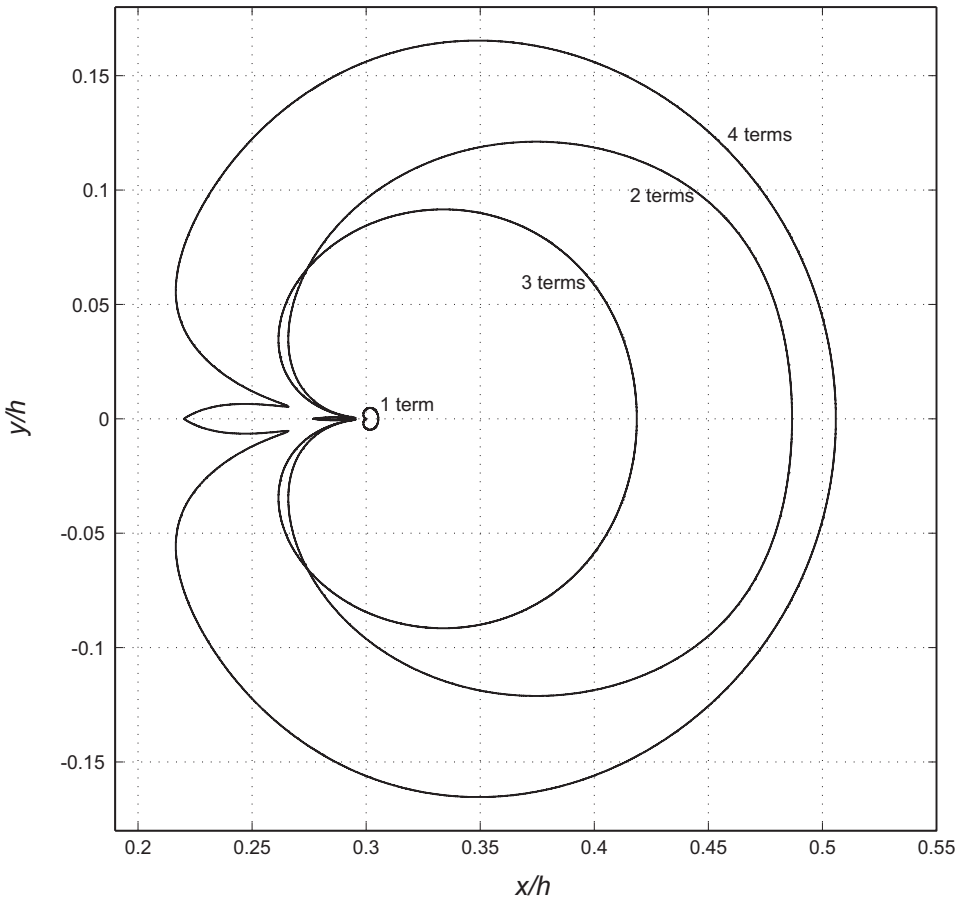

Figure 7.14: Region of dominance as quantified by the error measure (60) equal to 5% for an edge crack in a strip with normalized depth, *b/h = 0.3*.

7.4. Conclusions

The following two points are emphasized in this study: 1) the accurate determination of the mode I stress intensity and T-stress coefficients as defined by Equations (1) and (2), and 2) the comparison of the corresponding asymptotic fields to accurate full-field solutions. The method is based on a singular integral equation formulation. While this method is not versatile in handling complicated geometry, it has the potential to be very accurate. Special attention has been given to reach the full potential in this study. The crack opening displacement derivative is the unknownfunction in the singular integral equation. In this study this function is approximated by a truncated polynomial expressed in terms of orthogonal

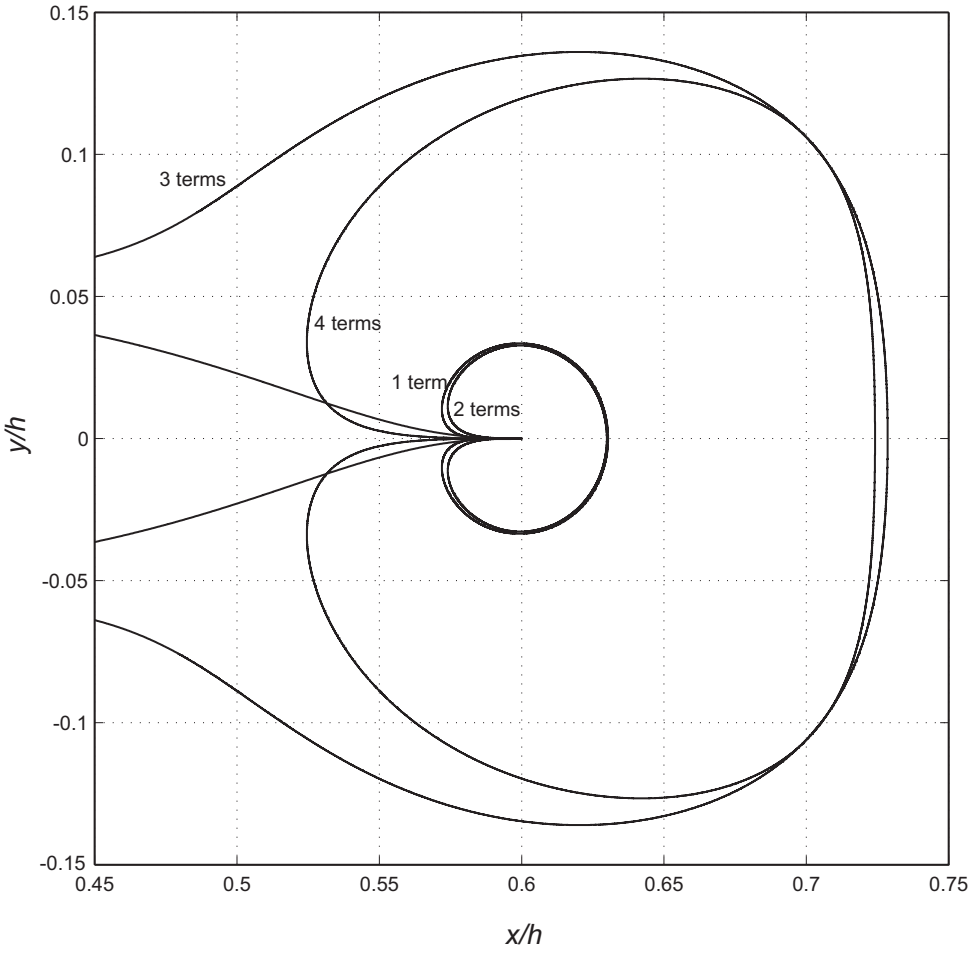

Figure 7.15: Region of dominance as quantified by the error measure (60) equal to 10% for an edge crack in a strip with normalized depth, *b/h = 0.6*.

polynomials (see Equations (11) and (27)). This numerical approach is used as it allows for very accurate and flexible numerical evaluation of integrals, since integration is uncoupled to the manner in which the unknown is represented. The example of an edge crack in a half space was used to assess the accuracy of the method for determining higher order coefficients, the results for which are presented in Tables 7.1 and 7.2. Using the approach it was demonstrated that the T_n coefficients, which result from an integral of the unknown function, are easier to determine than the k_n coefficients, which result from the derivative of the unknown function at the crack tip location. There is no difficulty determining k_n and T_n for n = 0, 1 for an edge crack in a finite

width strip of normalized depth, b/h = 0.95 (see Figure 7.1b and Tables 7.5-7.8). Furthermore, there is no difficulty determining the T_n coefficients for upwards of n = 30. However, for n = 2 and higher, the k_n coefficients become difficult to determine analytically from the orthogonal polynomials if large values of N are required to properly represent the unknown. The corresponding analytical expressions are (18) and (19) for internal cracks and (33) and (34) for edge cracks. Two alternative approaches are presented, one based on finite difference and the other based on using the power series given by (37). For the edge crack examples studied, these two alternatives were better for the k_2 and higher order k_n coefficients.

Given the accurate values of the higher order coefficients, the size of the zone in which an asymptotic series can adequately represent the stress field can be determined by a comparison with the full-field solution, which is obtained from the singular integral equation solution. This concept of a zone of dominance is fundamental to a continuum mechanics approach to fracture mechanics, in which a single or perhaps multiple parameters are used in a fracture criterion. In this study the focus of the results was an

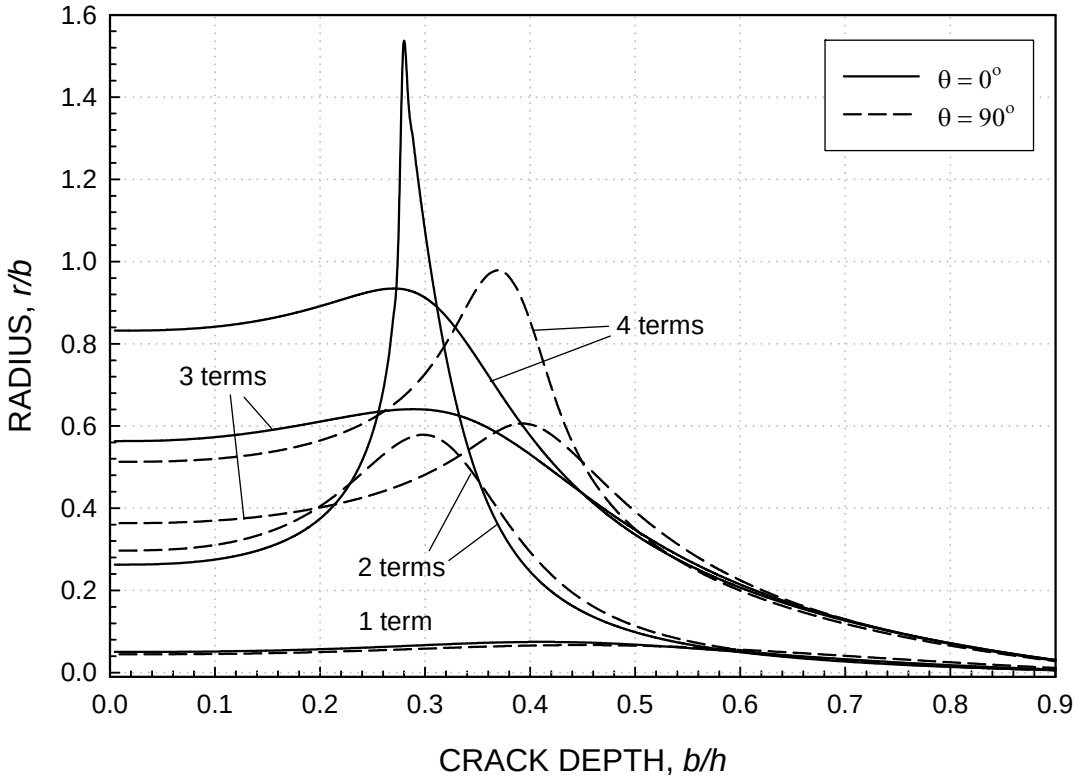

Figure 7.16: Region of dominance as quantified by the error measure (60) equal to 10% for an edge crack in a strip subjected to uniform tension. Values of the size of the zone are given at $\theta = 0$ and 90 degrees as a function of crack depth.

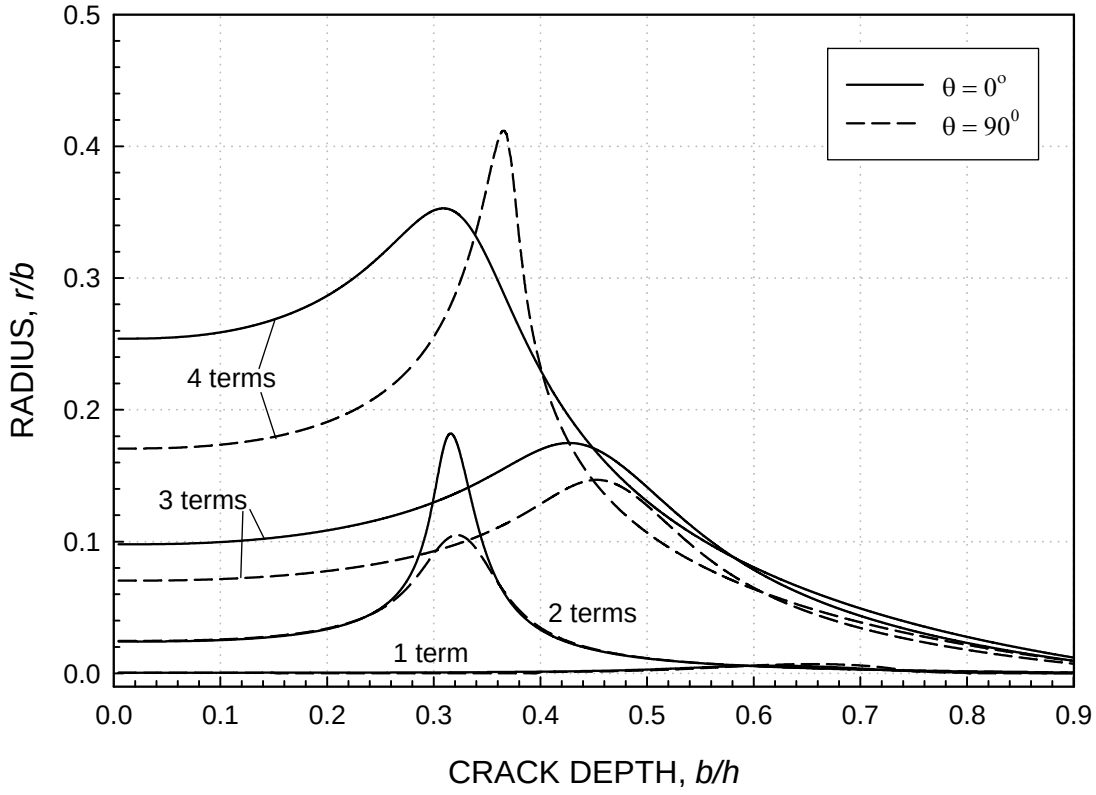

Figure 7.17: Same as Figure 7.16 for 1% error.

edge crack in a finite width strip subjected to mode I loading. Important conclusions based on the results are:

- The selection of an error tolerance value (60) used to define the size of an asymptotic zone is very important. The results indicate that often a 2-term expansion appears to be quite accurate, even more accurate than a 3- or 4-term expansion. This of course is not the case in the limit as the crack tip is approached, which corresponds to the limit as the error also approaches zero. For the case of an edge crack in a strip, for an error tolerance of 10%, in tension a two-term expansion has this behavior for crack depths ranging for approximately $0.25 < b/h < 0.35$ (see Figure 7.16), and in bending this occurs for approximately $0.05 <$

b/h < 0.15 (see Figure 7.18). As shown by Figure 7.8a for the case of a positive T-stress a 2-term expansion can be very poor, which is contrary to Figures 7.6a and 7.7a where the T-stress is negative.

- For deep cracks, where approximately b/h > 0.5 in tension and approximately b/h > 0.4 in bending, the T-stress term is no longer significant. In this case a 3-term expansion can be used to provide a significant enlargement of the asymptotic zone. For the case of an error tolerance of 10%, a fourth term does not provide much additional benefit.

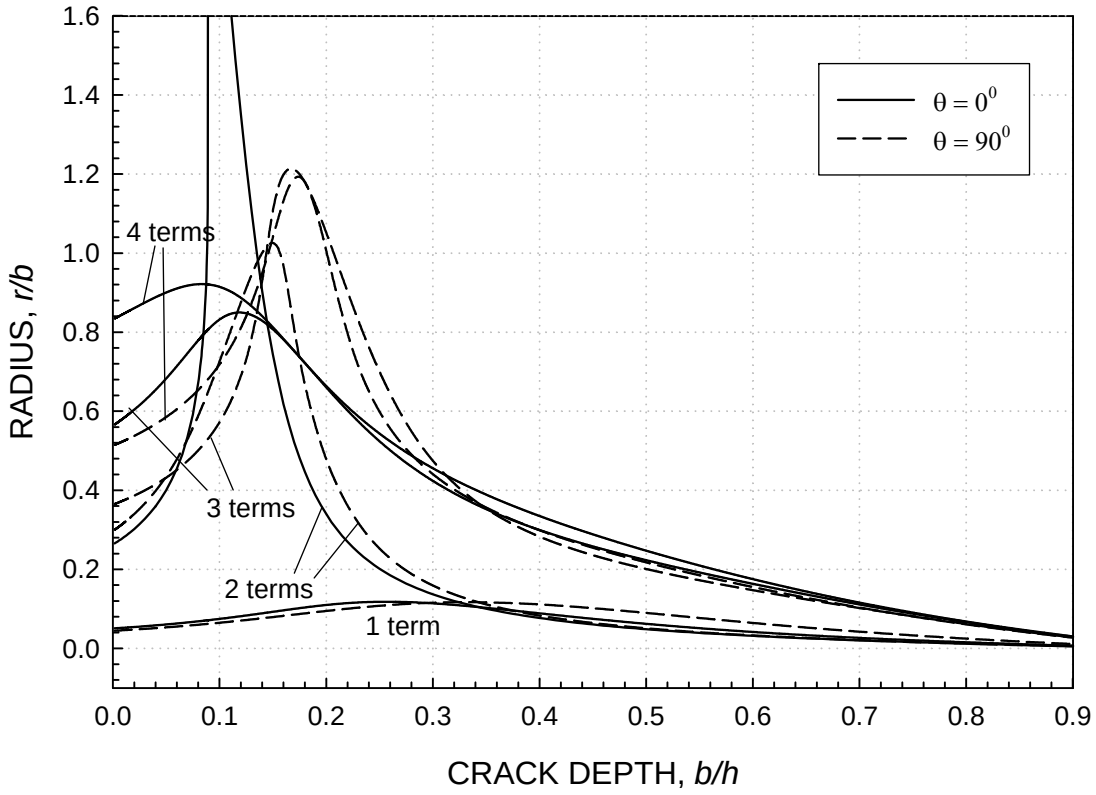

Figure 7.18: Region of dominance as quantified by the error measure (60) equal to 10% for an edge crack in a strip subjected to bending. Values of the size of the zone are given at θ = 0 and 90 degrees as a function of crack depth.

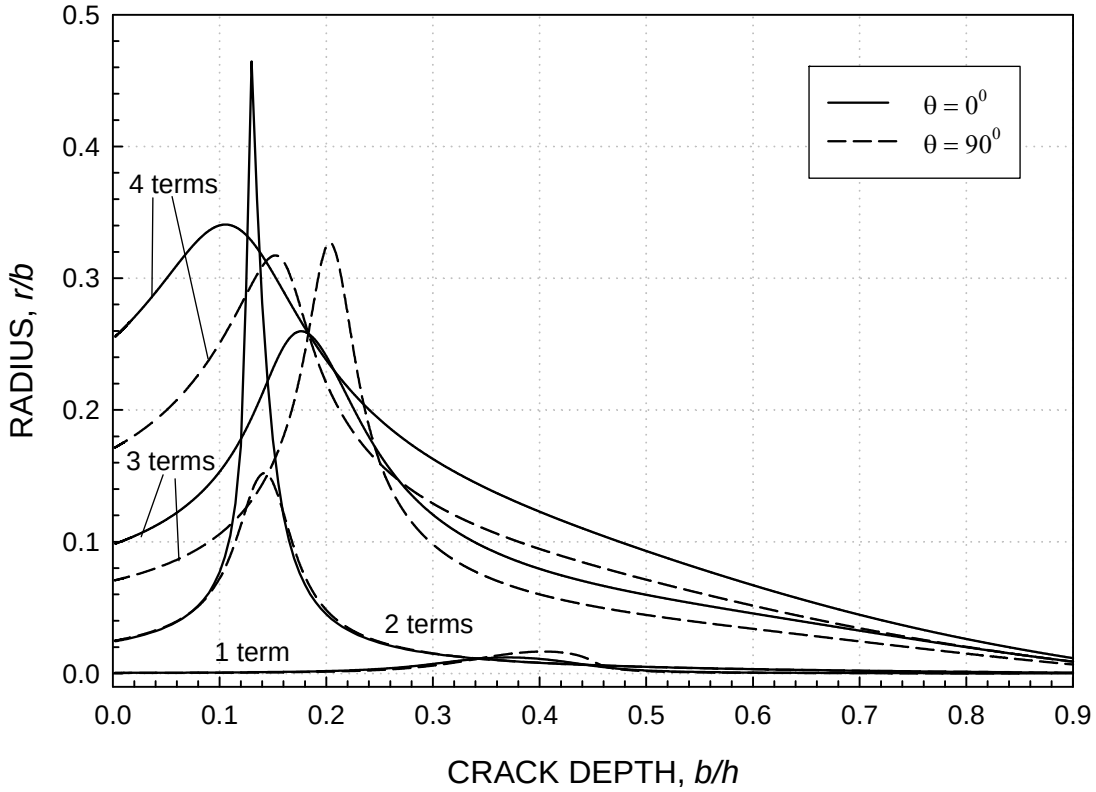

Figure 7.19: Same as Figure 7.18 for 1% error.

References

1. Williams, ML. On the Stress Distribution at the Base of a Stationary Crack", ASME Journal of Applied Mechanics. 1957;24:111-114.
2. Hutchinson, JW. Fundamentals of the phenomenological theory of nonlinear fracture mechanics. ASME Journal of Applied Mechanics. 1983;50:1042-1051.
3. Larsson, SG., and Carlsson, A.J. Influence of non-singular Stress Terms and Specimen Geometry on Small-Scale Yielding at the Crack Tips in Elastic-Plastic Material. Journal of the Mechanics and Physics of Solids. 1973;21:263-278.
4. Leevers, PS. and Randon, J.C. Inherenet stress biaxiality in various fracture specimen geometries. International Journal of Fracture. 1983;9:311-325.
5. Betegon, C. and Hancock, J.W. Two parameter characterization of elastic-plastic crack tip fields. Journal of Applied Mechanics. 1990;58:104-110.
6. Li, Y. and Wang, Z. High-order asymptotic field of tensile plane-strain nonlinear crack problems. Scientia Sinica. 1986;29:941-955.

7. Chao, YJ. and Zhu, XK. J-A_2 characterization of crack-tip fields: Extent of J-A_2 dominance and size requirements. International Journal of Fracture 1998;89:285-307.

8. Loghin, A. and Joseph, PF. Asymptotic Solutions for Mixed Mode Loading of Cracks and Wedges in Power Law Hardening Materials. Engineering Fracture Mechanics. 2001;68:1511-1534.

9. Loghin, A. and Joseph, PF. Mixed mode fracture in power law hardening materials near mode I. International Journal of Fracture. 2003;123:81-106.

10. Kfouri, AP. Some evaluations of the Elastic T-term using Eshelby's method. International Journal of Fracture. 1986;30:301-315.

11. Sham, T-L. The determination of the elastic T-term using higher order weight functions", International Journal of Fracture, 1991;84:81-102.

12. Karihaloo, BL and Xiao, QZ. Accurate determination of the coefficients of elastic crack tip asymptotic field by a hybrid crack element with p-adaptivity. Engineering Fracture Mechanics. 2001;68:1609-1630.

13. Song, C. Evaluation of power-logarithmic singularities, T-stresses and higher order terms of in-plane singular stress fields at cracks and multi-material corners. 2005;72:1498-1530.

14. Seed, GM and Nowell, D. Use of the distributed dislocation method to determine the T-stress. Fatigue and Fracture of Engineering Materials and Structures. 1994;17:605-618.

15. Olsen, PC. Determining the stress intensity factors K_I, K_{II} and T term via the conservation laws using the boundary element methods. Engineering Fracture Mechanics. 1994;49:49-60.

16. Fett, T. T-stresses in rectangular plates and circular disks. Engineering Fracture Mechanics. 1998;60:631-652.

17. Karihaloo, BL and Xiao, QZ. Higher order terms of the crack tip asymptotic field for a notched three-point bend beam. International Journal of Fracture. 2001;112:111-128.

18. Xiao, QZ, Karihaloo, BL and Liu, XY. Direct determination of SIF and higher order terms of mixed mode cracks by a hybrid crack element. International Journal of Fracture. 2004;125:207-225.

19. Capitaneanu, MM. Higher order terms in linear elastic fracture mechanics. MS Thesis, Clemson University, May 2000.

20. Kaya, AC and Erdogan, F. Integral equations with strongly singular kernels. Quarterly of Applied Mathematics. 1987;45:105-122.

21. Erdogan, F and Joseph, PF. Mechanical Modeling of Multilayered Films on an Elastic Substrate, - Part II: Results and Discussion. ASME Journal of Electronic Packaging, 1990;112:317-326.

22. Abramowitz, M and Stegun, IA. Handbook of mathematical functions. 1972. Dover.

23. Tricomi, FG. On the finite Hilbert transformation. Quarterly Journal of Mathematics, Oxford ser. (2). 1951;2:199-211.

24. Koiter, WT. Discussion of “Rectangular tensile sheet with symmetrical edge cracks,” by O. L. Bowie, Journal of Applied Mechanics, Transactions of the ASME 87, Series E. 1965;32:237.

25. Civelek, MB and Erdogan, F. Crack problems for a rectangular plate and an infinite strip. International Journal of Fracture. 1982;19:139-159.

26. Isida, M. Effect of width and length on stress intensity factors of internally cracked plates under various boundary conditions. International Journal of Fracture. 1971;7:301-316.

27. Cordes RD, and Joseph, PF. Surface and Internal Cracks in a Residually Stressed Plate. International Journal of Fracture. 1995;68:287-314.

28. Lee, JL and Rosakis, AJ. Interfacial cracks in plates: a three-dimensional numerical investigation. International Journal of Solids and Structures. 1993;30:3139-3158.

CHAPTER 8

Determination of Mode II higher order coefficients in Fracture Mechanics

Higher order coefficients associated with pure mode-II type fracture are determined using a singular integral equation approach in this paper. This chapter is an extension of Chapter 7 [1] where the method of extracting the higher order coefficients from the solution of the singular integral equation that arises in fracture mechanics problems is explained in more detail. In this chapter, several numerical examples with mode II type loads are considered and the higher order coefficients are presented. For the example of an edge crack in a half space, converged values of the first 10 mode II coefficients have been determined, and for an edge crack in a finite width strip subjected to constant, linear, quadratic and cubic shear loads, first 5 coefficients are presented. Coefficients for various edge and internal crack geometries in a strip subjected to end shear load at a specified distance are also presented. Finally for the case of an internal crack in a strip subjected to end shear, one crack tip begins to close i.e., $k_0^I = 0$ for certain crack geometry. The critical crack geometry along with the remaining non-zero higher order terms at that crack tip are also presented.

8.1 Introduction

Williams [2] was the first to express stresses and strains near the tip of a crack in terms of an asymptotic series for small distances from the crack tip. Using the polar coordinate system in Figure 8.1a, the asymptotic form of the stresses and displacements for the anti-symmetric, mode II case of loading can be expressed as

$$\sigma_{ij}(r,\theta) = \sum_{n=0}^{\infty} k_n^{II} (2r)^{n-\frac{1}{2}} f_{ij}^{IIk}(n,\theta) + \sum_{n=1}^{\infty} T_n^{II} (2r)^n f_{ij}^{IIn}(n,\theta), \qquad (1)$$

$$2\mu u_i(r,\theta) = \sum_{n=0}^{\infty} k_n^{II} (2r)^{n+\frac{1}{2}} g_i^{IIn}(n,\theta) + \sum_{n=1}^{\infty} T_n^{II} (2r)^{n+1} g_i^{IIn}(n,\theta), i = r,\theta \,, \qquad (2)$$

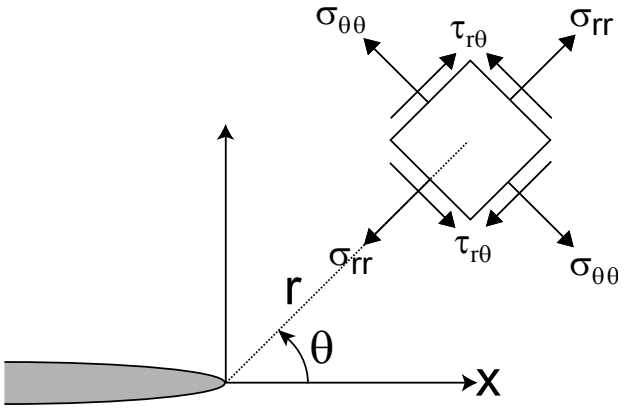

Figure 8.1a.

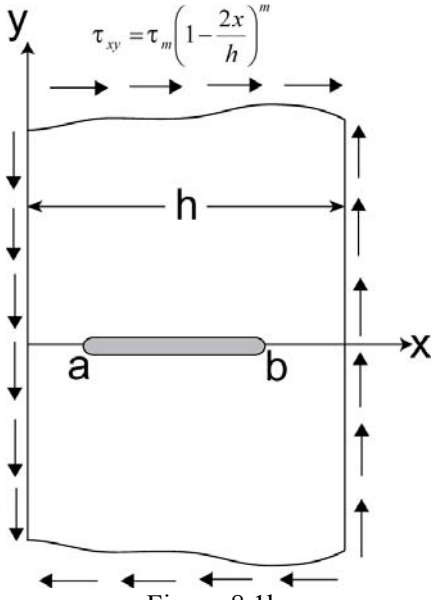

Figure 8.1b.

Figure 8.1. Problem geometry for the region around the crack tip (Figure 8.1a) and for a crack in an infinite strip (Figure 8.1b).

where the angular functions for both modes I and II are presented in Appendix B. These coefficients, k_n and T_n are referred to as the stress intensity factor coefficients and T-stress coefficients, respectively. Within the main body of the paper both superscripts "I" and "II" will be used to denote the mode I and mode II coefficients respectively, since numerical examples are considered where both types of coefficients arise.

Most of the research related to determination of higher order terms that arose in fracture mechanics are based on the finite element method and excellent reviews of the development of these finite element formulations dedicated to a direct determination of stress intensity factors, k_n and T-stress coefficients, T_n are given by Karihaloo and Xiao [3] and Song [4]. Other approaches used to obtain the T-stress include Seed and Nowell [5] who used a singular integral equation approach for an inclined edge crack in a half space, Olsen [6] who used the boundary element method and Fett [7] who used the boundary collocation method.

From the point of view of the current study, coefficients of terms of higher order than the T-stress term are of interest. For this case Fett [7], Karihaloo and Xiao [3,8], Xiao, et al. [9] and Song [4] have provided the key methods and solutions. In particular Karihaloo and Xiao [3] have used a special element (hybrid crack element) that allows for a direct calculation of the coefficients of higher order coefficients and Song [4], who has extended the scaled boundary finite-element method to determine directly higher order coefficients.

In this paper the details of determining the mode II coefficients are given. The details of determining the mode I coefficients are already given in the previous paper written by the same authors [1]. Also, in that paper, the size of the k-dominant zone, kT-dominant zone, and zones associated with three and four terms, is quantified around the crack tip. The current paper, which is an extension of the previous paper, reports the mode II coefficients for an edge and internal

crack in both a half space and a strip. Although, only the details of determining the mode II coefficients are given here, several numerical examples that give rise to both mode I and mode II coefficients are considered and their corresponding higher order terms are reported in this paper. Finally, coefficients for a finite width strip with an internal and edge crack subjected to shear load at one end is reported. Since there is a possibility of the crack closing at the right end of the internal crack, the crack depth at which the crack begins to close i.e., $k_0^I = 0$ is also reported for several crack geometries and the remaining higher order terms are reported.

8.2. Formulation

The anti-symmetric case of mode II is presented in the formulation. Based on the numerical solution of a singular integral equation, the mode II coefficients, $k_n = k_n^{II}$ and $T_n = T_n^{II}$ in the series (1) and (2), are determined for an internal and an edge crack.

8.2.1. The singular integral equation.

Consider a planer crack along the y = 0 line that extends from x = a to x = b (Figure 8.1b). For the mode II mixed boundary conditions,

$$U(x) = u_x(x,0^+) - u_x(x,0^-) = 0, \quad 0 < x < a, \; b < x \tag{3}$$

$$\tau_{xy}(x,0) = -q(x), \quad a < x < b \tag{4}$$

the resulting singular integral equation of the first kind can be represented by

$$\int_a^b \frac{\phi(t)}{t-x}\,dt + \int_a^b \phi(t)\,K(x,t)\,dt = -\pi\frac{1+\kappa}{2\mu}q(x), \quad a < x < b\,, \tag{5}$$

where $\phi(t)$ is the derivitive of the crack sliding displacement (CSD) defined by

$$\phi(t) = \frac{d}{dt}\left[u_x(t,0^+) - u_x(t,0^-)\right] = \frac{dU}{dt}\,. \tag{6}$$

and K(x,t) is a Fredholm kernel associated with the geomtetry of the particular crack problem under investigation. This equation can be solved for the unknown, $\phi(t)$ by using numerical methods. Once this function is determined, all of the field quantities can be determined in terms of integrals of ϕ. For example, the expression for y- component of displacement along the crack flanks is of the form,

$$\frac{\pi(1+\kappa)}{2} v(x,0) = \frac{1-\kappa}{4} \int_a^b \frac{U(t)}{t-x} dt + \int_a^b U(t) M(x,t)\, dt, \tag{7}$$

where U(t) is the crack sliding displacement defined by (6). Once again, the kernel M(x,t) are associated with a particular problem (see Section 3 for examples).

8.2.2. The internal crack.

For the case of an internal crack contained in a single material, the integral equation can be written in normalized form as

$$\int_{-1}^{+1} \frac{f(q)}{\sqrt{1-q^2}\,(q-s)} dq + \frac{b-a}{2} \int_{-1}^{+1} \frac{f(q)}{\sqrt{1-q^2}} K(x,t)\, dq = -\pi \frac{q(s)}{\tau_0} \quad , \quad -1 \le s \le 1, \tag{8}$$

where

$$t = \frac{b-a}{2} q + \frac{b+a}{2}, \quad x = \frac{b-a}{2} s + \frac{b+a}{2}, \quad \phi(t) = \frac{f(q)}{\sqrt{1-q^2}} \frac{(1+\kappa)\tau_0}{2\mu} \quad . \tag{9}$$

A numerical solution is sought in the approximate form

$$f(q) = \sum_{m=1}^{N} c_m T_m^{Ch}(q), \tag{10}$$

where the T_m^{Ch} are Chebychev polynomials of the first kind. Due to the orthogonality of these polynomials, by starting the sum at m = 1, the function f(q) satisfies the condition

$$\int_a^b \phi(t) dt = 0 \quad . \tag{11}$$

Following Kaya and Erdogan [10] and Erdogan and Joseph [11] for the details of the numerical procedure, once f(q) is determined, the crack opening displacement is given by

$$U(s) = -\frac{b-a}{2}\frac{(1+\kappa)\tau_0}{2\mu}\sum_{m=1}^{N}\frac{c_m}{m}\sqrt{1-s^2}U_{m-1}(s)\,, \quad -1<s<1\,, \tag{12}$$

where the $U_{m-1}(s)$ are Chebychev polynomials of the second kind.

At the crack tip at x = b, the expression (2) is used to obtain the asymptotic expression for the crack sliding displacement as

$$U(r) = -u_r(r,+\pi) + u_r(r,-\pi) = \frac{1+\kappa}{2\mu}\sum_{n=0}^{\infty}(-1)^n\frac{k_n^{II}}{2n+1}(2r)^{n+\frac{1}{2}} \quad , \tag{13}$$

which in terms of (1 - s), can be expressed as

$$U(s) = -u_r(r,+\pi) + u_r(r,-\pi) = \frac{1+\kappa}{2\mu}\sum_{n=0}^{\infty}(-1)^n\frac{k_n^{II}(b-a)^{n+\frac{1}{2}}}{2n+1}(1-s)^{n+\frac{1}{2}} \quad . \tag{14}$$

The next step is to expand U(s) from (12) about s = 1, which requires the expresion,

$$\frac{1}{m}\sqrt{1-s^2}\,U_{m-1}(s) = \frac{1}{m}\sin\left[m\left(\cos^{-1}s\right)\right] = \sqrt{2(1-s)}\sum_{n=0}^{\infty}d_n^m(1-s)^n\,, \tag{15}$$

where the d_n^m are

$$d_0^m = 1,\; d_n^m = \frac{d_{n-1}^m}{n(2n+1)}\left[\left(\frac{2n-1}{2}\right)^2 - m^2\right]. \tag{16}$$

Given (15), the two expressions for the crack sliding displacement from (12) and (14) can be matched term by term to give the approximation for the coefficients at the right crack tip (x = b),

$$\frac{k_n^{II}(b)(b-a)^n}{\tau_0\sqrt{\frac{b-a}{2}}} = (-1)^{n+1}(2n+1)\sum_{m=1}^{N}c_m d_n^m\,,\; n = 0,1,2,...,N\,. \tag{17}$$

The n = 0 term gives the stress intensity factor, while the n > 0 terms correspond to the higher order k_n^{II} coefficients. The coefficients for the left crack tip (x = a) are determined in a similar manner as

$$\frac{k_n^{II}(a)(b-a)^n}{\tau_0\sqrt{\frac{b-a}{2}}} = (-1)^{n+1}(2n+1)\sum_{m=1}^{N}(-1)^{m+1}c_m d_n^m \text{ , } n = 0,1,2,...,N\,. \tag{18}$$

The T-stress coefficients, T_n^{II} in equations (1) and (2), can be determined by $v(x,0) = -u_\theta(r,\pi)$ using (B.17). For the right crack tip, and for small values of (1 - s), the two integrals of (7) are treated separately. The singular integral can be expressed as

$$\frac{1}{2\pi}\frac{1-\kappa}{1+\kappa}\int_a^b \frac{U(t)}{t-x}dt = -\frac{1}{2\pi}\frac{1-\kappa}{1+\kappa}\int_{-1}^{1}\frac{\sqrt{1-q^2}\sum_{m=1}^{N}\frac{c_m}{m}U_{m-1}^{Ch}(q)}{(q-s)}dq$$

$$= \frac{1}{2}\frac{1-\kappa}{1+\kappa}\sum_{m=1}^{N}\frac{c_m}{m}T_m^{Ch}(s) = \sum_{n=0}^{N}\left\{\frac{1}{2}\frac{1-\kappa}{1+\kappa}\sum_{m=1}^{N}\frac{c_m}{m}e_n^m\right\}(1-s)^n\,, \tag{19}$$

where the e_n^m are

$$e_0^m = 1,\ e_n^m = -\frac{m^2-(n-1)^2}{n(2n-1)}e_{n-1}^m. \tag{20}$$

The Fredholm integral expanded about s = 1 (x = b) is given by

$$\frac{1}{\pi}\frac{2}{1+\kappa}\int_a^b U(t)M(x,t)\,dt = \frac{1}{\pi}\frac{2}{1+\kappa}\sum_{n=0}^{M}h_n^b(1-s)^n + O(1-s)^{M+1}\,, \tag{21}$$

where the h_n^b are constants determined by integration of known functions and M is any desired integer less than or equal to N. Comparing the sum of the two expressions (19) and (21) with (B.17) gives for the right crack tip,

$$\frac{T_{n-1}^{II}(b-a)^{n-1}}{\tau_0} = 4n(-1)^n\left\{\frac{1}{2}\frac{1-\kappa}{1+\kappa}\sum_{m=1}^{N}\frac{c_m}{m}e_n^m + \frac{1}{\pi}\frac{2}{1+\kappa}h_n^b\right\},\ n = 2,3,...,M\,. \tag{22}$$

The T-stress factors at the left crack tip i.e., x = a is obtained by refecting the crack and the loading about the a middle vertical line in the strip. Depending on the even or odd nature of the loading, the sign of the T-stress coefficents have to be changed. More details are given in the results section. This technique is used to avoid obtaining the analytical expressions for the Fredholms' kernel in the strip which can be very time consuming.

8.2.3. The edge crack.

Referring to Figure 8.1b, an edge crack of length b is assumed to exist from x = 0 to x = b. In this case, the normalized singular integral equation can be expressed as,

$$\int_{-1}^{+1} \frac{f(q)}{\sqrt{1-q}(q-s)}\,dq + \frac{b}{2}\int_{-1}^{+1} \frac{f(q)}{\sqrt{1-q}} K(x,t)\,dq = -\pi \frac{q(s)}{\tau_0} \quad , \quad -1 \le s \le 1 \,, \tag{23}$$

where

$$t = \frac{b}{2}q + \frac{b}{2}, \quad x = \frac{b}{2}s + \frac{b}{2}, \quad \phi(t) = \frac{f(q)}{\sqrt{1-q}} \frac{(1+\kappa)\tau_0}{2\mu} \quad . \tag{24}$$

The form of the function f(q) is approximated as the (N-1)th order polynomial,

$$\mathrm{f(q)} = \sum_{\mathrm{m}=0}^{\mathrm{N}-1} \mathrm{c_m P_m^{(\alpha,\beta)}(q)} \,, \tag{25}$$

where the $\mathrm{P_m^{(\alpha,\beta)}(q)}$ are Jacobi polynomials associated with the weight function, $\mathrm{w(q) = (1-q)^{\alpha}(1+q)^{\beta}}$, which for an edge crack requires α = -1/2 and β = 0. The derivative of the crack sliding displacement can therefore be expressed as

$$\frac{2}{b}\frac{2\mu}{(1+\kappa)\tau_0}\frac{dU(s)}{ds} = \frac{f(s)}{\sqrt{1-s}} = \frac{1}{\sqrt{1-s}}\sum_{m=0}^{N-1} c_m P_m^{\left(-\frac{1}{2},0\right)}(s), \quad -1 < s < 1 \,, \tag{26}$$

which has an associated displacement given by

$$\frac{2}{b}\frac{2\mu}{(1+\kappa)\tau_0}U(s) = -\sqrt{1-s}\left[2c_0 + (1+s)\sum_{m=1}^{N-1}\frac{c_m}{2m}P_{m-1}^{\left(\frac{1}{2},1\right)}(s)\right], \quad -1 < s < 1 \quad . \tag{27}$$

In order to obtain the k_n coefficients, the displacement derivative from (26) will be matched with the series expression from Appendix B. Starting with (B.19) and using (24), the displacement can be written as

$$U(s) = -u_r(r,+\pi) + u_r(r,-\pi) = \frac{1+\kappa}{2\mu}\sum_{n=0}^{\infty}(-1)^n \frac{k_n b^{n+\frac{1}{2}}}{2n+1}(1-s)^{n+\frac{1}{2}}, \tag{28}$$

which has the derivative

$$\frac{2}{b}\frac{2\mu}{(1+\kappa)}\frac{dU(s)}{ds} = \frac{1}{\sqrt{1-s}}\sum_{n=0}^{\infty}(-1)^{n+1}k_n b^{n-\frac{1}{2}}(1-s)^n. \tag{29}$$

Taking into account an N-1th order Taylor series of f(s) expanded about s = 1, the derivative of the crack sliding displacement from (26) can be expressed as

$$\frac{2}{b}\frac{2\mu}{(1+\kappa)\tau_0}\frac{dU(s)}{ds} = \frac{1}{\sqrt{1-s}}\sum_{n=0}^{N-1}\frac{(-1)^n}{n!}\left.\frac{d^n f}{ds^n}\right|_{s=1}(1-s)^n, \quad -1 < s < 1. \tag{30}$$

Comparing (29) and (30) gives the following result,

$$\frac{k_n^{II} b^n}{\tau_0\sqrt{b}} = -\frac{1}{n!}\left.\frac{d^n f}{ds^n}\right|_{s=1} = -\frac{1}{n!}f^n(1). \tag{31}$$

The nth derivative of f(s) from (25) at s = 1 can be obtained for $\alpha > -1$, $\beta > -1$, $\alpha \neq 0,1,2,\ldots$, as

$$f^n(1) = n!\sum_{m=n}^{N-1} c_m d_n^m, \tag{32}$$

where the d_n^m can be expressed in terms of binomial coefficients (see pages 10 and 775 of Abramowitz and Stegun [12]) as

$$d_n^m = \frac{1}{2^n}\sum_{j=0}^{n}\binom{m+\alpha}{m-j}\binom{m+\beta}{j}\binom{m-j}{n-j}. \tag{33}$$

For α = -1/2 and β = 0, this reduces to

$$d_0^m = \binom{m-1/2}{m} = \frac{1\times 3\times 5\times\cdots\times(2m-1)}{2\times 4\times 6\times\cdots\times(2m)},$$

$$d_n^m = \frac{(2m+2n-1)(m-n+1)}{2n(2n-1)} d_{n-1}^m \quad . \tag{34}$$

Convergence of (31) using (32) becomes more difficult as n increases due to the behavior of the coefficients from (34), especially for crack problems that require large values of N. In this case due to the m^2 multiplier in the recurrance relationship of (35), very accurate values of c_m are required for large m. An alternative to (33) is a backward finite difference evaluation of the n^{th} derivative of f(s) at s = 1, which takes advantage of the expression (25) to evaluate the function at any desired point.

The T-stress coefficients, T_n^{II} in equations (1) and (2), can be determined by $v(x,0) = -u_\theta(r,\pi)$ as seen by (B.17). For small values of (1 - s), the two integrals of (7) are treated separately. The singular integral can be expressed as:

$$\frac{1}{2\pi}\frac{1-\kappa}{1+\kappa}\int_0^b \frac{U(t)}{t-x}dt = -\frac{1}{2\pi}\frac{1-\kappa}{1+\kappa}\int_{-1}^{1}\frac{\sqrt{1-q}\left[2c_0 + (1+q)\sum_{m=1}^{N-1}\frac{c_m}{2m}P_{m-1}^{\left(\frac{1}{2},1\right)}(q)\right]}{(q-s)}dq$$

$$= -\sqrt{2}\frac{1}{2\pi}\frac{1-\kappa}{1+\kappa}\left\{c_0\sum_{n=0}^{\infty}\frac{4}{2^n(2n-1)}(1-s)^n + \sum_{m=1}^{N-1}c_m\sum_{n=0}^{\infty}e_n^m(1-s)^n\right\}, |s|\le 1 \tag{35}$$

where, from Tricomi [13], the e_n^m can be expressed in terms of gamma and factorial functions as

$$e_n^m = \frac{(-1)^m}{2^n}\frac{(m+n-1)!}{n!}\frac{\Gamma\left(n-m-\frac{1}{2}\right)}{\Gamma\left(n+\frac{1}{2}\right)}. \tag{36}$$

The Fredholm integral of (7) is given by

$$\frac{2}{1+\kappa}\frac{1}{\pi}\int_0^b U(t)M(x,t)\,dt = \frac{2}{1+\kappa}\frac{1}{\pi}\sum_{n=0}^{M} h_n(1-s)^n + O(1-s)^{M+1}\ , \tag{37}$$

where the h_n are constants determined by integration of known functions. Comparing the sum of the two expressions (35) and (37) with equation (B.17) for $u_\theta(r,\pi)$ gives,

$$\frac{T_{n-1}^{II} b^{n-1}}{\tau_0} = \frac{4n(-1)^{n+1}}{\pi}\left\{\frac{1}{2}\frac{1-\kappa}{1+\kappa}\left(\sqrt{2}\,\frac{4c_0}{2^n(2n-1)} + \sum_{m=1}^{N-1} c_m e_n^m\right) - \frac{2}{1+\kappa}h_n\right\},\ n = 2,3,...M \tag{38}$$

which is an analytical expression for calculating higher order T-stress coefficients. Another appraoch is to use the Taylor series expansion of the vertical displacement, v(x,0) around the crack tip and equating them with corresponding higher order T-stress coefficients from equation (B.17) as shown below:

$$\frac{T_{n-1}^{II} b^{n-1}}{\tau_0} = \frac{2\mu}{(1+\kappa)\tau_0}\frac{4}{(n-1)!}\left(\frac{b}{2}\right)^{n-1}\frac{d^n v(x,0)}{dx^n},\ n = 2,3,...M \tag{39}$$

Knowing the displacement around the crack tip by evaluating the right hand side of (7), the displacement derivatives are calculated using backward difference numerical differntiation routines which are then transformed into T-stress coefficients according to (39). In order to obtain accurate T-stress coefficients, orders of accuracy in calculating the numerical derivatives used was as high as 18. More details are given in section 3.1. In the next section, these techniques explained above will be applied to several fracture problems and their merits and disadvantages will be discussed.

8.3. Results

Referring to Figure 8.1b for geometry, examples are considered for the anti-symmetric (mode II) problems of an edge crack (a = 0) in a half space, an edge crack (a = 0) and an internal crack (0 < a < b < h) in an finite width strip.

8.3.1. Edge crack in a half space.

For the case of an edge crack in a half space, as given by the small b/h limit of the problem geometry in Figure 8.1b, the kernels K(x,t) and M(x,t) of (5,7) are

$$K(x,t) = \frac{-1}{(t+x)} + \frac{6x}{(t+x)^2} - \frac{4x^2}{(x+t)^3}, \tag{40}$$

$$M(x,t) = \left[\frac{1}{4}\frac{\kappa - 1}{(t+x)} - \frac{x}{2}\frac{(3+\kappa)}{(t+x)^2} + \frac{2x^2}{(t+x)^3} \right] \tag{41}$$

Values of k_n and T_n for an edge crack in a half space subjected to uniform shear, τ_0, are presented in Table 8.1 for the methods disscussed previously. Both k_n and T_n coefficients become increasingly difficult as n increases. The results for the T stress coefficients in the fifth and sixth columns of Table 8.1 were obtained from the vertical displacement along the crack. The closed form approches for both k_n in the first column of Table 8.1 and T_n in the fifth column lead to numerical error more quickly than the more numerically obtained results. A convergence study comparing the approaches for the determination of T_2 and T_3 is presented in Table 8.2. In this table, the value of

n	$\frac{k_n^{II} b^n}{\sigma_0 \sqrt{b}}$		$\frac{T_n^{II} b^n}{\sigma_0}$	
	Using the closed form solution from (31-34)	Using numerical differentiation of data from (25)	Using (35-38)	Using numerical differentiation of data from (39)
0	1.121522255230	1.121522255230	0	0
1	0.2417745989	0.241774599	-0.2815409	-0.28154091
2	0.02799	0.0279898	0.161176	0.161176
3	?	-0.019298	?	-0.0785
4		0.00748		0.035
5		-0.0024		?
6		?		

Table 8.1: Asymptotic coefficients defined by Equations (1) and (2) for an edge crack in a half space under pure shear.

N is limited to 240 as the computer round-off error in the closed form solution starts to become sizable enough beyond this value of N and affect the accuracy of the solution, while there is no such limitation for the numerical solution. Also for the same reason, it is not even possible to obtain a converged value of T_3 from closed form solution. In conclusion, the closed form solution is easier to apply but the round-off error limits the number of terms computed with it, whereas the numerical solution is not easy to calculate but the computer round-off error does not affect it easily.

N	$T_2 b^2 / \tau_0$ using closed form solution	$T_2 b^2 / \tau_0$ using numerical differentiation		$T_3 b^3 / \tau_0$ using numerical differentiation (x by -1/10)	
		$O(h^{12})$	$O(h^{18})$	$O(h^{12})$	$O(h^{18})$
144	0.1611848790	0.1611290620	0.1610501102	0.88167097410	0.83295526465
180	0.1611793573	0.1611775553	0.1611516028	0.78395637111	0.80194885838
192	0.1611782938	0.1611765920	0.1611758830	0.78525138559	0.78547431475
204	0.1611774803	0.1611764509	0.1611767505	0.78574439656	0.78574579498
216	0.1611768580	0.1611764464	0.1611761590	0.78581014090	0.78593469661
228	0.1611763811	0.1611764271	0.1611765353	0.78585138331	0.78580559184
240	0.1611760141	0.1611764196	0.1611765422	0.78586350162	0.78579464968

Table 8.2: Convergence study of asymptotic coefficients for n = 2 from Table 8.1 using 64-bit Solaris processor for computation in Quadruple precision.

In our earlier paper [1], T_n coefficients for 'n' as high as 30 could be easily calculated using the analyticalexpressions for mode I loading. The reason for this ease was the elimination of the singular integral by calculating them from the stress difference σ_{yy} - σ_{xx} on the crack surface, which is a larger source of numerical error in the calculation of the higher order terms. But for the mode II case, this elimianation is not possible as the T-stress coefficients only appear in the v displacement in the crack plane.

In order to show how the higher order terms represents the vertical displacement along the line of crack as in (7), the results in Figure 8.2 include the full-field solution along with one, two- and three-term representations from (B.17). As the number of terms used in calculating the displacement field increases, the accuracy of the solution also increases.

8.3.2. Internal crack in a strip.

For the case of an internal crack in a strip (Fig. 8.1b), the kernels K(x,t) and M(x,t) of (5,7) are given in Appendix D. For this crack problem, based on a finite element based solution, Xiao *et al.* [9] have reported the first four coefficients under pure shear. The data in Table 8.3 provide a comparison of results from these authors with those of the current approach. In the current study the strip is infinite in the vertical direction (Fig. 8.1b), while in the other study the values correspond to cases where the height is large, but finite.

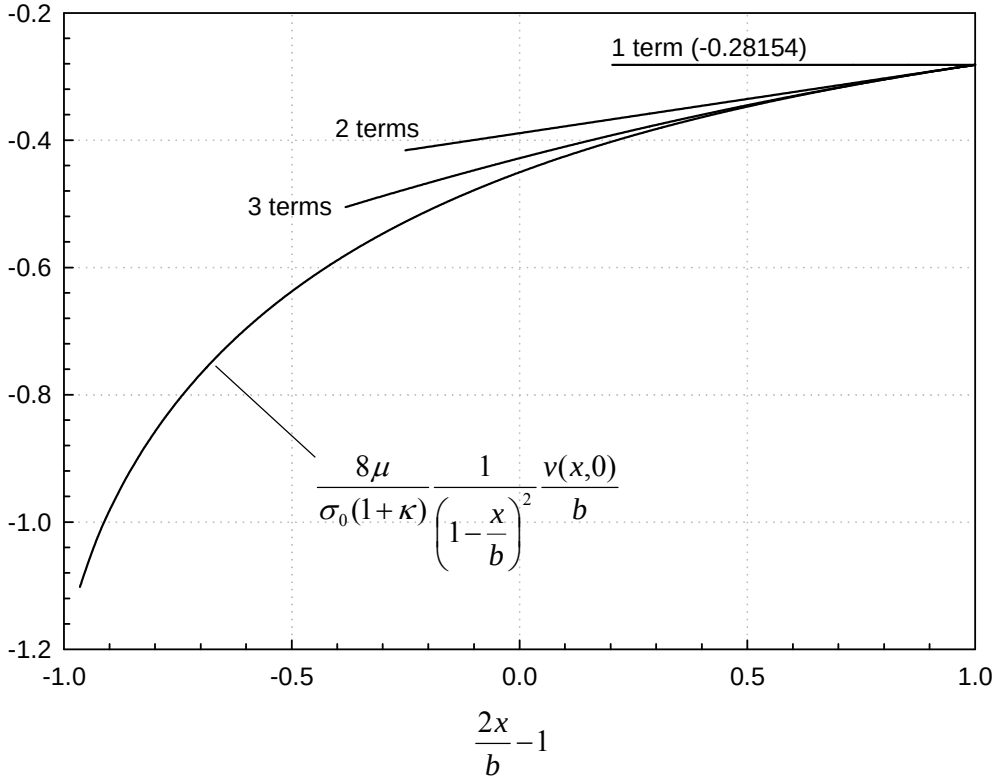

Fig.8.2. Comparisons are made between the full-field solution and the asymptotic solutions for an edge crack in a half space subjected to pure shear.

Coefficients	a/h = 0.4, b/h = 0.6		a/h = 0.25, b/h = 0.75		a/h = 0.15, b/h = 0.85	
	Current method	Ref. [1]	Current method	Ref. [1]	Current method	Ref. [1]
$k_0/(\tau_0\sqrt{(b-a)/2})$	1.02742	1.02748	1.20257	1.20257	1.51385	1.51244
$k_1(b-a)/(\tau_0\sqrt{(b-a)/2})$	0.77060	0.77041	0.90094	0.90093	1.10279	1.10256
$T_1(b-a)/\tau_0$	-4.9716E-3	-5.5072E-3	-0.33801	-0.33802	-2.98880	-2.98391
$k_2(b-a)^2/(\tau_0\sqrt{(b-a)/2})$	-0.16060	-0.16113	-0.23485	-0.23485	-1.12093	-1.12220

Table 8.3. Comparison of the first five asymptotic coefficients for the case of an internal crack in a strip subjected to pure shear (see B.3) for conversion of coefficients).

8.3.3. Edge crack in a strip.

For the case of a crack in an infinite strip (Figure 8.1b), the kernels K(x,t) and M(x,t) are presented in Appendix D. In addition to uniform shear, in this study as in the study by Cordes and Joseph [14], the crack surface loading is given by

$$\tau_{xy}(x,0)/\tau_m = (1-2x/h)^m,\ m = 0,1,2,3,.... \tag{42}$$

Any linear combination of the above loadings is also possible and the corresponding coefficients are calculated according to the principle of superposition. For example, in the case of parabolic shear stress distribution along the width of the strip that occurs during bending, the shear loading is given below as

$$\frac{\tau_{xy}(x,0)}{\tau_p} = 4\frac{x}{h}\left(1-\frac{x}{h}\right) = \left(1-\frac{2x}{h}\right)^0 - \left(1-\frac{2x}{h}\right)^2. \tag{43}$$

The stress used for normalization is identical to that given in equations (10) and (26) except that τ_m replaces τ_0. Furthermore, the loadings per unit thickness in Figure 8.1b for uniform and parabolic shear loads are respectively given by

$$\tau_0 = (P/t)/h, \quad \tau_p = \frac{3}{2}\frac{(P/t)}{h}. \tag{44}$$

The results for the first five coefficients are presented in Tables 8.4, 8.5, 8.6, and 8.7, respectively for uniform, linear, quadratic and cubic loadings according to equation (42). It is noted that great care has been taken in the current study to provide exact values of all the coefficients for the number of significant figures presented. Accuracy and the ability to do deep cracks are the strengths of the proposed method. While the difficulty with convergence increases with crack depth, all the digits presented in these tables are believed to be correct. Superposition of loadings

represented by values in these tables leads to stress and displacement field solutions near a crack tip under rather general loading conditions that are valid well beyond the k-dominant zone. All the higher order coefficients presented in the tables 8.5, 8.6 and 8.7 are Poisson's ratio dependant. However, this dependence vanishes when the coefficients are computed for a real loading as in bending of a strip considered in the coming sections.

b/h	$\frac{k_0^{II}}{\sigma_0\sqrt{b}}$	$\frac{k_1^{II}b}{\sigma_0\sqrt{b}}$	$\frac{T_1^{II}b}{\sigma_0}$	$\frac{k_2^{II}b^2}{\sigma_0\sqrt{b}}$	$\frac{T_2^{II}b^2}{\sigma_0}$
0.0	1.1215	0.2418	-0.2815	0.02799	0.1612
0.1	1.1219	0.2422	-0.28095	0.02814	0.164
0.2	1.1264	0.2465	-0.2761	0.02847	0.163
0.3	1.1419	0.2598	-0.2680	0.02864	0.158
0.4	1.1763	0.2861	-0.2718	0.02701	0.137
0.5	1.2391	0.32885	-0.3346	0.01806	0.063
0.6	1.3450	0.3917	-0.5921	-0.02015	-0.220
0.7	1.5229	0.4777	-1.5072	-0.1875	-1.46
0.8	1.8459	0.5771	-5.2207	-1.0858	-8.82
0.9	2.6037	0.5083	-31.319	-10.371	-108.45
0.95	3.6854	-0.4696	-149.99	-72.239	-1040.0

Table 8.4. Asymptotic coefficients for an edge crack in a strip for uniform shear.

b/h	$\frac{k_0^{II}}{\sigma_1\sqrt{b}}$	$\frac{k_1^{II}b}{\sigma_1\sqrt{b}}$	$\frac{T_1^{II}b}{\sigma_1}$	$\frac{k_2^{II}b^2}{\sigma_1\sqrt{b}}$	$\frac{T_2^{II}b^2}{\sigma_1}$
0.0	1.1215	0.2418	-0.2815	0.02799	0.1612
0.1	0.9853	0.076135	-0.4600	-0.00785	0.153
0.2	0.8524	-0.08635	-0.6352	-0.04357	0.141
0.3	0.7267	-0.2431	-0.8087	-0.07947	0.126
0.4	0.6104	-0.3938	-0.9915	-0.1166	0.102
0.5	0.5040	-0.5402	-1.2069	-0.1578	0.052
0.6	0.40655	-0.6862	-1.5053	-0.2129	-0.084
0.7	0.3169	-0.8414	-2.0174	-0.3182	-0.52
0.8	0.2331	-1.03795	-3.17925	-0.63465	-2.33
0.9	0.1500	-1.4335	-7.3238	-2.3184	-14.97
0.95	0.1023	-2.0190	-16.3952	-7.6715	-70.33

Table 8.5. Asymptotic coefficients for an edge crack in a strip for linearly varying shear loading for $\nu = 0.3$.

b/h	$\frac{k_0^{II}}{\sigma_2\sqrt{b}}$	$\frac{k_1^{II}b}{\sigma_2\sqrt{b}}$	$\frac{T_1^{II}b}{\sigma_2}$	$\frac{k_2^{II}b^2}{\sigma_2\sqrt{b}}$	$\frac{T_2^{II}b^2}{\sigma_2}$
0.0	1.1215	0.2418	-0.2815	0.02799	0.1612
0.1	0.8697	-0.04334	-0.5614	-0.01927	0.168
0.2	0.66265	-0.23275	-0.6830	-0.01733	0.223
0.3	0.5027	-0.3251	-0.6485	0.03357	0.327
0.4	0.3904	-0.3209	-0.4657	0.1327	0.477
0.5	0.3259	-0.2213	-0.1494	0.2782	0.662
0.6	0.3111	-0.02715	0.2654	0.4633	0.839
0.7	0.3529	0.2610	0.6640	0.6604	0.82
0.8	0.4733	0.6419	0.5031	0.7155	-0.69
0.9	0.7669	1.1008	-5.5556	-1.3852	-27.196
0.95	1.1595	1.2210	-39.6208	-18.867	-303.37

Table 8.6. Asymptotic coefficients for an edge crack in a strip for quadratic shear loading for $\nu = 0.3$.

b/h	$\frac{k_0^{II}}{\sigma_3\sqrt{b}}$	$\frac{k_1^{II}b}{\sigma_3\sqrt{b}}$	$\frac{T_1^{II}b}{\sigma_3}$	$\frac{k_2^{II}b^2}{\sigma_3\sqrt{b}}$	$\frac{T_2^{II}b^2}{\sigma_3}$
0.0	1.1215	0.2418	-0.2815	0.02799	0.1612
0.1	0.7716	-0.1276	-0.6087	-0.01580	0.194
0.2	0.5289	-0.2835	-0.6095	0.02983	0.288
0.3	0.3738	-0.2932	-0.4281	0.1067	0.356
0.4	0.2851	-0.2254	-0.2129	0.1562	0.305
0.5	0.2422	-0.1489	-0.1167	0.1190	0.036
0.6	0.2252	-0.1322	-0.3079	-0.06803	-0.57
0.7	0.2155	-0.2460	-1.0073	-0.4828	-1.74
0.8	0.1952	-0.5716	-2.6539	-1.2808	-4.27
0.9	0.1461	-1.2662	-7.2261	-3.3684	-15.97
0.95	0.1027	-2.0073	-15.9343	-8.422	-67.29

Table 8.7. Asymptotic coefficients for an edge crack in a strip for cubic shear loading for $\nu = 0.3$.

8.3.4. Edge crack in a strip subjected to end shear

Consider an example of a finite width strip that extends till infinity on one side and a constant shear load, 'P' per unit depth that is applied to the right at a position y = L from origin such that L >> h as shown in Figure 8.3. An edge crack of depth 'b' is also present in the strip along the x-axis. For the case of an edge or internal crack in a strip (Fig. 8.1b), the kernels K(x,t) and M(x,t) of (5,7) are given in Appendix D. Application of superposition principle is used to decouple the real problem into three simpler problems as shown in Figure 8.3:

1. Un-cracked problem with the same loading as the original problem.
2. Edge cracked strip with mode I type crack-surface loading,
3. Edge cracked strip with mode II type crack-surface loading.

For the un-cracked problem of Figure 8.3, a horizontal force of P per unit depth, t, is applied to the right at a position y = L. For this loading the stresses and displacements in rectangular coordinates are:

$$\frac{\tau_{xy}(x,y)}{\tau_p} = 4\frac{x}{h}\left(1-\frac{x}{h}\right) = \left[1-\left(1-\frac{2x}{h}\right)^2\right], \tag{45}$$

$$\frac{\sigma_y(x,y)}{\sigma_1} = \left(1-\frac{2x}{h}\right)\left(1-\frac{y}{L}\right), \tag{46}$$

$$\frac{h^2 2\mu u(x,y)}{\tau_p} = -\frac{3-\kappa}{4}(y-L)(2x-h)^2 - \frac{1+\kappa}{3}y^3 + (1+\kappa)Ly^2 + c_1 y + c_2, \tag{47}$$

$$\frac{h^2 2\mu v(x,y)}{\tau_p} = \frac{1+\kappa}{2}(y-L)^2(2x-h) - \frac{5+\kappa}{3}x^3 + \frac{5+\kappa}{2}hx^2 + c_3 x + c_4, \text{ where} \tag{48}$$

$$\tau_p = \frac{3(P/t)}{2h},\ \sigma_1 = \frac{6(LP/t)}{h^2} = \frac{6M/t}{h^2}, \tag{49}$$

and c_1, c_2, c_3 and c_4 are arbitrary constants that can be determined by displacement boundary conditions except for the requirement that

$$c_1 + c_3 = \frac{3-\kappa}{4}h^2 - (1+\kappa)L^2. \tag{50}$$

From (B.35) the following coefficients for use in (B.44) are obtained from (47) (taking into account that $v(x,0) = -u_\theta(r,\pi)$):

$$\bar{u}_{1\theta} = \frac{\tau_p}{2h^2}(5+\kappa)(2b-h),\ \ \bar{u}_{2\theta} = -\frac{\tau_p}{3h^2}(5+\kappa). \tag{51}$$

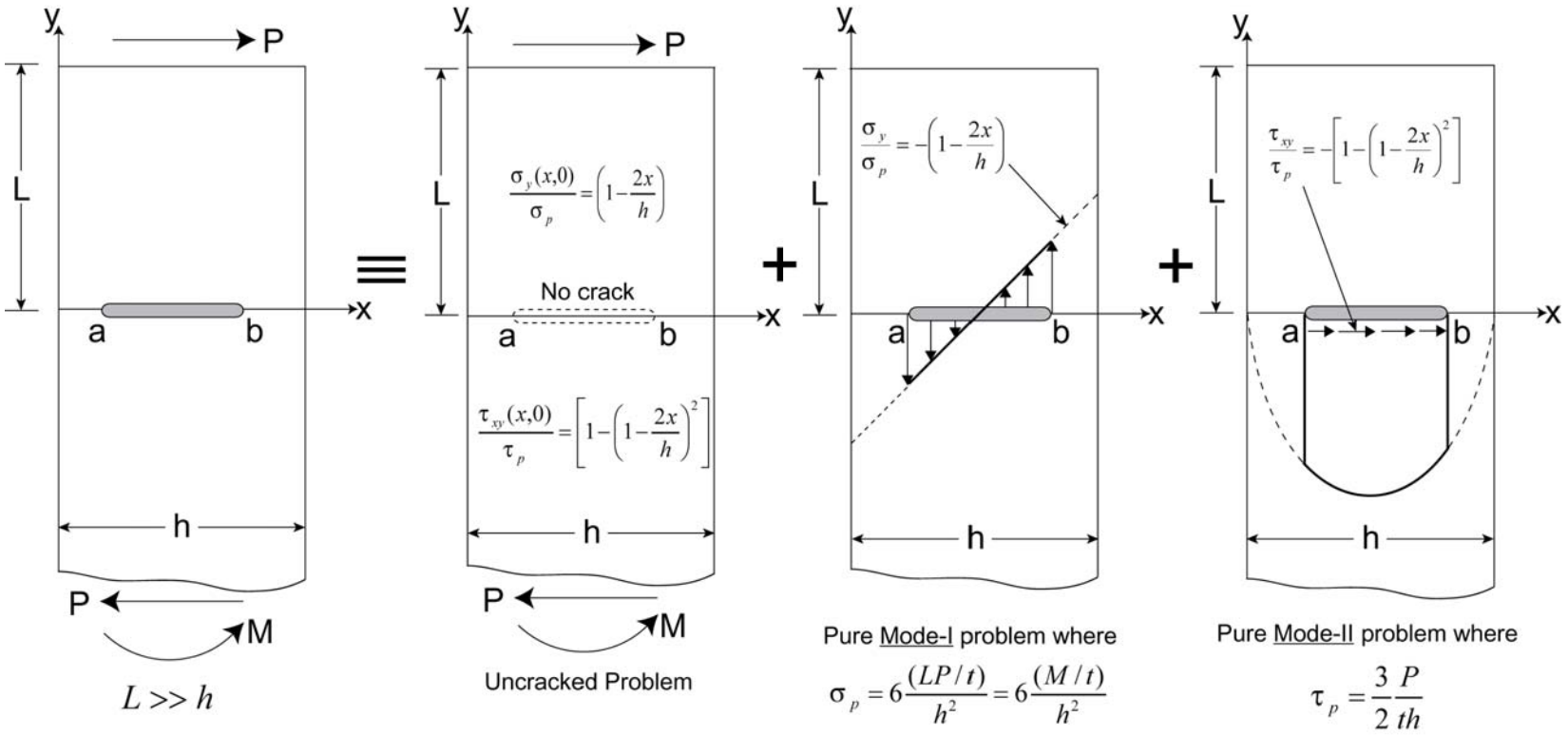

Figure 8.3. Application of the principle of superposition to relate the "original" problem on the left, with stress-free crack surfaces, to the uncracked and cracked problems on the right. The cracked problem on the right side has non-zero crack surface loading. The example of constant shear load, 'P' is illustrated above, but the loading in the original problem can be arbitrary, the only requirement being that the crack surface is not loaded.

From (B.48) the following coefficients for use in (B.53) are obtained from (48) (taking into account that $v(x,0) = -u_\theta(r,\pi)$):

$$\bar{u}_{0r} = \frac{\tau_p L}{h^2}(3-\kappa)(2b-h),\ \ \bar{u}_{1r} = \frac{\tau_p L}{h^2}(\kappa-3)\ . \tag{52}$$

For the cracked problem with Mode-I type loading, from a Saint-Venant's type of argument, we can assume that a linear normal load similar in magnitude to (B.47), but opposite in sign is applied to the crack surface as shown in Figure 8.3. k_n^I and T_n^I coefficients are calculated for the linear loads and added with the superposition part from the un-cracked problem from (B.53) gives the Mode I higher order terms as shown in Table 8.8 and compared with Song[3] and Xiao *et al.* (2004) [9].

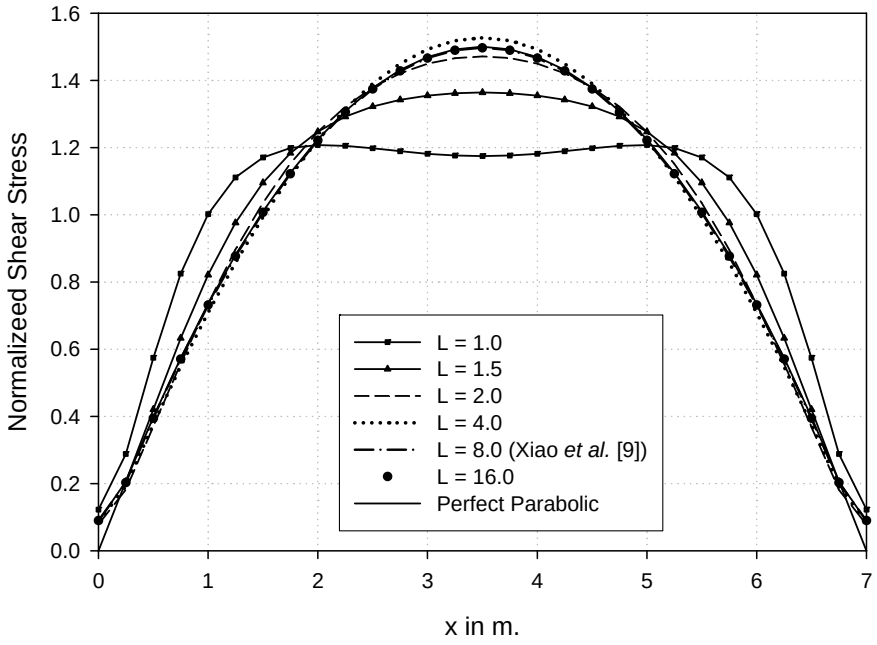

Figure 8.4: Extent of parabolic nature of the shear load, P at a distance from the crack plane. Xiao *et al.* [9] and Song [4] used L = 8m and h = 7m for evaluating the higher order terms in Table 8.8.

Type	Coefficients	Current Method*	Song (2005) [3]	Xiao *et al.* (2004) [9]	
				HCE	BCM
Mode I	$k_0^I/(\sigma_1\sqrt{b})$	1.4972	1.49705	1.4900	1.4697
	T_0^I/σ_1	0.3975	0.3974	0.3918	0.3901
	$k_1^I b/(\sigma_1\sqrt{b})$	-1.51245	-1.5125	-1.4876	-1.4847
	$T_1^I b/\sigma_1$	0.5772	0.5770	0.55615	0.5668
	$k_2^I b^2/(\sigma_1\sqrt{b})$	-0.4048	-0.4048	-0.3920	0.3975
	$T_2^I b/\sigma_1$	0.17588	-	-	-
Mode II	$k_0^{II}/(\tau_1\sqrt{b})$	0.9131	0.9128	0.9088	0.8965
	$k_1^{II} b/(\tau_1\sqrt{b})$	0.5502	0.5524	0.5482	0.5432
	$T_1^{II} b/\tau_1$	-0.1852	-0.1801	-0.1652	-0.1764
	$k_2^{II} b^2/(\tau_1\sqrt{b})$	-0.2601	-0.2593	-0.2477	-0.25465
	$T_2^{II} b/\tau_1$	-0.7303	-	-	-

Table 8.8. Comparison of the higher order coefficients for the case of a edge crack ($b/h = 0.5$) in a strip fixed at one end and subjected to pure shear at the other end as shown in Figure below (see B.3 for conversion of coefficients). * Mode I coefficients from Table 8.6 of our earlier paper [1].

Type	Coefficients	**b/h**				
		0.2	0.4	0.6	0.8	0.95
Mode I	$k_0^I/(\sigma_1\sqrt{b})$	1.0553	1.2606	1.9140	4.6764	34.299
	T_0^I/σ_1	-0.2382	0.1208	0.8339	3.92685	63.197
	$k_1^I b/(\sigma_1\sqrt{b})$	-0.1112	-0.7909	-2.9719	-19.3927	-674.06
	$T_1^I b/\sigma_1$	0.01899	0.3138	1.1199	9.5642	713.06
	$k_2^I b^2/(\sigma_1\sqrt{b})$	-0.05056	-0.20045	-0.9887	-15.931	-2644
	$T_2^I b/\sigma_1$	0.06149	0.09220	0.5290	15.7808	5792
Mode II	$k_0^{II}/(\tau_1\sqrt{b})$	0.46376	0.7859	1.03388	1.37258	2.52595
	$k_1^{II} b/(\tau_1\sqrt{b})$	0.47928	0.6070	0.41887	-0.06481	-1.69062
	$T_1^{II} b/\tau_1$	0.06469	0.3538	-1.0974	-6.6838	-112.08
	$k_2^{II} b^2/(\tau_1\sqrt{b})$	0.04580	-0.1057	-0.48345	-1.80135	-53.372
	$T_2^{II} b/\tau_1$	-0.08062	-0.4243	-1.24765	-8.4663	-737.08

Table 8.9. Asymptotic coefficients for an edge crack of different depth in a strip fixed at one end and subjected to pure shear load at the other end as shown in Figure below.

For the cracked problem with Mode II type loading from a Saint-Venant's type of argument, we can assume that a parabolic shear load similar in magnitude to (B.46), but opposite in sign is applied to the crack surface as shown in Figure 8.3. k_n^I and T_n^I coefficients are calculated for these loads and added with the superposition part from the un-cracked problem from (B.44) gives the Mode II higher order terms as shown in Table 8.8 and compared with Song[3] and Xiao *et al.* (2004) [9]. In the current study, L >> h, whereas in the study by Xiao *et al.* and Song, $L \approx 1.14h$. The implication of this approximation is the extent of linearity of the normal load and the parabolic nature of the shear load at the crack surface. Just as an example, the shear stress distributions along the crack surface for various L/h ratios are plotted in Figure 8.4. As can be seen in Figure 8.4, for the values of L and h, Song and Xiao used, the shear load is almost parabolic. However, a closer look would show a slight deviation from the perfect parabolic shear stress distribution. This difference is attributed to the slight difference in the computed higher order terms.

Finally, the converged higher order terms for edge crack in a strip with different crack depths of b/h = 0.2, 0.4, 0.6, 0.8 and 0.95 are given in Table 8.9 below. All the higher order ocefficents given in Tables 8.8 and 8.9 are not Poison's ratio dependant. While the raw coefficents from the computer program and the superposition part are Poison's ratio dependant, the final sum is Poison's ratio independent. This check was performed for all the studies presented in the paper to look for pssible errors or bugs in the computer program.

8.3.5. Internal crack in a strip subjected to end shear

Consider a similar example of a finite width strip that extends till infinity on one side and a constant shear load, 'P' per unit depth that is applied to the right at a position y = L such that L >> h as shown in Figure 8.3. The only difference is a presence of an internal crack crack instead

of an edge crack along the x-axis. For the case of an internal crack in a strip (Fig. 1b), the kernels K(x,t) and M(x,t) of (5,7) are given in Appendix D. Here again the superposition principle is used to decouple the problem, laoding is applied according to (B.47) and the higher order terms are obtained in a similar manner as the edge cracked strip. The higher order coefficients for various crack geometries are given in Table 8.10 below.

An interesting point to note here is that the mode I stress intensity factor, $\bar{k}_n^I(b)$ becomes zero for a particular crack geometry at the right tip. For a/h = 0.1 the critical depth is b/h = 0.6758, for a/h = 0.2 the critical depth is b/h = 0.6149 and for a/h = 0.3 the critical depth is b/h = 0.5707. The remaining higher order terms are still non-zero and they are tabulated in Table 8.10. There is no convergence issues at this crack depth and the computation of remaining higher order coefficients were straight forward.

8.4. Conclusions

The mode II stress intensity and T-stress coefficients as defined by Equations (1) and (2) are accurately determined in this paper. The method is based on a singular integral equation formulation. While this method is not versatile in handling complicated geometry, it has the potential to be very accurate. Special attention has been given to reach the full potential in this study and the comparison of the corresponding asymptotic fields to accurate full-field solutions is made. The crack sliding displacement derivative is the unknown function in the singular integral equation. In this study this function is approximated by a truncated polynomial expressed in terms of orthogonal polynomials (see Equations (10) and (25)). This

Coeffic ients	a/h = 0.1			a/h = 0.2		a/h = 0.3
	b/h = 0.3	b/h = 0.5	b/h = 0.6758	b/h = 0.4	b/h = 0.6149	b/h = 0.5707
$\bar{k}_0^I(a)$	0.790929	0.772807	0.695067	0.525839	0.433351	0.272675
$\bar{k}_1^I(a)$	0.949365	1.342730	1.621708	0.706278	0.981009	0.613937
$\bar{k}_2^I(a)$	0.009690	0.049157	0.031812	-0.047953	0.203876	0.128218
$\bar{k}_0^I(b)$	0.558385	0.282900	**0.0**	0.318693	**0.0**	**0.0**
$\bar{k}_1^I(b)$	0.0822069	-0.479518	-0.985488	-0.070253	-0.644436	-0.408611
$\bar{k}_2^I(b)$	-0.218783	-0.311329	-0.404041	-0.177532	-0.266412	-0.170017
$\bar{T}_0^I(a)$	-0.943392	-1.114807	-1.167821	-0.214243	-0.664324	-0.410831
$\bar{T}_1^I(a)$	-0.305141	-0.742624	-1.109991	0.206357	-0.465578	-0.274904
$\bar{T}_2^I(a)$	-0.0182	-0.00454	0.0508	-0.0014	-0.0144	-0.0010
$\bar{T}_0^I(b)$	-0.430991	-0.0340043	0.328954	-0.635390	0.213596	0.135510
$\bar{T}_1^I(b)$	0.223131	0.438262	0.614969	-0.216012	0.423473	0.271829
$\bar{T}_2^I(b)$	-0.0085	-0.0146873	0.0007	-0.0029	-0.002792	-0.00045
$\bar{k}_0^{II}(a)$	0.558880	0.7853651	1.00349292	0.775824	0.943700	0.964561
$\bar{k}_1^{II}(a)$	0.013582	-0.1258366	-0.2342002	0.272693	0.161269	0.476867
$\bar{k}_2^{II}(a)$	-0.342543	-1.002849	-2.2746981	-0.317885	-0.706284	-0.37715
$\bar{k}_0^{II}(b)$	0.777866	1.0388162	1.1651617	0.929247	1.076799	1.031284
$\bar{k}_1^{II}(b)$	0.841066	0.8804873	0.5206103	0.848901	0.671418	0.727706
$\bar{k}_2^{II}(b)$	-0.073712	-0.361217	-0.8787031	-0.146927	-0.509204	-0.301970
$\bar{T}_1^{II}(a)$	-1.083735	-3.013285	-5.977173	-0.743819	-1.771819	-0.677575
$\bar{T}_2^{II}(a)$	-0.299141	-2.811751	-9.581022	-0.140560	-0.867354	-0.240018
$\bar{T}_1^{II}(b)$	0.470870	-0.043061	-1.508235	0.2374275	-0.639428	-0.241230
$\bar{T}_2^{II}(b)$	-0.119861	-0.493614	-1.276071	-0.121434	-0.567058	-0.227773

Table 8.10. Higher order terms for an internal crack in a strip subjected to end shear as shown in Figure 8.3 for different crack geometry. Higher order coefficients are also given when the right crack tip begins to close i.e. $\bar{k}_n^I(b) = 0.0$.

numerical approach is used as it allows for very accurate and flexible numerical evaluation of integrals, since integration is uncoupled to the manner in which the unknown is represented.

The example of an edge crack in a half space was used to assess the accuracy of the methods for determining higher order coefficients, the results for which are presented in Tables 8.1 and 8.2. The analytical solution for the higher order coefficients given is easier to apply but the round-off error limits the number of terms computed whereas, the numerical solution is not easy to calculate but the computer round-off error does not affect solution accuracy easily.

Several other numerical examples were considered:

1. Edge crack in a strip subjected constant, linear, quadratic and cubic shear loads.
2. Symmetric internal crack in a strip only subjected to constant shear load.
3. Edge crack in a strip subjected to end shear.
4. Internal crack in a strip subjected to end shear.

Accurate higher order coefficents were calculated for all these examples which emphasizes the strength of this method. In the last example, although the right tip of the internal crack begins to close ie., $\bar{k}_n^I(b) = 0.0$, the remaining higher order terms were also determined in a straight forward manner using the same method.

References

1. B. Ananthasayanam, M. Capitaneanu, PF. Joseph, Determination of higher order coefficients and zones of dominance using a singular integral equation approach, Engineering Fracture Mechanics, 2007;74:2099-2131.
2. Williams, ML. On the Stress Distribution at the Base of a Stationary Crack", ASME Journal of Applied Mechanics. 1957;24:111-114.
3. Karihaloo, BL and Xiao, QZ. Accurate determination of the coefficients of elastic crack tip asymptotic field by a hybrid crack element with p-adaptivity. Engineering Fracture Mechanics. 2001;68:1609-1630.

4. Song, C. Evaluation of power-logarithmic singularities, T-stresses and higher order terms of in-plane singular stress fields at cracks and multi-material corners. 2005;72:1498-1530.

5. Seed, GM and Nowell, D. Use of the distributed dislocation method to determine the T-stress. Fatigue and Fracture of Engineering Materials and Structures. 1994;17:605-618.

6. Olsen, PC. Determining the stress intensity factors K_I, K_{II} and T term via the conservation laws using the boundary element methods. Engineering Fracture Mechanics. 1994;49:49-60.

7. Fett, T. T-stresses in rectangular plates and circular disks. Engineering Fracture Mechanics. 1998;60:631-652.

8. Karihaloo, BL and Xiao, QZ. Higher order terms of the crack tip asymptotic field for a notched three-point bend beam. International Journal of Fracture. 2001;112:111-128.

9. Xiao, QZ, Karihaloo, BL and Liu, XY. Direct determination of SIF and higher order terms of mixed mode cracks by a hybrid crack element. International Journal of Fracture. 2004;125:207-225.

10. Kaya, AC and Erdogan, F. Integral equations with strongly singular kernels. Quarterly of Applied Mathematics. 1987;45:105-122.

11. Erdogan, F and Joseph, PF. Mechanical Modeling of Multilayered Films on an Elastic Substrate, - Part II: Results and Discussion. ASME Journal of Electronic Packaging, 1990;112:317-326.

12. Abramowitz, M and Stegun, IA. Handbook of mathematical functions. 1972. Dover.

13. Tricomi, FG. On the finite Hilbert transformation. Quarterly Journal of Mathematics, Oxford ser. (2). 1951;2:199-211.

14. Cordes RD, and Joseph, PF. Surface and Internal Cracks in a Residually Stressed Plate. International Journal of Fracture. 1995;68:287-314.

CHAPTER NINE

Conclusions and Future Work

In this dissertation, the results of research done in two parallel directions are presented; the first involves the prediction of the final size and shape of a glass lens during a precision glass lens molding process and the second introduces a method to compute and quantify the importance of higher order terms in fracture mechanics for different modes of fracture.

9.1. Conclusions

A mathematical model was developed to simulate the precision lens molding process taking into account process details and the complex material behavior of glass to predict the final profile deviation of the lens with micron level accuracy. The important processing stages included in the model are heating, soaking, pressing, gap creation and cooling. The most important material behaviors of glass are the strongly temperature dependent viscoelastic behavior and structural relaxation. Structural relaxation behavior is nothing but a time-dependent thermal expansion behavior and is modeled in ABAQUS using user defined subroutines. The main objective of this research is to identify the key material properties and process parameters that can affect the final deviation. This comprehensive study will not only eliminate some of the parameters which have the least effect on the final size/shape, but also identify the key material properties and substantiate the need to obtain them more accurately through experimentation. At this time it should be mentioned that the some of the material and interface properties needed for the simulation of the molding process are not available in the literature.

Friction coefficient at the mold/glass interface is one of the important input parameters in the model. A ring compression test was used in the current research to find the friction coefficient. In this test, a “washer” or a ring shaped specimen is compressed between two

flat dies at the molding temperature and the change in internal diameter is correlated to a friction coefficient. The main strength of this test is the sensitive nature of the inner diameter change during pressing for different friction conditions at the interface, i.e. for two cases with slightly different friction behavior at their interface, the internal diameter change will be significantly different. The TOSHIBA lens molding machine was used with flat top and bottom molds to conduct the ring compression tests and a set of curves called the friction calibration curves were generated using finite elements for the different friction coefficients. The experimental data was close to the curve associated with a friction coefficient of 0.04 and hence this value was concluded to be the friction coefficient between L-BAL35 glass and DLC coated Tungsten Carbide mold. In addition to friction coefficient, approximate viscoelastic material properties and the TRS behavior were also determined using this test from the force and displacement data. The viscosity information obtained from the viscoelastic characterization using the ring compression test is very close to the experimental viscosity of L-BAL35 at the molding temperature.

Once the model was defined and validated for a known glass type, a sensitivity analysis on deviation was performed for various material properties and process parameters after validation and convergence were checked and the following important conclusions were made:

1. Deviation arises from both the thermal expansion behavior and the evolving stress state within glass during the course of molding.
2. Structural relaxation mechanism (time-dependent thermal expansion) in glass and thermal expansion of molds are the primary reasons for the deviation in the molded lens. Specifically, the activation energy constant $\Delta H/R$ and time constant parameter τ_0 are the key parameters of structural relaxation that affect deviation. Hence, glasses with different values of these parameters must be compensated differently. Clearly from a computational point of view, it

is essential to have the structural relaxation parameters well defined in order to predict the deviation within tolerance.

3. Internal stresses can also affect the deviation. The evolving internal stresses within glass can be affected by changing
    a. the TRS behavior of glass,
    b. friction at the glass/mold interface,
    c. the temperature at which the gap is created,
    d. the process parameters such as molding temperature and pressing force profile and cooling profile.

    Therefore characterizing the TRS material behavior near the molding temperature is crucial for accurate prediction of deviation. Also knowledge of when the gap is created, the molding temperature, the force profile and cooling profiles are important in predicting the deviation. These are readily available from the machine after the molding process is completed.
4. The deviation is sensitive to the location of the lens within the gap that is created in between the two cooling stages. In the molding process after this gap is created, the freshly molded lens mostly rests on the bottom mold, but sometimes "sticks" to the top mold. From the simulations, it was concluded that there is non-negligible difference in deviation between the two situations and might be one of the reasons for difficulty in mold compensation.
5. Finally, the process of mold compensation is demonstrated using the computational tool. It was found that if the lens rests on the bottom mold during the first attempt and then sticks to the top during the second attempt (after one compensation), it does not produce zero deviation in the lens and more than two attempts are required to achieve the tolerance of 0.5 microns.

In the research done in the other parallel direction that was done prior to the lens molding project, a method to determine higher order coefficients in fracture mechanics for mode I and mode II type fracture from the solution of a singular integral equation is presented. The coefficients are defined by

$$\sigma_{rr}(r,0)=\sum_{n=0}^{\infty} k_n (2r)^{n-\frac{1}{2}} + T_n (2r)^n ,$$

which gives the radial stress at a distance, r, in front of the crack tip. In this asymptotic series the stress intensity factor, k_0 is the first coefficient, and the T-stress, T_0 is the second coefficient. While this method is not versatile in handling complicated geometry, it is very accurate. Up to 12 higher order coefficients for the following problems have been determined to demonstrate the strength of this method:

1. Edge crack in a half space subjected to far field tension and pure shear loading
2. Edge crack in a strip subjected to constant, linear, quadratic and cubic type loading in the normal and shear.
3. Edge and internal crack in a strip subjected to end shear loading.

Finally, the size of the k-dominant zone, the kT-dominant zone and the zones associated with three and four terms are quantified, taking into account the entire region around the crack tip.

The following points are emphasized in this study:

1. the accurate determination of the mode I and mode II higher order coefficients as defined by Equations (1) and (2) in Chapter 7,
2. the comparison of the corresponding asymptotic fields to accurate full-field solutions.
3. Given the accurate values of the higher order coefficients, the size of the zone in which an asymptotic series can adequately represent the stress field can be determined by a

comparison with the full-field solution, which is obtained from the singular integral equation solution. This concept of a zone of dominance is fundamental to a continuum mechanics approach to fracture mechanics, in which a single or perhaps multiple parameters are used in a fracture criterion.

9.2. Future Work

1. The lens molding program can be used for applications beyond the final shape/size prediction. For example, birefringence which is very important to the optical designers, can be post-processed from the residual stress state in lens. The process parameters in the simulations can also be modified to study the variation of birefringence to these parameters.
2. The lens molding computational tool can be extended to study cracking issues in the lens during molding. The idea is to stop the analysis when the glass transitions form viscoelastic to elastic. Then, import the molded lens geometry and its stress state in ABAQUS CAE. Manually place minute flaws (one or many, with different orientations) in the form of "seam cracks" and restart the cooling analysis. Since glass will be elastic, the time dependence need not be taken into account and the restart is trivial. Depending on the stress intensity factor and the stress state the flaw or cracks may or may not propagate. Crack growth can be studies for various material and process parameters.
3. The stress relaxation parameters should be characterized more accurately, including the volumetric component. While the sensitivity analysis appeared to show that final size and shape are not too sensitive to accuracy in the characterization of stress relaxation, the residual stress state will likely be. Therefore, in order to investigate fracture in glass molded lens, a better characterization is recommended.

4. With respect to fracture mechanics research, the method could be used to determine the higher order coefficients for mixed mode problems, such as a crack parallel to an interface. In the important case of a crack close to an interface, the current method could identify the importance of a non-singular term.

APPENDICES

APPENDIX A

L-BAL35

Code(d) **589612**

Code(e) **591609**

Refractive Index	n_d	**1.58913**	Abbe Number	v_d	**61.2**	Dispersion	n_F-n_C	**0.00963**
		1.589130			61.15			0.009634
Refractive Index	n_e	1.591428	Abbe Number	v_e	60.93	Dispersion	n_F'-$n_{C'}$	0.009706

Refractive Indicies		
λ(μm)		
n_{2325}	2.32542	1.55775
n_{1970}	1.97009	1.56407
n_{1530}	1.52958	1.57069
n_{1129}	1.12864	1.57622
n_t	1.01398	1.57795
n_s	0.85211	1.58085
$n_{A'}$	0.76819	1.58276
n_r	0.70652	1.58448
n_C	0.65627	1.58618
$n_{C'}$	0.64385	1.58665
n_{He-Ne}	0.6328	1.58709
n_D	0.58929	1.58904
n_d	0.58756	1.58913
n_e	0.54607	1.59143
n_F	0.48613	1.59581
$n_{F'}$	0.47999	1.59636
n_{He-Cd}	0.44157	1.60031
n_g	0.435835	1.60100
n_h	0.404656	1.60528
n_i	0.365015	1.61256

Deviation of Relative Dispersions Δθfrom "Normal"	
$\Delta\theta_{C,t}$	0.0207
$\Delta\theta_{C,A'}$	0.0048
$\Delta\theta_{g,d}$	-0.0059
$\Delta\theta_{g,F}$	-0.0043
$\Delta\theta_{i,g}$	-0.0124

Constants of Dispersion Formula	
A_1	1.16262630E+00
A_2	3.25661051E-01
A_3	1.35132486E+00
B_1	1.25957437E-02
B_2	-3.26911050E-03
B_3	1.19214596E+02

Other Properties	
Bubble Quality Group B	
Specific Gravity d	2.82
Remarks	

Partial Dispersions	
n_C-n_t	0.008230
n_C-$n_{A'}$	0.003418
n_d-n_C	0.002952
n_e-n_C	0.005250
n_g-n_d	0.011867
n_g-n_F	0.005185
n_h-n_g	0.004288
n_i-n_g	0.011567
n_C-n_t	0.008702
n_e-$n_{C'}$	0.004778
n_F-n_e	0.004928
n_i-$n_{F'}$	0.016208

Thermal Properties		
Strain Point StP (℃)		489
Annealing Point AP (℃)		520
Transformation Temperature Tg (℃)		527
Yield Point At (℃)		567
Softening Point SP (℃)		619
Expansion Coefficients	(-30~+70℃)	66
α (10^{-7}/℃)	(+100~+300℃)	81
Thermal Conductivity k (W/m·K)		1.126

Mechanical Properties		
Young's Modulus E (10^8N/m^2)	1008	
Rigidity Modulus G (10^8N/m^2)	403	
Poisson's Ratio σ	0.252	
Knoop Hardness Hk[Class]	630	6
Abrasion Aa	100	
Photoelastic Constant β (nm/cm/10^5Pa)		2.29

Chemical Properties	
Water Resistance(Powder) Group RW(P)	2
Acid Resistance(Powder) Group RA(P)	4
Weathering Resistance(Surface) Group W(S)	3
Acid Resistance(Surface) Group SR	52.2
Phosphate Resistance PR	3.2

Temperature Coefficients of Refractive Index							
Range of Temperature (℃)	dn/dt relative (10^{-6}/℃)						
	t	C'	He-Ne	D	e	F'	g
-40~-20	3.9	4.3	4.3	4.4	4.5	4.8	5.1
-20~ 0	3.9	4.3	4.3	4.5	4.6	4.9	5.2
0~20	4.0	4.4	4.4	4.5	4.7	5.0	5.3
20~40	4.0	4.4	4.5	4.6	4.7	5.1	5.4
40~60	4.1	4.5	4.5	4.7	4.8	5.2	5.5
60~80	4.1	4.5	4.6	4.8	4.9	5.2	5.6

Relative Partial Dispersions	
$\theta_{C,t}$	0.8543
$\theta_{C,A'}$	0.3548
$\theta_{d,C}$	0.3064
$\theta_{e,C}$	0.5449
$\theta_{g,d}$	1.2318
$\theta_{g,F}$	0.5382
$\theta_{h,g}$	0.4451
$\theta_{i,g}$	1.2006
$\theta'_{C',t}$	0.8966
$\theta'_{e,C'}$	0.4923
$\theta'_{F',e}$	0.5077
$\theta'_{i,F}$	1.6699

Coloring			
λ_{80}	35	λ_5	30
λ_{70}			

Internal Transmittance	
λ(nm)	τ10mm
280	
290	
300	0.06
310	0.27
320	0.53
330	0.73
340	0.85
350	0.922
360	0.956
370	0.975
380	0.984
390	0.989
400	0.992
420	0.993
440	0.993
460	0.995
480	0.996
500	0.998
550	0.999
600	0.998
650	0.998
700	0.998
800	0.999
900	0.998
1000	0.997
1200	0.997
1400	0.991
1600	0.994
1800	0.989
2000	0.978
2200	0.934
2400	0.81

OHARA 02-06

Appendix B

Asymptotic Stresses and Displacements for Modes I and II types of fracture.

Following the eigenfunction expansion approach of Williams (1952), the in plane stress and displacement components near the tip of a stress free crack can be expressed as follows:

$$\sigma_{ij}(r,\theta) = \sum_{n=0}^{\infty} (2r)^{n-\frac{1}{2}} \left[k_n^{I} f_{ij}^{Ik}(n,\theta) + k_n^{II} f_{ij}^{IIk}(n,\theta) \right] + T_0^{I} f_{ij}^{IT}(0,\theta) + \sum_{n=1}^{\infty} (2r)^{n} \left[T_n^{I} f_{ij}^{IT}(n,\theta) + T_n^{II} f_{ij}^{IIT}(n,\theta) \right], \quad i = r,\theta;\ j = r,\theta, \tag{B.1}$$

$$2\mu u_i(r,\theta) = \sum_{n=0}^{\infty} (2r)^{n+\frac{1}{2}} \left[k_n^{I} g_i^{Ik}(n,\theta) + k_n^{II} g_i^{IIk}(n,\theta) \right] + T_0^{I}(2r) g_i^{IT}(0,\theta) + \sum_{n=1}^{\infty} (2r)^{n+1} \left[T_n^{I} g_i^{IT}(n,\theta) + T_n^{II} g_i^{IIT}(n,\theta) \right], \quad i = r,\theta\,. \tag{B.2}$$

The angular functions with a superscript of "I" are symmetric functions which correspond to mode I, while the superscript of "II" is for the antisymmetric case of mode II. The factor of two multiplying the radial distance r is included so that the n = 0 constants correspond to the standard modes I and II stress intensity factors, $k_0^{I} = K_I/\sqrt{\pi}$ and $k_0^{II} = K_{II}/\sqrt{\pi}$. The relationships between these constants and those of [18] are:

$$k_n^{I} = \frac{(2n+1)}{2^{n-\frac{1}{2}}} a_{2n+1},\ T_n^{I} = \frac{(n+1)}{2^{n-2}} a_{2n+2},\ k_n^{II} = -\frac{(2n+1)}{2^{n-\frac{1}{2}}} b_{2n+1},\ T_n^{II} = \frac{(n+1)}{2^{n-2}} b_{2n+2} \tag{B.3}$$

B.1 Pure mode I

The coefficients, k_n^{I} and T_n^{I}, are defined by the normalizations,

$$f_{\theta\theta}^{Ik}(n,\theta=0) = 1 \text{ and } f_{rr}^{IT}(n,\theta=0) = 1, \quad n = 0,...,\infty, \tag{B.4}$$

which gives

$$f_{rr}^{Ik} = \frac{1}{4}\left\{-(2n-5)\cos\left[\frac{(2n-1)\theta}{2}\right]+(2n-1)\cos\left[\frac{(2n+3)\theta}{2}\right]\right\}$$

$$f_{rr}^{IT} = \frac{1}{4}\left\{-(n-2)\cos(n\theta)+(n+2)\cos[(n+2)\theta]\right\}$$

$$f_{\theta\theta}^{Ik} = \frac{1}{4}\left\{(2n+3)\cos\left[\frac{(2n-1)\theta}{2}\right]-(2n-1)\cos\left[\frac{(2n+3)\theta}{2}\right]\right\}$$

$$f_{\theta\theta}^{IT} = \frac{n+2}{4}\left\{\cos(n\theta)-\cos[(n+2)\theta]\right\}$$

$$f_{r\theta}^{Ik} = \frac{2n-1}{4}\left\{\sin\left[\frac{(2n-1)\theta}{2}\right]-\sin\left[\frac{(2n+3)\theta}{2}\right]\right\}$$

$$f_{r\theta}^{IT} = \frac{1}{4}\left\{n\sin(n\theta)-(n+2)\sin[(n+2)\theta]\right\} \qquad \text{(B.5)}$$

$$g_{r}^{Ik} = \frac{1}{4(2n+1)}\left\{(2\kappa-2n-1)\cos\left[\frac{(2n-1)\theta}{2}\right]+(2n-1)\cos\left[\frac{(2n+3)\theta}{2}\right]\right\}$$

$$g_{r}^{IT} = \frac{1}{8(n+1)}\left\{(\kappa-n-1)\cos(n\theta)+(n+2)\cos[(n+2)\theta]\right\}$$

$$g_{\theta}^{Ik} = \frac{1}{4(2n+1)}\left\{(2\kappa+2n+1)\sin\left[\frac{(2n-1)\theta}{2}\right]-(2n-1)\sin\left[\frac{(2n+3)\theta}{2}\right]\right\}$$

$$g_{\theta}^{IT} = \frac{1}{8(n+1)}\left\{(\kappa+n+1)\sin(n\theta)-(n+2))\sin[(n+2)\theta]\right\}. \qquad \text{(B.6)}$$

B.2. Pure mode II.

There are two key differences between the symmetric and antisymmetric forms of the T_n terms. First, in the antisymmetric case the T_n^{II} coefficient for n = 0 does not exist. Second, the stress components along the line of the crack associated with T_n^{II} are zero, and therefore, these coefficients are defined by a displacement component. The normalizations used for the mode II coefficients are

$$f_{r\theta}^{IIk}(n,\theta=0)=1,\ n=0,...,\infty \quad \text{and} \quad g_{\theta}^{IIT}(n,\theta=\pm\pi)=\frac{\kappa+1}{8(n+1)}(-1)^n,\ n=1,...,\infty, \qquad \text{(B.7)}$$

which results in the mode II eigenfunctions:

$$f_{rr}^{IIk} = \frac{1}{4}\left\{-(2n-5)\sin\left[\frac{(2n-1)\theta}{2}\right] + (2n+3)\sin\left[\frac{(2n+3)\theta}{2}\right]\right\}$$

$$f_{rr}^{IIT} = \frac{1}{4}\left\{(n-2))\sin(n\theta) - n\sin\left[(n+2)\theta\right]\right\}$$

$$f_{\theta\theta}^{IIk} = \frac{2n+3}{4}\left\{\sin\left[\frac{(2n-1)\theta}{2}\right] - \sin\left[\frac{(2n+3)\theta}{2}\right]\right\}$$

$$f_{\theta\theta}^{IIT} = \frac{1}{4}\left\{-(n+2)\sin(n\theta) + n\sin\left[(n+2)\theta\right]\right\}$$

$$f_{r\theta}^{IIk} = \frac{1}{4}\left\{-(2n-1)\cos\left[\frac{(2n-1)\theta}{2}\right] + (2n+3)\cos\left[\frac{(2n+3)\theta}{2}\right]\right\}$$

$$f_{r\theta}^{IIT} = \frac{n}{4}\left\{\cos(n\theta) - \cos\left[(n+2)\theta\right]\right\}. \qquad \text{(B.8)}$$

$$g_{r}^{IIk} = \frac{1}{4(2n+1)}\left\{(2\kappa-2n-1)\sin\left[\frac{(2n-1)\theta}{2}\right] + (2n+3)\sin\left[\frac{(2n+3)\theta}{2}\right]\right\}$$

$$g_{r}^{IIT} = \frac{1}{8(n+1)}\left\{-(\kappa-n-1)\sin(n\theta) - n\sin\left[(n+2)\theta\right]\right\}$$

$$g_{\theta}^{IIk} = \frac{1}{4(2n+1)}\left\{-(2\kappa+2n+1)\cos\left[\frac{(2n-1)\theta}{2}\right] + (2n+3)\cos\left[\frac{(2n+3)\theta}{2}\right]\right\}$$

$$g_{\theta}^{IIT} = \frac{1}{8(n+1))}\left\{(\kappa+n+1)\cos(n\theta) - n\cos\left[(n+2)\theta\right]\right\}. \qquad \text{(B.9)}$$

B.3. Stresses and displacements along the line of a stress-free crack

Stress and displacement components in front of the crack tip along θ=0 for arbitrary loading are:

$$\sigma_{rr}(r,0) = \sum_{n=0}^{\infty} k_n^{I}(2r)^{n-\frac{1}{2}} + \sum_{n=0}^{\infty} T_n^{I}(2r)^{n} \qquad \text{(B.10)}$$

$$\sigma_{\theta\theta}(r,0) = \sum_{n=0}^{\infty} k_n^{I}(2r)^{n-\frac{1}{2}} \qquad \text{(B.11)}$$

$$\sigma_{r\theta}(r,0) = \sum_{n=0}^{\infty} k_n^{II}(2r)^{n-\frac{1}{2}} \qquad \text{(B.12)}$$

$$2\mu u_r(r,0) = \frac{\kappa-1}{2}\sum_{n=0}^{\infty}\frac{k_n^{I}}{2n+1}(2r)^{n+\frac{1}{2}} + \frac{\kappa+1}{8}\sum_{n=0}^{\infty}\frac{T_n^{I}}{n+1}(2r)^{n+1} \qquad \text{(B.13)}$$

$$2\mu u_\theta(r,0) = -\frac{\kappa-1}{2}\sum_{n=0}^{\infty}\frac{k_n^{II}}{2n+1}(2r)^{n+\frac{1}{2}} + \frac{\kappa+1}{8}\sum_{n=1}^{\infty}\frac{T_n^{II}}{n+1}(2r)^{n+1} \qquad \text{(B.14)}$$

Similarly, the non-zero stresses and displacements along the crack flanks where $\theta = \pm\pi$ are:

$$\sigma_{rr}(r,\pm\pi) = \sum_{n=0}^{\infty}(-1)^n T_n^I (2r)^n \mp 2\sum_{n=0}^{\infty}(-1)^n k_n^{II}(2r)^{n-\frac{1}{2}} \tag{B.15}$$

$$2\mu u_r(r,\pm\pi) = \frac{\kappa+1}{8}\sum_{n=0}^{\infty}(-1)^n \frac{T_n^I}{n+1}(2r)^{n+1} \mp \frac{\kappa+1}{2}\sum_{n=0}^{\infty}(-1)^n \frac{k_n^{II}}{2n+1}(2r)^{n+\frac{1}{2}}, \tag{B.16}$$

$$2\mu u_\theta(r,\pm\pi) = \mp\frac{\kappa+1}{2}\sum_{n=0}^{\infty}(-1)^n \frac{k_n^{I}}{2n+1}(2r)^{n+\frac{1}{2}} + \frac{\kappa+1}{8}\sum_{n=1}^{\infty}(-1)^n \frac{T_n^{II}}{n+1}(2r)^{n+1}. \tag{B.17}$$

In all of the quantities in (B.10-17), even though the loading is mixed, there is only one arbitrary constant associated with a given power of r. Therefore any of these quantities can be used to determine a set of constants which appear in the expression. For example, u_r and u_θ along the crack flanks can be used to determine all of the coefficients, i.e., T_n^I and k_n^{II} from (B.15) and k_n^I and T_n^{II} from (B.17).

Other important quantities along the line of the crack are the crack opening displacement for mode I and the crack shift displacement for mode II. These are given by:

$$COD = u_y^+ - u_y^- = -u_\theta^+ + u_\theta^- = \frac{\kappa+1}{2\mu}\sum_{n=0}^{\infty}(-1)^n \frac{k_n^I}{2n+1}(2r)^{n+\frac{1}{2}}. \tag{B.18}$$

$$CSD = u_x^+ - u_x^- = -u_r^+ + u_r^- = \frac{\kappa+1}{2\mu}\sum_{n=0}^{\infty}(-1)^n \frac{k_n^{II}}{2n+1}(2r)^{n+\frac{1}{2}}. \tag{B.19}$$

Next the effect of crack surface loading will be considered. For this the superposition in Figure 1in this Appendix will be used to relate the case of stress free crack surfaces presented in Equations (B.1 – B.19) to the case of crack surfaces that are loaded. Since the uncracked problem in Figure 1 does not contribute to the k_n coefficients as demonstrated by (B.18) and (B.19), only the T_n coefficents are altered by crack surface loading. The cases of modes I and II are considered separately.

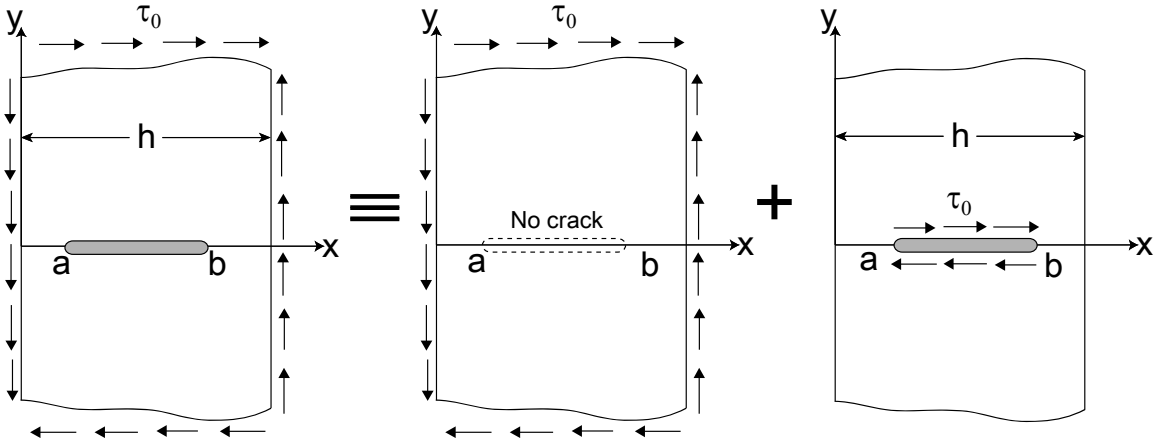

Figure B.1. Application of the principle of superposition to relate the "original" problem on the left, with stress-free crack surfaces, to the uncracked and cracked problems on the right. The cracked problem on the right side has non-zero crack surface loading. The example of constant shear is illustrated above, but the loading in the original problem can be arbitrary, the only requirement being that the crack surface is not loaded.

B.4. Mode I Eigenfunctions associated with $\overline{T}_n^I$ for arbitrary crack surface loads

Referring to Figure 1, given crack surface loading of the form

$$\sigma_{\theta\theta}(r,\pm\pi) = -\sum_{n=0}^{N} \overline{\sigma}_{ny} r^n \tag{B.20}$$

and knowing the σ_x stress for the uncracked problem as

$$\sigma_x(x,0) = \sigma_{rr}(r,\pm\pi) = \sum_{n=0}^{N} \overline{\sigma}_{nx} r^n, \tag{B.21}$$

the stresses and displacements associated with the T-terms are:

$$\sigma_{rr}(r,\theta) = \sum_{n=0}^{\infty} (2r)^n \left[\overline{T}_n^I f_{rr}^{IT}(n,\theta) + (-1)^n \frac{n-2}{n+2} \frac{\overline{\sigma}_{ny}}{2^n} \cos(n\theta) \right] \tag{B.22}$$

$$\sigma_{\theta\theta}(r,\theta) = \sum_{n=0}^{\infty} (2r)^n \left[\overline{T}_n^I f_{\theta\theta}^{IT}(n,\theta) + (-1)^{n+1} \frac{\overline{\sigma}_{ny}}{2^n} \cos(n\theta) \right] \tag{B.23}$$

$$\tau_{r\theta}(r,\theta)=\sum_{n=0}^{\infty}(2r)^n\left[\overline{T}_n^I f_{r\theta}^{IT}(n,\theta)+(-1)^{n+1}\frac{n}{n+2}\frac{\overline{\sigma}_{ny}}{2^n}\sin(n\theta)\right] \tag{B.24}$$

$$2\mu u_r(r,\theta)=\sum_{n=0}^{\infty}(2r)^{n+1}\left[\overline{T}_n^I g_r^{IT}(n,\theta)+(-1)^{n+1}\frac{\overline{\sigma}_{ny}}{2^{n+1}}\frac{\kappa-(n+1)}{(n+1)(n+2)}\cos(n\theta)\right] \tag{B.25}$$

$$2\mu u_\theta(r,\theta)=\sum_{n=0}^{\infty}(2r)^{n+1}\left[\overline{T}_n^I g_\theta^{IT}(n,\theta)+(-1)^{n+1}\frac{\overline{\sigma}_{ny}}{2^{n+1}}\frac{\kappa+(n+1)}{(n+1)(n+2)}\sin(n\theta)\right] \tag{B.26}$$

Note that $\overline{T}_n$ is not the same as T_n in (B.1) and (B.2), i.e., the T-terms are different when the crack is unloaded (in the original problem) compared to when it is loaded in the corresponding superposition problem. As mentioned above, the k-terms are identical for the two cases.

It is required that σ_x along the line of the crack from the original problem equal the superposition of σ_x from the cracked problem with that of the un-cracked problem. This requirement gives:

$$\begin{aligned}\sigma_{rr}(r,\pm\pi)&=\sum_{n=0}^{\infty}(2r)^n T_n^I f_{rr}^{IT}(n,\pm\pi)\\&=\sum_{n=0}^{\infty}(2r)^n\left[\overline{T}_n^I f_{rr}^{IT}(n,\pm\pi)+\frac{n-2}{n+2}\frac{\overline{\sigma}_{ny}}{2^n}\right]+\sum_{n=0}^{N}\frac{\overline{\sigma}_{nx}}{2^n}(2r)^n,\end{aligned} \tag{B.27}$$

which, taking into account (B.4),

$$\sum_{n=0}^{\infty}(-1)^n(2r)^n T_n^I=\sum_{n=0}^{\infty}(2r)^n\left[(-1)^n\overline{T}_n^I+\frac{n-2}{n+2}\frac{\overline{\sigma}_{ny}}{2^n}\right]+\sum_{n=0}^{N}\frac{\overline{\sigma}_{nx}}{2^n}(2r)^n. \tag{B.28}$$

Next defining

$$(-1)^n\hat{T}_n^I=(-1)^n\overline{T}_n^I+\frac{n-2}{n+2}\frac{\overline{\sigma}_{ny}}{2^n}, \tag{B.29}$$

from (B.28)

$$\sum_{n=0}^{\infty}(-1)^n(2r)^n T_n^I = \sum_{n=0}^{\infty}(-1)^n(2r)^n \hat{T}_n^I + \sum_{n=0}^{N}\frac{\overline{\sigma}_{nx}}{2^n}(2r)^n . \tag{B.30}$$

Equating the coefficients of like powers of r gives,

$$(-1)^n T_n^I = (-1)^n \hat{T}_n^I + \frac{\overline{\sigma}_{nx}}{2^n} \tag{B.31}$$

or

$$T_n^I = \hat{T}_n^I + (-1)^n \frac{\overline{\sigma}_{nx}}{2^n} . \tag{B.32}$$

The $\hat{T}_n^I$ constants are obtained as given by the expressions, (42) or (45) from Ananthasayanam, *et al.* [1]. The above expression shows that these constants are identical to the T_n^I constants when $\overline{\sigma}_{nx} = 0$ such as for tension and bending. Otherwise, the above relationship must be used to convert from the crack surface load problem to that of the original problem without crack surface loading. Knowing these constants, from (B.1) and (B.2) all the stresses and displacements can be determined. In order to obtain the $\overline{T}_n^I$ constants, from (B.29)

$$\overline{T}_n^I = \hat{T}_n^I + (-1)^{n+1}\frac{n-2}{n+2}\frac{\overline{\sigma}_{ny}}{2^n} . \tag{B.33}$$

B.5. Mode II Eigenfunctions associated with $\overline{T}_n^{II}$ for arbitrary crack surface loads

Referring to Figure 1, given crack surface loading of the form

$$\sigma_{r\theta}(r,\pm\pi) = -\sum_{n=0}^{N}\overline{\tau}_n r^n \tag{B.34}$$

and knowing u_θ for the uncracked problem as

$$2\mu u_\theta(r,\pm\pi) = -2\mu u_y(x,0) = \sum_{n=0}^{N}\overline{u}_{n\theta} r^{n+1} , \quad x < b , \tag{B.35}$$

the stresses and displacements associated with the T-terms are:

$$\sigma_{rr}(r,\theta) = -\bar{\tau}_0 \sin(2\theta) + \sum_{n=1}^{\infty} (2r)^n \left[\bar{T}_n^{II} f_{rr}^{IIT}(n,\theta) + (-1)^{n+1} \frac{n-2}{n} \frac{\bar{\tau}_n}{2^n} \sin(n\theta) \right] \tag{B.36}$$

$$\sigma_{\theta\theta}(r,\theta) = \bar{\tau}_0 \sin(2\theta) + \sum_{n=1}^{\infty} (2r)^n \left[\bar{T}_n^{II} f_{\theta\theta}^{IIT}(n,\theta) + (-1)^{n} \frac{n+2}{n} \frac{\bar{\tau}_n}{2^n} \sin(n\theta) \right] \tag{B.37}$$

$$\tau_{r\theta}(r,\theta) = -\bar{\tau}_0 \cos(2\theta) + \sum_{n=1}^{\infty} (2r)^n \left[\bar{T}_n^{II} f_{r\theta}^{IIT}(n,\theta) + (-1)^{n+1} \frac{\bar{\tau}_n}{2^n} \cos(n\theta) \right] \tag{B.38}$$

$$2\mu u_r(r,\theta) = -\bar{\tau}_0 r \sin(2\theta) + \sum_{n=1}^{\infty} (2r)^{n+1} \left[\bar{T}_n^{II} g_r^{IIT}(n,\theta) + (-1)^{n} \frac{\bar{\tau}_n}{2^{n+1}} \frac{\kappa-(n+1)}{n(n+1)} \sin(n\theta) \right] \tag{B.39}$$

$$2\mu u_\theta(r,\theta) = -\bar{\tau}_0 r \cos(2\theta) + \sum_{n=1}^{\infty} (2r)^{n+1} \left[\bar{T}_n^{II} g_\theta^{IIT}(n,\theta) + (-1)^{n+1} \frac{\bar{\tau}_n}{2^{n+1}} \frac{\kappa+(n+1)}{n(n+1)} \cos(n\theta) \right] \tag{B.40}$$

It is required that u_θ along the line of the crack from the original problem equal the superposition of u_θ from the cracked problem with that of the un-cracked problem. This requirement gives:

$$\begin{aligned} 2\mu u_\theta(r,\pm\pi) &= \frac{\kappa+1}{8} \sum_{n=1}^{\infty} (-1)^n \frac{T_n^{II}}{n+1} (2r)^{n+1} \\ &= -\bar{\tau}_0 r + \sum_{n=1}^{\infty} (2r)^{n+1} \left[\bar{T}_n^{II} (-1)^n \frac{\kappa+1}{8(n+1)} - \frac{\bar{\tau}_n}{2^{n+1}} \frac{\kappa+(n+1)}{n(n+1)} \right] + \sum_{n=0}^{N} \frac{\bar{u}_{n\theta}}{2^{n+1}} (2r)^{n+1} \end{aligned} \tag{B.41}$$

Next, for n > 0, defining

$$\frac{\kappa+1}{8}(-1)^n \frac{\hat{T}_n^{II}}{n+1} = \bar{T}_n^{II}(-1)^n \frac{\kappa+1}{8(n+1)} - \frac{\bar{\tau}_n}{2^{n+1}} \frac{\kappa+(n+1)}{n(n+1)}, \tag{B.42}$$

from (B.41)

$$\frac{\kappa+1}{8}\sum_{n=1}^{\infty}(-1)^n\frac{T_n^{II}}{n+1}(2r)^{n+1}=-\overline{\tau}_0 r+\frac{\kappa+1}{8}\sum_{n=1}^{\infty}(-1)^n\frac{\hat{T}_n^{II}}{n+1}(2r)^{n+1}+\sum_{n=0}^{N}\frac{\overline{u}_{n\theta}}{2^{n+1}}(2r)^{n+1}.$$

(B.43)

Equating the coefficients of like powers of r gives for n > 0,

$$\frac{\kappa+1}{8}(-1)^n\frac{T_n^{II}}{n+1}=\frac{\kappa+1}{8}(-1)^n\frac{\hat{T}_n^{II}}{n+1}+\frac{\overline{u}_{n\theta}}{2^{n+1}},$$ (B.44)

or

$$T_n^{II}=\hat{T}_n^{II}+(-1)^n\frac{4}{\kappa+1}\frac{n+1}{2^n}\overline{u}_{n\theta}.$$ (B.45)

For the case of n = 0, from (B.1) and (B.2), $T_0^{II}=0$. The program, however, will determine a non-zero value of $\hat{T}_0^{II}$. In this case the coefficient of r associated with the even portion of u_θ is made zero by satisfying rigid body rotation in the superposition of the cracked and un-cracked problems (right hand side of Figure 1).

The $\hat{T}_n^{II}$ constants are obtained as given by the expressions, (41) or (42). The above expression shows that these constants are identical to the T_n^{II} constants when $\overline{u}_{n\theta}=0$. Otherwise, the above relationship must be used to convert from the crack surface load problem to that of the original problem without crack surface loading. Knowing these constants, from (B.1) and (B.2) all the stresses and displacements can be determined. In order to obtain the $\overline{T}_n^{II}$ constants, from (B.42)

$$\overline{T}_n^{II}=\hat{T}_n^{II}+(-1)^n 4\frac{\kappa+n+1}{n(\kappa+1)}\frac{\overline{\tau}_n}{2^n}.$$ (B.46)

B.6. Mode I Eigenfunctions associated with $\overline{T}_n^I$ for arbitrary crack surface loads using displacements.

Referring to Figure 1, given crack surface loading of the form

$$\sigma_{\theta\theta}(r,\pm\pi) = -\sum_{n=0}^{N} \overline{\sigma}_{ny} r^n \tag{B.47}$$

and knowing the u_r displacement for the un-cracked problem as

$$2\mu u_r(r,\pm\pi) = \sum_{n=0}^{N} \overline{u}_{nr} r^{n+1}, \tag{B.48}$$

the stresses and displacements associated with the T-terms are defined in equations (B.22-B.26).

It is required that u_r along the line of the crack from the original problem equal the superposition of u_r from the cracked problem with that of the un-cracked problem. This requirement gives:

$$\begin{aligned} 2\mu u_r(r,\pm\pi) &= \frac{\kappa+1}{8}\sum_{n=1}^{\infty}(-1)^n \frac{T_n^I}{n+1}(2r)^{n+1} \\ &= \sum_{n=0}^{\infty}(2r)^{n+1}\left[\overline{T}_n^I(-1)^n\frac{\kappa+1}{8(n+1)} - \frac{\overline{\sigma}_n}{2^{n+1}}\frac{\kappa-(n+1)}{(n+1)(n+2)}\right] + \sum_{n=0}^{N}\frac{\overline{u}_{nr}}{2^{n+1}}(2r)^{n+1} \end{aligned} \tag{B.49}$$

Next, for n ≥ 0, defining

$$\frac{\kappa+1}{8}(-1)^n\frac{\hat{T}_n^I}{n+1} = \overline{T}_n^I(-1)^n\frac{\kappa+1}{8(n+1)} - \frac{\overline{\sigma}_n}{2^{n+1}}\frac{\kappa-(n+1)}{(n+1)(n+2)}, \tag{B.50}$$

from (B.49)

$$\frac{\kappa+1}{8}\sum_{n=1}^{\infty}(-1)^n\frac{T_n^I}{n+1}(2r)^{n+1} = \frac{\kappa+1}{8}\sum_{n=1}^{\infty}(-1)^n\frac{\hat{T}_n^I}{n+1}(2r)^{n+1} + \sum_{n=0}^{N}\frac{\overline{u}_{nr}}{2^{n+1}}(2r)^{n+1}. \tag{B.51}$$

Equating the coefficients of like powers of r gives for n ≥ 0,

$$\frac{\kappa+1}{8}(-1)^n \frac{T_n^I}{n+1} = \frac{\kappa+1}{8}(-1)^n \frac{\hat{T}_n^I}{n+1} + \frac{\overline{u}_{nr}}{2^{n+1}}, \tag{B.52}$$

or

$$T_n^I = \hat{T}_n^I + (-1)^n \frac{4}{\kappa+1}\frac{n+1}{2^n}\overline{u}_{nr}. \tag{B.53}$$

Appendix C

Kernels for edge or internal cracked strip under Mode-I loading

Given the following form for stresses along the line of the crack,

$$\sigma_{yy}(x,0) = \frac{4\mu}{\pi(\kappa+1)}\int_a^b \frac{dv}{dt}\left[\frac{1}{(t-x)} + K(x,t)\right]dt\,, \tag{C.1}$$

$$\sigma_{xx}(x,0) = \frac{4\mu}{\pi(\kappa+1)}\int_a^b \frac{dv}{dt}\left[\frac{1}{(t-x)} + L(x,t)\right]dt\,, \tag{C.2}$$

the kernels are given by:

$$K(x,t) = \frac{-1}{(t+x)} + \frac{6x}{(t+x)^2} - \frac{4x^2}{(x+t)^3} + \frac{1}{(x+t-2h)} + \frac{2(t-h)(x-t)}{(x+t-2h)^3} + K_\infty(x,t)\,, \tag{C.3}$$

$$L(x,t) = \frac{-1}{(t+x)} - \frac{2x}{(t+x)^2} + \frac{4x^2}{(x+t)^3} + \frac{1}{(x+t-2h)} - \frac{2(t-h)(t+3x-4h)}{(x+t-2h)^3} + L_\infty(x,t)\,, \tag{C.4}$$

where

$$K_\infty(x,t) = \int_0^\infty \left[s_{y\infty}(x,t,\alpha) - s_{y\infty}(h-x,h-t,\alpha) + s_y(x,t,\alpha) - s_y(h-x,h-t,\alpha)\right]d\alpha\,, \tag{C.5}$$

$$L_\infty(x,t) = \int_0^\infty \left[s_{x\infty}(x,t,\alpha) - s_{x\infty}(h-x,h-t,\alpha) + s_x(x,t,\alpha) - s_x(h-x,h-t,\alpha)\right]d\alpha\,, \tag{C.6}$$

and

$$s_{x\infty}(x,t,\alpha) = \frac{\alpha e^{-\alpha(x+t)}}{D}\begin{Bmatrix} e^{-2\alpha h}(2tx\alpha - x + t) - 8\alpha^3 h^2 xt - 4\alpha^2 h^2 (t-x) \\ -\alpha(2hx + 2tx + 2th - 2h^2) - (t-x) \end{Bmatrix}, \tag{C.7}$$

$$s_x(x,t,\alpha) = \frac{e^{\alpha(x-t)}}{D}\left\{e^{-2\alpha h}\alpha(x-t) - 4th\alpha^2(x-h) + 2\alpha h(x+t-h) + (t-x)\right\}, \tag{C.8}$$

$$s_{y\infty}(x,t,\alpha)=\frac{e^{-\alpha(x+t)}}{D}\begin{Bmatrix}-e^{-2\alpha h}\left(2\alpha^2xt-\alpha(x+3t)+2\right)+8\alpha^4h^2xt-4\alpha^3h^2(x+3t)\\+2\alpha^2\left[hx+3h^2+xt+ht\right]-\alpha\left[x+3t+4h\right]+2\end{Bmatrix},$$

(C.9)

$$s_y(x,t,\alpha)=\frac{e^{\alpha(x-t)}}{D}\begin{Bmatrix}e^{-2\alpha h}\left[\alpha(t-x)-2\right]-\alpha^3\left[4h^2t-4hxt\right]+2h\alpha^2(h+3t-x)\\+\alpha(x-t-4h)+2\end{Bmatrix}, \quad \text{(C.10)}$$

$$D=e^{2\alpha h}-4\alpha^2h^2-2+e^{-2\alpha h} \quad . \quad \text{(C.11)}$$

Appendix D

Kernels for edge or internal cracked strip under Mode-II loading

Given the following form for shear stress and vertical displacement along the line of the crack,

$$\tau_{xy}(x,0)=\frac{2\mu}{\pi(\kappa+1)}\int_a^b \phi(t)\left[\frac{1}{(t-x)}+K(x,t)-K(h-x,h-t)-K_\infty(x,t)\right]dt \tag{D.1}$$

$$\frac{\pi(1+\kappa)}{2}v(x,0)=\frac{1-\kappa}{4}\int_a^b \frac{U(t)}{t-x}dt+\int_a^b U(t)\left[M(x,t)-M(h-x,h-t)+M_\infty(x,t)\right]dt, \tag{D.2}$$

the kernels are given by:

$$K(x,t)=\frac{-1}{(t+x)}+\frac{6x}{(t+x)^2}-\frac{4x^2}{(x+t)^3}, \tag{D.3}$$

$$M(x,t)=\left[\frac{1}{4}\frac{\kappa-1}{(t+x)}-\frac{x}{2}\frac{(3+\kappa)}{(t+x)^2}+\frac{2x^2}{(t+x)^3}\right], \tag{D.4}$$

$$K_\infty(x,t)=\int_0^\infty \left[s_k(x,t,\alpha)-s_k(h-x,h-t,\alpha)+s_{k\infty}(x,t,\alpha)-s_{k\infty}(h-x,h-t,\alpha)\right]d\alpha \tag{D.5}$$

$$M_\infty(x,t)=\int_0^\infty \left[s_m(x,t,\alpha)-s_m(h-x,h-t,\alpha)+s_{m\infty}(x,t,\alpha)-s_{m\infty}(h-x,h-t,\alpha)\right]d\alpha, \tag{D.6}$$

where

$$s_k(x,t,\alpha)=\frac{e^{\alpha(t-x)}\alpha}{D}\begin{Bmatrix}e^{-2\alpha h}\alpha(t-x)+4\alpha^3hx(h-t)+2h\alpha^2(t+x-h)\\+\alpha(x-t)\end{Bmatrix},$$

$$s_{k\infty}(x,t,\alpha)=\frac{e^{-\alpha(x+t)}\alpha}{D}\begin{Bmatrix}e^{-2\alpha h}\left(2\alpha^2xt+\alpha(x-t)\right)-8\alpha^4h^2xt+4\alpha^3h^2(t-x)\\-2\alpha^2(xh+tx+th-h^2)+\alpha(t-x)\end{Bmatrix}, \tag{D.7}$$

$$s_m(x,t,\alpha)=\frac{e^{\alpha(x-t)}}{2D}\begin{Bmatrix} e^{-2\alpha h}\left(\alpha(x-t)+\frac{1}{2}(\kappa+1)\right)+4\alpha^3 th(h-x) \\ +2\alpha^2 h(x-t\kappa-h)+\alpha(t+h+h\kappa-x)-\frac{1}{2}(\kappa+1) \end{Bmatrix}$$

$$s_{m\infty}(x,t,\alpha)=\frac{e^{-\alpha(x+t)}}{2D}\begin{Bmatrix} e^{-2\alpha h}\left(2\alpha^2 xt-\alpha(x+t\kappa)+\frac{1}{2}(\kappa+1)\right)-8\alpha^4 h^2 xt+4\alpha^3 h^2(x+t\kappa) \\ -2\alpha^2(xt+hx+th+\kappa h^2)+\alpha(x+h+t\kappa+h\kappa)-\frac{1}{2}(\kappa+1) \end{Bmatrix}$$

(D.8)

$$D=e^{2\alpha h}-4\alpha^2 h^2-2+e^{-2\alpha h} \tag{D.9}$$